

**Best  
Available  
Copy**

AD-A280 609

AGE

Form Approved  
OMB No. 0704-0188Please read the instructions  
for preparing and submitting  
information to the  
Department of Defense  
Collection of Information  
and Reports (DODCIR)Include the time for reviewing instructions, searching existing data sources,  
for information, send comments regarding this burden estimate or any other aspect of this  
questionnaire, including suggestions for reducing the burden, to Washington, DC 20503  
Agencies: Paperwork Reduction Project (0704-0188) Washington, DC 20503

## 1. AGENCY USE

2. REPORT DATE  
6/30/94

## 3. REPORT TYPE AND DATES COVERED

Final Report 7/01/90 - 6/30/94

## 4. TITLE AND SUBTITLE

Diamond Deposition and Defect Chemistry Studied Via  
Solid State NMR

## 5. FUNDING NUMBERS

N00014-90-J-1901

## 6. AUTHOR(S)

Karen K. Gleason

## 7. PERFORMING ORGANIZATION NAME(S) AND ADDRESS(ES)

M.I.T. Department of Chemical Engineering  
Cambridge, MA 021398. PERFORMING ORGANIZATION  
REPORT NUMBER

9181AL

## 9. SPONSORING / MONITORING AGENCY NAME(S) AND ADDRESS(ES)

Max N. Yoder, ONR-3140, Room 607  
Department of the Navy  
Office of Naval Research  
800 North Quincy Street  
Arlington, VA 22217-566010. SPONSORING / MONITORING  
AGENCY REPORT NUMBER

## 11. SUPPLEMENTARY NOTES

## 12a. DISTRIBUTION / AVAILABILITY STATEMENT

Approved for public release; distribution unlimited.

## 12b. DISTRIBUTION CODE

## 13. ABSTRACT (Maximum 200 words)

Diamond defects were quantified by nuclear magnetic resonance (NMR). While maintaining the macroscopic integrity of the films, concentrations between 0.001 and 1.0 at.% H were measured, among the lowest ever reported by solid-state  $^1\text{H}$  NMR. These concentrations were correlated to infrared absorption in the 8 to 10 micron region and to thermal conductivity. Despite the low concentrations, Multiple Quantum NMR reveals a high degree of hydrogen clustering consistent with grain boundary passivation. Most hydrogen is rigidly held, but some, probably in  $-\text{OCH}_3$  and  $-\text{NCH}_3$  defects, undergoes rotation at room temperature. Similar results were obtained for hot-filament, microwave-plasma and DC arc-jet films, suggesting a common surface chemistry, but no hydrogen was detected in an as-deposited combustion film.  $^{13}\text{C}$  NMR provided the first quantitative determination of non-diamond bonded carbon defects, providing a benchmark for Raman spectroscopy, the primary characterization method for diamond. Selective  $^{13}\text{C}$  labeling demonstrated heterogeneous reactions involving carbon occur at the hot-filament. With high-speed magic-angle-spinning  $^{19}\text{F}$  NMR,  $\text{CF}_x$  ( $x=1-3$ ) functionalities were resolved on the surface of plasma-treated diamond powder. Understanding these defects impacts the understanding of film growth mechanisms and structure-property relationships for CVD diamond.

## 14. SUBJECT TERMS

Diamond, NMR, CVD, Defects, Thin Films, Isotopic Substitution

## 15. NUMBER OF PAGES

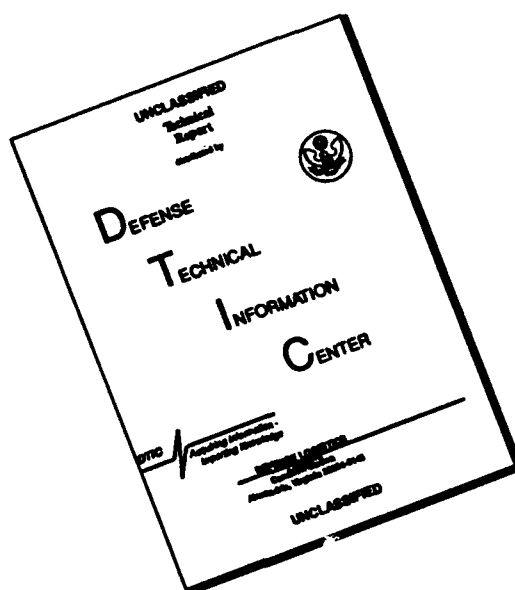
## 16. PRICE CODE

17. SECURITY CLASSIFICATION  
OF REPORT  
UNCLASSIFIED18. SECURITY CLASSIFICATION  
OF THIS PAGE  
UNCLASSIFIED19. SECURITY CLASSIFICATION  
OF ABSTRACT  
UNCLASSIFIED20. LIMITATION OF ABSTRACT  
UL

94-19081

94 6 22 007

# DISCLAIMER NOTICE



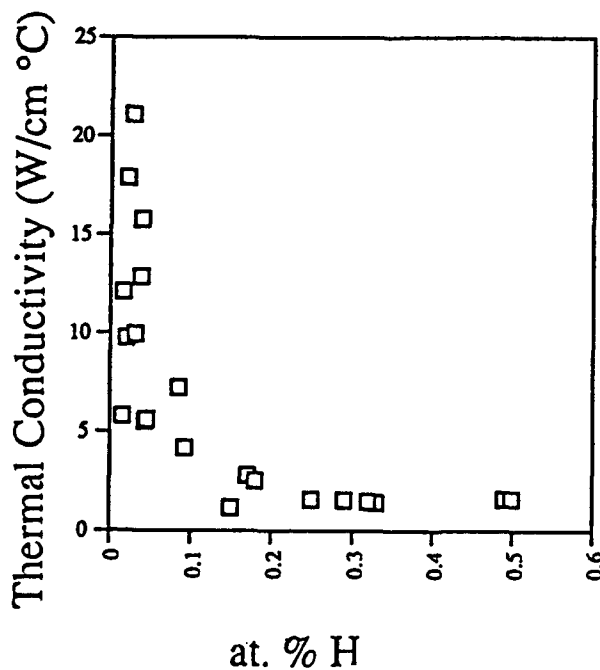
**THIS DOCUMENT IS BEST QUALITY AVAILABLE. THE COPY FURNISHED TO DTIC CONTAINED A SIGNIFICANT NUMBER OF PAGES WHICH DO NOT REPRODUCE LEGIBLY.**

## INTRODUCTION

A unique approach to studying chemical bonding environments in diamond thin films on  $<10 \text{ \AA}$  scale is the use of solid-state nuclear magnetic resonance (NMR). Since conventional surface science studies of diamond surfaces are difficult, NMR has proved particularly valuable for examining hydrogen on diamond surfaces. Understanding the incorporation of hydrogen into polycrystalline films may elucidate some of the mechanisms responsible for film growth and provide insight into structure-property relationships for CVD diamond. In addition,  $^{13}\text{C}$  and  $^{19}\text{F}$  nuclei were used as probes of diamond defect chemistry. A summary of these results and related work supported by this contract follows below with details provided in copies of the publications which are attached.

### $^1\text{H}$ NMR

Hydrogen is commonly a key reactant for diamond film growth. Using NMR, my group has detected as little as 0.001 at. % H in diamond films. We have investigated how deposition and subsequent thermal treatments alter these hydrogenated defects. Significantly, our NMR measured hydrogen contents correlate with the optical absorption of polycrystalline diamond in the 8 to 10 micron wavelength infrared region, where transparency is desired. We have also correlated the distribution of hydrogen to the electrical resistivity and thermal conductivity of polycrystalline diamond films. This latter data has not yet been published, but is shown below.



Accession For	
NTIS	CRA&I
DTIC	TAB
Unannounced	
Justification	
By	
Distribution /	
Availability Codes	
Dist	Avail and/or Special
A-1	

Films remain intact during analysis since our  $^1\text{H}$  NMR probe was specially designed to accept 0.5 cm by 2.0 cm sections of films deposited onto silicon or free standing films of similar size. Using multiple pieces can provide  $> 100\text{ cm}^2$  of single crystalline surface area per sample. By not employing a conventional NMR sample tube or rotor, background signal is minimized and the macroscopic integrity of thin-film samples is maintained. Gas purging and surface cleaning procedures were also developed with the aim of minimizing background hydrogen signals. With the methodology we have detected as few as  $3.5 \times 10^{16}$  protons/sample, corresponding to nearly monolayer detection on a single crystal surface when  $>100\text{ cm}^2$  of single crystal surface area resides in the probe.

A typical  $^1\text{H}$  spectra of diamond is well represented by two components, a narrow Lorentzian and a broad Gaussian, indicating at least two different bonding configurations for hydrogen in polycrystalline diamond. In CVD diamond with relatively high hydrogen concentrations, often only the broad feature can be resolved. Similar contents and lineshapes have been found in films produced by hot-filament, microwave plasma and DC arc-jet deposition methods. However, no hydrogen was detected by NMR in the as-deposited combustion film. Thus, the diamond surfaces and grain boundaries produced under hot-filament and combustion chemical vapor deposition (CVD) differ. Exposure to a hydrogen plasma while holding the combustion-deposited film at  $800^\circ\text{C}$ , produces a significant hydrogen concentration which can be detected by NMR. This concentration is consistent with the passivation of grain boundary sites. In addition, the NMR spectrum of plasma treated film exhibits a narrow and a broad component, as typically seen for hot-filament CVD materials. Since bulk diffusivity is likely to be slow, the hydrogen plasma treatment most likely passivates grain boundary sites in the film. In addition, its fast, non-exponential  $^1\text{H}$  NMR spin-lattice relaxation indicates direct communication between protons and relaxation centers, suggesting that paramagnetic surface states are also present at the grain boundaries. Since hydrogen atoms are very mobile in diamond films at  $800^\circ\text{C}$ , passivation of defects containing unpaired electrons is possible. The degree of such passivation is expected to strongly influence hopping conduction of electrons in diamond films.

A "hole-burning" NMR experiment showed these two resolved hydrogen environments are in close proximity. When a 1 kHz wide region, 20 kHz from the center of the lineshape, was selectively saturated, uniform attenuation of both components is observed after a 2 ms delay. This indicates rapid dipolar communication occurs between protons in the two environments, requiring internuclear distances of  $<5\text{\AA}$ . At 100 K, the Lorentzian component is broadened, while the Gaussian component is not significantly affected. Thus, at room temperature, the narrow Lorentzian lineshape results from motional averaging, while the broad Gaussian line indicates

rigidly held hydrogen. The mobile groups are speculated to be  $\text{OCH}_3$  and  $\text{NCH}_3$  at grain boundaries, which also give rise to resolvable CH stretch absorptions in the infrared spectra.

The homonuclear broadening resulting from static distributions of hydrogen bonded in a rigid polycrystalline lattice can be calculated by the van Vleck equation. For polycrystalline diamond samples, if all hydrogen in the Gaussian component were randomly distributed as CH, the resulting linewidth would be more than two orders of magnitude smaller than typically observed values of  $\sim 60$  kHz. Randomly dispersed  $\text{CH}_2$  groups also provide too little homonuclear broadening. These discrepancies indicate locally high hydrogen concentrations, requiring significant segregation of hydrogen in polycrystalline diamond. However, this analysis cannot distinguish between isolated small clusters and larger groupings of spins.

Possible locations for segregation are hydrogen decorated defects and voids within the crystal, a heavily hydrogenated phase stable at the deposition temperature or at the grain boundaries in polycrystalline diamond. If hydrogen was uniformly distributed on a surface, a density of  $3 \times 10^{15} \text{ H/cm}^2$  would be required to give the observed  $\Delta\nu_{1/2} = 60 \text{ kHz}$ . This compares favorably with areal densities of  $3.1 \times 10^{15}$ ,  $2.2 \times 10^{15}$ , and  $1.8 \times 10^{15} \text{ H/cm}^2$  for fully hydrogen passivated, unreconstructed  $\langle 100 \rangle$ ,  $\langle 110 \rangle$  and  $\langle 111 \rangle$  diamond surfaces, respectively.

In order to account for the NMR observed bulk hydrogen incorporation of 0.01 to 0.22 at.%, monolayer hydrogen coverage of films composed of 0.5 to 150  $\mu\text{m}$  cubes is required, dimensions which compare favorably to observed crystallite sizes in CVD films. The structure of hydrogenated surfaces present during growth may resemble those preserved at grain boundaries, which would allow these  $^1\text{H}$  NMR measurements to act as a potential test of surface chemistry models of diamond growth.

The assumption of a surface distribution of hydrogen in polycrystalline diamond films is also supported by multiple quantum (MQ) NMR studies. Using MQ NMR, up to 20 spins were found within a  $\sim 20 \text{ \AA}$  radius despite the very low ( $< 0.1$  at%) bulk hydrogen concentrations in these films. Thus, MQ NMR confirms that large scale clustering of hydrogen occurs in CVD diamond. Further analysis of the MQ data reveals that this hydrogen forms a two-dimensional distribution, consistent with the hypothesis of hydrogen passivation of grain boundaries. Similar MQ data was obtained for both hot-filament and DC arc-jet films, suggesting similar surface chemistry has occurred in both types of reactors.

The hydrogen measurements resulting from this work are among the lowest ever achieved by solid-state NMR. This work has demonstrated the versatility of solid state NMR and has shown general applicability of NMR for studying bulk materials and thin films with low hydrogen content. This capability is important, since hydrogen is an ubiquitous impurity in optoelectronic materials, either as an undesirable contaminate or as intentional component, introduced to passivate defects. Such measurements are difficult, if not impossible, by other techniques. In addition, the ability of MQ NMR to identify the composition of internal surfaces is a powerful new tool for probing the surfaces of polycrystalline diamond films and potentially other polycrystalline and nanocrystalline materials.

### $^{13}\text{C}$ NMR

Our  $^{13}\text{C}$  NMR measurements are the first quantitative determination of non-diamond bonded carbon defects in these diamond films, providing a benchmark for Raman spectroscopy, the primary tool utilized for characterizing diamond. The isotropic chemical shift of  $^{13}\text{C}$  nuclei was used to resolve  $\text{sp}^2$  from  $\text{sp}^3$  bonded carbon. Bulk diamond is characterized by a single resonance at  $36 \pm 2$  ppm relative to tetramethylsilane. The  $\text{sp}^2$  carbon peak generally appears between 120 to 200 ppm, with the lower values observed for amorphous carbon films, while soot gives a peak centered at 189 ppm. The ratio of  $\text{sp}^2/\text{sp}^3$  bonded carbon is quantitatively determined from the ratio of the integrated area under the peaks corresponding to these respective environments and has been experimentally demonstrated for diamond powder and soot mixture of known weight fraction.

Unfortunately,  $\text{sp}^2$  bonded carbon in visibly faceted films produced via hot-filament, DC arc-jet, or microwave plasma CVD is generally below the  $^{13}\text{C}$  NMR detection limit. An  $\text{sp}^2$  resonance has been observed in a hot-filament film of poor morphology and no detectable diamond one-phonon Raman absorption. The static NMR spectra of this film intact on its substrate resolves both broad  $\text{sp}^2$  and  $\text{sp}^3$  peaks at  $\sim 120$  and  $\sim 38$  ppm. The ratio of the areas of these two peaks gives a quantitative  $\text{sp}^2/\text{sp}^3$  ratio of  $0.11 \pm 0.02$ , indicating that  $\sim 10\%$  of the carbon in this film is bonded in an  $\text{sp}^2$  configuration. The MAS linewidth of the  $\text{sp}^3$  peak narrows to only  $\Delta\nu_{1/2} = 690$  Hz, indicating some disorder in the  $\text{sp}^3$  environment, while the lineshape of the  $\text{sp}^2$  peak remains relatively unaltered, indicating a high degree of disorder in this phase.

As expected, Raman is extremely sensitive to  $\text{sp}^2$  bonded carbon, identifying small amounts below the detection limit of the NMR spectrometer. Comparison of the two techniques, however, indicates that Raman spectroscopy may be so sensitive to  $\text{sp}^2$  bonded carbon that  $\text{sp}^3$  bonded

carbon in films containing as much as 90 %  $sp^3$  bonded material may remain undetected. This is undesirable when new deposition conditions are being explored, since conditions which yield a majority of  $sp^3$  bonded sites can be overlooked by the Raman analysis.

These two techniques also differ in that NMR spectroscopy is sensitive to short-range order, while Raman spectroscopy probes order over a longer range. NMR provides only information averaged over the entire sample volume and requires relatively large samples and long acquisition times. Raman has the advantage of giving fast, spatially resolved information. A combination of the two techniques is desirable for obtaining reliable information for all types of diamond.

Isotopic enrichment was sometimes employed to decrease sample size requirements. In addition, selective  $^{13}C$  labeling was used to gain insight into the chemistry of diamond formation when more than one chemically distinct carbon is present in the gas-phase reactant mixture. Films were grown using acetone, selectively  $^{13}C$  labeled at either the methyl or carbonyl site, as the reactive carbon source. The degree of enrichment which results in the film was determined from the linewidth of the  $sp^3$  diamond peak in the static  $^{13}C$  spectra which is dominated by homonuclear dipole broadening. Measuring the resulting  $^{13}C$  concentration in a pair of otherwise identical films, determines the relative efficiency at which the methyl and carbonyl sites from the selectively labeled acetone incorporate into diamond. When such experiments were carried out in a hot-filament reactor, both labels are incorporated equally when a tantalum filament is used. In contrast, diamond deposits preferentially from the methyl site when a rhenium filament is employed. However, some growth from the carbonyl site is still observed when rhenium is used. Such experiments demonstrate the importance of heterogeneous chemistry at the filament in this type of CVD reactor.

## $^{19}F$ NMR

The lower substrate temperatures which have been achieved using fluorine containing CVD reactants, opens the possibility of depositing diamond onto materials of low thermal stability, such as organic polymers. In addition, fluorination has been proposed to enhance the chemical inertness and lower the coefficient of friction of diamond surfaces. Thus, knowledge of surface passivation of diamond by fluorine is desirable.

Solid-state  $^{19}F$  NMR has been used to characterize the surfaces of diamond powder after 100%  $CF_4$  and 98%  $CF_4$ /2%  $O_2$  radio frequency plasma treatments. The pure  $CF_4$  plasma results in  $7.1 \times 10^{14}$  F/cm<sup>2</sup>, a coverage equivalent to approximately half of the available surface bond density.



With the addition of 2% O<sub>2</sub>, the equivalent coverage is reduced by roughly an order of magnitude, to  $7.4 \times 10^{13}$  F/cm<sup>2</sup>. MQ NMR reveals the <sup>19</sup>F is not distributed uniformly on either surface.

High-speed magic-angle-spinning NMR was used to average the effects of chemical shift anisotropy. On both surfaces, only CF<sub>x</sub> (x=1-3) functionalities were observed, with the majority species being carbon monofluoride. Only 5 to 10% of the fluorine was bonded as CF<sub>3</sub>. The isotropic chemical shifts were resolved and assigned relative to CFC1<sub>3</sub> as follows: CF = 148±1 ppm; CF<sub>2</sub> = 106±2 and 123 ppm; CF<sub>3</sub> = 78±1 ppm. The peak at 123 ppm was only observed in the CF<sub>4</sub>/O<sub>2</sub> plasma-treated sample and is speculated to be the result of atomic fluorine etching of diamond.

## RELATED STUDIES

To relate the NMR work to other studies, complementary characterization techniques were employed throughout: infrared, Raman, UV-visible, and secondary ion mass spectroscopy, scanning and transmission electron microscopy, x-ray diffraction, and thermal conductivity measurements. Some of this analysis was obtained in collaboration with other researchers, as indicated in a section which follows.

In order to obtain greater control over the sample available for our characterization work and in order to interpret our results, we constructed and modeled a hot-filament diamond deposition reactor. The influence of radiation and hydrogen atom recombination on substrate temperature uniformity was calculated and verified by experimental measurements. A two-dimensional finite element model was developed to examine the relative importance of heterogenous and homogenous chemistry in the production of atomic hydrogen. Our calculations show that catalytic activity is responsible for at least 95% of the atomic hydrogen production. In addition, the concentration of atomic hydrogen at the filament is far below thermal equilibrium values. The effect of recombination of hydrogen atoms at the growing surface was also studied. An analysis of experimental data reveals an activation energy of 150 kJ/mol for the filament-catalyzed reaction. From these measurements, a kinetic expression is developed to explain catalytic production of atomic hydrogen at the surface. Work on using zeolites as a novel substrate for diamond deposition was also pursued in this reactor.

## **COLLABORATIONS**

This work has benefited greatly from interactions with a variety of colleagues. In addition to valuable discussions with many individuals, I would like to acknowledge the following material contributions to this project:

For providing samples:

Dr. Michael Geis, MIT Lincoln Laboratory

Dr. Curtis Johnson, Naval Weapons Center, China Lake

Dr. Kevin Grey, Norton

Dr. Clifford J. Robinson, Raytheon

Dr. Karen McNamara, General Electric

For performing micro-Raman analysis:

Dr. James E. Butler and Mr. Daniel J. Vestyck, Naval Research Laboratory

For performing infrared spectroscopy:

Dr. Clifford J. Robinson, Raytheon

Dr. Kevin Grey, Norton

For providing matching funds to this contract as part of the Young Investigators Program (YIP):

Dr. Lawrence T. Kabocoff, N.S.W.C.

Dr. Curtis Johnson, N.W.C.

## **PERSONNEL SUPPORTED BY THIS CONTRACT:**

Dr. Karen M. McNamara (Ph.D. recipient)

Dr. Saibal Mitra (postdoctoral associate)

Mr. Michael C. Kwan (current doctoral student)

**PUBLICATIONS ACKNOWLEDGING THIS CONTRACT:**

*(Copies of each follow in order given below)*

- . K.M. McNamara and K.K. Gleason , "*Carbon Bonding Environments in CVD Diamond Thin Films Investigated via Solid-State NMR*" Proceedings of the NATO ASI on Diamond and Diamond-Like Films and Coatings, NATO-ASI Series B:Physics, **266**, 541 (1991).
- . K.M. McNamara and K.K. Gleason, "*Selectively  $^{13}\text{C}$  Enriched CVD Diamond Films Studied by NMR*", J. Appl. Phys. **71**, 2884 (1992).
- . K.M. McNamara, D.H. Levy, K.K. Gleason, and C.J. Robinson, "*Nuclear Magnetic Resonance and Infrared Absorption Studies of Polycrystalline Diamond*". Appl. Phys. Letts. **60**, 580 (1992).
- . K.M. McNamara, K.K. Gleason, and C.J. Robinson, "*Quantitative Correlation of Infrared Absorption with Nuclear Magnetic Resonance Measured Hydrogen Content in Diamond Films.*" J. Vac. Sci. Technol. A **10**, 3143 (1992).
- . S. Mitra, J. Pope, K.K. Gleason, Y. Makarovsky, A.L. LaFleur, and J.B. Howard, "*Synthesis of Fullerenes (C60 and C70) by Combustion of Hydrocarbons in Flat Flame Burner*", MRS Symp. Proc. **270**, 149 (1992).
- . K.M. McNamara, K.K. Gleason, D.J. Vestyck and J.E. Butler, "*Evaluation of Diamond Films by NMR and Raman Spectroscopy*". Diamond and Related Materials **1**, 1145 (1992).
- . C.A. Wolden, S. Mitra and K.K. Gleason, "*Radiative Heat Transfer in Hot-Filament Diamond Reactors*", J. Appl. Phys. **72**, 3750 (1992).
- . K.M. McNamara and K.K. Gleason, "*Comparison of Tantalum and Rhenium Filaments in Diamond Chemical Vapor Deposition*". J. Electrochem. Soc. **140**, L22 (1993).
- . S. Mitra and K.K. Gleason, " *$^1\text{H}$  NMR Studies on the Effects of Annealing on Chemical Vapor Deposition (CVD) Diamond*", Diamond and Related Materials, **1**, 1145 (1992).
- 0. B.E. Scruggs and K.K. Gleason, "*Analysis of Fluorocarbon Treated Diamond Powders by Solid-State F-19 Nuclear Magnetic Resonance*" , J. Phys. Chem., **97**, 9187 (1993).

1. S. Mitra, K.K. Gleason, and K.V. Ravi, " *$^1\text{H}$  NMR of Combustion Deposited and Hydrogen Plasma Treated Diamond*", ECS Symp. Proc., 93-17, 256 (1993) .
2. K.M. McNamara and K.K. Gleason, "*Comparison of Tantalum and Rhenium Filaments in CVD Diamond Using Selective C-13 Labeling*", ECS Symp. Proc., 93-17, 297 (1993).
3. K.M. McNamara and K.K. Gleason, "*Radial Distribution of Hydrogen in CVD Diamond*", Chem. of Materials, 6, 39 (1994).
4. M.C. Kwan and K.K. Gleason, "*Using Zeolites as Substrates for Diamond Thin Film Deposition*", MRS Symp. Proc. (in press, meeting held 12/93).
5. K.M. McNamara, B.E. Williams, K.K. Gleason and B.E. Scruggs, "*Identification of Defects and Impurities in Chemical Vapor Deposited Diamond through Infrared Spectroscopy*", J. Appl. Phys. (submitted).
6. K.K. Gleason, "Diamond Thin Films" for the "*Encyclopedia of Nuclear Magnetic Resonance*" edited by D.M. Grant and R.K. Harris (Wiley, to be published 1995). *invited review chapter*.

# CARBON BONDING ENVIRONMENTS IN CVD DIAMOND FILMS INVESTIGATED VIA SOLID-STATE NMR

Karen Mary McNamara and Karen K. Gleason

Department of Chemical Engineering  
Massachusetts Institute of Technology  
Cambridge, MA 02139

## INTRODUCTION

Diamond films are typically produced by both plasma and thermally assisted CVD using methane as the carbon source in an excess of hydrogen<sup>1</sup>. Although these films have been characterized using a wide variety of techniques, nuclear magnetic resonance (NMR) spectroscopy can yield valuable new information. Both hydrogen and carbon-13 NMR spectroscopy can be used to examine polycrystalline diamond films<sup>2</sup>, even those with a hydrogen content of < 1%. NMR, however, has not been used extensively to date.

NMR is quantitative in that each nuclei gives rise to the same integrated NMR signal, regardless of its chemical environment, provided complete spin-lattice relaxation occurs between averages<sup>3</sup>. Gem-quality natural diamond can have a spin-lattice relaxation times > 1 day, making averaging painfully slow. The presence of paramagnetic defects decreases the relaxation time of neighboring <sup>13</sup>C nuclei to several seconds<sup>4</sup>. Increasing the <sup>13</sup>C concentration reduces the spin-lattice relaxation time of <sup>13</sup>C nuclei removed from the defect site through increased homonuclear dipolar communication as well as increasing the total signal. In addition, <sup>13</sup>C enrichment, if done selectively, can be used to gain insight into diamond chemistry.

Very high enrichments will, however, limit spectral resolution of sp<sup>2</sup> versus sp<sup>3</sup> carbon due to <sup>13</sup>C homonuclear dipolar line broadening. Resolution can be restored by magic-angle spinning, but this requires crushing the sample, destroying its physical integrity. Unlike magic-angle spinning, static NMR experiments do not require sample destruction. In fact, slivers of diamond films can be inserted directly into the NMR coil while intact on their substrate. Also, the low-energy radio-frequency irradiation

used in NMR is unlikely to result in chemical alteration of the diamond samples.

In materials with high hydrogen concentrations, like polymers and diamond-like carbon films, cross-polarization enhances the carbon-13 spectrum<sup>5,6</sup>. At the low hydrogen concentrations found in polycrystalline diamond films, carbon nuclei located far from hydrogen are less effectively cross-polarized, and thus, the quantitative character of the NMR experiment is lost. Direct-polarization <sup>13</sup>C NMR, while requiring larger samples, is a means of obtaining quantitative sp<sup>2</sup>/sp<sup>3</sup> ratios.

To date, Raman spectroscopy is used to identify sp<sup>2</sup> and sp<sup>3</sup> bonded carbon in diamond films. However, the Raman results are difficult to quantify since the scattering efficiency of sp<sup>2</sup> bonded carbon differs from sp<sup>3</sup> bonded material. These scattering efficiencies may vary from film to film, as well. The sensitivity of Raman spectroscopy is also controlled, in part, by the spot size of the instrument. With a small spot size, it is possible to overlook inclusions of graphitic carbon and overestimate the quality of the film.

#### NATURAL ABUNDANCE CARBON-13 FILM

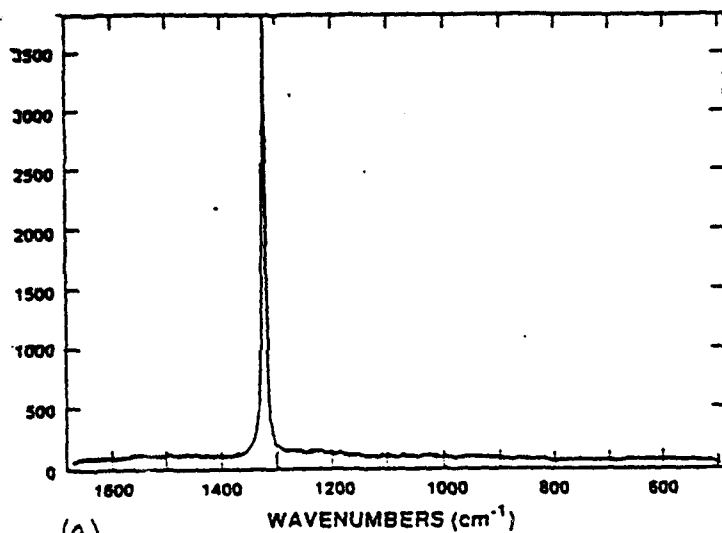
A free-standing polycrystalline diamond film was provided by Dr. James E. Butler of the Naval Research Laboratory. The film was produced from 0.5% methane in hydrogen in a hot-filament reactor. The total pressure was 34 torr, and the substrate temperature was ~1150K. After 93 hours, an opaque, almost black film was obtained. The micro-Raman spectrum, obtained by Dr. Butler, is shown in Figure 1a. Several locations were probed, and the micro-Raman indicated the presence of sp<sup>3</sup> bonded carbon, only. The static direct-polarization NMR spectrum of the ~0.1 g sample was obtained on a commercial 4.7 T IBM Instruments spectrometer. Two peaks are present, one centered at 34 ppm and the second centered at 120 ppm, indicative of sp<sup>3</sup> and sp<sup>2</sup> bonded carbon, respectively<sup>4-6</sup>.

Thus, NMR has detected sp<sup>2</sup> carbon in a black, opaque CVD diamond film which was not apparent from the Raman spectrum. Differences between the NMR and Raman spectrum could arise for several reasons, as discussed in the introduction. The NMR spin-lattice relaxation behavior for this sample has not yet been determined. When the period between averages is adjusted for the relaxation time, the relative intensities of the sp<sup>2</sup> and sp<sup>3</sup> peaks may vary. In order to reduce concerns about relaxation time and to decrease total deposition time, carbon-13 enriched films were examined.

#### CARBON-13 ENRICHED FILMS

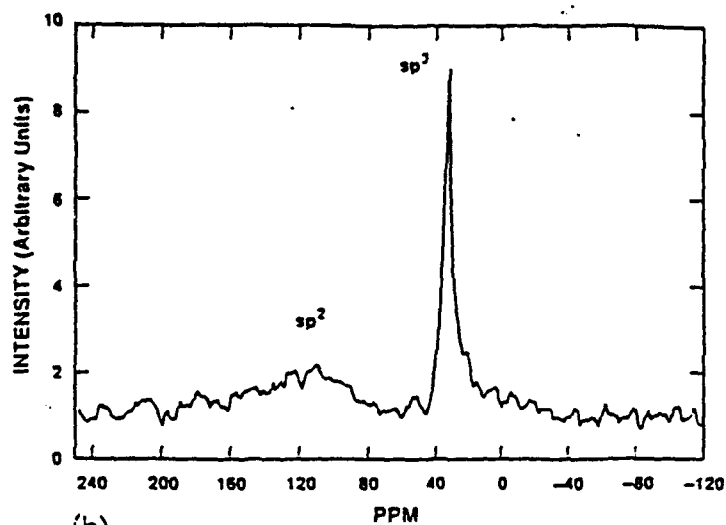
Oxygen containing carbon sources such as acetone, ethanol, and carbon monoxide have been used to produce films at higher growth rates and/or with improved morphology<sup>7,8</sup>. Although

## RAMAN SPECTRUM



(a)

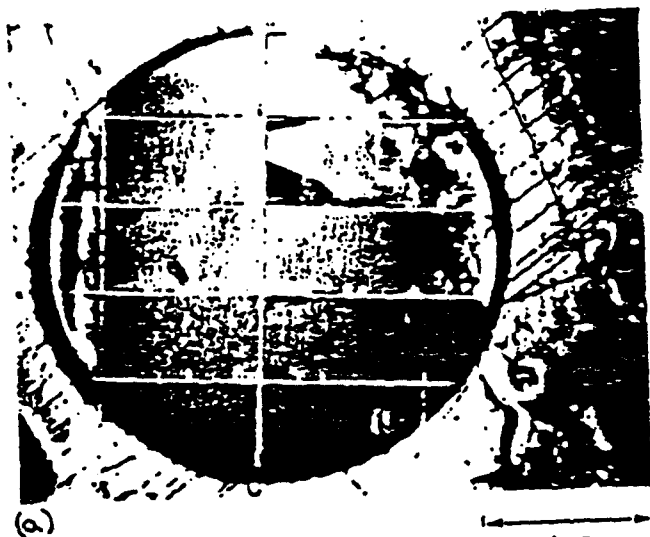
## CARBON-13 NMR SPECTRUM



(b)

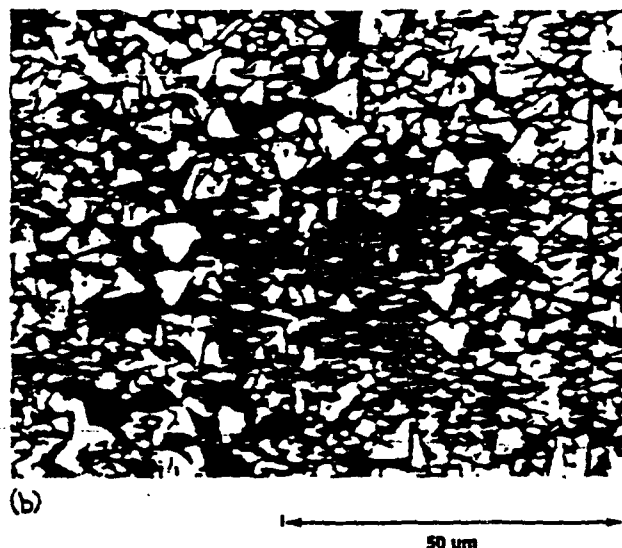
Figure 1. (a) The Raman spectrum of a natural abundance, hot-filament CVD film shows an intense adsorption for diamond at 1332  $\text{cm}^{-1}$ . The presence of  $\text{sp}^2$  bonded carbon is not apparent. (b) The NMR spectrum of the same sample clearly shows a peak at a chemical shift of 34 ppm with respect to TMS, indicative of diamond. The peak at 120 ppm indicates a significant amount of  $\text{sp}^2$  bonded carbon in the sample.

## CVD DIAMOND ON SILICON



(a)

## POLYCRYSTALLINE CVD DIAMOND FILM



(b)

Figure 2. (a) This photograph shows a 12  $\mu\text{m}$  thick diamond deposit over a one-inch silicon substrate. The cuts show how slivers are prepared for intact insertion into the NMR probe where non-destructive evaluation takes place. The black edge regions appear where clips were used to hold the sample in place during deposition. Some of the film was chipped off the silicon substrate while under the diamond saw. (b) Optical micrographs show a highly faceted, continuous, polycrystalline morphology. The average particle size is 5-10  $\mu\text{m}$ , and the film is ~12  $\mu\text{m}$  thick.

there has been much speculation about the role of oxygen in such depositions, little has been proven at this time. Choosing acetone as a reactant and using selective isotopic labeling, resulted in higher growth rates, reducing reactant costs, and allowed insight into the role of oxygen in the deposition.

Two polycrystalline diamond films were deposited in a hot-filament reactor. The carbon source was 33%  $^{13}\text{CH}_3\text{CO}^{13}\text{CH}_3$  or 66%  $\text{CH}_3^{13}\text{COCH}_3$  in normal acetone, for an overall 22% gas-phase  $^{13}\text{C}$  enrichment. The acetone and hydrogen flowrates were 2 sccm and 100 sccm, respectively. A 1" diameter silicon substrate was seeded with natural diamond grit prior to deposition. The filament was a 2 mm diameter tantalum wire maintained at a temperature of ~2600K, and the substrate temperature was ~1150K. The total pressure in the reactor was 150 torr.

Figure 2a shows the silicon substrate after 3.5 hours of growth in the carbonyl-enriched reactant. The area exposed during deposition is covered with a 12  $\mu\text{m}$  thick polycrystalline film. Figure 2b is an optical micrograph of the film, showing a highly faceted surface with primarily  $\langle 111 \rangle$  crystal planes and typical crystal sizes between 5 and 10  $\mu\text{m}$ . Similar results were obtained with the methyl-enriched reactant. The 4 mm x 9 mm slivers, cut using a diamond saw, were inserted directly into the NMR probe, allowing non-destructive evaluation of the sample.

The static direct-polarization NMR spectra of the enriched films were obtained on a home-built, 6.3 Tesla spectrometer. Both spectra of the films produced from the methyl (Figure 3a) and carbonyl (Figure 3b) labeled reactants contain only one peak, centered at 34 ppm, indicative of  $\text{sp}^3$  bonded carbon. Any signal upfield near 120 ppm, where  $\text{sp}^2$  bonded carbon would be found, was below the noise level in our spectra.

The carbon-13 concentration in the films can be calculated from the second moment of the NMR lineshapes using the van Vleck equation for a spin-1/2 nuclei<sup>9</sup>,

$$\langle \Delta\omega^2 \rangle = \frac{9}{20} C \gamma^4 \hbar^2 \sum_k r_{jk}^{-6}$$

where

- $\langle \Delta\omega^2 \rangle$  is the second moment;
- C is the fraction of sites occupied by  $^{13}\text{C}$ ;
- $\gamma$  is the gyromagnetic ratio of the nuclei;
- $\hbar$  is Plank's constant/ $2\pi$ ; and,
- $r_{jk}$  is the internuclear distance between sites j and k, determined from diamond's crystallographic structure.



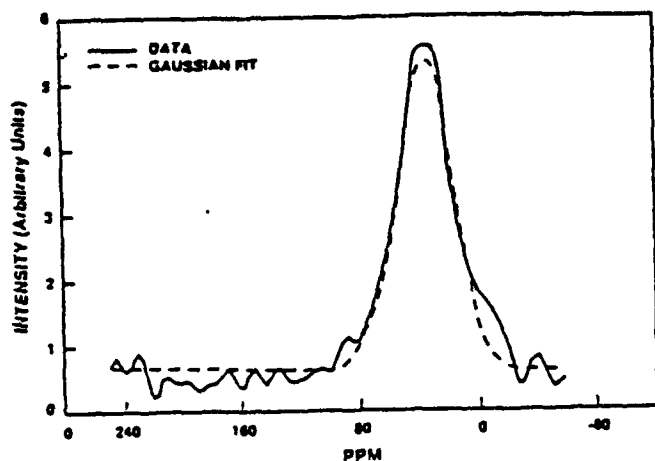
The dashed lines in Figure 3 represent the best Gaussian fit to these lineshapes. For a Gaussian, the full-width at half-maximum (FWHM) equals  $2.35 \langle \Delta w^2 \rangle^{1/2}$ . For both of the films, the FWHM is  $45 \pm 2$  ppm at 67.7 MHz corresponding to a carbon-13 concentration in the film is  $22 \pm 1\%$ , identical to the degree of gas-phase enrichment.

#### ANALYSIS OF HETEROGENEOUS CHEMISTRY

The incorporation of carbons from the carbonyl position of the acetone reactant raises questions about the role of oxygen and the chemistry within the reactor. There are three possible pathways for carbonyl-carbon incorporation into the diamond film - as CO incorporated directly from the gas phase, through homogeneous gas-phase conversion to a precursor species, or through heterogeneous conversion to a precursor species. The first, direct incorporation of CO from the gas phase, might be expected to follow a pathway analogous to the Boudouard reaction, ( $2 \text{ CO}_{\text{gas}} \rightarrow \text{CO}_2 + \text{C}_{\text{solid}}$ ), for soot formation, although no evidence for this process in diamond growth has been found to date<sup>10</sup>. The kinetics of the Boudouard reaction are greatly enhanced by surfaces and iron contamination, suggesting the importance of heterogeneous chemistry. There are many possible routes for the second method of incorporation, homogeneous carbon scrambling, but based on published homogeneous reaction rate constants for CO in the combustion literature, these are likely to be slow. In addition, through isotopic studies it has been shown that homogeneous scrambling of CO is minimal<sup>11</sup>. Scrambling of hydrocarbons, on the other hand, is essentially complete<sup>12,13</sup>. One final possibility is that the enol form of the acetone reactant provides a pathway for homogeneous conversion. Harris has measured a CO concentration of 0.018 mol% in the gas-phase when 1.0 mol% of  $\text{O}_2$  enters the reaction zone<sup>14</sup>. This is close to the equilibrium CO concentration of 0.017 mol% at the filament temperature. Similar agreement was found at the other oxygen concentrations checked between 0% and 3%. However, the pathway by which this CO would form, directly from carbonyl carbons or through other homogeneous reaction, has not been determined.

We have used secondary ion mass spectrometry (SIMS) to evaluate the role of heterogeneous exchange between the carburized tantalum filament and gas-phase carbonyl-derived carbons. Figure 4a shows the SIMS spectrum obtained from a filament exposed for several hours to normal acetone in excess hydrogen. The peaks at mass 193 and mass 195 represent  $\text{Ta}^{12}\text{C}$  and its hydride,  $\text{Ta}^{12}\text{CH}_2$ , respectively. The peaks at mass 197 and 198 are  $\text{TaO}$  and  $\text{TaOH}$ , respectively. Figure 4b shows the SIMS spectrum of a tantalum filament exposed to normal acetone and hydrogen in the same manner as the first and then exposed to carbon-13 enriched acetone

### STATIC CARBON-13 NMR SPECTRUM CARBONYL-LABELED ACETONE



### STATIC CARBON-13 NMR SPECTRUM METHYL-LABELED ACETONE

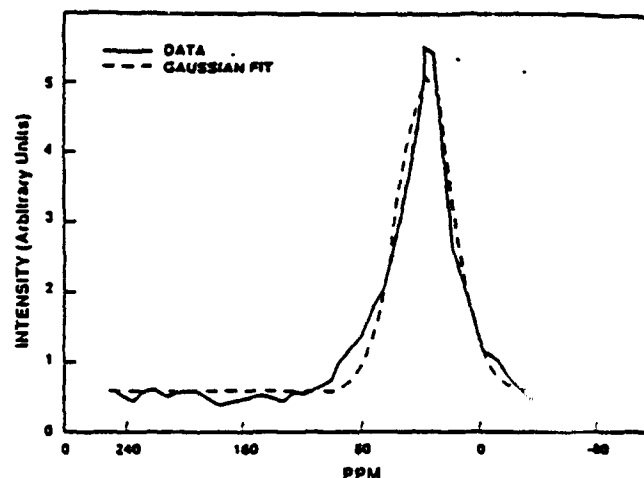
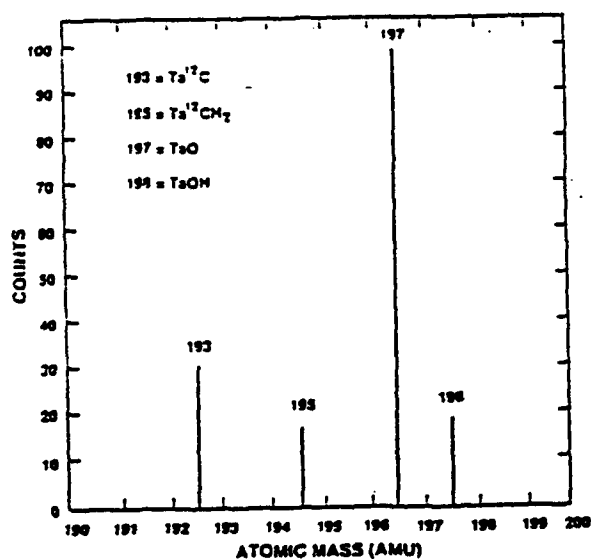


Figure 3. The carbon-13 NMR spectrum of both the film produced from the carbonyl and the methyl labeled acetone show only one peak, centered at 34 ppm, which is indicative of  $sp^3$  bonded material. Relating the full-width at half-maximum of the best-fit gaussian to the second moment gives a carbon-13 content of 22% in each film.

### NATURAL ABUNDANCE ACETONE



### CARBON-13 ENRICHED ACETONE

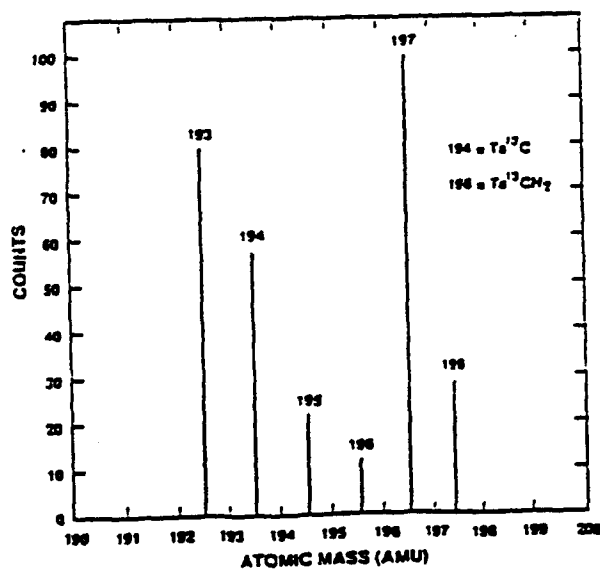


Figure 4. (a) SIMS spectrum taken from a tantalum filament exposed only to natural  $^{13}\text{C}$  abundance acetone show peaks at 193, 195, 197, and 198 a.m.u. These are representative of  $\text{Ta}^{12}\text{C}$ ,  $\text{Ta}^{12}\text{CH}_2$ ,  $\text{TaO}$ ,  $\text{TaOH}$ , respectively. (b) SIMS spectra taken from a filament initially carburized with normal acetone and then exposed to  $^{13}\text{C}$ -labeled acetone, enriched at the carbonyl carbon, show the four peaks observed in spectrum (a) as well as peaks at 194 and 196 a.m.u. These represent  $\text{Ta}^{13}\text{C}$  and  $\text{Ta}^{13}\text{CH}_2$  and show that heterogeneous carbon exchange does take place at the filament.

labeled at the carbonyl carbon and an excess of hydrogen for several hours. The peaks at mass 193, 195, 197, and 198 appear as before. Two new peaks appear, however, at mass 194 and 196 indicating  $\text{Ta}^{13}\text{C}$  and  $\text{Ta}^{13}\text{CH}_2$ . Depth profiling to > 2000 Å indicates that exchange has also occurred in the interior of the filament.

## CONCLUSION

Nuclear magnetic resonance spectroscopy provided a non-destructive means of quantitatively evaluating diamond films. It was sensitive to the local environment throughout the sample and identified  $\text{sp}^2$  bonded carbon in a film where it was not apparent from Raman analysis. Isotopic enrichment was used to decrease sample size requirements and spin-lattice relaxation times, increasing sensitivity. This will allow quantitative  $\text{sp}^2/\text{sp}^3$  ratios to be obtained. Selective isotopic labeling was used to raise questions and gain insight into the chemistry of diamond formation as well. NMR has shown that the carbonyl carbons from acetone are incorporated into diamond films, and SIMS has been used to show that heterogeneous exchange reactions in the filament, involving the carbonyl carbon, occur.

## ACKNOWLEDGEMENTS

We gratefully acknowledge Dr. Mike Geis and Mr. Keith Krohn of Lincoln Laboratories, MIT for their help in producing carbon-13 enriched samples. We also thank Dr. James E. Butler of the Naval Research Laboratories for providing the natural abundance sample and its micro-Raman spectra. Funding for this work was provided by ONR Grant #N00014-90-J-1901 and ACS-PRF #22595-G5.

## REFERENCES

1. R.C. DeVries, Ann. Rev. Mater. Sci. 17, 161 (1987) and references therein.
2. K.M. McNamara, K.K. Gleason and M.W. Geis, MRS Symposium Proceedings, 162 (1989). In press.
3. A. Abragam, "The Principles of Nuclear Magnetism" (Oxford, New York, 1983).
4. P.M. Hendricks, M.L. Cofield, R.H. Young, and J. M. Hewitt, J. Magn. Res. 58, 85 (1984).
5. S. Kaplan, F. Jansen, and M. Machonkin, Appl. Phys. Lett. 47, 750 (1985).
6. M.A. Petrich, K.A. Gleason, J.A. Reimer, Phys. Rev. B, 6(18), 9722 (1987).
7. Y. Hirose and Y. Terasawa, Jap. J. Appl. Phys. 25, L519 (1982).
8. A. Hirayama, T. Ito, and K. Ito, Paper presented at Diamond Technology Initiative Symposium, SDIO/IST-ONR, Crystal City, VA, 12-14 July 1988.
9. J.H. van Vleck, Phys. Rev. 74, 1168 (1948).
10. A.G. Gaydon and H.G. Wolfhard, "Flames" (Chapman and Hall, London, 1979).
11. R. E. Ferguson, J. Chem. Phys. 23, 2085 (1955).

12. R. E. Ferguson, Combustion and Flame, 1, 431 (1957).
13. C.J. Chu, R.H. Hauge, M.P. D'Evelyn, and J.L. Margrave, MRS Symposium Proceedings, 162 (1989). In press.
14. S. J. Harris, J. Appl. Phys. 65(8), 3044 (1989).

# Selectively $^{13}\text{C}$ -enriched diamond films studied by nuclear magnetic resonance

K. M. McNamara and K. K. Gleason

*Department of Chemical Engineering, MIT, Cambridge, Massachusetts 02139*

(Received 12 September 1991; accepted for publication 27 November 1991)

The quality of hot-filament chemical-vapor-deposited diamond films has been quantitatively assessed by  $^1\text{H}$  and  $^{13}\text{C}$  nuclear-magnetic-resonance (NMR) spectroscopy. As the carbon mole fraction increases from 0.053 to 0.074 in the gas phase, film quality in terms of  $sp^2$  carbon content, bonding disorder, and spin-lattice relaxation times deteriorates, in agreement with the qualitative results of Raman spectroscopy and scanning electron microscopy. Selective isotopic labeling of the acetone reactant and subsequent  $^{13}\text{C}$  NMR analysis shows that the carbonyl carbon of acetone is incorporated into the growing diamond films. Secondary-ion mass spectroscopy reveals that heterogeneous exchange reactions, involving the carbonyl carbon at the tantalum filament, are responsible for this phenomena.

## I. INTRODUCTION

The commercial exploitation of diamond in many materials and electronic applications is limited by the ability to produce high-quality, defect-free diamond films and coatings. The successful production and use of such films requires greater understanding of these materials, their structure, and the chemistry of their formation. In recent years, a large research effort has been devoted to the study of low-pressure diamond deposition by various methods. Films can be deposited from hydrogen-hydrocarbon gas mixtures,<sup>1</sup> as well as mixtures containing oxygen and halogen species.<sup>1-5</sup>

Diamond is typically produced by plasma or hot-filament chemical-vapor deposition (CVD), and the carbon source is usually methane. However, studies of carbon sources containing oxygen have shown promising results. Acetone,<sup>2,3</sup> ethanol,<sup>3,4</sup> and carbon monoxide<sup>5</sup> are among the species that have been used. Both oxygen and atomic hydrogen are thought to play important roles in diamond formation and in inhibiting the growth of graphite through selective etching, although the exact mechanisms for these processes are not fully understood.<sup>1</sup> Although these proposed reactions indicate the importance of heterogeneous chemistry in the diamond reactor, the majority of the kinetic models of diamond formation proposed to date focus primarily on homogeneous gas-phase reactions. Heterogeneous reactions occurring at the hot-filament surface have received little attention.

Diamond films are characterized using a wide variety of techniques.<sup>1-6</sup> However, nuclear-magnetic-resonance (NMR) spectroscopy has been largely neglected. Both  $^1\text{H}$ <sup>7</sup> and  $^{13}\text{C}$  NMR spectroscopy can be used to examine polycrystalline diamond films, even those with hydrogen contents of <0.5 at. %. While these low hydrogen contents prohibit the use of cross-polarization techniques to enhance  $^{13}\text{C}$  signals, direct polarization of carbon is certainly possible. Larger samples are required, however, to obtain sufficient NMR signal. Hydrogen NMR spectroscopy may be performed on samples containing as few as

$10^{17}$  protons<sup>7</sup> while  $^{13}\text{C}$  NMR is typically performed on samples containing greater than  $5 \times 10^{18}$   $^{13}\text{C}$  nuclei. Both of these direct-polarization techniques provide quantitative information that is unattainable by other techniques.

NMR is quantitative in that each nuclei gives rise to the same integrated NMR signal intensity, regardless of its chemical environment, provided complete spin-lattice relaxation occurs between averages, and broadening from paramagnetic centers is insignificant. Gem-quality natural diamond can have spin-lattice relaxation times >1 day,<sup>8</sup> making signal averaging unreasonably slow. The presence of paramagnetic defects decreases the relaxation time of the neighboring  $^{13}\text{C}$  nuclei to several seconds. However,  $^{13}\text{C}$  nuclei within a 2 Å radius of a paramagnetic center may be shifted in frequency to such an extent that their resonance is indistinguishable from the baseline. Fortunately, only a small fraction of the nuclei in the sample are in such close proximity to a paramagnetic center, and the effect can usually be neglected. Comparison of the observed NMR signal intensity to that calculated for the number of  $^{13}\text{C}$  nuclei in the sample, based on weight and enrichment estimates, insures the entire sample is represented. In addition to increasing the total signal, increasing the  $^{13}\text{C}$  concentration reduces the spin-lattice relaxation time of  $^{13}\text{C}$  nuclei removed from the defect site through increased homonuclear dipolar communication. The  $^{13}\text{C}$  enrichment, if done selectively, can also be used to gain insight into diamond chemistry.

Very high enrichments will, however, limit spectral resolution of  $sp^2$  vs  $sp^3$  carbon due to homonuclear dipolar line broadening. Resolution may be restored by magic-angle spinning (MAS), but this typically requires crushing the sample and destroying its physical integrity. Unlike magic-angle spinning, static NMR experiments do not require sample destruction. In fact, slivers of diamond can be inserted directly into the NMR coil while intact on their substrates. Also, the low-energy radio-frequency irradiation used in NMR is unlikely to result in chemical alteration of the diamond samples.

TABLE I. Summary of data for films A', B, C, and A, indicating that as the carbon mol % in the gas-phase increases, the quality of the films deteriorates, in terms of  $sp^2$  content, disorder of the  $sp^3$  phase, spin-lattice relaxation-time constants, crystallite size, and  $sp^3$  intensity in the Raman spectra.

Film	Site of enrichment	Carbon mol %	at. % $sp^2$	$sp^3$ linewidth (kHz)		$T_1$ (s)	at. % H	Crystallite size ( $\mu\text{m}$ )	$I_{1332}/I_{1580}$
				Static	MAS				
A	methyl	5.3	$0 \pm 2$	2.8	0.15	18	0.50	10	2.44
B	methyl	6.4	$0 \pm 1$	2.8	0.20	4	0.05	5	1.68
C	methyl	7.4	$10 \pm 2$	4.2	0.69	1	0.42	...	0.00
A'	carbonyl	5.3	$0 \pm 1$	2.8	...	20	0.39	8	1.99

## II. EXPERIMENT

A series of three polycrystalline diamond films were produced in a hot-filament reactor using acetone as the carbon source. All of the substrates were silicon, seeded with  $0.25 \mu\text{m}$  natural diamond particles. After 2–3 h of deposition, the films were examined under optical microscope. The thickness varied from 5 to  $10 \mu\text{m}$ , and the films were nearly continuous over the 1-in.-diam substrate. To facilitate  $^{13}\text{C}$  NMR measurements, the acetone was labeled with  $^{13}\text{C}$  at the methyl site to provide an overall gas-phase enrichment of 22%. The acetone flowrate was varied in each run to give total carbon mol % in the gas feed as shown in Table I. The hydrogen flowrate was held fixed at 100 sccm. The filament used to thermally activate the gas feed was a tantalum wire, resistively heated to  $\sim 2600 \text{ K}$ . The temperature of the silicon substrate was  $\sim 1150 \text{ K}$ , and the total pressure in the reactor was 150 Torr. A fourth film was also produced at these conditions, this time using acetone labeled at the carbonyl carbon to give a 5.3 carbon mol % in the gas phase. This selective labeling allowed us to examine differences between chemistry experienced by the carbon atoms in each bonding environment of the acetone molecule. The samples were prepared for NMR studies using a diamond saw to cut the silicon substrate into  $4 \times 9 \text{ mm}$  slivers.

The carbon-13 concentration in the films can be calculated from the second moment of the NMR line shapes using the van Vleck equation<sup>9</sup> for a spin-1/2 nuclei,

$$\langle \Delta\omega^2 \rangle = \left( \frac{\gamma}{2\pi} \right)^2 C \gamma^4 \hbar^2 \sum_{jk} r_{jk}^{-6}, \quad (1)$$

where  $C$  is the fraction of sites occupied by  $^{13}\text{C}$ ,  $\gamma$  is the gyromagnetic ratio of the nuclei,  $\hbar$  is Planck's constant over  $2\pi$ , and  $r_{jk}$  is the internuclear distance between sites  $j$  and  $k$ , determined from diamond's crystallographic structure. For a Gaussian line shape, the full-width at half-maximum (FWHM) equals  $2.35 \langle \Delta\omega^2 \rangle^{1/2}$ . A FWHM of 3.0 kHz, therefore, corresponds to a sample enriched with 22%  $^{13}\text{C}$ . In natural diamond, calculation of the enrichment based on the experimental linewidth yields 1.1%  $^{13}\text{C}$ , as expected for a natural abundance sample. The linewidth due to dipolar interactions is independent of the static magnetic field and is given in units of kHz.

Additional broadening may occur in CVD films due to chemical-shift anisotropy (CSA), magnetic susceptibility

effects caused by the substrate, and a broader distribution of bond angles. In addition the broadening caused by these effects may result in an asymmetric line. These broadening mechanisms, as well as the isotropic part of the chemical-shift interaction, are linearly proportional to the applied field and are reported in units of parts per million (ppm) of the applied external field. Thus, for our 7 T spectrometer, 1 ppm is equivalent to 75 Hz for  $^{13}\text{C}$ .

Static direct-polarization  $^{13}\text{C}$  NMR was performed by inserting slivers of diamond directly into the NMR coil while they remained intact on the silicon substrate. The spectra were obtained on a home-built, 7.0 T NMR spectrometer with quadrature detection. Background carbon concentrations in the static NMR probe were below the detection limit of  $5 \times 10^{18}$  for natural abundance  $sp^2$ -bonded  $^{13}\text{C}$  atoms. This detection limit was determined experimentally using test mixtures containing  $sp^2$ -bonded soot and natural diamond powder of known quantities, and the relaxation-time constant for each material was determined independently. The detection limit for  $sp^3$ -bonded carbon of  $1 \times 10^{18}$  is lower than that for  $sp^2$ -bonded material due to  $sp^3$  carbon's narrower linewidth. Between 3000 and 50 000 free-induction decays were signal averaged for each sample, as determined by the desired signal-to-noise ratio of the final spectrum. The delay between averages was five times the spin-lattice relaxation-time constant of the film, ensuring that the  $^{13}\text{C}$  nuclei return to equilibrium with the static magnetic field between averages.

Spin-lattice relaxation is the process by which the  $^{13}\text{C}$  nuclei exchange energy with the surrounding lattice and typically follows the Bloch equation,<sup>10</sup>

$$\frac{M(t) - M_{\text{eq}}}{M_0 - M_{\text{eq}}} = \exp\left(\frac{-t}{T_1}\right), \quad (2)$$

where  $M(t)$  is the net magnetization parallel to the external magnetic field at time  $t$ ,  $M_0$  is the initial magnetization at  $t = 0$ , and  $T_1$  is the exponential spin-lattice relaxation-time constant. In natural diamond, the relaxation-time constant is extremely long and may exceed 24 h.<sup>8</sup> In synthetic diamond, however, grain boundaries, unterminated bonds, and other paramagnetic defects, and ferromagnetic defects provide additional mechanisms through which relaxation may occur, reducing observed relaxation-time constants to minutes or even seconds.<sup>8</sup> Relaxation due pre-

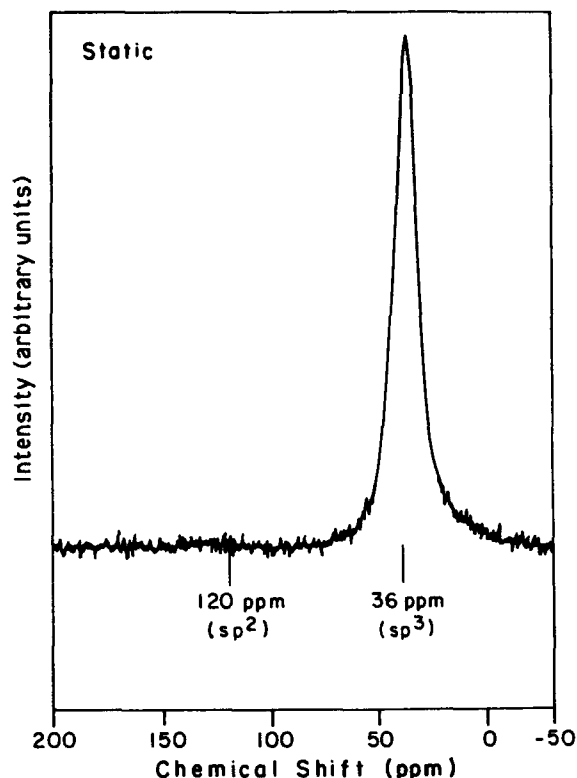


FIG. 1. Static  $^{13}\text{C}$  NMR spectrum of natural diamond powder. The peak at  $36 \pm 2$  ppm is characteristic of  $sp^3$ -bonded carbon, and its  $\sim 0.5$  kHz linewidth corresponds to the 1.1% natural abundance of  $^{13}\text{C}$ . The absence of a peak in the 120 ppm region indicates the  $sp^2$ -bonded carbon is below the detection limit of  $50 \times 10^{18}$   $^{13}\text{C}$  per sample.

dominantly to paramagnetic centers may exhibit behavior different from that predicted by the Bloch equation.<sup>11,12</sup> However, in the case of rapid spin diffusion, such as that found in our enriched samples, it is likely that an exponential decay will be observed even in the presence of paramagnetic centers.<sup>11</sup> Here, spin-lattice relaxation times were measured by the saturation recovery technique.

For comparison with deposited films, a static direct-polarization  $^{13}\text{C}$  NMR spectrum of natural diamond powder is shown in Fig. 1. The peak centered at  $36 \pm 2$  ppm, is typical of the isotropic chemical shift of  $sp^3$ -bonded carbon relative to that of tetramethyl silane. The diamond peak is nearly symmetric, revealing little CSA, as expected for a tetrahedrally symmetric bonding environment. As anticipated, we see virtually no intensity in the region near 120 ppm, where  $sp^2$ -bonded carbon is typically found. The significant separation of the  $sp^2$  and  $sp^3$  carbon chemical shifts allows us to resolve these features in all but the most highly enriched samples. Since the static linewidth of the symmetric NMR peak is related to the  $^{13}\text{C}$  concentration in the film by the van Vleck equation [Eq. (1)], lines become broader and more difficult to resolve at higher enrichments.

With additional broadening by other interactions, such as the CSA and magnetic susceptibility effects, the resolution of  $sp^2$  and  $sp^3$  carbon peaks may be difficult. To improve this resolution, the peaks may be narrowed by a

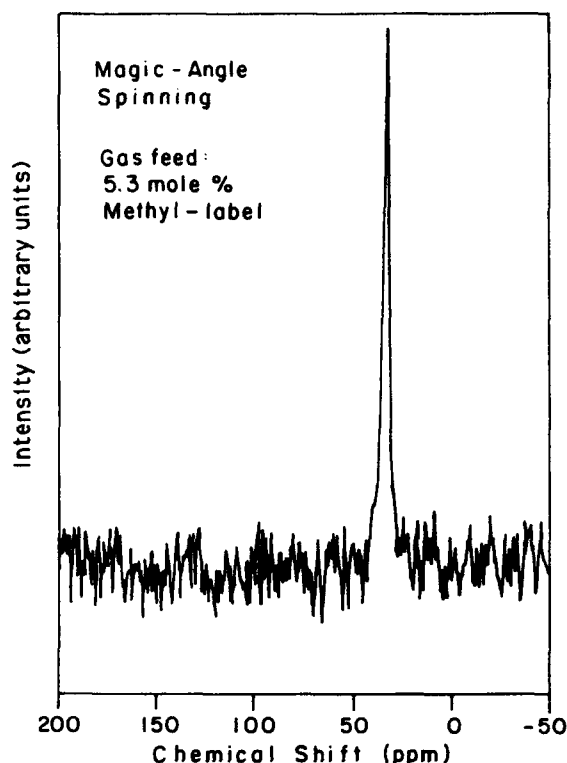


FIG. 2. Magic-angle spinning spectra of film A. Only  $sp^3$  carbon is observed, having a similar chemical shift to natural diamond (Fig. 1) and a narrow linewidth (0.15 kHz), indicating a low degree of bond angle disorder in the CVD diamond.

technique known as magic-angle spinning (MAS). While the isotropic chemical shift remains unaffected by MAS, broadening due to the CSA may be eliminated. Broadening due to bond angle disorder, however, cannot be eliminated by MAS. MAS NMR has often been used in the study of amorphous carbons.<sup>13,14</sup> For this measurement, samples must be crushed into fine powders to allow high-speed spinning. Crushing the films reduces magnetic susceptibility effects by reducing spatial variations within the sample and averaging orientation effects. In order to eliminate broadening due to a given type of interaction, the spinning speed of the sample must exceed the frequency of that interaction, usually requiring speeds in excess of 3 kHz.

### III. CARBON CONCENTRATION STUDIES

The integrated area under the  $^1\text{H}$  NMR line, by comparison with a known sample, was quantitatively used to determine the hydrogen concentration of each sample (Table I). In all cases, the total hydrogen content was less than 0.5 at. %. This low hydrogen content prevents the use of cross-polarization techniques in analyzing our films.

However, the direct-polarization  $^{13}\text{C}$  NMR spectra were obtained for film A, produced with 5.3 carbon mol % in the gas feed. The MAS-NMR spectrum of the crushed film (Fig. 2) compared favorably to the spectrum of natural diamond (Fig. 1). The  $sp^3$  NMR line is completely narrowed to 0.15 kHz, indicating little broadening due to bond angle distribution. A single peak is centered at 36

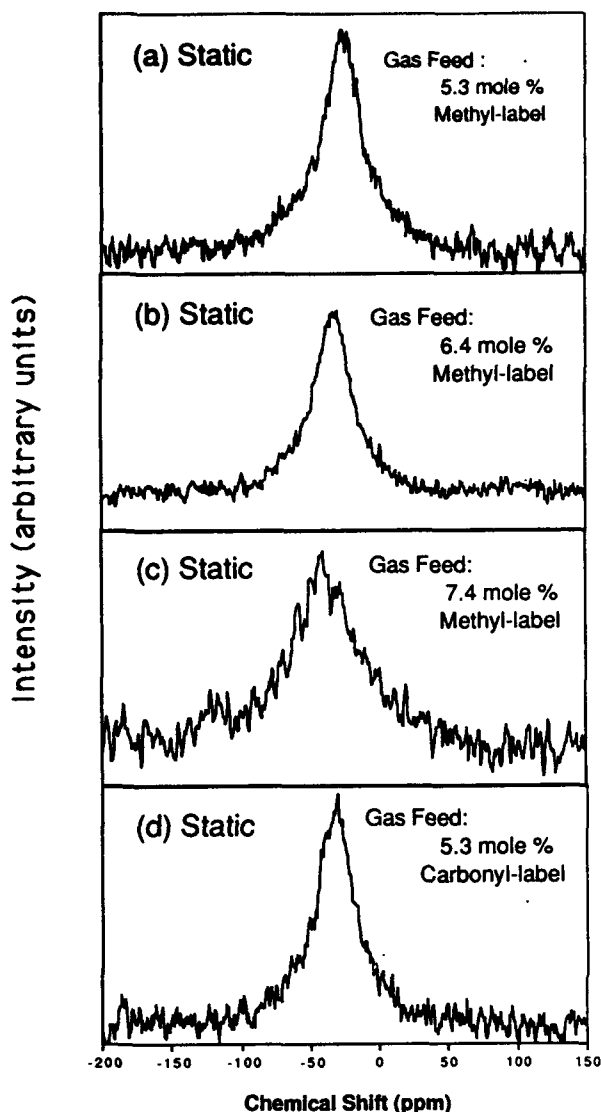


FIG. 3. (a)–(d) Direct-polarization static  $^{13}\text{C}$  NMR spectra of films A, B, C, and A', respectively. (a), (b), and (d) show a single line at  $\sim 36$  ppm having widths characteristic of 22%  $^{13}\text{C}$  enrichment. (c) Shows a broader  $sp^3$  line due, in part, to increased bond angle disorder. Also, the additional peak at  $\sim 120$  ppm in (c) indicates the presence of  $sp^2$ -bonded carbon. A deterioration in film quality as the carbon mol % is increased is observed from film A to B to C. Furthermore, the similarity of the spectra for films A and A' shows that the methyl and carbonyl carbons of the acetone feed are incorporated with equal efficiency.

ppm, indicating the presence of only  $sp^3$ -bonded carbon. Prior to crushing film A, the static NMR spectra [Fig. 3(a)] gives a linewidth of 2.8 kHz at half-maximum intensity. This is broader than that of natural diamond (Fig. 1) and is consistent with the calculated value [Eq. (1)] for a film enriched with 22%  $^{13}\text{C}$ . The poorer signal-to-noise ratio of the static spectra [Fig. 3(a)] relative to the MAS spectra is a result of additional broadening interactions present in the static spectra. The isotopic shift of the  $1332\text{ cm}^{-1}$  diamond line in the Raman spectrum to  $1324\text{ cm}^{-1}$  is also consistent with 22% enrichment. The Raman spectra of this film show a strong absorbance at  $1324\text{ cm}^{-1}$  and little evidence of the  $1350$  or  $1580\text{ cm}^{-1}$  absorbances as-

sociated with amorphous carbon and graphite, in agreement with the NMR results and scanning electron micrographs (SEM), which show highly faceted, multiply twinned surfaces with predominantly  $\langle 111 \rangle$ -oriented  $10\text{ }\mu\text{m}$  crystallites.

The static NMR spectrum of film B [Fig. 3(b)], produced at 6.4 carbon mol % in the feed gas, is similar to that obtained from film A [Fig. 3(a)] in that no  $sp^2$ -bonded carbon is observed and that the static linewidth is consistent with a 22%  $^{13}\text{C}$  enrichment. Again, the  $sp^3$  peak, centered at 36 ppm, is narrowed to 0.20 kHz by magic-angle spinning, indicating that broadening due to bond angle disorder is not a significant factor. The Raman spectra of this film also shows absorbance at  $1324\text{ cm}^{-1}$ , but additional absorbance is observed where the isotopically shifted  $1350$  and  $1580\text{ cm}^{-1}$  lines should appear, indicating this film is of slightly lower quality than film A. This is also in agreement with the SEM data, which shows a randomly oriented, less faceted surface with  $5\text{ }\mu\text{m}$  particles for film B.

Figure 3(c) shows that the static NMR spectrum of film C, produced at 7.4 carbon mol % in the feed gas, appears quite different from that of films A and B. In this case, the  $sp^3$  line, centered at  $\sim 38$  ppm, is significantly broader and less symmetric. In addition, a peak centered at 120 ppm appears, indicating the presence of  $sp^2$ -bonded carbon as well. The integrated areas under the two NMR peaks correspond to  $10 \pm 2\%$   $sp^2$ -bonded carbon. This  $sp^2$  formation, however, is not accompanied by a significant change in hydrogen content. Both  $sp^2$ - and  $sp^3$ -bonded carbon were also seen by MAS NMR. However, the  $sp^3$  peak of film C is not narrowed to the same degree as those of films A and B by MAS, maintaining a linewidth of 0.69 kHz, even at spinning speeds in excess of 4.0 kHz. This indicates that the  $sp^3$ -bonding environment in film C is probably more disordered than those found in films produced at lower carbon concentrations, although less disordered than those of amorphous carbon films which have MAS linewidths of 2.25 kHz. The Raman spectrum obtained from film C shows only the isotopically shifted  $1580\text{ cm}^{-1}$  graphite line and the  $1350\text{ cm}^{-1}$  disordered carbon line.<sup>15</sup> No absorbance is observed at  $1324\text{ cm}^{-1}$ , the location of the isotopically shifted diamond line. It is interesting to note that Raman spectroscopy failed to detect any  $sp^3$ -bonded carbon, which comprises 90% of film C. This is undesirable for a characterization tool when new deposition conditions are being explored, since conditions which yield a majority of  $sp^3$ -bonded sites can be overlooked by the Raman analysis. SEM confirms the poor quality of this sample, showing a dark film with no identifiable crystal facets.

The spin-lattice relaxation-time constant  $T_1$  is also an indicator of film quality, since as the number of defects increases,  $T_1$  decreases. Table I shows a decline in film quality, as indicated by the decrease in  $T_1$ , as the carbon concentration in the feed increases. None of the values measured approaches that of natural diamond ( $\sim 1$  day), indicating a high defect concentration. Possible sources of such defects are tantalum incorporated from the filament or incorporated nitrogen, both of which would act as para-



magnetic relaxation centers. The relaxation observed follows an exponential decay as predicted by the Bloch equation. However, this does not eliminate the possibility of paramagnetic centers, since nonexponential relaxation behavior is only observed in the limit of slow spin diffusion.<sup>11</sup> In our enriched samples,  $^{13}\text{C}$  nuclei removed from the defect site will experience increased relaxation due to increased homonuclear dipolar communication, and we expect to observe an exponential decay. The decrease in  $T_1$  generally follows a decrease in grain size, indicating that defects at grain boundaries may be important sites for relaxation.

#### IV. SELECTIVE ISOTOPIC ENRICHMENT STUDIES

Figure 3(d) shows the static  $^{13}\text{C}$  NMR spectra of the film A', produced from carbonyl-labeled acetone at the same carbon mol % employed in the gas phase as for film A. As with the previous samples, the total gas-phase  $^{13}\text{C}$  enrichment was 22%, and the resulting linewidth is close to the expected value for a 22% enrichment in the solid phase. Like film A, produced with methyl labeled acetone, film A' has an  $sp^2$ -bonded carbon concentration below our detection limit, gives a high-quality Raman spectrum with strong  $sp^3$  absorbance, and shows a highly faceted structure with 8  $\mu\text{m}$  rectangular crystallites by SEM.

The incorporation of carbon from the carbonyl position of the acetone reactant in film A' raises questions about the role of oxygen and the chemistry within the reactor. There are three possible pathways for carbonyl-carbon incorporation into the diamond film, as CO incorporated directly from the gas phase, through homogeneous gas-phase conversion to a precursor species, or through heterogeneous conversion to a precursor species.

The first, direct incorporation of CO from the gas phase might be expected to follow a pathway analogous to the Boudouard reaction,



for soot formation, although no evidence for this process in diamond growth has been found.<sup>16</sup> The kinetics of the Boudouard reaction are greatly enhanced by surfaces and iron contamination, suggesting the importance of heterogeneous chemistry.

There are many possible routes for the second method of incorporation, homogeneous carbon scrambling, but based on published homogeneous reaction rate constants for CO scrambling in the literature, these are likely to be slow. In addition, through isotopic studies, it has been shown that homogeneous scrambling of CO is minimal.<sup>17,18</sup> Homogeneous scrambling of hydrocarbons at these temperatures, on the other hand, is quite rapid.<sup>19</sup> One final possibility is that the enol form of the acetone reactant provides a pathway for homogeneous carbon conversion.<sup>20</sup>

The presence of CO in the gas phase during diamond deposition also occurs when reactants other than acetone are used in the gas feed. Harris has measured a CO concentration of 0.018 mol % in the gas phase when 7.0 mol %  $\text{CH}_4$  and 1.0 mol % of  $\text{O}_2$  enters the reaction zone.<sup>21</sup> This is close to the equilibrium CO concentration

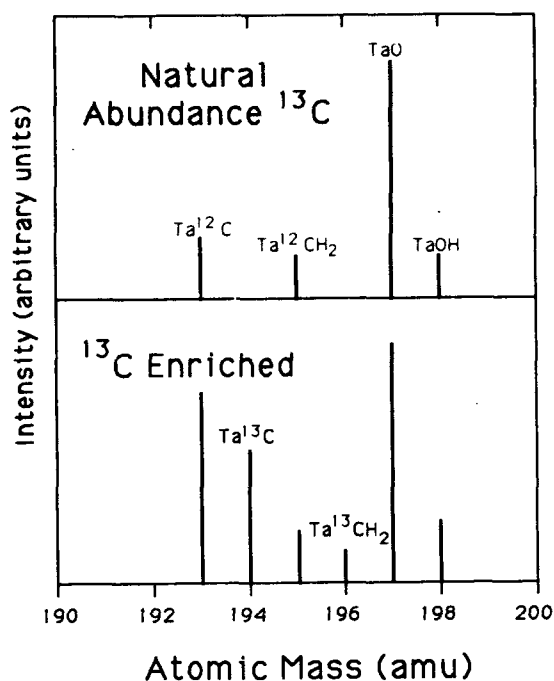


FIG. 4. (a) SIMS spectrum taken from a tantalum filament exposed to only natural  $^{13}\text{C}$  abundance acetone shows peaks at 193, 195, 197, and 198 u. These are representative of  $\text{Ta}^{12}\text{C}$ ,  $\text{Ta}^{12}\text{CH}_2$ ,  $\text{TaO}$ , and  $\text{TaOH}$ , respectively. (b) SIMS spectrum taken from a filament initially carburized with natural abundance acetone and then exposed to  $^{13}\text{C}$ -enriched acetone, labeled at the carbonyl carbon, shows the four peaks observed in spectrum (a) as well as additional peaks at 194 and 196 u. These represent  $\text{Ta}^{13}\text{C}$  and  $\text{Ta}^{13}\text{CH}_2$  and show that heterogeneous exchange does take place in the filament.

of 0.017 mol % at the filament temperature and reactor pressure. Similar agreement was found at other oxygen concentrations checked between 0% and 3%. However the pathway by which this CO would form, directly from carbonyl carbons or through other homogeneous reaction, has not been determined. In any case, the fate of the CO carbons in the hot-filament reactor is of interest since the CO species is expected to form in most systems containing oxygen in the feed gas.

We have used secondary-ion mass spectrometry (SIMS) to evaluate the role of heterogeneous exchange between the carburized tantalum filament and the gas-phase carbonyl-derived carbons. Since the filament is the highest-temperature surface in the reactor, it is a more likely site for heterogeneous reaction than, for example, the water-cooled aluminum reactor walls. The SIMS spectrum in Fig. 4(a) was obtained from a tantalum filament exposed for several hours to an unenriched gas feed at typical reactor conditions. The peaks at 193 and 195 u represent  $\text{Ta}^{12}\text{C}$  and its hydride  $\text{Ta}^{12}\text{CH}_2$ , respectively, while  $\text{TaO}$  and  $\text{TaOH}$  appear at 197 and 198 u, respectively. The SIMS spectrum of a tantalum filament exposed to unenriched acetone and hydrogen for several hours in the same manner as the first and then exposed to 22%  $^{13}\text{C}$ -enriched acetone, labeled at the carbonyl carbon, and an excess of hydrogen for several hours at typical operating conditions is shown in Fig. 4(b). The peaks at 193, 195,

197, and 198 u appear as before. Two new peaks appear, however, at 194 and 196 u, indicating the presence of Ta  $^{13}\text{C}$  and Ta  $^{13}\text{CH}_2$ , respectively. Depth profiling of the filament to greater than 2000 Å gives similar  $^{13}\text{C}$  levels, indicating that exchange has occurred on the interior as well as the surface of the filament. The complete exchange at the filament accounts for the identical degree of enrichment in films produced with both methyl-labeled or carbonyl-labeled  $^{13}\text{C}$  acetone.

Although it is well known that the filament carburizes initially, heterogeneous chemistry continues even after this initial period. Current models of gas-phase chemistry do not account for reactions at the filament surface. For species near equilibrium in the hot-filament reactor, such as  $\text{C}_2\text{H}_2$ , variation in mechanisms will produce only small changes in predicted species concentrations. However, for other species, this effect should be considered.

## V. CONCLUSIONS

Nuclear-magnetic-resonance spectroscopy provides a nondestructive means of quantitatively evaluating diamond films. As gas-phase carbon concentration increases, the film quality, in terms of  $sp^2$  content,  $sp^3$ -bonding disorder, spin-lattice relaxation and active defect concentration, strength of the  $sp^3$  Raman absorption, and SEM observed morphology is observed to decrease. The hydrogen incorporated into these films cannot account for these variations in the range of carbon concentrations studied. Isotopic enrichment can be used to decrease sample size requirements and spin-lattice relaxation times, increasing sensitivity and decreasing acquisition times. Selective isotopic labeling was used to raise questions and gain insight into the chemistry of diamond formation as well. NMR has shown that the carbonyl carbon of acetone is incorporated into the growing film, and SIMS has been used to show that heterogeneous exchange reactions, involving the carbonyl carbon, occur at the hot filament.

## ACKNOWLEDGMENTS

The authors wish to thank Dr. Mike Geis of Lincoln Laboratories for generously allowing us to use his diamond deposition system, Dr. James E. Butler of the Naval Research Laboratory for the Raman spectroscopy, and Dr. Ed Gleason of Lincoln Laboratories for the SEM work. We gratefully acknowledge the support of the Office of Naval Research and NSF Grant No. CTS-9006705.

- <sup>1</sup>R. C. DeVries, *Am. Rev. Mater. Sci.* **17**, 161 (1987).
- <sup>2</sup>Y. Hirose and K. Iwasaki, *Jitsumu Hyomen Gijutsu* **34**, 255 (1987).
- <sup>3</sup>Y. Hirose and Y. Terasawa, *Jpn. J. Appl. Phys.* **25**, L519 (1986).
- <sup>4</sup>F. Akatsuka, Y. Hirose, and K. Komaki, *Jpn. J. Appl. Phys.* **27**, 1600 (1987).
- <sup>5</sup>J. Suzuki, H. Kawarada, K. S. Mar, J. Wei, Y. Yokota, and A. Hiraki, *Jpn. J. Appl. Phys.* **28**, 281 (1989).
- <sup>6</sup>S. C. Sharma, C. A. Dark, R. C. Hyer, M. Green, T. D. Black, A. R. Chourasia, D. R. Chopra, and K. K. Mishra, *Appl. Phys. Lett.* **56**, 1781 (1990).
- <sup>7</sup>K. M. McNamara, D. H. Levy, K. K. Gleason, and C. J. Robinson, *Appl. Phys. Lett.* **60**, 580 (1992).
- <sup>8</sup>P. M. Henrichs, M. L. Coffield, R. H. Young, and J. M. Hewitt, *J. Magn. Reson.* **58**, 85 (1984).
- <sup>9</sup>J. H. van Vleck, *Phys. Rev.* **74**, 1168 (1948).
- <sup>10</sup>A. Abragam, *The Principles of Nuclear Magnetism* (Oxford, New York, 1983).
- <sup>11</sup>W. E. Blumberg, *Phys. Rev.* **119**, 79 (1959).
- <sup>12</sup>D. Tse and S. R. Hartmann, *Phys. Rev. Lett.* **21**, 511 (1968).
- <sup>13</sup>M. A. Petrich, *Mater. Sci. Forum* **52-53**, 387 (1989).
- <sup>14</sup>K. C. Bustillo, M. A. Petrich, and J. A. Reimer, *Chem. Mater.* **2**, 202 (1990).
- <sup>15</sup>D. S. Knight and W. B. White, *J. Mater. Res.* **4**, 385 (1985).
- <sup>16</sup>A. G. Gaydon and H. G. Wolfhard, *Flames* (Capman and Hall, London, 1979).
- <sup>17</sup>R. E. Ferguson, *J. Chem. Phys.* **23**, 2085 (1955).
- <sup>18</sup>R. E. Ferguson, *Combustion and Flame* **1**, 431 (1957).
- <sup>19</sup>C. J. Chu, R. H. Hague, M. P. D'Evelyn, and J. L. Margrave, *Mater. Res. Soc. Symp. Proc.* **162** (1989).
- <sup>20</sup>A. Streitwieser, Jr. and C. H. Heathcock, *Introduction to Organic Chemistry* (Macmillan, New York, 1981).
- <sup>21</sup>S. J. Harris, *J. Appl. Phys.* **65**, 3044 (1989).

# Nuclear magnetic resonance and infrared absorption studies of hydrogen incorporation in polycrystalline diamond

K. M. McNamara, D. H. Levy, and K. K. Gleason  
Department of Chemical Engineering, M.I.T., Cambridge, Massachusetts 02139

C. J. Robinson  
Raytheon Company, Lexington, Massachusetts 02173

(Received 26 July 1991; accepted for publication 13 November 1991)

Hydrogen incorporated into polycrystalline diamond was found to correlate with the optical absorption in the 8 to 10  $\mu\text{m}$  wavelength IR region, where transparency is desired. In this first detailed study of diamond films by  $^1\text{H}$  NMR, average concentrations were found to be  $<0.25$  at. % H. However, segregation produces regions of extremely high local hydrogen density as evidenced by a broad (50–70 kHz) Gaussian NMR component. The majority of this clustered hydrogen is rigidly held, while a fraction undergoes motional narrowing at room temperature, most likely due to methyl group rotation. Sites at grain boundaries are capable of accounting for a significant fraction of this hydrogen, as are defects and voids within the crystal or a heavily hydrogenated phase stable at the deposition temperature.

Polycrystalline diamond films are desired for many applications, including tribological coatings, x-ray lithographic membranes, and durable infrared (IR) windows. These films are usually deposited from gas-phase mixtures containing predominately hydrogen. Although the role of hydrogen in the diamond growth process has been the subject of much speculation,<sup>1</sup> less attention has been focused on the location and distribution of hydrogen in polycrystalline diamond. This information should provide insight into both deposition chemistry and the effect of hydrogen incorporation on bulk film properties.

Previously, concentrations of  $<0.25$  at. % H in polycrystalline diamond films were measured by nuclear reaction analysis.<sup>2</sup> In contrast,  $>50$  at. % H can be incorporated into amorphous carbon films.<sup>1</sup> This difference in hydrogen content reflects both the increased atomic order and higher deposition temperatures of the polycrystalline film. To date, little has been reported on hydrogen bonding configurations in polycrystalline diamond.

This letter will examine if the low concentrations of hydrogen, incorporated during hot-filament diamond deposition, affect optical absorption in the 8 to 10  $\mu\text{m}$  wavelength IR region, where transparency is desired. In this work, quantitative hydrogen concentrations and information on hydrogen spacing and motion are provided by first detailed  $^1\text{H}$  nuclear magnetic resonance (NMR) study of diamond films. Complementary data on  $\text{CH}_x$  stretching modes, as well as absorption in the 8 to 10  $\mu\text{m}$  region, were measured by Fourier transform infrared (FTIR) spectroscopy.

The diamond films were deposited from a feed of 2%  $\text{CH}_4$  in 1.0  $\ell/\text{min}$   $\text{H}_2$  onto a rotating 1 in. diameter silicon substrate positioned 4 mm from a hot tantalum filament. For each film, the remaining deposition conditions are listed in Table I. Then, the substrate was removed by a  $\text{HF}/\text{HNO}_3$  etch, leaving a free-standing film. In all three samples, large (30 to 60  $\mu\text{m}$ ), well-faceted crystallites were observed by electron and optical microscopy, while film

texture was observed by x-ray diffraction. Also, a sharp 1332  $\text{cm}^{-1}$  Raman line and a 36 ppm  $sp^3$   $^{13}\text{C}$  NMR peak, characteristic of diamond, were observed for all three films, while  $sp^2$  bonded carbon concentrations were below the detection limit of both techniques.

The Fourier transformed 270 MHz  $^1\text{H}$  NMR spectra, shown in Fig. 1, represents  $\sim 1500$  signal averages, performed at 5 s intervals since all spin-lattice time constants were  $<1$  s. By eliminating the NMR sample tube and purging the NMR probe with dry nitrogen, the background signal was reduced below the detection limit of  $\sim 5 \times 10^{16}$  H/sample. Integrating these spectra yielded concentrations ranging from 0.017 to 0.219 at. % H (Table I). Each spectrum was least-squares fit to the sum of a broad Gaussian and a narrow Lorentzian component. The full-width at half-maximum (FWHM) and at. % H of each component are also given in Table I. These two line shapes indicate two different bonding configurations for hydrogen in polycrystalline diamond.

Figure 2 shows the IR absorbance spectra for samples A, B, and C. Absorbance in this context is defined as  $A = \ln(T_0/T)$  where  $T$  is the measured transmittance and

TABLE I. Summary of deposition conditions and characterization results for the three diamond films studied.

	A	B	C
Filament temperature ( $^{\circ}\text{C}$ )	2150	2100	2150
Pressure (Torr)	300	100	100
Film thickness ( $\mu\text{m}$ )	190	420	342
Growth rate ( $\mu\text{m}/\text{hr}$ )	3.96	1.83	1.38
at. % H-Total	0.219	0.049	0.017
at. % H-Gaussian	0.217	0.047	0.015
at. % H-Lorentzian	0.002	0.002	0.0012
FWHM (kHz)			
Gaussian	51.5	56.0	66.5
Lorentzian	3.6	4.1	6.6
Film texture	(100)	(100)	(110)

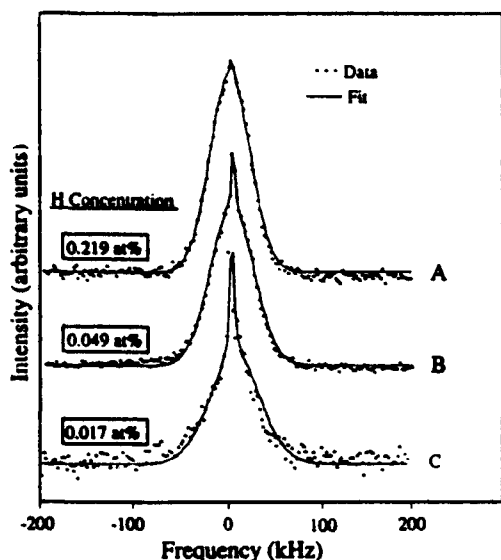


FIG. 1. NMR spectra (solid triangles) of samples A, B, and C at room temperature normalized to the same peak height. The best fit of each spectrum (solid line) to the sum of a broad Gaussian and a narrow Lorentzian component indicates the existence of two different hydrogen environments. The fraction of the Gaussian component decreases from sample A to C as revealed by the increasing sharpness of the Lorentzian peak.

$T_0$  is an appropriate polynomial base line fit used to eliminate the estimated contributions arising from internal and surface scattering processes. The spectra are dominated by two phonon absorptions in the range  $1333\text{--}2666\text{ cm}^{-1}$  which are intrinsic to pure diamond. Below  $1333\text{ cm}^{-1}$  single-phonon absorptions are observed which are nor-

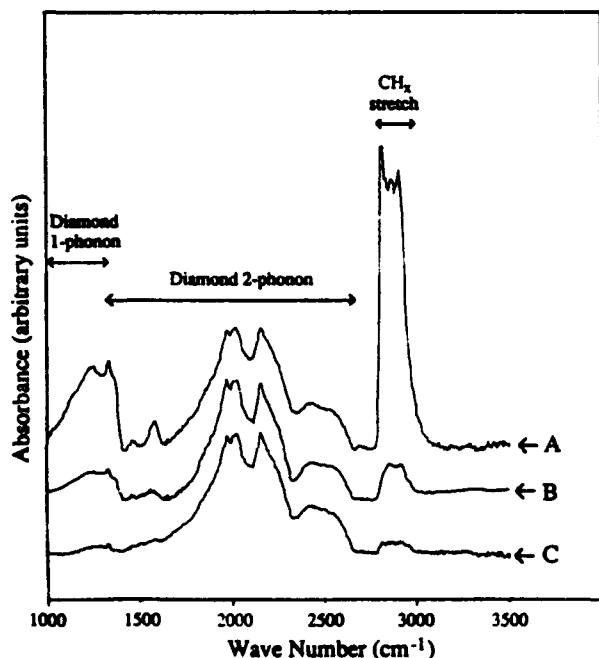


FIG. 2. IR spectra of samples A, B, and C, revealing the one- and two-phonon vibrations as well as a  $\text{CH}_x$  stretch absorption peak. The intensity of the one-phonon and  $\text{CH}_x$  stretch grow with the increasing NMR measured  $^1\text{H}$  content.

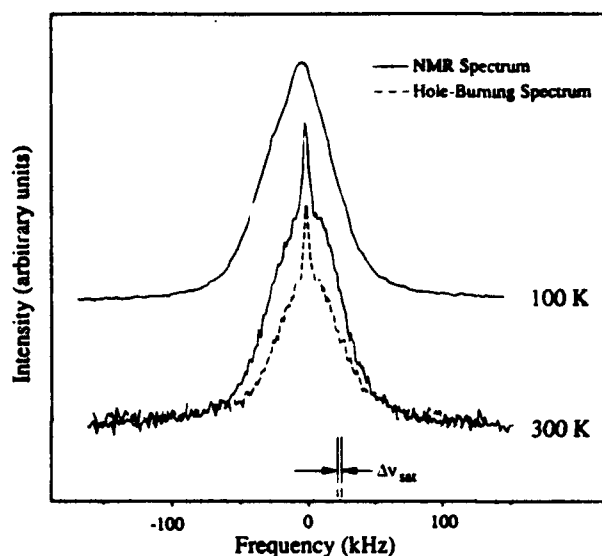


FIG. 3. For sample B, the  $^1\text{H}$  NMR spectra (solid lines) taken at 300 and 100 K show the sharp Lorentzian component broadens as temperature is lowered, consistent with the behavior of rotating methyl groups. A 300 K hole-burning NMR spectra (dotted line) shows uniform attenuation of both components of the line shape after a small frequency band,  $\Delta\nu_{\text{sat}}$ , has been saturated, indicating spacial proximity of the two hydrogen environments.

mally disallowed in pure diamond. These absorptions become active in the IR in CVD diamond films as a result of defects which disrupt the translational symmetry of the host lattice and have been discussed in detail elsewhere.<sup>3</sup> Hydrogenated defects are one of many potential sources of such a disruption. In Fig. 2, the intensity of the one-phonon regions is observed to follow the same trend as those of the  $\text{CH}_x$  stretch region ( $2800\text{--}3000\text{ cm}^{-1}$ ) and the  $\text{CH}_x$  bending modes ( $> 1340\text{ cm}^{-1}$ ), as well as the NMR determined at % H, but no quantitative relationship was found between any pair of these measurements.

To determine if these two hydrogen environments are spatially isolated, a "hole-burning" NMR experiment was employed.<sup>4</sup> A "hole" in the NMR spectrum, 1 kHz wide and 30 kHz from the center of the line shape, was created by selective saturation, which directly reduces only the intensity of the broad Gaussian line shape. After completing the selective saturation and allowing a 2 ms delay, the magnitude of the Lorentzian component will be attenuated only if rapid dipolar communication occurs between protons in the two environments, requiring short  $< 5\text{ \AA}$  internuclear distances. The observed uniform attenuation of the NMR hole-burning spectra of film B, shown in Fig. 3, indicates that both bonding configurations for hydrogen are in close spatial proximity.

Rotational or translational motion involving species containing hydrogen, such as  $\text{H}_2$ ,  $\text{H}_2\text{O}$ , or  $\text{CH}_3$  groups, can produce a temperature-dependent NMR linewidth. Figure 3 shows that when the temperature of sample B is decreased to 100 K, the Lorentzian component is broadened, while the Gaussian component is not significantly affected. Thus, at room temperature, the narrow Lorentzian line-shape results from motional averaging, while the broad

Gaussian line indicates rigidly held hydrogen. NMR relaxation studies have shown that methyl groups in polymer systems, while capable of rapid rotation at room temperature, will slow sufficiently at 100 K to produce a broadened line.<sup>5</sup> Trapped H<sub>2</sub>, as observed in amorphous silicon films,<sup>6</sup> would also give rise to a narrow line at room temperature. However, this line would not be significantly broadened at 100 K. No evidence of absorbed H<sub>2</sub>O is seen in the IR spectra. Hence, the narrow Lorentzian component most likely arises from methyl groups, which rotate at room temperature.

For static distributions of hydrogen, such as CH and CH<sub>2</sub> bonded in a rigid polycrystalline lattice, the van Vleck equation<sup>7</sup> for a Gaussian line shape due to homonuclear dipolar broadening of chemically equivalent protons *i* and *j* reduces to

$$\text{FWHM} = 189.6 \left( \sum_{j \neq i} r_{ij}^{-6} \right)^{1/2} (\text{\AA}^3 \text{ kHz}), \quad (1)$$

revealing a strong dependence on  $r_{ij}$ , the interproton distance. Thus, the dipolar linewidth is usually dominated by couplings occurring over distances of <10 Å. For the polycrystalline diamond samples, if all hydrogen in the Gaussian component were distributed uniformly as CH, the resulting FWHM range would be more than two orders of magnitude narrower than observed. Evenly dispersed CH<sub>2</sub> groups would only give rise to a 34 kHz linewidth.<sup>8</sup> This discrepancy indicates locally high hydrogen concentrations, requiring significant segregation of hydrogen in polycrystalline diamond.

The local hydrogen concentrations required for the observed linewidth are of the order of those in amorphous carbon films, in which 35 at. % H gives rise to 78 kHz Gaussian linewidth.<sup>9</sup> However, during deposition, the substrate temperature exceeds the 600 °C anneal required to remove *sp*<sup>3</sup> CH<sub>x</sub> from amorphous carbon films<sup>10</sup> and most likely exceeds the 800 °C required for little or no hydrogen to remain in diamond-like amorphous carbon films.<sup>1</sup> Also, the majority of intensity in the CH<sub>x</sub> stretch region occurs at <2960 cm<sup>-1</sup>, indicating H is bound predominately to *sp*<sup>3</sup> carbon, further constraining the identity of such a heavy hydrogenated phase.

Another possibility is a hydrogen passivated diamond surface. For example, a 60 kHz FWHM would result for four nearest neighbors at 1.77 Å, equivalent to 3 × 10<sup>15</sup> H/cm<sup>2</sup>, within the range of atomic surface densities possible for different diamond orientations. Unequal hydrogen spacing would reduce the surface density required for a given linewidth, as would having two opposing hydrogenated surfaces in a microvoid or at a grain boundary. At this surface coverage, a grain boundary area of ~3 μm<sup>2</sup>/μm<sup>3</sup> is required to account for the observed 0.046 at. % H in film B, which corresponds to the surface-to-volume ratio of 2-μm-sided crystallites. The density of these small crystallites, which arise from secondary nucleation on the large columnar grain structures, differs from film to film. The variation in dimension, shape, and surface roughness, coupled with orientation-dependent surface density, both static and motionally narrowed, may allow

grain boundary sites to account for a significant fraction of the observed hydrogen. Films with large crystallites and a low degree of secondary nucleation would provide the lowest grain boundary area for potential hydrogen passivation. The chemical structure of hydrogenated surfaces preserved after film growth is complete may resemble those present during deposition, providing a potential test of surface chemistry growth models.

Film growth conditions influence hydrogen incorporation in polycrystalline diamond. Decreasing the filament temperature by 50 °C (film B to C) maintains a <110> orientation, but increases the growth rate by 30%, incorporating 2.6 times more hydrogen (Table I). Changing deposition pressure from 100 to 300 Torr (film C to film A) has the more dramatic effect of producing a threefold increase in growth rate and a 12-fold increase in hydrogen content. This observation is consistent with previous work where increasing CH<sub>4</sub> pressure during deposition led to an increased absorption in the CH<sub>x</sub> stretch region.<sup>1</sup> Of the three films, film A had the highest density of small (<3 μm) secondarily nucleated crystallites, providing more grain boundary area for possible hydrogen passivation.

In conclusion, these polycrystalline diamond films had low-average bulk concentrations of <0.25 at. % H. The NMR spectra reveal that hydrogen is segregated into regions of extremely high local density. The majority of this hydrogen is rigidly held but is intermingled with a smaller fraction of hydrogenated species undergoing motional narrowing at room temperature, most likely corresponding to the rotation of methyl groups. Sites at grain boundaries are capable of accounting for a significant fraction of the hydrogen, as are defects and voids within the crystal, or a heavily hydrogenated phase stable at the deposition temperature. Among the hot-filament grown films studied, there is a strong qualitative correlation between film growth rate, the degree of secondary nucleation, the concentration of rigidly held hydrogen measured by NMR and the absorption in the one-phonon region of the diamond IR spectra.

The authors wish to acknowledge the National Science Foundation Grant No. CTS-9006705, the Office of Naval Research and the Naval Weapons Centers for partial support of this work.

<sup>1</sup> R. C. Devries, *Annu. Rev. Mater. Sci.* 17, 161 (1987).

<sup>2</sup> K. E. Spear, *Earth Miner. Sci.* 56, 53 (1987).

<sup>3</sup> C. A. Klein, T. M. Hartnett, R. P. Miller, and C. J. Robinson, *Proceedings 2nd International Conference on Diamond Materials* (Electrochemical Society, Pennington, NJ, 1991), pp. 435-442.

<sup>4</sup> J. A. Reimer, R. W. Vaughan, and J. C. Knights, *Phys. Rev. B* 24, 3360 (1981).

<sup>5</sup> C. P. Slichter, *J. Polym. Sci.: Part C* 14, 33 (1966).

<sup>6</sup> J. B. Boyce and M. Stolzmann, *Phys. Rev. Lett.* 54, 562 (1985).

<sup>7</sup> A. Abragam, *Principles of Nuclear Magnetic Resonance* (Oxford, London, 1961).

<sup>8</sup> This configuration would be a Pake doublet rather than a Gaussian line shape.

<sup>9</sup> J. A. Reimer, *J. Vac. Sci. Technol.* 19, 53 (1981).

<sup>10</sup> B. Dischler, A. Bubenzer, and P. Koidl, *Solid State Commun.* 48, 105 (1983).

<sup>11</sup> X. X. Bi, P. C. Ekland, J. G. Zhang, A. M. Rao, T. A. Perry, and C. P. Beetz, Jr., *J. Mater. Res.* 5, 811 (1990).

# Quantitative correlation of infrared absorption with nuclear magnetic resonance measurements of hydrogen content in diamond films

K. M. McNamara and K. K. Gleason  
*Department of Chemical Engineering, MIT, Cambridge, Massachusetts 02139*

C. J. Robinson  
*Raytheon Company, Lexington, Massachusetts 02173*

(Received 16 December 1991; accepted 4 April 1992)

Hydrogen concentrations in polycrystalline diamond films were found to correlate well with the integrated intensity of the CH-stretch region in the infrared (IR) spectrum for films with a total hydrogen content  $<0.10$  at. %. Comparison of IR to nuclear magnetic resonance (NMR) measurements yielded an effective absorption coefficient for the CH-stretch region of  $4.3 \pm 0.8 \times 10^3 / \text{mol}^{-1} \text{cm}^{-2}$ , similar to literature values for condensed-phase hydrocarbons. In several films, the dominant stretch modes occur at  $\sim 2850$  and  $2920 \text{ cm}^{-1}$ , typical of  $\text{CH}_2$  groups. The presence of these modes is accompanied by an increase in the Gaussian linewidth in the NMR spectrum, indicating a decrease in the interproton spacings within the film. In films with higher total hydrogen contents, a simple linear relationship between hydrogen content and intensity in the CH-stretch region is no longer applicable.

## I. INTRODUCTION

Polycrystalline diamond films are suitable for many applications, including those requiring transmission in the  $8\text{--}10 \mu\text{m}$  region of the infrared (IR). Most other materials which are transparent in this region are soft, making diamond's durability very attractive. However, while gem-quality diamond exhibits no absorption in this region, synthetic polycrystalline films often do. Increased absorption in the  $8\text{--}10 \mu\text{m}$  region is usually associated with a similar increase in absorption in the CH-stretch region, qualitatively indicating an increase in total hydrogen content.<sup>1,2</sup> In this paper, we extend earlier findings and report the first quantitative correlation of the infrared absorption in the CH-stretch region and the total hydrogen content, determined by solid-state nuclear magnetic resonance (NMR) spectroscopy.

Fourier transform infrared (FTIR) spectroscopy is an attractive technique for analyzing hydrogen in synthetic diamond since it is nondestructive and may be performed relatively quickly. In addition, FTIR can be used to identify specific hydrocarbon groups responsible for absorption. Quantitative information may also be obtained for materials with similar absorption coefficients. Absorption coefficients observed in the literature for systems which may be similar to synthetic diamond, such as alkanes,<sup>3</sup> paraffinic hydrocarbons,<sup>4</sup> and  $\alpha\text{-Si:C:H}$ ,<sup>5</sup> show only small variation, indicating that it may be possible to identify an effective absorption coefficient characteristic of polycrystalline diamond and obtain quantitative information from the FTIR spectrum of these materials.

Solid-state NMR spectroscopy is a quantitative method for examining hydrogen contents in polycrystalline diamond. The integrated intensity under the  $^1\text{H}$  NMR line shape is directly proportional to the number of hydrogen nuclei in the sample, independent of bonding environment.<sup>6,7</sup> This technique is also nondestructive but may require longer sampling times than those used in

FTIR. In addition, solid-state NMR equipment is not routinely available in many laboratories. Thus, it would be beneficial to determine a correlation between the hydrogen content measured using NMR spectroscopy and the integrated absorption in the infrared spectrum.

In addition, information on the distribution and motion of hydrogen can be obtained from the solid-state NMR spectrum. Earlier work<sup>2</sup> has shown that the  $^1\text{H}$  NMR line shape of polycrystalline diamond contains two components. One is a narrow Lorentzian line shape most likely caused by rotating surface methyl groups. The second is a broad Gaussian component rising from static closely spaced hydrogen and accounts for more than 90% of the total hydrogen. It has been proposed that hydrogenated grain boundaries may account for a significant portion of the hydrogen observed in this component.<sup>2</sup>

## II. EXPERIMENT

A set of ten polycrystalline diamond films (Table I) were produced at a variety of conditions in a hot-filament chemical vapor deposition (CVD) reactor, yielding diamond films with varying hydrogen contents. The reactant gas contained between 1% and 2% methane, diluted in hydrogen. For each run, the tantalum filament was placed between 3 and 4 mm from the substrate, and the filament temperature, measured by optical pyrometry, was between 2100 and 2475 K, resulting in growth rates ranging from 1 to  $4 \mu\text{m/h}$ . For nine of the samples, the total pressure was 100 Torr, while the tenth sample, film J, was deposited at 300 Torr. The 1 in. silicon wafer substrate was rotated to improve film uniformity. After growth, the substrate was etched away in a solution of  $\text{HF}/\text{HNO}_3$ , leaving a free standing diamond film between 45 and  $600 \mu\text{m}$  thick. Scanning electron microscopy (SEM) showed crystallites between 1 and  $100 \mu\text{m}$ , with thinner films showing smaller crystallites. Secondary nucleation resulted in small 2 to  $3 \mu\text{m}$  crystallites also being observed in some of the thicker,

TABLE I. Process conditions for ten polycrystalline diamond films.

	Film									
	A	B	C	D	E	F	G	H	I	J
$D_f$ (mm)	3.5	4	4	4	4	4	3	3	3.5	4
$T_f$ (K)	2425	2425	2375	2475	2150	2375	2375	2200	2100	2150
$P$ (Torr)	100	100	100	100	100	100	100	100	100	300
$d$ ( $\mu\text{m}$ )	600	342	45	50	135	420	350	83	50	135
(Rate) <sub>G</sub> ( $\mu\text{m}/\text{h}$ )	1.75	1.38	1.87	...	1.78	1.83	1.52	2.07	1.06	3.96

larger grain size films. The high quality of these films was confirmed by Raman and  $^{13}\text{C}$  NMR spectroscopy, yielding sharp  $1332\text{ cm}^{-1}$  lines and  $36\text{ ppm}$   $sp^3$  resonances<sup>6</sup> and little evidence of  $sp^2$  bonded carbon.

Hydrogen contents for the films were obtained by solid-state NMR as described in our earlier work.<sup>2</sup> Comparison of the total integrated area under the  $^1\text{H}$  NMR line with that of a polymethyl-methacrylate (PMMA) standard enables us to determine the number of hydrogen nuclei within the sample. Spectra were obtained on a 270 MHz home-built  $^1\text{H}$  NMR spectrometer. Approximately 1500 signal averages, performed at 5 s intervals, achieved the desired level of signal-to-noise. The 5 s interval was chosen to allow the system to come to equilibrium with the static magnetic field between experiments, since the spin-lattice relaxation time constant for these films is  $< 1\text{ s}$ . Spin-lattice relaxation time constants  $T_1$  were determined using the inversion recovery technique and subsequent application of the Bloch equation<sup>7</sup>

$$\frac{M(t) - M_{\text{eq}}}{M_0 - M_{\text{eq}}} = \exp(-t/T_1), \quad (1)$$

where  $M(t)$  is the net magnetization parallel to the external magnetic field at time  $t$ ;  $M_{\text{eq}}$  is the equilibrium magnetization; and  $M_0$  is the initial magnetization at time  $t = 0$ . The detection limit for  $^1\text{H}$  in our spectrometer is  $10^{17}$  protons. For a film with 0.05 at. %  $^1\text{H}$  this corresponds to  $\sim 4\text{ mg}$  or  $1.13 \times 10^{-3}\text{ cm}^3$ .

FTIR spectra were obtained for all samples. Contributions due to surface and internal scattering processes were estimated using an appropriate polynomial base line fit. The absorbance  $A$  is then defined as  $A = \ln(T_0/T)$ , where  $T$  is the measured transmittance; and  $T_0$  refers to the base line fit. The frequency range of the spectra extends from  $1000$  to  $3500\text{ cm}^{-1}$ . Two-phonon absorption, intrinsic to pure diamond, occurs in the range  $1333$ – $2666\text{ cm}^{-1}$ . Below  $1333\text{ cm}^{-1}$ , absorptions in pure diamond are disallowed due to lattice symmetry. These lower wave number absorptions appear in synthetic diamond as a result of defects and/or impurities which disrupt the symmetry of the host lattice. Absorption in this region is observed to follow the trends observed in the region between  $2750$  and  $3050\text{ cm}^{-1}$ , known as the CH-stretch region.<sup>2</sup> It is the absorption in the CH-stretch region which correlates with the hydrogen content measured by NMR spectroscopy.

### III. RESULTS AND DISCUSSION

Three representative  $^1\text{H}$  NMR spectra are shown in Fig. 1. The total area under these spectra is directly proportional to the number of hydrogen atoms in the film and decreases in these three samples from I to H to B. In addition, these spectra and those of the remaining samples are well represented by two components, a narrow Lorentzian and a broad Gaussian, as observed previously.<sup>2</sup> This is shown by the solid line least-squares fit to the data. The theoretical full-width at half-maximum of the Gaussian ( $\text{FWHM}_G$ ) component can be calculated using the Van Vleck equation<sup>8</sup> which reduces, for a polycrystalline material with densely spaced protons, to

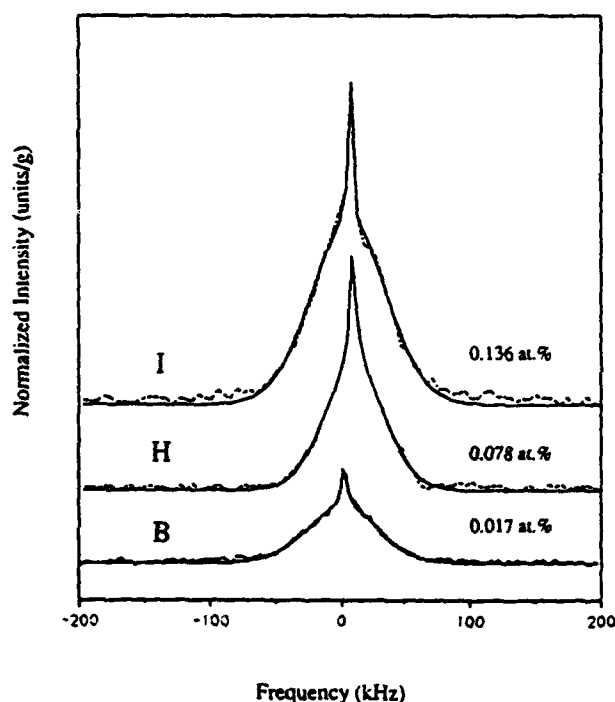


FIG. 1. Solid-state hydrogen NMR spectra for three representative diamond films. I, H, and B, respectively from the top of the figure. The dashed line represents the data, while the solid line represents the best two-component fit to the data. The Gaussian component may be attributed to closely spaced static hydrogen, while the Lorentzian may be attributed to mobile surface methyl groups (Ref. 2). The area under the curve is directly proportional to the hydrogen content in the sample.

TABLE II. Data from IR and NMR measurements for ten polycrystalline diamond films.<sup>a</sup>

	Film									
	A	B	C	D	E	F	G	H	I	J
at. % H	<0.001	0.017	0.031	0.039	0.045	0.049	0.067	0.078	0.136	0.219
at. % H <sub>G</sub>	<0.001	0.015	0.022	0.035	0.036	0.047	0.058	0.058	0.129	0.217
FWHM <sub>G</sub> (kHz)	...	66.5	62.2	58.0	71.7	56.0	71.5	56.1	69.7	51.5
A <sub>eff</sub> (× 10 <sup>3</sup> / mol <sup>-1</sup> cm <sup>-2</sup> )	...	3.47	3.11	4.86	5.49	3.58	3.43	4.57	6.49	7.06
Asymm. CH <sub>2</sub>	...	w	w	w	s	w	s	s	s	w

<sup>a</sup>G = Gaussian component; w = weak; s = strong.

$$\text{FWHM}_G = 189.6 \left( \sum_{j \neq i} r_{ij}^{-6} \right)^{1/2} \text{ \AA}^3 \text{ kHz} \quad (2)$$

showing the strong increase in linewidth as the interproton spacing  $r_{ij}$  decreases. Therefore, information about the distribution of hydrogen within the film can be obtained by comparison of the calculated FWHM<sub>G</sub> for a given configuration with that measured experimentally. The experimental Gaussian linewidth and total hydrogen content of each film is given in Table II. Measured values of the FWHM<sub>G</sub> are large, falling within the range of 50 to 70 kHz corresponding to an average interproton spacing of 1.9 to 2.0 Å, significantly smaller than those predicted for randomly distributed hydrogen at the observed concentrations. This indicates a locally high hydrogen concentration, requiring significant segregation of hydrogen within diamond films.<sup>2</sup>

One possibility is that hydrogen segregates at grain boundaries in polycrystalline diamond. For uniformly spaced hydrogen, a 60 kHz FWHM<sub>G</sub> corresponds to a surface density of  $3 \times 10^{15}$  H/cm<sup>2</sup>, which is in the range of values possible for various orientations of diamond surfaces. Unequal spacing of hydrogen and opposing grain boundaries would tend to reduce this density requirement.

Assuming only surface hydrogen at a density of  $3 \times 10^{15}$  H/cm<sup>2</sup>, Fig. 2 shows the average at. % H of a film composed of simple cubic crystallites as a function of crystallite size. The crystallite size required for the range between our detection limit and a hydrogen content of 0.22 at. % is 0.5 to 150 μm, which compares favorably to observed crystallite sizes. As the hydrogen content in the film increases, the observed crystallite size in the scanning electron micrograph (SEM) decreases. Figure 3 shows the SEMs of samples A, D, and J which contain <0.001, 0.039, and 0.219 at. % H, respectively. The average grain sizes observed in these films are approximately 100, 15, and <1 μm, respectively, consistent with the predictions in Fig. 2. Variations in crystal shape, dimension, orientation, and surface roughness in real polycrystalline films may allow grain boundary sites to account for large portions of the hydrogen incorporated into these films.

Figure 4 shows the IR spectra in the CH-stretch region (2750–3050 cm<sup>-1</sup>) for the three films whose NMR spectra are shown in Fig. 1. Film I has the second highest hydrogen content of all the films studied, and shows an intense CH-stretch absorption. Films H and B show weaker ab-

sorptions in the CH-stretch region, indicating lower hydrogen contents in agreement with NMR determinations. In addition, no absorptions corresponding to  $sp^2$  bonded CH<sub>x</sub> groups (> 3000 cm<sup>-1</sup>) appear in any of the IR spectra. Both films I and H exhibit strong absorption modes at 2850 and 2919 cm<sup>-1</sup>, due to the symmetric and asymmetric stretches of  $sp^3$  bonded CH<sub>2</sub> groups, respectively.<sup>9</sup> Several other films show similar absorptions, as indicated in Table II. Film B, like the remaining films in Table II, does not show the strong CH<sub>2</sub> absorptions. All films show some evidence of a shoulder at ~2960 cm<sup>-1</sup>, which may be attributed to the asymmetric stretch of CH<sub>3</sub> groups.<sup>3</sup> This is particularly pronounced in the spectrum of film H (Fig. 4) and is consistent with the interpretation of the Lorentzian component of the NMR line shape as a mobile surface methyl group.<sup>2</sup>

Several features were noted in the IR spectra outside of the CH-stretch region (see Fig. 5). Absorption in the 8–10 μm region was qualitatively observed to increase with increasing absorption in the CH-stretch region, consistent with earlier findings.<sup>1,2</sup> Several films showed a weak absorbance at ~1600 cm<sup>-1</sup>, which is often associated with the stretching mode of a C=C double bond (see Fig. 5).<sup>9</sup> Both <sup>13</sup>C NMR and Raman spectroscopy, however, failed to

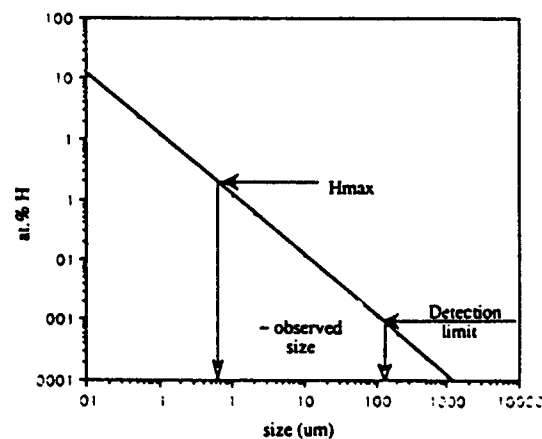
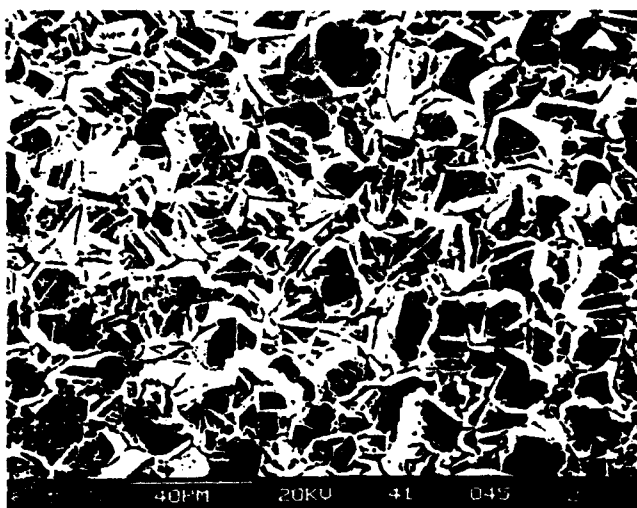


FIG. 2. A plot of the crystallite size required to provide sufficient surface area with a surface coverage of  $3 \times 10^{15}$  H/cm<sup>2</sup> to account for the observed average at. % H. The range of sizes required between our detection limit and 0.22 at. % H is ~0.5 to 150 μm. The experimentally observed grain sizes in polycrystalline diamond films fall into this range.

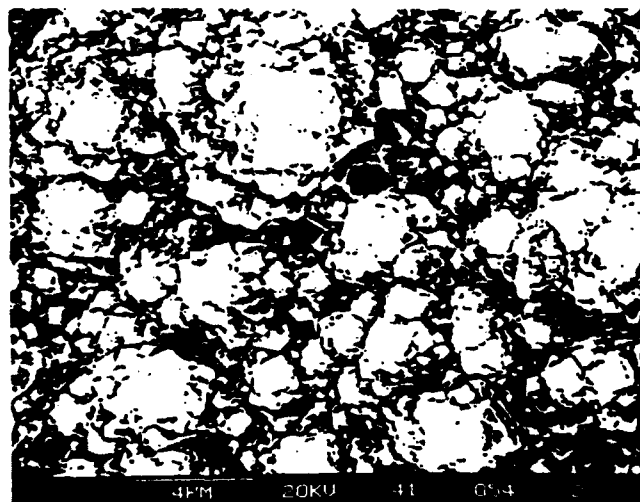




(a)



(b)



(c)

FIG. 3. Scanning electron micrographs (SEMs) of samples A, D, and J, demonstrating the observed decrease in crystallite size with increasing total hydrogen content. The magnification for samples A and D is 500 $\times$ , while the magnification for sample J is 5000 $\times$ . The total hydrogen contents for these films are <0.001, 0.039, and 0.219 at. %, respectively, while the average grain sizes are approximately 100, 15, and <1  $\mu$ m, respectively.

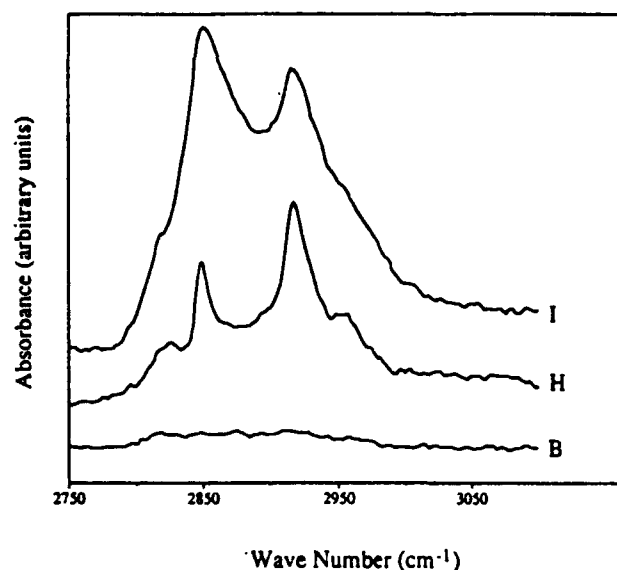


FIG. 4. CH-stretch region of the IR spectra (2750–3050  $\text{cm}^{-1}$ ) of three representative diamond films whose NMR spectra are shown in Fig. 1, films I, H, and B. Films I and H both show dominant absorptions at  $\sim 2850$  and  $\sim 2920$   $\text{cm}^{-1}$  due to the symmetric and asymmetric  $\text{CH}_2$  stretching modes. Film B shows a broad, less defined absorption over the CH-stretch region. Film H exhibits an absorption at 2824  $\text{cm}^{-1}$  whose source is uncertain. The shoulder at  $\sim 2960$   $\text{cm}^{-1}$  is typical of an asymmetric  $\text{CH}_3$  stretch.

detect any  $sp^2$  bonding environment in these films.

An effective absorption coefficient  $A_{\text{eff}}$  was calculated for the CH-stretch region (2750–3050  $\text{cm}^{-1}$ ) in each sample. Spectra were calibrated to the two-phonon absorption of

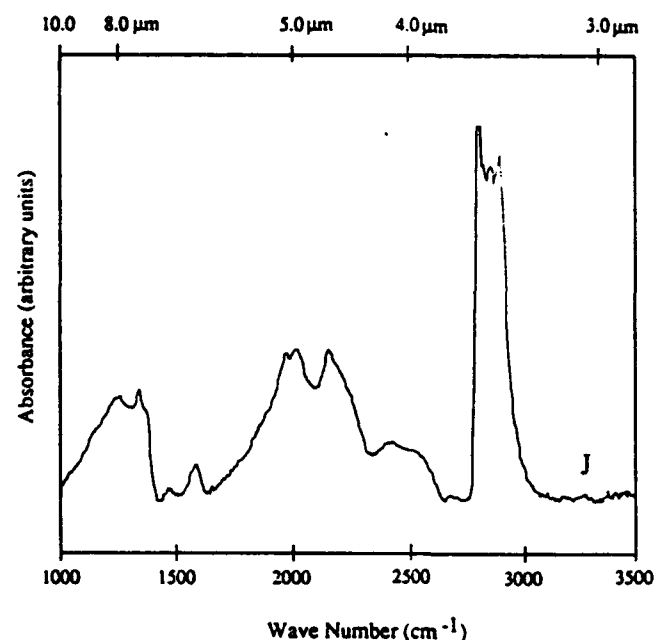


FIG. 5. IR spectra of film J over full range from 1000 to 3500  $\text{cm}^{-1}$ , showing the greatest absorption observed in all ten samples in both the CH-stretch and the 8–10  $\mu$ m region. Absorption is also observed at  $\sim 1600$  and at 2820  $\text{cm}^{-1}$  the source of which is not well understood.

TABLE III. Comparison of diamond absorption coefficient with literature values.

Species	$A \times 10^{-3}$ ( $\text{cm}^{-2}/\text{mol}$ of CH bonds)
$\text{CH}_2$ in <i>n</i> -octane (Ref. 3)	3.6
$\text{CH}_2$ in paraffinic hydrocarbons (Ref. 4)	3.75
CH in $\alpha\text{-Si:C:H}$ (Ref. 5)	2.83
$\text{CH}_2$ in polycrystalline diamond (Fig. 4)	4.3

natural type IIb diamond to allow this semiquantitative calculation. This absorption coefficient can be defined as<sup>1</sup>

$$A_{\text{eff}} = 1/c \int \alpha(\nu) d\nu, \quad (3)$$

where  $c$  is the concentration of C-H bonds in  $\text{mol}/\text{cm}^{-3}$ ,  $\int \alpha(\nu) d\nu$  is the integrated intensity of the CH-stretch region in  $\text{cm}^{-2}$ , and  $A_{\text{eff}}$  is in  $\text{cm}^{-1}/\text{mol}^{-1}$ . Values of  $A_{\text{eff}}$  for each film are given in Table II. For samples with hydrogen contents  $<0.10$  at. %, the values for  $A_{\text{eff}}$  are  $4.1 \pm 1.4 \times 10^3 \text{ cm}^{-1}/\text{mol}^{-1}$ . Literature values of  $A$  for a variety of condensed-phase carbon-hydrogen compounds are given in Table III. The absorption coefficient determined for polycrystalline diamond is in good agreement with those given for alkanes and for  $\text{CH}_2$  in paraffinic hydrocarbons.

Correlation of the intensity in the CH-stretch region with the NMR determined total hydrogen content indicates that a majority of the hydrogen is covalently bound to carbon. The integrated intensities in the CH-stretch region and the total at. % H, for samples containing  $<0.10$  at. % H, are shown in Fig. 6. The linear least-squares fit to the data gives

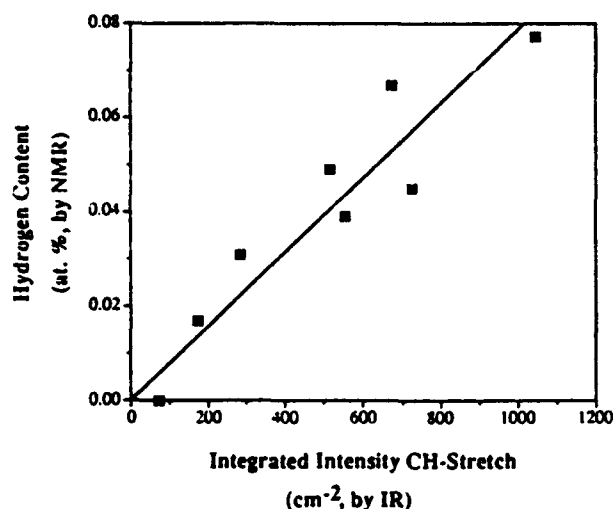


FIG. 6. A plot of total hydrogen content, determined from the integrated area under the NMR line, vs integrated absorption in the CH-stretch region and the line corresponding to a linear least-squares regression. The effective absorption coefficient determined from the slope of the line is  $4.3 \pm 0.8 \times 10^3 / \text{mol}^{-1} \text{ cm}^{-2}$ , similar to literature values for condensed-phase hydrocarbons. This correlation is only applicable when hydrogen content is  $<0.10$  at. % and becomes more complex at higher hydrogen content.

$$c = \frac{\int \alpha(\nu) d\nu \times 10^{-3}}{4.3 \pm 0.8 / \text{mol}^{-1} \text{ cm}^{-2}} \quad (4)$$

for the total hydrogen content. The concentration  $c$  is given in  $\text{mol}/\text{cm}^{-3}$  which can be converted to atomic fraction by dividing by  $(c + 292)$  based on a diamond concentration of  $1.76 \times 10^{23} \text{ atom cm}^{-3}$ . Thus, the hydrogen content can be estimated directly from the IR spectra when the integrated intensity of the CH-stretch absorption is below  $\sim 1500 \text{ cm}^{-2}$ .

Both films with hydrogen contents  $>0.10$  at. % yield absorbance values which fall outside of the above range. Figure 5 shows the IR spectrum of one of these, film J. The NMR determined hydrogen content for this sample is approximately half that predicted by Eq. (3) as indicated by the calculated absorption coefficient for this film,  $7.1 \times 10^3 / \text{mol}^{-1} \text{ cm}^{-2}$  (Table II). Similar discrepancy is found for film I, as well. Thus the correlation in Eq. (4) is only accurate over the investigated range where at. % H  $<0.10$ . Additional information is required to determine higher hydrogen concentrations from the absorption in the CH-stretch region.

Film J differs from the remainder of the films in that it was produced at a higher pressure of 300 Torr which resulted in a higher growth rate. In addition, the orientation of the film is  $\langle 100 \rangle$  textured, while the other nine films show a  $\langle 110 \rangle$  texture. The CH-stretch region of the IR spectrum of film J is also atypical. While the absorbance of the symmetric and asymmetric  $\text{CH}_2$  groups are still present, additional absorbance is present at  $\sim 2875 \text{ cm}^{-1}$ , typical of the symmetric  $\text{CH}_3$  absorption<sup>9</sup> and a strong absorption is observed at  $\sim 2820 \text{ cm}^{-1}$ . The source of this absorption, which is present but much weaker in several other samples (Fig. 4), is unclear. Literature values for absorption of  $\text{CH}_x$  groups are normally above  $2840 \text{ cm}^{-1}$ .<sup>9,10</sup> It is possible that the intensity at  $2820 \text{ cm}^{-1}$  is a combination band of the absorptions observed at 1445 and  $1375 \text{ cm}^{-1}$  (Fig. 5). Normally, such bands are weak, but they can be enhanced by the presence of absorption at a nearby frequency. Such combination bands in the CH-stretch region would cause Eq. (4) to underpredict the hydrogen content as is observed. The  $2820 \text{ cm}^{-1}$  absorption decreases at lower hydrogen contents, where a good correlation between the intensity of the CH-stretch absorption and the hydrogen content is observed.

#### IV. CONCLUSION

In conclusion, we have observed low hydrogen contents and a characteristic two-component NMR line shape in CVD diamond samples. We have shown that the absorption in the CH-stretch region of the IR correlates well with the total hydrogen content in the films as measured by NMR for films containing  $<0.10$  at. % hydrogen, indicating that a majority of the hydrogen in the sample is covalently bound to carbon. The effective absorption coefficient for diamond films in this range is  $4.3 \pm 0.8 \times 10^3 / \text{mol}^{-1} \text{ cm}^{-2}$ , similar to literature values for condensed-phase hydrocarbons. At higher hydrogen content, this simple correlation to the intensity of the CH-stretch region no

longer holds, and additional information is needed to determine the hydrogen content in CVD diamond films.

#### ACKNOWLEDGMENTS

The authors would like to acknowledge the National Science Foundation Grant No. CTS-9006705, the Office of Naval Research, and the Naval Weapons Center for support of this work.

<sup>1</sup>T. M. Hartnett and R. P. Miller, SPIE Proc. 1307, 60 (1990).

<sup>2</sup>K. M. McNamara, D. H. Levy, K. K. Gleason, and C. J. Robinson, Appl. Phys. Lett. 60, 580 (1992).

<sup>3</sup>S. A. Francis, J. Phys. Chem. 18, 861 (1950).

<sup>4</sup>J. C. Angus, J. E. Stultz, P. J. Shiller, J. R. MacDonald, M. J. Mirtich, and S. Domitz, Thin Solid Films 118, 311 (1984).

<sup>5</sup>K. Nakazawa, S. Ueda, M. Kumeda, A. Morimoto, and T. Shimizu, Jpn. J. Appl. Phys. 21, L176 (1982).

<sup>6</sup>K. M. McNamara, and K. K. Gleason, J. Appl. Phys. 71, 2884 (1992).

<sup>7</sup>A. Abragam, *The Principles of Nuclear Magnetism* (Oxford University, New York, 1983).

<sup>8</sup>J. H. van Vleck, Phys. Rev. 74, 1168 (1948).

<sup>9</sup>C. J. Pouchert, *The Aldrich Library of Infrared Spectra*, 3rd ed. (Aldrich Chem. Co., Milwaukee, 1981).

<sup>10</sup>B. Dischler, A. Bubenzer, and P. Koidl, Solid State Commun. 48, 105 (1983).

## SYNTHESIS OF FULLERENES ( $C_{60}$ AND $C_{70}$ ) BY COMBUSTION OF HYDROCARBONS IN A FLAT FLAME BURNER

S. Mitra, C. J. Pope, K. K. Gleason, Y. Makarovsky, A. L. Lafleur, and J. B. Howard,  
Department of Chemical Engineering, Center for Environmental Health Sciences and Energy  
Laboratory, M.I.T., Cambridge, MA 02139.

### ABSTRACT

Fullerene ( $C_{60}$  and  $C_{70}$ ) synthesis by combustion of ethylene and benzene in a flat flame burner was investigated. This method of fullerene synthesis is particularly attractive because of its potential of scale up. Also the ability to change the flame conditions and control the yield of  $C_{60}$  and  $C_{70}$  makes this method versatile. No fullerenes were found in soot samples collected from the ethylene flame. However, fullerenes were formed in a benzene flame with  $C/O = 0.88$  and operated at 40 torr, with cold gas velocity of 25.3 cm/s (273 K) and containing 10% argon. The concentration of fullerenes in this flame was found to depend strongly on the height above the burner surface. It exhibited a strong maxima at about 1.0 cm above the burner height suggesting the presence of both growth and destruction mechanisms.

### INTRODUCTION

When carbon vapor is formed in an inert gas atmosphere (argon or helium) either by laser irradiation [1] or by resistive heating of graphite [2-4], fullerenes ( $C_{60}$  and  $C_{70}$ ) are found to be formed. In addition, macroscopic quantities of both  $C_{60}$  and  $C_{70}$  have now also been synthesized in flames operating over a wide range of conditions [5]. The possibility that fullerenes can be generated in flames was first suggested by Smalley and his coworkers [6,7] and by Kroto and McKay [8]. Indeed, all-carbon ions having the same m/e ratio as fullerenes were subsequently detected by mass spectroscopy in sooting acetylene and benzene flames by Homann and coworkers [9,10].

An advantage of synthesizing fullerenes in flames lies in the fact that by tuning the flame conditions, the fullerene yield can be varied. Also, since design of industrial scale burners is an established technology, fullerene synthesis by combustion offers the possibility of scale up. Hence, an understanding of the processes leading to fullerene synthesis in flames is particularly important.

The yield of both  $C_{60}$  and  $C_{70}$  depends on the chamber pressure, equivalence ratio (normalized C/O ratio), temperature and the residence time in flames [5,11]. In this work we investigated the formation of fullerenes as a function of residence time in the flame. Soot samples were collected with a quartz probe at different heights above burner (h) from a moderately sooting benzene/oxygen/argon and ethylene/oxygen/argon flame. The extracted soot was weighed and sonicated in toluene. Both  $C_{60}$  and  $C_{70}$  are easily soluble in toluene and their amount was estimated from high performance liquid chromatography (HPLC) measurements. The experimental details are described below.

### EXPERIMENTAL DETAILS

Premixed laminar benzene/oxygen/argon and ethylene/oxygen/argon flames were stabilized on a water cooled burner. The burner, which was designed to produce a one-dimensional flat flame, was a circular copper plate of diameter 10 cm with 1 mm holes drilled on the surface at regular intervals. It had two separate regions. The inner core region (of

diameter 7.0 cm) supported the experimental flame while a non-sooting ethylene/oxygen flame was burned in the outer annular region. The outer flame acted as a shield to the core flame allowing it to be approximated to a one-dimensional flame. This ensured that both temperature and species concentration varied only with the distance from the burner surface. The entire burner was placed in a steel chamber which was connected to a vacuum pump. All flames were operated under subatmospheric pressures. The details of the burner and the fuel delivery system can be found elsewhere [12].

The flame characteristics depend on a number of parameters. The flame conditions depend on (a) equivalence ratio, (b) pressure, (c) cold gas velocity, and (d) diluent. The effect of the various parameters are described briefly.

#### Equivalence ratio ( $\phi$ )

This quantity describes the carbon to oxygen (C/O) ratio of the flame and is defined as the actual fuel to oxidant ratio normalized with respect to the stoichiometric ratio and is controlled by the amount of fuel and oxygen that is fed to the burner. As  $\phi$  is increased the flame changes from non sooting to heavily sooting. The onset of sooting for benzene under present conditions is at  $\phi = 1.9$  (i.e. C/O = 0.76) and is called the critical equivalence ratio.

#### Pressure (P)

Pressure is an important parameter that must be controlled carefully. Many chemical processes in flames, including those in which collision activation or stabilization is important, (e.g. radical recombination and unimolecular isomerization) depend on the operating pressure. An increase in pressure increases the rate of bimolecular coagulation of soot particles and their polyaromatic precursors thus increasing the soot produced in the flame. Note that the critical value of  $\phi$  at which sooting begins is not affected by pressure.

#### Cold gas velocity (v)

For a given burner of surface area A, the total gas flowrate determines v. As v is increased, the flame front stabilizes farther from the burner surface and the heat lost to the water cooled burner surface decreases. Consequently, the flame burns hotter.

#### Effect of diluent

An inert gas, argon in this work, is generally added to the premixed gas mixture. Its addition affects the rate of reaction by providing additional third bodies thereby accelerating radical recombination which reduces the radical pool and thus slowing down all the flame processes. The thermal conductivity of the diluent gas also plays an important role since it determines the amount of heat that is conducted away.

### EXPERIMENTAL RESULTS AND DISCUSSION

Premixed laminar flames of ethylene and benzene were investigated in this work. In either cases argon was added as a diluent. The soot samples were collected with a quartz probe tapered to a 0.08 cm diameter orifice at its tip. The probe, whose inner surface was lined with an aluminum foil and pyrex wool, was connected to a vacuum pump and the flame gas pulled through the probe was collected in an inverted water column. Since the probe is

assumed to collect samples from a position located about 2.5 times its orifice diameter upstream of its tip, all heights above burner ( $h$ ) values quoted in this work have been corrected accordingly. Once soot samples are collected, toluene was added and the fullerenes were extracted by sonication.

#### Ethylene:

Two moderately sooting flames were operated at  $P = 40$  torr,  $v = 25.3 \pm 0.2$  cm/s at 296 K with 10% argon and C/O ratios of 1.3 ( $\phi = 3.9$ ) and 1.0 ( $\phi = 3.0$ ). In both cases, soot samples were collected from the chamber walls and with a quartz probe placed 4.0 cm above the burner surface. The samples were analyzed using the procedure described above and there was no evidence of fullerene formation in either flames.

#### Benzene:

A sooting benzene flame containing 10% argon operating at 40 torr,  $v = 25.3 \pm 0.2$  cm/s at 273K, and C/O=0.88 ( $\phi=2.2$ ) was studied in considerable detail. Soot samples of mass ranging from 2.4 to 12.5 mg. were collected at different values of  $h$  and the fullerenes were extracted by sonication of the soot samples in toluene and the content estimated by HPLC.

A flame is a region of sharp thermal and concentration gradients. The variation of the volume fraction of soot  $F_v$  (which is defined as the ratio of the volume of the soot collected and the corresponding volume of flame gas pulled through the probe) and the flame temperature at various heights above burner is shown in Fig.1. The temperature profile shown here was taken from an earlier work on an identical flame [12]. Note that the temperature profile exhibits a maxima at 1.0 cm above the burner surface while the measured value of  $F_v$  is the largest at about 0.5 cm from the surface. The general trend of  $F_v$  is in good agreement with the results of McKinnon which clearly show a peak in this region of the flame.

The gas phase concentration of both  $C_{60}$  and  $C_{70}$  in the flame as a function of the height above burner ( $h$ ) is shown in Fig. 2 and contains several important features. First, the concentration of  $C_{70}$  is greater than that of  $C_{60}$  at all values of  $h$ . This result should be contrasted with other commonly used methods of fullerene synthesis like laser irradiation and resistive heating of graphite where  $C_{60}$  is more abundant than  $C_{70}$ . The molar ratio ( $R$ ) of  $C_{70}$  and  $C_{60}$  as a function of position in the flame is demonstrated in Fig. 3. It is clear that  $C_{70}$  is more prevalent than  $C_{60}$  in benzene flames operated under a wide range conditions [5,11,13].

The second interesting feature in the profile in Fig. 2 is the presence of a strong peak 1.0 cm above the burner surface. Note that though most soot was collected 0.5 cm above the burner surface (Fig. 1), little or no fullerenes were present in this soot. At 1.0 cm from the burner surface,  $F_v$  clearly decreases while the amount of fullerenes found in the soot shows a sharp increase. The error in the concentration profile of the fullerenes is estimated to be less than 20% for the first three points and less than 50% for the remaining points. A similar peak at about the same region in the flame has also been observed in a  $\phi = 2.3$  flame with other parameters being constant [13]. The presence of the peak in the profile implies the occurrence of both formation and destruction, with the two being in balance in the region of the peak. The rate of formation first exceeds and then becomes less than the rate of destruction as the flow proceeds from upstream to downstream of the peak concentration. Three possible destruction mechanism may be (a) oxidation, (b) unimolecular decomposition and (c) heterogeneous reaction at the surface of the soot particle, with subsequent soot surface growth incorporating the fullerene carbon into the soot structure. Note that this does not imply that fullerenes contribute to the formation of the soot nuclei.

The fullerene profiles bear similarities to the observed flame profiles of planar PAH

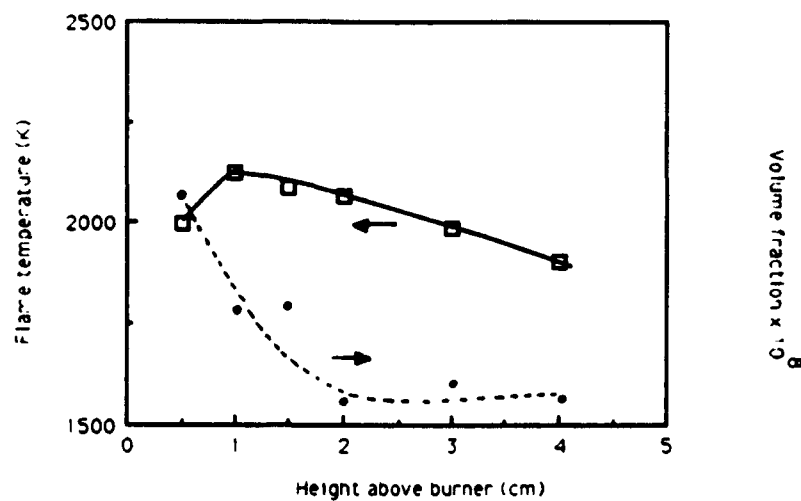


Fig. 1 The dependence of flame temperature (open symbols) and the volume fraction of soot collected (solid symbols) on the height above burner. The temperature data was taken from ref. 12.

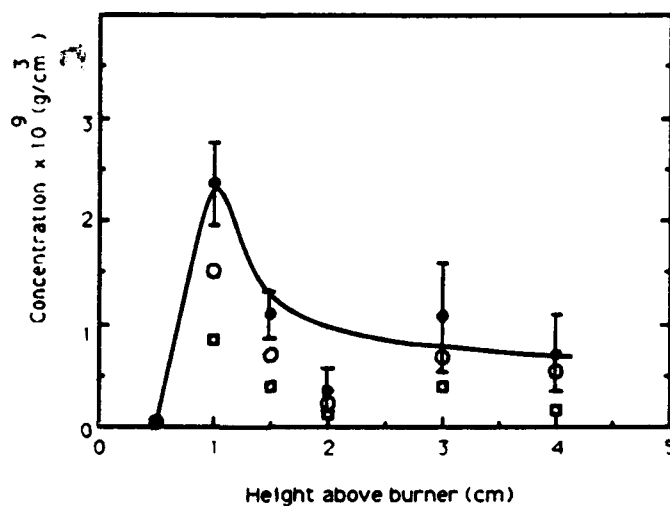


Fig. 2. The gas phase concentration profiles of C60 (open squares) and C70 (open circles) and their total (solid circles) as measured in the benzene flame. Note the peak at 1.0 cm.

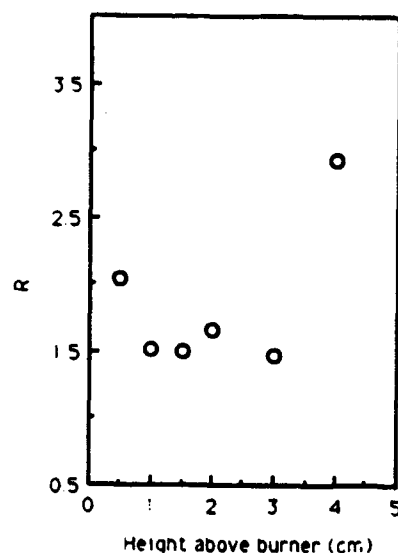


Fig 3 The molar ratio  $R$  of C70 and C60 as a function of height above burner. Note that  $R$  is greater than unity for all positions.

(polycyclic aromatic hydrocarbons) [14-16]. High molecular weight planar PAH have long been considered soot precursors [17]. Like PAH, the fullerene profiles peak early in the flame in the region where soot grows rapidly and reaches its maximum concentration, then show a sharp decline followed by a flat or gradually rising region. This implies that fullerenes are products of the same kind of growth and destruction processes as PAH, that of successive addition of light hydrocarbons (mostly  $C_2H_2$ ) to a growing aromatic structure with simultaneous oxidative and pyrolytic destruction. Fullerene formation is therefore expected to occur in much the same way as planar PAH, but with fullerene precursors being curved, and therefore strained PAH and thus having different reactivities (compared to planar PAH) in the growth and destruction processes [18].

There is notable difference from planar PAH profiles in that the peak in the fullerene profile occurs after the soot peak, similar to previous observations reflecting both structural and thermodynamic barriers to fullerene formation [16,19]. The curved PAH precursors are strained, requiring more energy for their formation, and concurrently slowing formation rates for strained rings with respect to planar PAH formation. The decline in planar PAH concentration precedes the peak soot concentration since they react together or coagulate to form soot nuclei [17]. This gives further evidence that fullerenes do not greatly contribute to soot particle inception.

Clearly additional work is needed to understand the various mechanisms involved in the synthesis of fullerenes in flames. Currently, a systematic study is underway to investigate the formation of fullerenes by changing the various flame parameters.

#### ACKNOWLEDGEMENTS

The combustion research was supported by the Division of Chemical Science, Office of Basic Energy Sciences, Office of Energy Research, U.S. Department of Energy under grant No. DE-FG02-84ER13282. The chemical analyses were performed in facilities supported by the National Institute of Environmental Health Sciences Center Grant EHS-5P30-ES02109-10 and Program Grant EHS-5P01-ES01640-11. SM and KKG would also like to acknowledge partial support from ONR.



## LIST OF REFERENCES

1. W. Kroto, S. C. O'Brien, R. F. Curl, and R. E. Smalley, *Nature* **318**, 162 (1985).
2. W. Kratschmer, L. D. Lamb, K. Fostiropoulos, and D. R. Huffman, *Nature* **347**, 354 (1990).
3. R. Taylor, J. P. Hare, A. K. Abdul-Sada, and H. W. Kroto, *J. Chem. Soc. Chem. Commun.* 1423 (1990).
4. H. Aijie, M. M. Alvarez, S. J. Anj, R. D. Beck, F. Diederich, K. Fostiropoulos, D. R. Huffman, W. Kratschmer, Y. Rubin, K. E. Schriver, D. Sensharma, and R. L. Whetten, *J. Phys. Chem.* **94**, 8630 (1990).
5. J. B. Howard, J. T. McKinnon, Y. Makarovsky, A. L. Lafleur, and M. E. Johnson, *Nature* **331**, 328 (1988).
6. R. E. Smalley and R. F. Curl, *Science* **242**, 1017 (1988).
7. Q. L. Zhang, S. C. O'Brien, J. F. Heath, Y. Lin, R. F. Curl, H. W. Kroto, and R. E. Smalley, *J. Phys. Chem.* **90**, 525 (1986).
8. H. W. Kroto and K. McKay, *Nature* **331**, 328 (1988).
9. Ph. Gerhart, S. Loffler, K. H. Homann, *Chem. Phys. Lett.* **137**, 306 (1987).
10. S. Loffler and K. H. Homann, Twenty-Third Symposium (International) on Combustion; The Combustion Institute, Pittsburgh 355 (1991).
11. J. B. Howard, J. T. McKinnon, M. E. Johnson, Y. Makarovsky, and A. L. Lafleur, *J. Phys. Chem.* (submitted).
12. J. T. McKinnon, Ph.D Thesis, Massachusetts Institute of Technology, (1989).
13. J. B. Howard, A. L. Lafleur, Y. Makarovsky, S. Mitra, C. J. Pope, and T. K. Yadav, Carbon (submitted).
14. H. Bockhorn, F. Fetting, H. W. Wenz, *Ber.Bunsenges.Phys.Chem.*, **87** 1067 (1983).
15. J. D. Bittner, J. B. Howard, Eighteenth Symposium (International) on Combustion, The Combustion Institute, 1105 (1981).
16. C. J. Pope, M.S. Thesis, Massachusetts Institute of Technology, Cambridge, MA (1988).
17. J. T. McKinnon and J. B. Howard, *Combust. Sci. and Tech.*, **74** 175 (1990).
18. C. J. Pope, private communication.
19. Ph. Gerhart, S. Loffler, K. H. Homann, Twenty-Second Symposium (International) on Combustion, The Combustion Institute, 395, 1988.

# Evaluation of diamond films by nuclear magnetic resonance and Raman spectroscopy

K. M. McNamara and K. K. Gleason

*Department of Chemical Engineering, MIT, Cambridge, MA 02139 (USA)*

D. J. Vestyck

*Geo-Centers Incorporated, Fort Washington, MD 20744 (USA)*

J. E. Butler

*Gas Surface Dynamics Section, Naval Research Laboratory, Code 6174, Washington, DC 20375 (USA)*

(Received April 17, 1992; accepted in final form July 2, 1992)

## Abstract

The quality of chemically vapor deposited diamond films was assessed in terms of  $sp^2/sp^3$  content as determined by solid-state nuclear magnetic resonance (NMR) and Raman spectroscopy. While the results of the two techniques are in qualitative agreement, only the NMR spectra yield quantitative values for the  $sp^2/sp^3$  ratio. Only  $sp^3$  carbon was observed in the NMR spectra of very high quality hot-filament, microwave plasma, and d.c. arc-jet chemically vapor deposited films. As expected, Raman spectroscopy is extremely sensitive to  $sp^2$  bonded carbon, identifying small amounts below the detection limit of the NMR spectrometer. Comparison of the two techniques, however, indicates that Raman spectroscopy may be so sensitive to  $sp^2$  bonded carbon that  $sp^3$  bonded carbon in films containing as much as 90%  $sp^3$  bonded material may remain undetected. NMR linewidths indicate that the  $sp^3$  carbon in such material shows more disorder than that found in high-quality polycrystalline films.

## 1. Introduction

Polycrystalline diamond films have been produced at low pressure by several techniques using a variety of processing conditions [1, 2]. The deposition of diamond under conditions where it is metastable appears to involve a kinetic competition of the deposition and removal of various forms of carbon ranging from diamond (tetrahedral  $sp^3$  bonded carbon), through amorphous carbons ( $sp^3$  and  $sp^2$ ), to graphitic carbon ( $sp^2$ ) [3]. Many of the potential applications for such films require high quality, defect-free diamond. Consistent reproduction of such high quality material requires an understanding of process conditions and their affect on diamond structure and properties. While many techniques have been used to evaluate diamond film quality, few provide the quantitative data necessary to evaluate process conditions and achieve controlled, reproducible results. In this work, we compare two analysis techniques sensitive to the nature of the carbon bonding and structural order existing in the diverse types of carbon materials: vibrational Raman spectroscopy and nuclear magnetic resonance (NMR) spectroscopy.

Raman spectroscopy is one of the most common methods of diamond film characterization because of its

ability to distinguish between different forms of carbon. Raman spectroscopy is non-destructive and is readily available to most laboratories [3-15]. The observed "Raman" spectra are often the sum of contributions from the Raman scattering of the excitation photons, as well as fluorescence-photoluminescence from states excited in the material, and resonance Raman contributions due to nearby electronic states [16]. This latter effect is particularly important when experiments are performed with photon energies exceeding the band gap of components in the material analyzed [17]. Care must be taken in assigning bands in any single spectrum because of these interfering effects. A simple method to distinguish Raman scattering from fluorescence-photoluminescence is to change the energy of the incident photon source and observe changes in the inelastic energy loss shift or intensity of the band. An example of this technique is found in Fig. 1, where the Raman spectra of a diamond film at two different incident energies are shown. Only the features with the same shift are attributed to Raman effects.

The single phonon (first order) Raman spectra of carbon produced using visible photons (e.g. 514.5 nm from an Ar<sup>+</sup> ion laser) may comprise four general types of features characteristic of diamond (a single band at

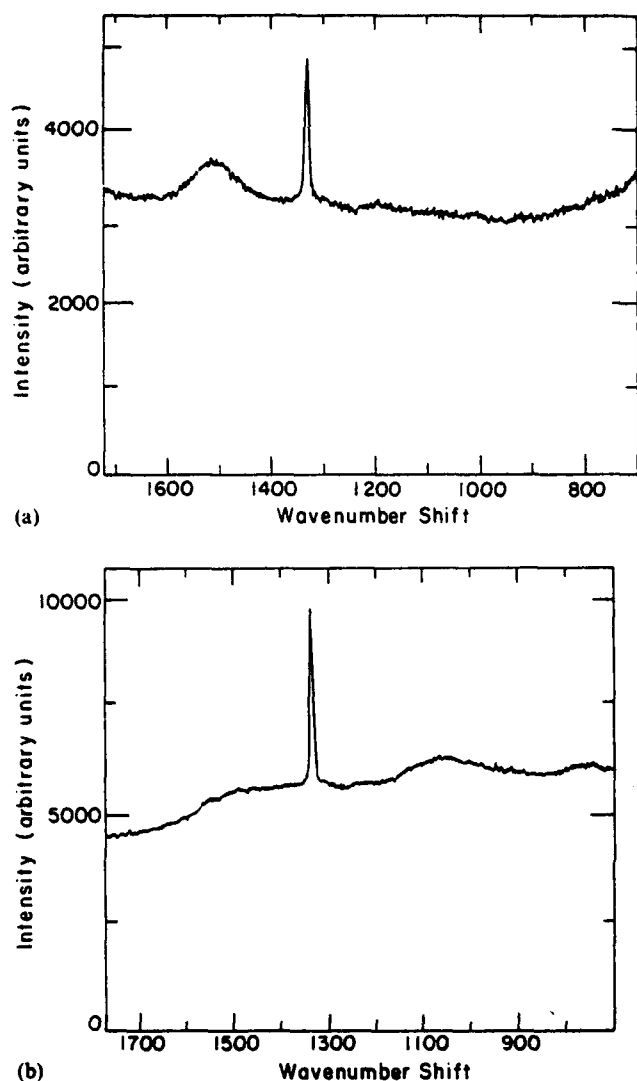


Fig. 1. Raman spectra of a hot-filament CVD diamond film at two different incident photon energies, demonstrating the effect of fluorescence-photoluminescence on the Raman spectra of carbon-containing materials: (a) 514.5 nm, (b) 488.0 nm.

1332  $\text{cm}^{-1}$ ) [4, 12, 18], crystalline graphite (a single band at 1580  $\text{cm}^{-1}$ ) [4, 12, 19], defective or microcrystalline graphite (two broad bands at ca. 1580 and 1350  $\text{cm}^{-1}$ ) [4, 12, 20], and amorphous carbon (a broad asymmetric band peaking at around  $1500 \pm 40 \text{ cm}^{-1}$ ) [4, 12, 20, 21]. An additional band is occasionally observed at ca. 1120–1140  $\text{cm}^{-1}$  [8, 12, 13], which has not been definitely assigned. The effective scattering efficiencies vary considerably, owing in part to resonant Raman effects [17]. For example, crystalline graphite has a scattering efficiency approximately 50 times greater than that of single-crystal diamond [22].

The position of the Raman band for diamond as well as that of the other forms of carbon is dependent on the isotopic composition [6, 23, 24], temperature [25–27], and stress in the material [4, 26, 28]. In pure

$^{13}\text{C}$  diamond, the diamond band shifts to 1280  $\text{cm}^{-1}$  from its 1332  $\text{cm}^{-1}$  position in a diamond having a natural abundance of the  $^{13}\text{C}$  isotope, 1.1%. The position of the 1350  $\text{cm}^{-1}$  band of disordered graphite has also been observed to shift with changes in the excitation photon energy [17]. Raman scattering immediately above the 1332  $\text{cm}^{-1}$  diamond phonon band has been assigned to  $\text{sp}^2$  containing carbon materials [12]. As the disorder in the sample increases, the Raman bandwidth increases, and the band center may shift slightly.

The spatial resolution of most instruments is of the order of 0.1–1 mm with standard optics. Raman spectroscopy through microscopes can achieve resolutions of less than 1  $\mu\text{m}$  and a significant increase in signal collection using high numerical aperture optics [14]. Care must be taken in micro-Raman spectroscopy to avoid local heating or burning of the samples due to high laser power density [29]. Quantitative analysis of inhomogeneous or multicomponent carbon materials with Raman spectroscopy is nearly impossible because of the differing contributions of each component to the penetration of the exciting photon beam into the sample and the escape of the scattered photons. However, the qualitative use of Raman spectroscopy has been invaluable to the rapid development of diamond chemical vapor deposition (CVD) technology [14, 15].

A second method by which we can differentiate carbon bonding environments in diamond films is solid-state nuclear magnetic resonance (NMR) spectroscopy. In a magnetic field, atomic nuclei which possess a magnetic moment will interact with r.f. irradiation, elucidating information about nuclear spin interactions. Such interactions, in turn, yield information about the composition and structure of the sample. For a spin 1/2 nucleus such as  $^{13}\text{C}$ , in a uniform external magnetic field, these interactions can be described by the total Hamiltonian [30]:

$$H_{\text{tot}} = H_z + H_{d,ii} + H_{d,is} + H_{es} + H_{rf}(t) + R(t) \quad (1)$$

where  $H_z$  is the Zeeman interaction between the observed nucleus and the external magnetic field;  $H_{d,ii}$  is the interaction between the observed nucleus and the magnetic field generated by neighboring nuclei of the same species (homonuclear dipolar coupling);  $H_{d,is}$  is the interaction between the observed nucleus and the magnetic field generated by neighboring nuclei of a different species (heteronuclear dipolar coupling);  $H_{es}$  is the interaction between the observed nucleus and nearby bonding electrons (chemical shift interaction);  $H_{rf}(t)$  is the experimentally controlled Hamiltonian produced by r.f. irradiation;  $R(t)$  is the coupling of observed nuclei to fluctuating magnetic fields in the lattice, primarily a result of phonon modes or due to paramagnetic centers. This last component represents the process by which the spin system comes to equilibrium with the external

field and is known as spin-lattice relaxation. The time scale for these processes is several orders of magnitude larger than for the interactions described above and is observed in a separate NMR experiment.

The Zeeman interaction is the dominant term in the total Hamiltonian, and the other terms are treated as perturbations on the Zeeman term. The effects of this term can be eliminated from eqn. (1) by changing the reference frame to one rotating at the resonance frequency of the observed nuclei. In addition, the manipulation of  $H_{rf}(t)$  allows selective suppression of the remaining Hamiltonians, simplifying the interpretation of the resulting spectra.

The homonuclear and heteronuclear dipolar couplings,  $H_{d,ii}$  and  $H_{d,ij}$ , between NMR active nuclei are responsible for a significant portion of the line broadening observed in the NMR spectra of solids. For diamond films with low hydrogen concentrations, the heteronuclear coupling term  $H_{d,ij}$  is small, and only the homonuclear term will be important. The dipolar coupling between  $^{13}\text{C}$  nuclei is a strong function of internuclear spacing and depends on the angle between the internuclear vector and the direction of the applied magnetic field. This broadening can be suppressed by sophisticated experimental techniques and equipment; however, in suppressing these effects, we lose information about the system [30].

The unsuppressed spectral line broadening due to homonuclear dipolar couplings can be related to the  $^{13}\text{C}$  concentration in diamond films through the van Vleck equation [31] for a spin-1/2 nucleus, which defines the second moment as

$$\langle \Delta\omega^2 \rangle = (9/20) C \gamma^4 h^2 \sum_k (r_{jk})^{-6} \quad (2)$$

where  $C$  is the fraction of sites occupied by  $^{13}\text{C}$ ;  $\gamma$  is the gyromagnetic ratio of the nuclei;  $h$  is Planck's constant divided by  $2\pi$ ;  $r_{jk}$  is the internuclear distance between lattice sites  $j$  and  $k$ , in the spacings of the diamond lattice.

For a Gaussian lineshape, the measured full width at half-maximum (FWHM) intensity equals  $2.35(\Delta\omega^2)^{1/2}$ . Thus, we can determine the enrichment of a diamond film from the width of the NMR lineshape. For example, a 22%  $^{13}\text{C}$  enrichment corresponds to a 3.0 kHz dipolar linewidth. Such linewidths are independent of the external magnetic field and are typically expressed in units of kilohertz.

While solid-state  $^{13}\text{C}$  NMR spectroscopy has been used in the study of amorphous carbon films [32], it has not been applied extensively to diamond films [33]. These films contain very low concentrations of hydrogen, less than 0.5 at.%, eliminating the heteronuclear dipolar coupling  $H_{d,ij}$  term from the total Hamiltonian and prohibiting the use of cross-polarization techniques normally employed to examine polymers and amorphous

carbon samples. However, direct polarization experiments which rely on the homonuclear dipolar coupling  $H_{d,ii}$  between  $^{13}\text{C}$  nuclei are still possible, provided sufficient sample can be obtained. The detection limit for  $^{13}\text{C}$  NMR is  $5 \times 10^{18}$   $^{13}\text{C}$  nuclei for a 2.5 kHz half-width. In a natural abundance film, this corresponds to approximately 10 mg of sample or a 10  $\mu\text{m}$  thick film covering an area of 2.8  $\text{cm}^2$ .

In samples which are free of paramagnetic defects, direct-polarization NMR experiments are quantitative in that each  $^{13}\text{C}$  nuclei gives rise to the same integrated signal intensity, regardless of its bonding environment. In samples containing paramagnetic impurities, a small fraction of nuclei in close proximity to such defects will remain undetected as a result of extreme line broadening due to interaction with the unpaired electron of the paramagnetic impurity [34, 35]. However, such nuclei comprise only a small fraction (less than 0.1 at.%) of the  $^{13}\text{C}$  nuclei in diamond films and should not significantly affect quantitative results within our detection limits. A technique known as spin-counting may be used to verify this assumption. In this technique, the integrated area under the NMR lineshape is compared with that of a well characterized standard, such as ethylene glycol, to estimate the number of  $^{13}\text{C}$  nuclei detected. This value is compared with the expected number of  $^{13}\text{C}$  nuclei calculated from the mass of the sample and its isotopic enrichment (1.1% for natural abundance  $^{13}\text{C}$ ) to verify that all of the  $^{13}\text{C}$ , within our detection limit, is observed.

It is also important to ensure that a sufficient delay is used between signal acquisitions to ensure that equilibrium has been re-established within the sample. This delay is determined by the spin-lattice relaxation rate of the sample,  $R(t)$  as described above. Gem-quality natural diamonds require a delay of greater than 1 day between signal acquisitions [34]. However, the presence of paramagnetic defects, other defects, or an enrichment in  $^{13}\text{C}$  will significantly increase the spin-lattice relaxation rate [33–38],  $R(t)$ , typically reducing delays to less than 1 min, making the NMR experiment reasonable.  $^{13}\text{C}$  enrichment also increases the NMR signal for a given sample, reducing the overall sample size requirement.

Like Raman spectroscopy, NMR is sensitive to both the  $\text{sp}^2$  and  $\text{sp}^3$  bonding environments of carbon through the chemical shift interaction  $H_{cs}$ . The position of the natural diamond peak at  $36 \pm 2$  ppm [8] is typical of the isotropic chemical shift of  $\text{sp}^3$  bonded carbon relative to the standard, tetramethylsilane. The isotropic chemical shift is linearly proportional to the applied field and is reported in parts per million (ppm) of the Larmor frequency of the observed nuclei. For our 7 T spectrometer,  $^{13}\text{C}$  has a Larmor frequency of 75 MHz, thus 1 ppm corresponds to 75 Hz. The peak for  $\text{sp}^2$  carbon is well resolved from the  $\text{sp}^3$  carbon peak and appears between

120 and 200 ppm [30, 36, 39–43]. In amorphous carbon films, the  $sp^2$  peak is typically observed near the lower value [30, 41]. The  $sp^2$  peak is generally broader and less symmetric than that of diamond, and its center may vary depending on the specific chemical environment. This type of asymmetric broadening can be caused by the chemical shift anisotropy (a result of non-spherically symmetric bonding environments), magnetic susceptibility effects of the substrate, and a broader distribution of bond angles and bond lengths within a given bonding

environment. In any case, the integrated area under the curve remains constant and proportional to the number of NMR active nuclei in the given bonding configuration.

To demonstrate the quantitative nature of NMR, Fig. 2 shows four  $^{13}C$  NMR spectra for various mixtures of natural diamond powder (approximately 1  $\mu m$ ) and soot (approximately 0.1  $\mu m$ ). The natural diamond powder was purchased from Johnson-Matthey, while soot samples were produced from benzene in a flat-flame burner. The top spectrum is that of pure natural diamond

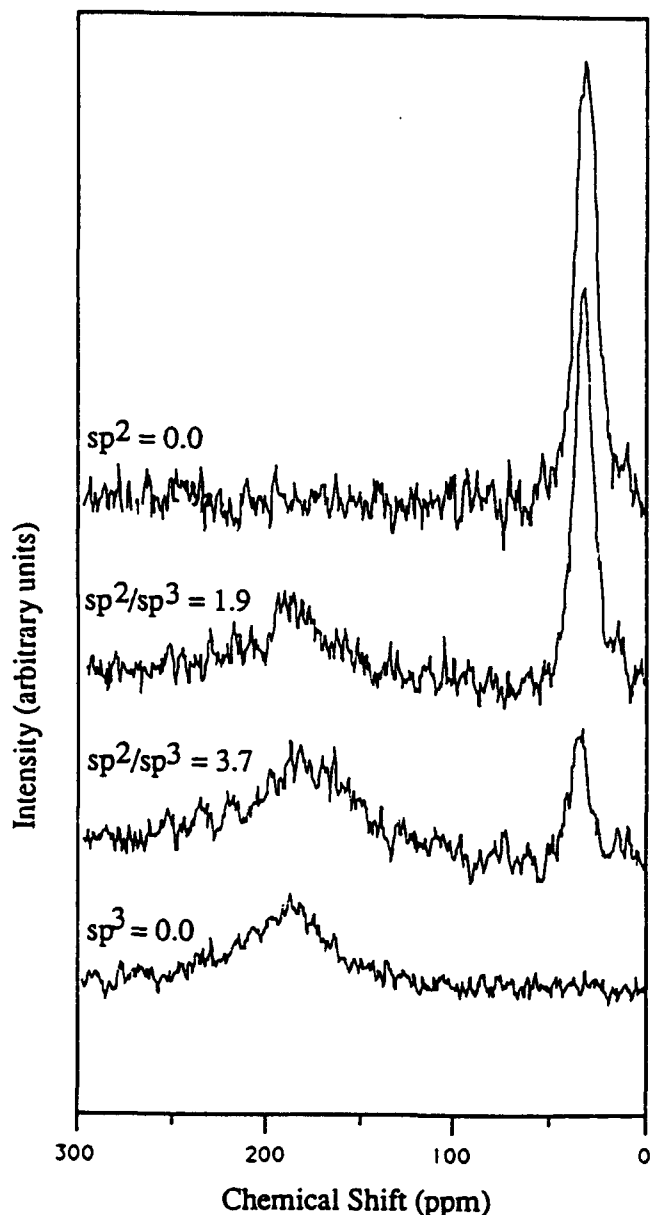


Fig. 2. Four NMR spectra of natural-diamond-soot mixtures with varying  $sp^2/sp^3$  ratios to demonstrate the quantitative nature of  $^{13}C$  NMR. The spectra are shown for samples having  $sp^2/sp^3$  ratios of 0:1, 1.9:1, 3.7:1 and 1:0, from top to bottom of the figure. The integrated area under the curves gives ratios of 0:1,  $1.6 \pm 0.3:1$ ,  $3.5 \pm 0.3:1$  and 1:0 respectively. The spectra are offset for clarity.

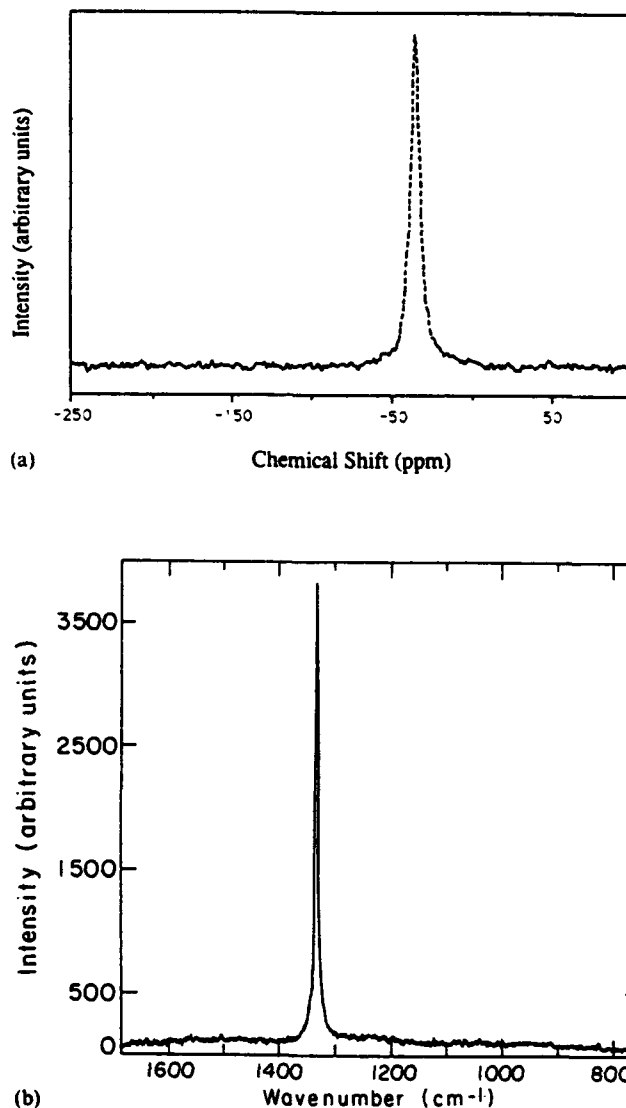


Fig. 3. (a) The  $^{13}C$  NMR spectrum of a high-quality natural  $^{13}C$  abundance diamond film produced at the Naval Research Laboratory using the hot-filament CVD technique. The spectrum shows only one peak, centered at 36.0 ppm and indicative of the  $sp^3$  phase. (b) Micro-Raman spectrum from the same sample, showing only the  $1332\text{ cm}^{-1}$  diamond band and no indication of  $sp^2$  bonded carbon at either  $1580\text{ cm}^{-1}$  or  $1350\text{ cm}^{-1}$ . These results are typical of a large number of high-quality diamond films produced by a variety of techniques (see Table I).

powder, showing only one peak at 36 ppm, with a half-width at half-maximum intensity of 0.40 kHz, indicative of ordered  $sp^3$  bonding. The bottom spectrum is that of pure soot. It shows a broad, slightly asymmetric line centered at 189 ppm and no evidence of an  $sp^3$  bonded phase. Much of the broadening is a result of the bond angle disorder in the  $sp^2$  phase. The middle two spectra are those of mixtures of natural diamond powder and soot. In the second and third spectra from the top, the ratios of  $sp^2$  to  $sp^3$  bonded carbon, determined by the mass of each powder used in the mixture, are 1.9:1 and 3.7:1 respectively. The ratio of the integrated areas under the peaks for these two samples is  $1.6 \pm 0.3:1$  and  $3.5 \pm 0.3:1$  respectively, confirming that, within experimental uncertainty, NMR can yield quantitative  $sp^2/sp^3$  ratios in environments similar to those found in diamond films.

The absence of a signal between 120 and 200 ppm in the pure diamond spectra confirms our identification of the soot peak and eliminates the question of background signal from the probe. This background is a problem with most commercial NMR probes which are designed for  $^1H$ - $^{13}C$  cross-polarization experiments as performed on polymers and a-C:H [7]. Since only hydrogenated carbon is detected in the cross-polarization experiment, fluorinated polymers are used for construction materials in these probes. However, diamond films contain little hydrogen and must be observed by direct polarization. In this experiment, all  $^{13}C$  is detected, including that found in the fluorinated material in the probe. A carbon-free probe was, therefore, designed and constructed in our laboratory for these experiments.

NMR spectroscopy provides information on local bonding environments from the entire sample. Diamond

films may remain intact on the substrate when inserted into the NMR sample coil. In order to ensure that the substrate does not influence the NMR results, it must be non-magnetic, have low conductivity, and contain no  $^{13}C$ . Conductive samples may be observed but present additional tuning problems, affecting the signal-to-noise ratio, which leads to difficulty in obtaining accurate quantitative information from the spectrum. Broadening of the NMR line may be observed due to variations in the magnetic susceptibility of the sample and its substrate. Since all the  $^{13}C$  atoms are not equidistant from the substrate, the field experienced by the sample will not be homogeneous, causing additional line broadening effects, hindering the quantitative interpretation of spectra. In addition, if the skin-depth for r.f. penetration into the sample is smaller than the sample thickness, only the outer part of the sample will be observed. In all cases here, however, the skin-depth greatly exceeds sample thickness. The only restriction on sample size is that of the NMR coil itself, typically 1 cm in diameter and 2 cm in length. As mentioned,  $^{13}C$  enrichment enhances the signal, however, very high enrichments may effect the resolution owing to increased line broadening as a result of increased homonuclear dipole-dipole interactions. For this reason,  $^{13}C$  enrichment in the samples discussed here is below 25%.

## 2. Experimental details

The majority of the films used in this study were produced by hot-filament CVD. Typically, natural  $^{13}C$  abundance films were produced using 0.5%–2% methane in a bulk hydrogen gas feed at a total reactor

TABLE I. NMR and Raman results for  $sp^3$  bonded carbon in diamond films

Deposition method	Source	$^{13}C$ enrichment (%)	NMR frequency (ppm)	NMR half-width (kHz)	Raman frequency ( $cm^{-1}$ )	Raman full-width ( $cm^{-1}$ )
Hot filament <sup>a</sup>	NRL	1.1	36.0	0.35	1332	6.1
Hot filament <sup>a</sup>	Raytheon	1.1	35.5	0.45	1332	7.5
Hot filament <sup>a</sup>	Raytheon	1.1	36.0	0.31	1332	8.75
Hot filament <sup>a</sup>	Raytheon	1.1	36.0	0.40	1335	15.0
Hot filament <sup>a</sup>	Raytheon	1.1	35.5	0.34	1332	11.0
Hot filament <sup>a</sup>	Raytheon	1.1	36.5	0.50	1334	10.0
D.c. arc-Jet <sup>a</sup>	Norton	1.1	36.0	0.35	1332	10.5
Microwave plasma <sup>a</sup>	NWC	1.1	36.0	0.45	1334	9.7
Microwave plasma <sup>a</sup>	NWC	$\approx 12$	34.0	0.85	1328	17.1
Microwave plasma <sup>a</sup>	NWC	$\approx 12$	35.0	1.10	1328	11.1
Hot filament <sup>b</sup>	LL	22	36.0	1.40	1324	9.3
Hot filament <sup>b</sup>	LL	22	36.0	1.40	1324	16.4
Hot filament <sup>b</sup>	LL	22	38.0	2.10	None	None

<sup>a</sup> Methane as carbon source.

<sup>b</sup> Acetone as carbon source.

NRL Naval Research Laboratory, NWC Naval Weapons Center, LL Lincoln Laboratory.

pressure of 100 Torr, and a filament temperature of approximately 2350 K. The tantalum filament was placed 4 mm from the substrate, which was rotated to improve film uniformity. For the sample produced at the Naval Research Laboratory (NRL), the filament was tungsten, and the sample was stationary. The substrates were silicon which could be etched away in HF-HNO<sub>3</sub> to leave free-standing diamond films for characterization. These free-standing films were on the order of 100  $\mu\text{m}$  thick. Enriched films were produced at Lincoln Laboratory from <sup>13</sup>C-labeled acetone in a hot-filament reactor at a pressure of 150 Torr as described elsewhere [33], and at the Naval Weapons Center (NWC) from <sup>13</sup>C-labeled methane in a microwave plasma. Owing to the enrichment, a film of approximately 10  $\mu\text{m}$  thickness provided sufficient sample for the NMR measurements. Some of these films were discontinuous in some areas and remained attached to

the silicon substrate for support. The substrate was 635  $\mu\text{m}$  thick and had a resistivity in excess of 10 k $\Omega$ . All samples were cut to fit the NMR sample coil with a diameter of 1 cm and a length of 2 cm.

Macro-Raman spectroscopy was performed on all natural abundance films, with the exception of the NRL sample. The frequency of the incident beam was 647.1 nm, and the power was 120 mW. The results of 1 to 5 scans were averaged to obtain a reasonable noise level. Micro-Raman experiments were performed for all <sup>13</sup>C enriched samples and the sample from NRL. Several locations on each sample were observed using this technique. An attempt to obtain macro-Raman spectra for these samples was unsuccessful or produced spectra with very low signal-to-noise ratios owing to the large degree of scatter caused by the substrate.

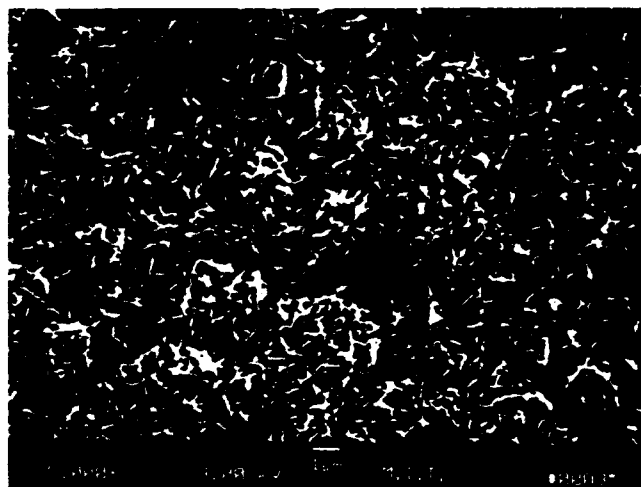
The NMR data for all films were obtained on a home-



(a)



(b)



(c)

Fig. 4. Scanning electron micrographs of three hot-filament CVD diamond films produced with <sup>13</sup>C enriched acetone: (a) film A, (b) film B, and (c) film C.

built 7.0 T solid-state NMR spectrometer in our laboratory. Static direct-polarization experiments were carried out by inserting slivers of free-standing diamond films or films still attached to the silicon substrate directly into the NMR coil. Between 3000 and 50 000 scans were signal averaged to produce spectra with the desired level of signal-to-noise ratio. Sufficient delay was used between averages (typically greater than or equal to 30 s) to ensure that the nuclei had returned to equilibrium with the static magnetic field between averages. In this way, we preserved the quantitative nature of the resulting NMR spectra.

The process by which  $^{13}\text{C}$  nuclei exchange energy with the lattice and come into equilibrium with the static magnetic field is spin-lattice relaxation. The spin-lattice relaxation time constant is typically defined by the Bloch equation [41],

$$\frac{M(t - M_{\text{eq}})}{M_0 - M_{\text{eq}}} = \exp(-t/T_1) \quad (3)$$

where  $M(t)$  is the net magnetization parallel to the external magnetic field at time  $t$ ;  $M_0$  is the initial magnetization at  $t=0$ ;  $T_1$  is the exponential spin-lattice relaxation time constant. This relaxation is observed in samples free of paramagnetic defects and in all samples with rapid spin-diffusion, such as  $^{13}\text{C}$ -enriched samples [35, 38]. In magnetically dilute systems which may contain paramagnetic defects, such as natural  $^{13}\text{C}$  abundance diamond films, this behavior may not be observed [34, 37]. Such impurities increase the spin-lattice relaxation rate and give rise to non-exponential behavior.

Spin-lattice relaxation times were determined using the saturation-recovery technique. Polycrystalline diamond films showing well faceted scanning electron micrographs have significantly faster  $T_1$  values (typically less than 30 s) than those measured for natural diamond (approximately 1 day) [17, 18]. In the CVD diamond, defects at grain boundaries, unterminated bonds, and paramagnetic and ferromagnetic impurities all provide additional relaxation mechanisms for  $^{13}\text{C}$  nuclei. Enrichment in  $^{13}\text{C}$  will further enhance the relaxation rate by increasing the rate of spin-diffusion in isotopically labeled samples.

The ratio of  $\text{sp}^2/\text{sp}^3$  bonded carbon is determined from the ratio of the integrated area under the peaks corresponding to those environments. Information about the extent of disorder in a bonding environment can be obtained from its linewidth in the static NMR spectrum. A distribution of bond angles and bond lengths will cause the chemical shift to be distributed over a wider range of values. Since we can determine the expected linewidth due to dipolar broadening [31, 33], we can identify any additional broadening. As mentioned, there are several possible sources of such broadening. By crushing the sample and performing a magic-angle spinning experiment at a spinning rate greater than the  $^{13}\text{C}$

linewidth, we can eliminate both the broadening due to the magnetic susceptibility of the substrate and the chemical shift anisotropy of a given  $^{13}\text{C}$  site [36]. Any broadening which remains after the magic-angle spinning can then be attributed to a wider distribution of bond angles and lengths in the sample.

### 3. Results and discussion

Figure 3 shows the static  $^{13}\text{C}$  NMR and macro-Raman spectra of the first sample listed in Table 1, a natural abundance, free-standing diamond film. The film was produced from 1% methane in  $\text{H}_2$  at 34 Torr. The  $^{13}\text{C}$  NMR spectrum shows only one peak, centered at

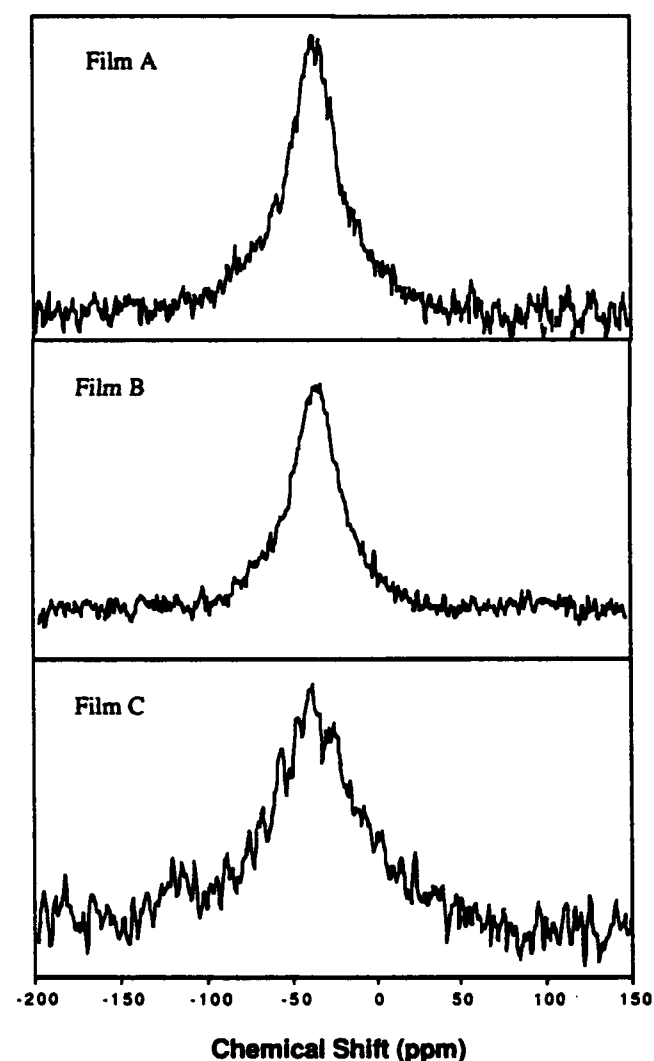


Fig. 5.  $^{13}\text{C}$  NMR spectra from the same three samples shown in Fig. 4. For films A and B only one peak, at 36 ppm is present, indicating only  $\text{sp}^3$  bonded carbon. However, for film C, two peaks, at 38 ppm and 120 ppm exist, indicative of  $\text{sp}^3$  and  $\text{sp}^2$  carbon respectively. The ratio of the peak areas is 0.11, and the  $\text{sp}^3$  peak is broader than expected for a 22% enriched film, indicating disorder in the system.



36.0 ppm shift relative to the tetramethylsilane reference standard. The peak is symmetric and narrow, having a half-width at half-maximum of 0.35 kHz. This width is comparable with that of natural diamond powder (0.40 kHz), indicating order in this  $sp^3$  phase. The Raman spectrum, likewise, contains only one peak, centered at  $1332\text{ cm}^{-1}$ , indicative of the diamond phase. This peak is also relatively narrow, having a width of  $6.1\text{ cm}^{-1}$ , only slightly larger than that of natural diamond ( $2\text{ cm}^{-1}$ ) [4], thus supporting the NMR identification of an ordered phase. The amount of  $sp^2$  bonded carbon in this film, if any, is below the detection limit of both techniques. Similar results were obtained for the next

seven natural-abundance, high-quality diamond films and are shown in Table I. These films were produced from methane by hot-filament, d.c. arc-jet, or microwave plasma CVD.

Figures 4, 5, and 6 show the scanning electron micrographs,  $^{13}\text{C}$  NMR and micro-Raman spectra obtained from three samples produced with  $^{13}\text{C}$ -enriched acetone respectively. The  $^{13}\text{C}$  enrichment in these films is 22%, increasing the observed NMR linewidth and shifting the Raman frequencies. Film A was produced with a gas-phase carbon concentration of 5.3%, while film B was produced at a concentration of 6.4% and film C at 7.4% [8]. All other conditions were identical for each run.

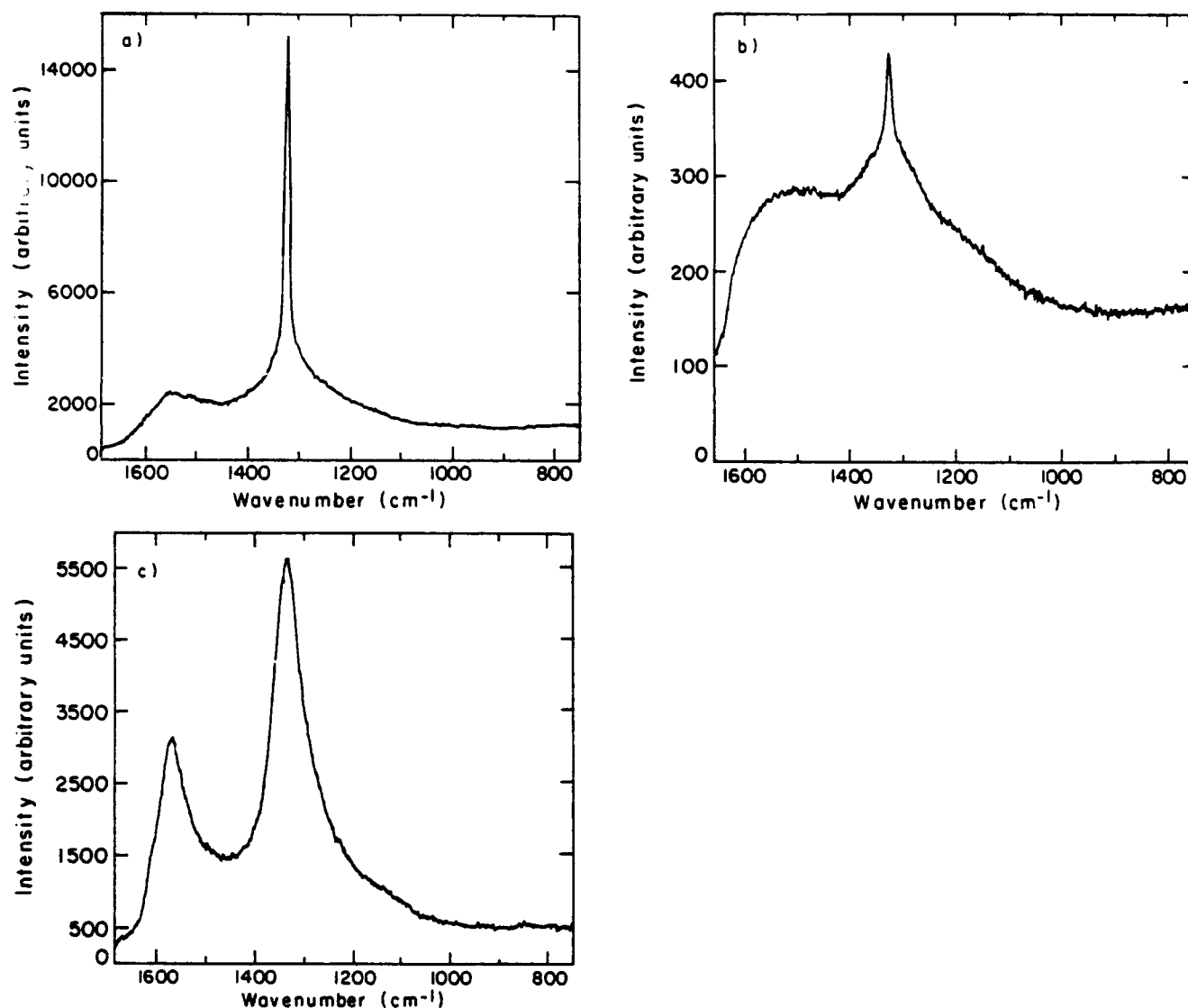


Fig. 6. Micro-Raman spectra from the same samples shown in Figs. 4 and 5. For films A and B ((a) and (b)), sharp peaks are seen at  $1324\text{ cm}^{-1}$ , the isotopically shifted position of the diamond band. In addition, there may be evidence of  $sp^2$  bonded carbon, present in quantities below the detection limit of the NMR. Film C (c) gives a spectrum showing only the shifted graphite and amorphous carbon bands at  $1570\text{ cm}^{-1}$  and  $1330\text{ cm}^{-1}$  respectively. There is no evidence of the diamond band, even though the quantitative NMR results show it makes up approximately 90% of the sample. This demonstrates the sensitivity of Raman spectroscopy to  $sp^2$  bonded carbon, and the need for caution in interpreting results.

The NMR half-width of a diamond lattice enriched with 22%  $^{13}\text{C}$  can be calculated from the van Vleck equation [31] (eqn. (2)), yielding a value of 1.5 kHz, consistent with the observed broadening in films A and B (Figs. 5(a) and 5(b)). The symmetric lineshape indicates little chemical shift anisotropy, as expected for a tetrahedral bonding environment, or magnetic susceptibility broadening from the substrate. In addition, upon grinding the sample and performing magic-angle spinning  $^{13}\text{C}$  NMR, the majority of the broadening could be eliminated to give a linewidth of only 0.15 kHz, indicating that the broadening was not caused by disorder in the  $\text{sp}^3$  phase.

The corresponding micro-Raman spectra, for films A (Fig. 6(a)) and B (Fig. 6(b)), contain a sharp diamond band shifted to  $1324\text{ cm}^{-1}$  owing to the isotopic enrichment. In addition, some evidence of an  $\text{sp}^2$  bonded environment is observed in each spectrum in a band at approximately  $1550\text{ cm}^{-1}$  corresponding to isotopically shifted graphite and in a broadening at the base of the  $1324\text{ cm}^{-1}$  band caused by overlap with the isotopically shifted amorphous carbon band at  $1330\text{ cm}^{-1}$ . The Raman spectrum of film A has a lower intensity in these bands than observed for film B, as expected for a film produced from a lower gas-phase carbon concentration. In each case, the amount of  $\text{sp}^2$  bonded material is below the detection limit of the NMR spectrometer.

The NMR and Raman spectra, shown in Figs. 5(c) and 6(c), were obtained from film C, produced with 7.4% carbon in the gas phase. At this higher carbon concentration, we see an expected deterioration in film quality revealed in both the micro-Raman and  $^{13}\text{C}$  NMR spectra. The  $^{13}\text{C}$  NMR spectrum shows two broad peaks at approximately 38 ppm and 120 ppm, indicative of  $\text{sp}^3$  and  $\text{sp}^2$  bonding respectively. The  $\text{sp}^2$  peak appears at a shift closer to that observed in amorphous carbon films than to that observed in pure soot. The ratio of the area under these two peaks gives a quantitative  $\text{sp}^2/\text{sp}^3$  ratio of  $0.11 \pm 0.2$ , indicating that approximately 10% of the carbon in this sample is in an  $\text{sp}^2$  bonding configuration. When magic-angle spinning NMR was performed on this sample, the  $\text{sp}^3$  peak was only partially narrowed to a linewidth of 0.69 kHz, indicating some broadening due to disorder in the  $\text{sp}^3$  bonding environment. The  $\text{sp}^2$  peak narrows very little, consistent with the greater bond angle and bond length variation expected in this phase.

The micro-Raman spectrum of film C (Fig. 6(c)) contains two isotopically shifted peaks—one indicative of graphitic carbon at approximately  $1570\text{ cm}^{-1}$  and one indicative of amorphous carbon at approximately  $1330\text{ cm}^{-1}$ . Both bands are extremely broad (greater than  $60\text{ cm}^{-1}$ ), indicating substantial disorder, in agreement with the NMR results. This micro-Raman spectrum shows no evidence of a diamond phase, in

contrast to the quantitative NMR results which show that 90% of the sample has an  $\text{sp}^3$  bonding configuration. However, the NMR spectrum indicates disorder in this  $\text{sp}^3$  phase. Thus, it is possible that the symmetry of tetrahedral bonding is no longer present, disallowing this transition in the Raman spectrum, explaining the absence of the  $1332\text{ cm}^{-1}$  band.

There are several other possible explanations for the results observed in Figs. 5(c) and 6(c). Recalling that the Raman scattering efficiency of  $\text{sp}^2$  bonded carbon greatly exceeds that of  $\text{sp}^3$  bonded material, it may be that the  $\text{sp}^3$  signal is simply obscured by the strong amorphous carbon peak. This has serious implications for quantitative evaluation of film quality using Raman spectroscopy. In some cases, the  $\text{sp}^3$  content of the film may be much higher than that anticipated from the Raman spectrum. In addition to differences in scattering behavior, the  $\text{sp}^2$  and  $\text{sp}^3$  bonded carbon may have different absorptivities which can lead to non-uniform sampling as a function of depth in the film. These and other sampling difficulties have been discussed previously [5].

One final hypothesis is that the micro-Raman spectrum was simply obtained at a position within the film containing no  $\text{sp}^3$  bonded carbon while the NMR spectra is indicative of the entire sample. With a  $1\text{ }\mu\text{m}$  spot-size, this may be a reasonable concern. To determine whether this was the case, seven or more locations in films B and C were sampled. A map of the sampling pattern is shown in Fig. 7, and the three typical corresponding spectra are shown in Fig. 8. Note the non-uniform sampling in film C reflects the non-continuous nature of the sample. As these figures show, there was

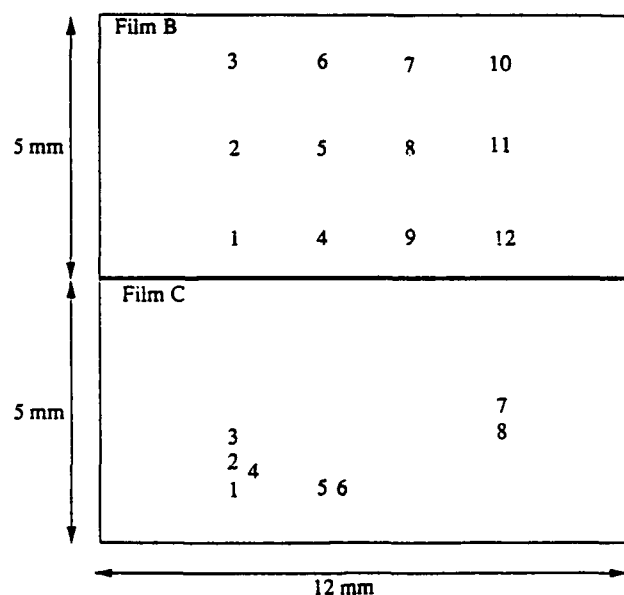


Fig. 7. Map showing the micro-Raman sampling pattern for  $5 \times 12\text{ mm}^2$  slivers of enriched films B and C. Note that the pattern for sample C reflects the non-continuous nature of this sample.

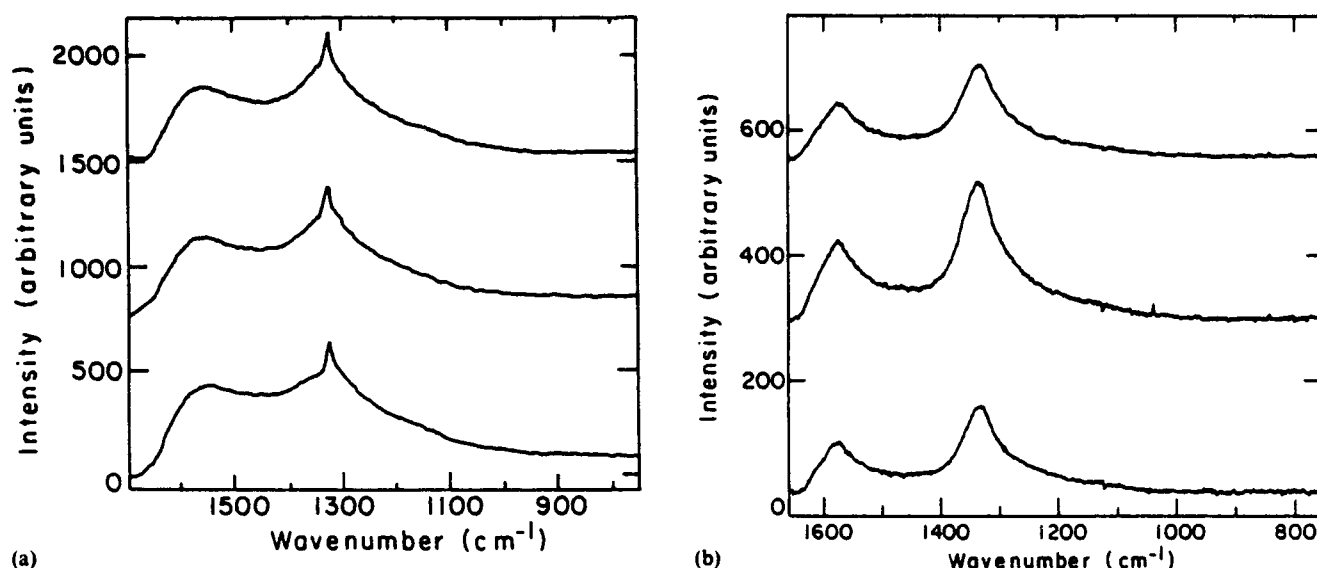


Fig. 8. From top to bottom, three micro-Raman spectra from positions (a) 7, 8, and 9 in film B and (b) 1, 5, and 7 in film C as indicated in Fig. 7. These demonstrate the consistency of the spectra obtained throughout the samples. Thus, variation in quality with sample location does not explain the differences between the Raman and NMR results for film B vs. film C.

little variation in the Raman spectra as a function of sampling position in each case. Some decrease in the quality of the Raman spectra was observed at the outermost edge of film B. However, the Raman spectrum of film C was consistent across the sample. The results obtained for other sampling locations were consistent with these observations. Thus it is unlikely that sampling position is the cause of the differences in the results between films B and C.

#### 4. Conclusion

We have shown that both Raman and NMR spectroscopy provide useful information on carbon bonding environments within diamond films. NMR spectroscopy examines the local short-range order within the sample, while Raman spectroscopy probes order over a longer range. NMR provides quantitative information, independent of bonding environment, but requires relatively large samples and long acquisition times. In a diamond film containing 90%  $sp^3$  bonded carbon, as determined quantitatively by  $^{13}C$  NMR, the  $1332\text{ cm}^{-1}$  Raman band was not detected. Raman spectroscopy has the advantage of giving fast, spatially resolved information. It is, however, extremely sensitive to  $sp^2$  bonded carbon and as a result, care must be taken not to underestimate the  $sp^3$  nature of films showing strong amorphous carbon absorptions (approximately  $1350\text{ cm}^{-1}$ ). It is also possible that a disordered  $sp^3$  phase does not allow the  $1332\text{ cm}^{-1}$  transition, leaving disordered  $sp^3$  bonded carbon undetected in the Raman spectrum. A combina-

tion of the two techniques is necessary to obtain reliable information for all types of diamond films.

#### Acknowledgments

The authors wish to thank Dr. Mike Geis of Lincoln Laboratories for the use of his hot-filament system for the deposition of  $^{13}C$ -enriched films. We would also like to thank Dr. Cliff Robinson of Raytheon Corporation, Dr. Kevin Gray of Norton Company, and Dr. Curtis Johnson of the Naval Weapons Center for providing samples used in this study. Also, we wish to thank Ted Kobelfisch and Dr. Richard Clark of Boston University for their assistance and the use of their Raman equipment. We gratefully acknowledge the support of the Office of Naval Research, the 3M Company, and National Science Foundation grant no. CTS-9006705.

#### References

- 1 P. K. Bachmann, D. Leers, and H. Lydtin, *Diamond Relat. Mater.*, **1** (1991) 1.
- 2 R. C. DeVries, *Am. Rev. Mater. Sci.*, **17** (1987) 161.
- 3 F. G. Celii and J. E. Butler, *Annu. Rev. Phys. Chem.*, **42** (1991) 643.
- 4 D. S. Knight and W. B. White, *J. Mater. Res.*, **4** (1985) 385.
- 5 R. J. Nemanich, L. Bergman, Y. M. LeGrice and R. E. Shroder, *New Diamond Sci. Technol.*, (1991) 741.
- 6 R. M. Chenko, *J. Appl. Phys.*, **63** (12) (1988) 5873.
- 7 F. G. Celii, H. H. Nelson and P. E. Pehrsson, *J. Mater. Sci.*, **5** (11) (1990) 2337.

- 8 P. Bou and L. Vandenbulcke, *J. Electrochem. Soc.*, **138** (10) (1991) 2991.
- 9 K. E. Spear, *Earth Min. Sci.*, **56** (1987) 53.
- 10 J. E. Butler, F. G. Celii, D. B. Oakes, L. M. Hanssen, W. A. Carrington and K. A. Snail, *High Temp. Sci.*, **27** (1990) 183.
- 11 Y. Liou, R. Weimer, D. Knight and R. Messier, *Appl. Phys. Lett.*, **56** (5) (1990) 437.
- 12 R. E. Shroder, R. J. Nemanich and J. T. Glass, *Phys. Rev. B*, **41** (6) (1990) 3738.
- 13 R. J. Nemanich, L. Bergman, Y. M. LeGrice and R. E. Shroder, *New Diamond Sci. Technol.*, (1990) 741.
- 14 D. B. Oakes, J. E. Butler, K. A. Snail, W. A. Carrington and L. M. Hanssen, *J. Appl. Phys.*, **69** (4) (1991) 2602.
- 15 L. M. Hanssen, K. A. Snail, W. A. Carrington, J. E. Butler, S. Kellogg and D. B. Oakes, *Thin Solid Films*, **196** (1991) 271.
- 16 C. D. Clark and C. B. Dickerson, *J. Phys. Condens. Matter*, **4** (1992) 869.
- 17 J. Wagner, C. Wild and P. Koidl, *Appl. Phys. Lett.*, **59** (7) (1991) 779.
- 18 S. A. Solin and A. K. Ramdas, *Phys. Rev. B*, **1** (4) (1970) 1687.
- 19 F. Tuinstra and J. L. Koenig, *J. Chem. Phys.*, **53** (1969) 1126.
- 20 R. B. Wright, R. Varma and D. M. Gruen, *J. Nucl. Mater.*, **63** (1976) 415.
- 21 T. J. Dines, D. Tither, A. Dehbi and A. Matthews, *Carbon*, **29** (2) (1991) 225.
- 22 N. Wada and S. A. Solin, *Physica B*, **105** (1981) 353.
- 23 Y. Sato, M. Kamo, H. Kanda and N. Setaka, *Hyomen Kagaku*, **1** (1980) 60.
- 24 W. F. Banholzer and T. R. Anthony, *Thin Solid Films*, in the press.
- 25 H. Herchen and M. A. Cappelli, *Phys. Rev. B*, **43** (14) (1991) 11740.
- 26 E. S. Zouboulis and M. Grimsditch, *Phys. Rev. B*, **43** (15) (1991) 12490.
- 27 A. Tardieu, F. Cansell and J. P. Petitot, *J. Appl. Phys.*, **68** (7) (1990) 3243.
- 28 T. P. Mernagh and L. G. Liu, *J. Phys. Chem. Solids*, **52** (3) (1991) 507.
- 29 N. J. Everall, J. Lumsdon and D. J. Christopher, *Carbon*, **29** (2) (1991) 133.
- 30 M. A. Petrich, *Mater. Sci. Forum*, **52-53** (1990) 387.
- 31 J. H. van Vleck, *Phys. Rev.*, **74** (1948) 1168.
- 32 K. C. Bustillo, M. A. Petrich and J. A. Reimer, *Chemistry of Materials* 1989.
- 33 K. M. McNamara and K. K. Gleason, *J. Appl. Phys.*, **71** (6) (1992) 2884.
- 34 P. M. Henrichs, M. L. Cofield, R. H. Young and J. M. Hewitt, *J. Magn. Reson.*, **58** (1984) 85.
- 35 M. J. R. Hoch and E. C. Reynhardt, *Phys. Rev. B*, **37** (16) (1988) 9222.
- 36 B. C. Gerstein, High resolution solid-state NMR of  $^{13}\text{C}$ . In G. C. Levy (ed.), *Topics in Carbon-13 NMR Spectroscopy*, Wiley, New York.
- 37 W. E. Blumberg, *Phys. Rev.*, **119** (1) (1960) 79.
- 38 D. Tse and S. R. Hartmann, *Phys. Rev. Lett.*, **21** (5) (1968) 511.
- 39 C. A. Wilkie, T. C. Ehlert and D. T. Haworth, *J. Inorg. Nucl. Chem.*, **40** (1978) 1983.
- 40 H. L. Retcofsky and R. A. Friedel, *J. Phys. Chem.*, **77** (1973) 68.
- 41 S. Kaplan, F. Jansen and M. Machonkin, *Appl. Phys. Lett.*, **47** (7) (1985) 750.
- 42 H. Rosenberger, G. Scheler and E. Kunstner, *Fuel*, **67** (1988) 508.
- 43 R. H. Newman, M. N. Sim, J. H. Johnston and J. D. Collen, *Fuel*, **67** (1988) 420.
- 44 A. Abragam, *The Principles of Magnetic Resonance*, Oxford, NY, 1983.

# Radiative heat transfer in hot-filament chemical vapor deposition diamond reactors

C. Wolden, S. Mitra, and K. K. Gleason<sup>A)</sup>

*Department of Chemical Engineering, Massachusetts Institute of Technology, Cambridge, Massachusetts 02139*

(Received 11 March 1992; accepted for publication 19 June 1992)

Hot-filament chemical vapor deposition is a common method employed for diamond deposition. Due to the filament-substrate proximity, large temperature variations across the substrate is often possible. Variations in substrate temperature need to be minimized in order to deposit polycrystalline diamond films of uniform thickness over large areas. Thus heat transfer calculations which consider radiation from the filament to the substrate, radiation from the substrate to the reactor walls, and finally conduction in the silicon wafer have been developed to predict substrate temperature profiles as a function of the filament shape and geometry. The calculated values are found to be in reasonable agreement with experimentally measured substrate temperatures. It was found that hydrogen atom recombination makes a significant contribution to the absolute substrate temperature, but that the normalized temperature profiles are determined primarily by the radiation flux distribution. The effects of the other deposition parameters are also discussed. Comparison with experimental results show an apparent correlation between growth rate profiles and radiation flux profiles from the filament as predicted by the calculations.

## I. INTRODUCTION

In the past decade there has been considerable increase in the study of polycrystalline diamond films.<sup>1-10</sup> The impetus for these studies has been provided by the discovery that diamond films can be grown on a variety of substrates under metastable conditions.<sup>2,3</sup> Diamond films have now been grown using a variety of deposition techniques and under a wide range of conditions.<sup>11</sup> Since, in most of these methods diamond films are deposited in subatmospheric pressures and relatively low substrate temperatures, it is anticipated that many of the unique mechanical and optoelectronic properties of diamond can now be commercially exploited.

Hot-filament chemical vapor deposition (hot-filament CVD) has been used extensively to deposit diamond films. Typically in this method, a dilute mixture (0.5%–3%) of a carbon containing gas such as methane or acetone in hydrogen is thermally activated at subatmospheric pressures (~25–300 Torr) by a filament held at ~2500 K. A substrate is held between 0.5 and 1.5 cm from the filament, resulting in substrate temperatures of 900–1200 K and polycrystalline diamond is deposited at rates ~1  $\mu\text{m/h}$ . Advantages of this method are its simplicity and potential for scale-up. However, the ability to grow films of uniform thickness and high quality over large areas and at acceptable growth rates demands an improved substrate temperature uniformity.<sup>12</sup>

Variations in the substrate temperature in hot-filament CVD are a result of high filament temperatures and a small filament-substrate distance. Thus the radiation flux from

the filament induces temperature variations across the substrate even in the presence of external heating. In order to obtain a deeper insight into these effects, heat transfer in a hot-filament CVD reactor has been numerically modeled and the resulting predictions have been compared with experimental substrate temperature measurements. The calculations were used to determine the substrate temperature profiles as a function of filament temperature, material, and substrate separation. In addition this model was then used to compare different filament geometries and the effect of rotating the substrate with the goal of improving substrate temperature uniformity.

## II. EXPERIMENT

A schematic diagram of the hot-filament CVD reactor used in this work is shown in Fig. 1. A mixture of acetone vapor and hydrogen was introduced through the bottom of the reactor and heated by tantalum filaments held between 0.5 and 2.0 cm from a 4-in.-diameter silicon wafer. The filaments were supported by zirconium rods to ensure a constant filament-substrate separation during operation. The operating conditions unless noted differently were 100 Torr and  $T_f = 2600$  K. For each condition a separate run in the absence of a substrate allowed the filament to be viewed directly. By matching its color to that of one internal to a pyrometer the filament's temperature was obtained. A copper plate with holes of diameter 1/16 in. drilled at 45° increments on circles of radii 0, 1, 2, 3, 4, and 5 cm was placed on top of the quartz plate external to the reactor. The temperature of the unpolished backside of the silicon wafer, which faces the quartz plate, was measured by a Raytek optical pyrometer model S3AHTCF4 operat-

<sup>A)</sup> author to whom correspondence should be addressed.

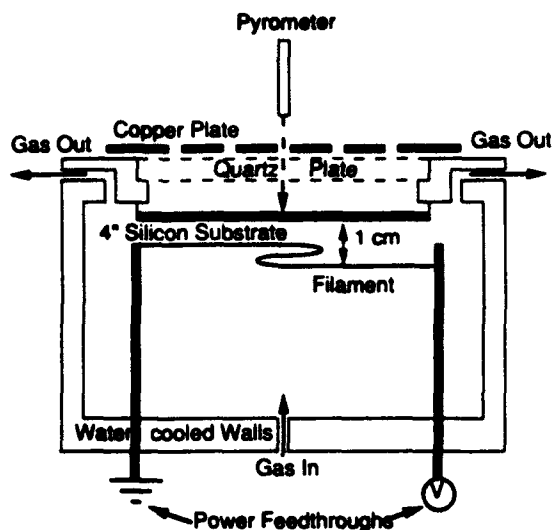


FIG. 1. A schematic diagram of the hot-filament CVD reactor used in this work. For temperature profile measurements, a copper plate with holes drilled at regular intervals was placed on top of the quartz plate.

ing at  $2.2 \mu\text{m}$  with a spot size of  $0.2 \text{ cm}$  at its focus. The accuracy of the pyrometer was  $\pm 1.0\%$  of the temperature reading. The temperature at various locations on the substrate was measured by aligning the pyrometer over the holes in the copper plate to ensure reproducible positioning. The introduction of the copper plate was not found to change the substrate temperature within experimental accuracy. Care was taken to hold the pyrometer perpendicular to the surface of the copper plate in order to ensure greater accuracy of the profiles. A one-dimensional steady-state energy balance calculation on the  $500\text{-}\mu\text{m}$ -thick silicon wafer indicates the difference in temperature between the front (growing) and the back surfaces is  $< 1^\circ\text{C}$ , which is smaller than the rated accuracy of the pyrometer. Consequently, the temperature indicated by the pyrometer is equal to that of the growing surface. The temperature profile measurements were taken after the reactor had attained steady state conditions for at least 1 h. This ensured complete carburization of the tantalum filament and thus eliminated any changes in its emissivity with time. The temperature at the center of the substrate was monitored at regular intervals to monitor any long term drift of the operating conditions.

At each point, the substrate temperature was calculated from the pyrometer reading of black body temperature using the temperature-dependent grey body emissivity of the substrate. This temperature dependence cannot be ignored since the emissivity of silicon, the substrate used in this work, has a strong increase from 0.3 at 500 K to 0.85 at 900 K, beyond which it decreases slowly with temperature.<sup>13</sup> Measurements at each open position on the copper plate immediately yield temperature profiles which can be directly compared with those predicted by the heat transfer calculations.

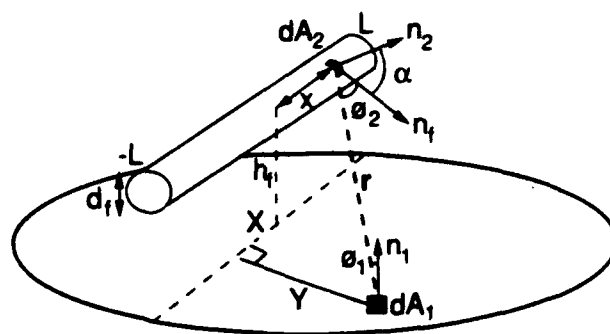


FIG. 2. A schematic of a simple filament geometry. The radiation flux to a differential substrate area is proportional to the shape factor, the fraction of radiant energy leaving the filament that is incident on the substrate at that point.

### III. HEAT TRANSFER CALCULATIONS

Three possible mechanisms are available for heat transfer from the filament to the substrate: radiation, conduction, and convection. Since the filament temperatures are very high (typically around  $\sim 2500 \text{ K}$ ), radiative heat transfer dominates over both conduction and convection. The Peclet number, a measure of the relative importance of convection to conduction,<sup>14</sup> is estimated to be  $\sim 10^{-4}$  and consequently the heat loss by convection can be safely neglected. The effect of conduction in the gas phase, though small, is not negligible. In addition, it has been observed that the recombination of hydrogen atoms on the surface increases the substrate temperature.<sup>15</sup> The contributions of these two effects were examined experimentally and are discussed later in the text. As both of these effects are minimized at low pressure, radiation is assumed to be the only mechanism in heat transfer from the filament to the substrate.

Consider the simple filament geometry as shown in Fig. 2 of a straight filament of length  $2L$ , temperature  $T_f$ , centered at the coordinates  $(0, 0, h_f)$ . In Fig. 2,  $d_f$  is the diameter of the filament and  $\phi_1$  is the angle formed by the vector  $r$  joining  $dA_1$  and  $dA_2$  and the substrate normal,  $n_1$ . The position of the differential filament element  $dA_2$  is defined by the distance from the filament center,  $x$ , and its surface normal,  $n_2$ . The angle  $\alpha$  ( $0 < \alpha < 2\pi$ ) is formed between  $n_2$  and  $n_f$ , the normal vector in the plane containing  $r$  and the center of the filament. Likewise, the angle  $\phi_2$  is formed between  $r$  and  $n_f$ . The shape factor between the two surfaces depends on  $r$ ,  $\alpha$ ,  $\phi_1$ , and  $\phi_2$ . Since  $r$  is much greater than the filament radius, the magnitude of  $r$  is nearly independent of  $\alpha$ . Thus, the dependence on the angle  $\alpha$  can be treated by integrating over a cylindrical element of area  $\pi d_f dx$  which yields an effective surface area  $dA_f = d_f dx$ , radiating in the direction  $n_f$ . The shape factor for diffuse radiation between the filament and a differential substrate area  $dA_1$  simplifies to<sup>14</sup>

$$F_{fs} = \int_{-L}^L \frac{\cos \phi_1 \cos \phi_2 d_f dx}{\pi r^2} \quad (1)$$

For the substrate element  $dA_1$  fixed at coordinates  $= (X, Y, 0)$  and a filament at  $(-L < x < L, 0, h_f)$ , the terms in Eq. (1) become:

$$r = [(x - X)^2 + Y^2 + h_f^2]^{0.5}, \quad (2)$$

$$\cos \phi_1 = \frac{h_f}{r}, \quad (3)$$

$$\cos \phi_2 = \frac{(h_f^2 + Y^2)^{0.5}}{r}. \quad (4)$$

Upon substitution into Eq. (1), one obtains an expression for  $F_{fs}$  that is only a function of  $x$  that can be evaluated analytically at each grid point,  $(X_n, Y_n, 0)$ . When multiple filaments are used the shape factors of the individual filaments are simply superposed. For filaments that are not straight the shape factor must be computed numerically. Finally, the radiative heat absorbed by a differential substrate area  $dA_1$  from the filament,  $Q_{fs}$ , is given by

$$Q_{fs} = F_{fs} \epsilon_f \sigma T_f^4 \epsilon_s dA_1 \quad (W) \quad (5)$$

where  $\epsilon_f$  and  $\epsilon_s$  are the grey-body emissivities of the filament and substrate,  $\sigma$  is the Stefan-Boltzmann constant ( $5.67 \times 10^{-12} \text{ W/cm}^2 \text{ K}^4$ ).

Three calculations were compared to illustrate the relative importance of various factors. In the first, only the radiation flux from the filament was considered, while radiation from the substrate to the reactor walls was ignored. It follows from Eq. (5) that the radiation flux from the filament at any given point on the substrate is proportional to the shape factor at that point. Assuming a constant filament temperature, the problem in this case reduces to evaluation of the shape factor at different points on the substrate. It is assumed that the substrate temperature is proportional to  $Q_{fs}$  and thus, only normalized temperature profiles can be predicted which depends only on the filament shape and geometry through  $F_{fs}$ .

The second calculation improves upon the first by considering heat losses from the substrate to the reactor walls by radiation. The water-cooled walls of our reactor (Fig. 1) are assumed not to reflect incident radiation and hence are modeled as infinite heat sinks. Thus, the energy lost by the substrate to its surroundings  $Q_{sw}$  is given by

$$Q_{sw} = 2\epsilon_s(T_s)T_s^4 dA_1 \quad (W), \quad (6)$$

where  $T_s$  is the substrate temperature and  $\epsilon_s(T_s)$  is the temperature dependent grey-body emissivity of the substrate<sup>13</sup> which was fitted to a third degree polynomial for  $500 \text{ K} < T_s < 1200 \text{ K}$ ,

$$\epsilon_s(T_s) = -2.8324 + 1.0379 \times 10^{-2} T_s - 9.653 \times 10^{-6} T_s^2 + 2.963 \times 10^{-9} T_s^3. \quad (7)$$

The factor of 2 in Eq. (3) accounts for heat loss by both surfaces of the substrate. At steady state conditions,  $Q_{fs}$  equals  $Q_{sw}$ , and  $T_s$  is determined from Eqs. (5) and (6). For each calculated temperature profile, the wafer surface was divided into a mesh of square grids of area  $0.25 \text{ cm}^2$ . Further grid refinement did not alter the results of the

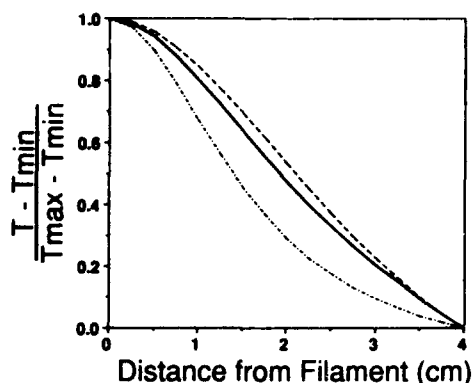


FIG. 3. A comparison between normalized calculated temperature profiles for a single filament at  $y=0 \text{ cm}$ , length  $= 9 \text{ cm}$ ,  $d_f = 1.27 \text{ mm}$ , and  $h_f = 1.6 \text{ cm}$ . Radiation flux from filament (---), radiation balance (—), radiation balance plus lateral conduction (— · —).

calculations. Initial guesses for the minimum and maximum substrate temperature provided the starting values, and successive substitution was used to solve for new temperature values, and the entire process was iterated until a convergence criteria of  $0.25 \text{ K}$  was met.

In the final calculation, the effect of lateral conduction of heat in the wafer was also included. The amount of heat  $Q_c$  conducted between a grid point on the surface and one of its four neighbors can be written as

$$Q_c = k_s(T_s)t_s(T_s - T_n) \quad (W). \quad (8)$$

Here  $t_s(\text{cm})$  and  $T_n$  are the thickness of the substrate and the temperature of a neighboring grid, respectively. The temperature dependence of the thermal conductivity of silicon,  $k_s(T_s)$  ( $\text{W/cm K}$ ),<sup>14</sup> is accounted for by the polynomial,

$$k_s(T_s) = 2.4408 - 5.1269 \times 10^{-2} T_s + 4.2304 \times 10^{-6} T_s^2 - 1.2292 \times 10^{-9} T_s^4. \quad (9)$$

Temperature profiles were calculated as outlined previously, except now there are four additional terms of the form of Eq. (8)—one for each neighboring grid—that must be included in the energy balance. The final calculation will be used throughout the final results and discussion section unless otherwise indicated.

## IV. RESULTS AND DISCUSSION

### A. Comparison of heat transfer calculations

The temperature profiles, as predicted by the three calculations, were compared for the simplest case of a single, straight Ta filament of  $9 \text{ cm}$  length. The temperature variation on the centerline of the substrate perpendicular to the filament is shown in Fig. 3. It is clear that even when only radiation flux is taken into account, the predicted temperature profile is in reasonable agreement with the other two profiles representing the radiation balance and radiation plus conduction.

A consequence of lateral heat conduction in the wafer is that it reduces both the maximum substrate temperature

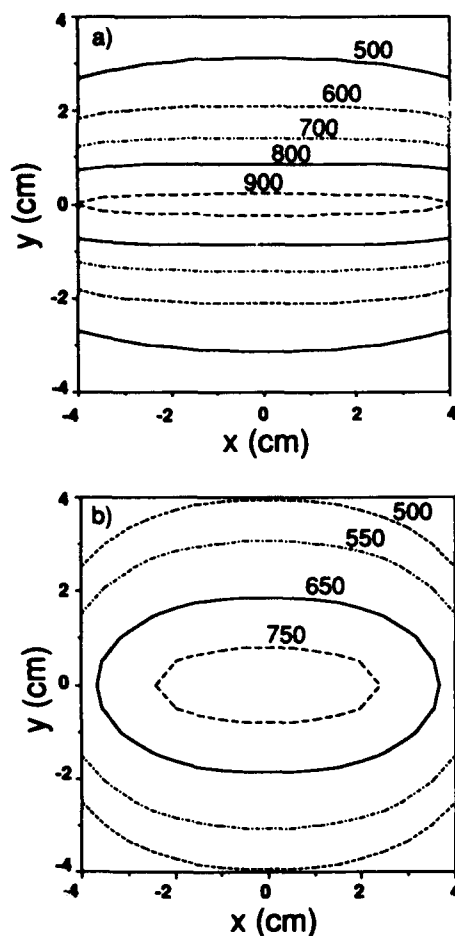


FIG. 4. Temperature contours for a single filament of length 9 cm, diameter 1.27 mm,  $T_f=2600$  K, and  $\epsilon_f=0.5$  as calculated from (a) a radiation balance and (b) with lateral conduction.

and the gradients across the substrate. The predicted contour plots are drawn for a single straight filament of 9 cm length for the radiation balance with and without lateral heat conduction (Fig. 4). The maximum temperature (located at the center of the wafer) as predicted are 975 and 790 K, respectively. The temperature gradients along the direction perpendicular to the filament axis are also smaller when the effect of lateral heat conduction along the wafer is also taken into account. For instance, the distance between  $100^\circ$  contours is  $\sim 0.5$  cm for the radiation only calculation, but takes place over  $\sim 0.9$  cm distance when conduction is included. Increasing the wafer thickness or mounting the wafer on a solid support would increase the effect of conduction and improve temperature uniformity. However, the general shape of the profile imposed by radiation will remain.

### B. Calculation versus measurement

The substrate temperature profile predicted by the final calculation was compared to values measured under vacuum for the case of three parallel tantalum filaments (Fig. 5). Since the experiment was performed in vacuum, the calculation considers all means of the heat transfer and

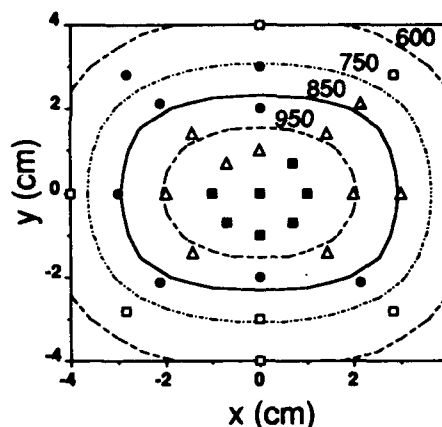
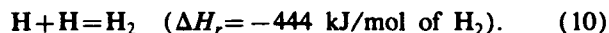


FIG. 5. Comparison between calculated temperature contours (K) for three parallel tantalum filaments at  $y=0, \pm 1.5$  cm under vacuum and measured data. 950–1015 K: solid squares, 850–950 K: open triangles, 750–850 K: solid circles, 650–750 K: open squares. Filament parameters were  $d_f=1.6$  mm,  $h_f=0.9$  cm, length=6.2 cm.

contains no adjustable parameters. The experimental data agrees well considering the filaments tend to bend during operation.

The calculation neglects heat transfer due to conduction and hydrogen atom recombination. In order to estimate and distinguish the effect of these two contributions the temperature of the center of the substrate was monitored in a vacuum, and at 30 Torr in helium and in hydrogen. Raising the pressure from vacuum to 30 Torr in helium resulted in a  $20^\circ\text{C}$  increase in the center temperature. Repeating the experiment in hydrogen resulted in a  $90^\circ\text{C}$  increase. Based on the thermal conductivities of the two gases, approximately  $60 \pm 5^\circ\text{C}$  of the temperature rise is attributed to the H atom recombination and  $25 \pm 5^\circ\text{C}$  to conduction. These findings are in good agreement with previous observations.<sup>15</sup> Further increasing the reactor pressure up to 300 Torr did not effect the substrate temperature in either gas. No change in conduction is expected as the thermal conductivity of gases is nearly invariant to pressure. However, the insensitivity to pressure also indicates that the H atom recombination rate at the center of the substrate is limited by the surface reaction under these conditions. From the difference observed in substrate temperature between vacuum and a hydrogen atmosphere, it is calculated that the contribution by H atom recombination and conduction to the energy flux from the filament to the substrate at deposition conditions is  $33 \pm 5\%$  of the flux due to radiation. The recombination of H atoms at substrate temperatures is a very exothermic reaction<sup>16</sup>



From the heat of reaction and estimated energy flux, the H atom recombination rate was calculated to be  $5 \times 10^{-6}$  mol/cm<sup>2</sup> s. Using recent measurements of the H atom concentration in a hot-filament CVD system by Hsu,<sup>17</sup> it is calculated that H atoms bombard the substrate at a rate of  $1 \times 10^{-4}$  mol/cm<sup>2</sup> s. Although these are rough



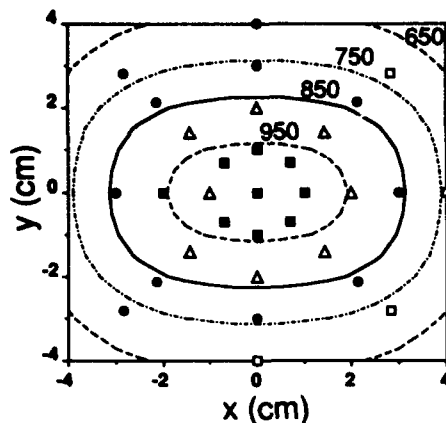


FIG. 6. Comparison between calculated temperature contours (K) for three parallel tantalum filaments at  $y=0$ ,  $\pm 1.5$  cm at 100 Torr, and measured data. 1050–1100 K: solid squares, 950–1050 K: open triangles, 850–950 K: solid circles, 750–850 K: open squares. Filament parameters were  $d_f=1.27$  mm,  $h_f=1.2$  cm, length=7 cm.

estimates, the differences in magnitude indicate that the surface reaction is indeed rate limiting at the center of the wafer.

Radiation-based calculations were compared to temperature profiles measured under diamond growth conditions (Fig. 6). The overall shape and gradients of the predicted contours show good agreement with measurements, but the actual temperatures were  $\sim 100^\circ\text{C}$  greater than predicted, as can be accounted for by H atom recombination and conduction. The importance of atomic hydrogen in the deposition of diamond has been reviewed.<sup>18</sup> The concentration of atomic hydrogen in the gas phase depends on the carbon concentration, filament diameter, and filament temperature.<sup>17,19,20</sup> Therefore, it is expected that the number and shape of the filaments will have an effect on the quality of the film, perhaps in a complicated way. The agreement of experimental and calculated temperature gradients in Fig. 6, despite the omission of hydrogen chemistry, suggests that the H atom flux has a similar dependence on filament geometry as the radiation flux.

### C. Maximum substrate temperature

The effect of parameters like filament diameter ( $d_f$ ), emissivity ( $\epsilon_f$ ), temperature ( $T_f$ ), and the filament-substrate separation ( $h_f$ ) has a profound effect on both the substrate and gas-phase temperatures, which influence both the growth rate and the quality of the film. Varying one of the first three variables does not appreciably change the substrate temperature profiles, but they influence the magnitude of the surface temperatures and thus can be examined through consideration of the maximum substrate temperature. The effect of these parameters are not independent of each other. Thus, the growth conditions are altered in a complex manner.

All experimental determination of the true filament temperature requires knowledge of the emissivity of the filament, which not only depends on the surface roughness

TABLE I. Emissivity of common refractory materials.\*

$\lambda$	W	Re	Ta
0.66 $\mu\text{m}$	0.36	0.41	0.38
1.6 $\mu\text{m}$	0.29	0.30	n/a
2.6 $\mu\text{m}$	0.22	0.21	n/a

\*See Ref. 21.

but also on the filament material. Table I summarizes the emissivity data of refractory metals commonly used in hot-filament CVD.<sup>21</sup>

Calculations with the same filament geometry show that the maximum substrate temperature is sensitive to  $\epsilon_f$  [Fig. 7(a)]. For example a change from 0.3 to 0.4 increases the temperature by 73 K. Note that both tungsten and tantalum form carbides during deposition, and variations in emissivity may significantly effect the substrate temperature during carburization.

Though radiation flux from the filament is proportional to  $T_f^4$ , the maximum substrate temperature increases only linearly with  $T_f$  since this effect is balanced by increased radiation from the substrate to the wall [Fig. 7(b)]. The substrate temperature only varies  $10^\circ$  with a  $25^\circ$  change in  $T_f$ . Therefore, errors in our optical determination of the filament temperature will not significantly effect the results of the calculations. For deposition of high quality material for optical and electronic applications, a more important concern is the strong temperature dependence of the vapor pressure ( $P_{\text{vap}}$ ) of common filament materials such as Ta, W, and Re.<sup>22</sup> For example,  $P_{\text{vap}}$  for tantalum is almost five times greater at 2600 K than at 2500 K.<sup>21</sup> Thus, the concentration of impurities from the filament incorporated into the growing film depends strongly on temperature as demonstrated by Jansen and co-workers<sup>22</sup> for rhenium filaments. Thus the level of acceptable impurity concentration would determine the upper limit of the operating filament temperature. The lower limit appears to be 2400 K, the temperature required to thermally activate the necessary gas-phase chemistry.<sup>15</sup>

A better way to control the substrate temperature is through variation of the filament diameter. The maximum substrate temperature is strongly dependent on filament diameter as the radiation flux is directly proportional to the filament diameter [Fig. 7(c)]. The substrate temperature increases by  $105^\circ\text{C}$  as  $d_f$  increases from 0.5 to 1 mm.

Increasing the filament-substrate separation,  $h_f$ , decreases the maximum substrate temperature because it decreases the view factor [Fig. 7(d)]. However, the temperature drops only  $10^\circ$  for a 1 mm increase in  $h_f$ . However, the effect of  $h_f$  will be more pronounced for filaments close to the substrate ( $< 5$  mm). The effect of  $h_f$  on the temperature contours is discussed further in the next subsection.

### D. Substrate temperature uniformity

The model provides a convenient tool to investigate novel filament geometries to improve temperature uniformity. First, the effect of the number of filaments and their spacing was examined. The temperature profiles for paral-

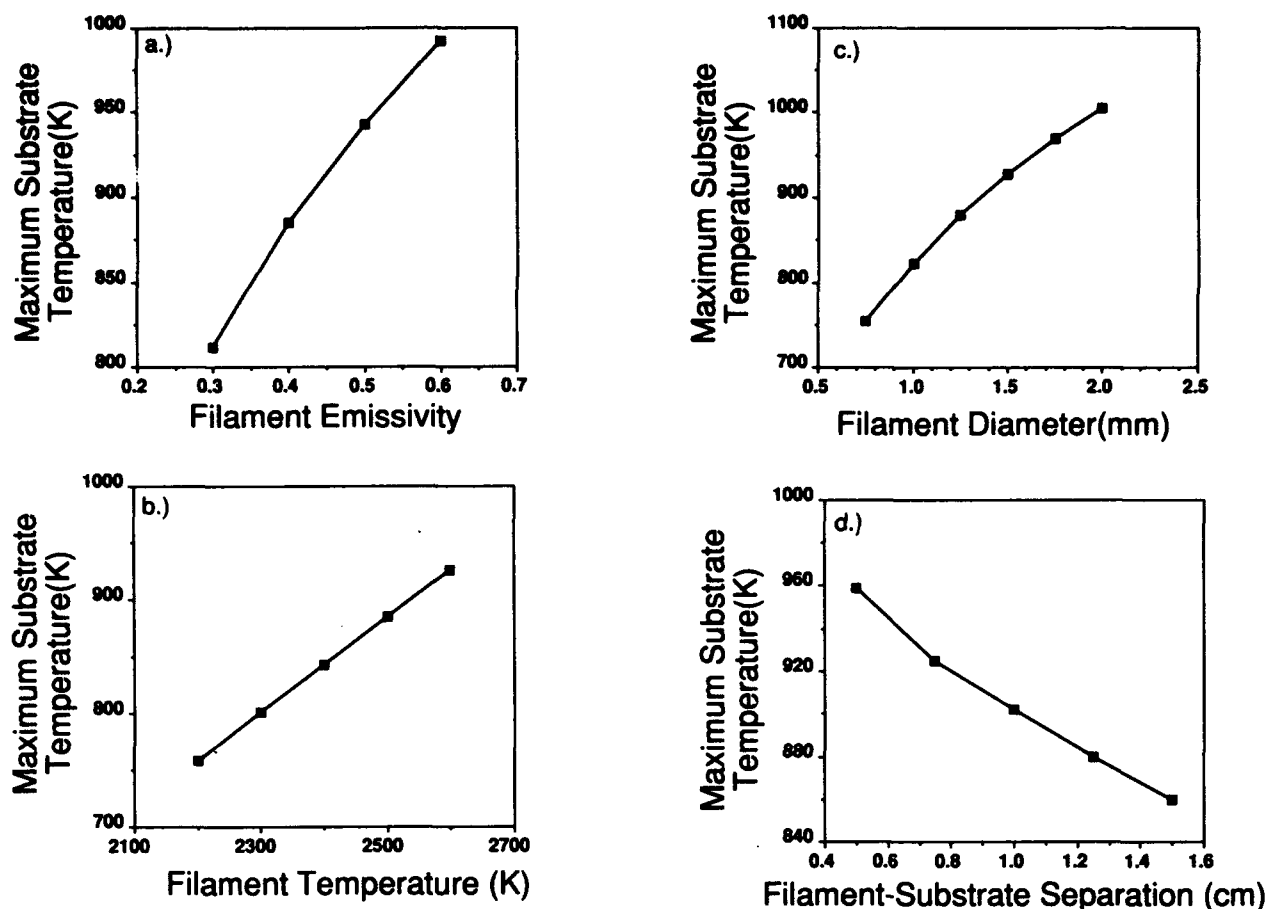


FIG. 7. The dependence of calculated maximum substrate temperature on (a) filament emissivity  $\epsilon_f$ , (b) filament temperature  $T_f$ , (c) filament diameter  $d_f$ , and (d) filament-substrate separation  $h_f$ . Calculations for three 10 cm parallel filaments at  $y=0, \pm 2$  cm. The other parameters used are  $d_f=1.25$  mm,  $h_f=1.2$  cm,  $\epsilon_f=0.4$ ,  $T_f=2500$  K.

lel filaments separated by 2 cm are shown in Fig. 8. Comparing contours for 1, 5, and 15 filaments demonstrates that temperature uniformity is significantly improved when the filament number is increased [Figs. 8(a), 8(b), and 8(c)]. The difference between minimum and maximum substrate temperature in the three cases is 225, 45, and 15 °C, respectively. Hence, increasing the number of filaments improves temperature uniformity at the expense of simplicity and increased energy consumption.

In addition, temperature uniformity is improved as the filament-substrate separation,  $h_f$ , is increased while the distance between filaments is held constant. For an infinite number of long, parallel filaments, it was found that when  $h_f$  was  $0.75 \pm 0.05$  of the filament spacing, the temperatures across a 4 in. silicon wafer varied by < 10%. These calculations suggest that  $h_f$  should be as large as the separation between the filaments to ensure reasonable temperature uniformity. However, the transport of species from the hot filament to the substrate is dominated by diffusion.<sup>23</sup> Consequently, the maximum value of  $h_f$  is limited by the need to maintain a sufficient flux of H atoms and diamond precursors to the substrate. Characteristic diffusion lengths, the distance a species will diffuse before being consumed chemically, were estimated for hot-filament CVD condi-

tions by Goodwin and Gavillet.<sup>24</sup> These values are summarized for important species in Table II.

An alternative to increasing the number of filaments is using unique filament shapes. The calculations were used to design the filament shown in Fig. 9(a). The solid line is the actual shape of the filament used and the dotted line is the straight filament approximation used for the calculations. The measured substrate temperature over the shaded  $2 \times 6$  cm area was  $1060 \pm 30$  K, while the calculated contour which shows  $T=910 \pm 30$  K over the same area [Fig. 9(b)]. Note that for this filament geometry the difference between calculated and measured values is 150 K, which is accounted for by the H atom recombination and conduction and the approximation of the true filament geometry, but again it did not affect the gradients.

As mentioned previously, the effect of filament parameters are not independent. These interrelationships may be manipulated judiciously to design filament geometries for improved substrate temperature uniformity as shown in Fig. 10. Figure 10(a) shows the temperature profiles for three parallel filaments of the same diameter and filament-substrate separation. The maximum substrate temperature is 958 K. By slightly decreasing  $d_f$  of the middle filament

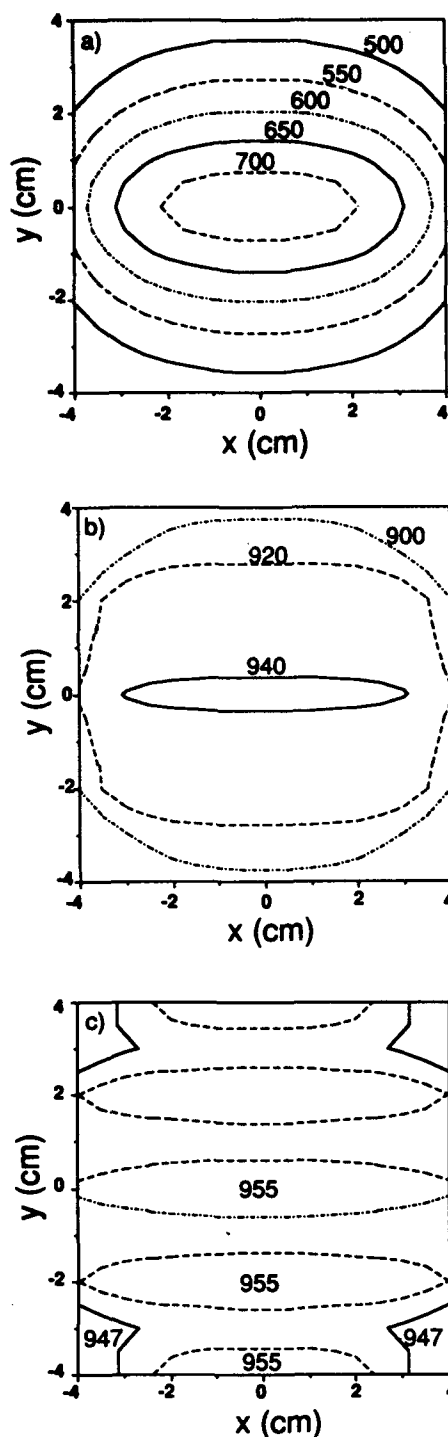


FIG. 8. Comparison of calculated temperature profiles for (a) 1 filament at  $y=0$  cm; (b) 5 filaments at  $y=0, \pm 2, \pm 4$  cm; (c) 15 filaments at  $y=0, \pm 2, \pm 4, \pm 6, \pm 8, \pm 10, \pm 12, \pm 14$  cm. In each case length=16 cm,  $d_f=1$  mm,  $h_f=1$  cm,  $T_f=2600$  K.

and  $h_f$  of the outer filaments, an  $18 \text{ cm}^2$  area is obtained where  $T_s=915 \pm 15$  K [Fig. 10(b)].

To investigate another method of achieving substrate temperature uniformity the calculations were used to analyze the effect of rotating the substrate. Equations (1)–(4) were used to compute the shape factor for points at radius

TABLE II. Characteristic diffusion lengths for several species.<sup>a</sup>

Species	Diffusion lengths (cm)
$\text{C}_2\text{H}_2$	3.0
H	1.0
$\text{CH}_4$	0.2–0.8
$\text{C}_2\text{H}_4$	0.3
$\text{CH}_3$	0.2–0.007

<sup>a</sup>See Ref. 24.

$R$  and angular position  $\phi$ . The average shape factor for a given radius is given by

$$F(R)_{\text{avg}} = \frac{1}{2\pi} \int_0^{2\pi} F_{fs}(R, \phi) d\phi. \quad (11)$$

The averaged shape factor was used in conjunction with Eqs. (5)–(9) to generate temperature profiles as before. Figure 11 shows a comparison between a stationary and rotating substrate for three parallel filaments. In addition to gaining symmetry, the temperature gradients are much smaller in the rotating case. Rotation decreases the maximum temperature difference across the substrate from 220 to 140 K. The reason for this improvement is that the

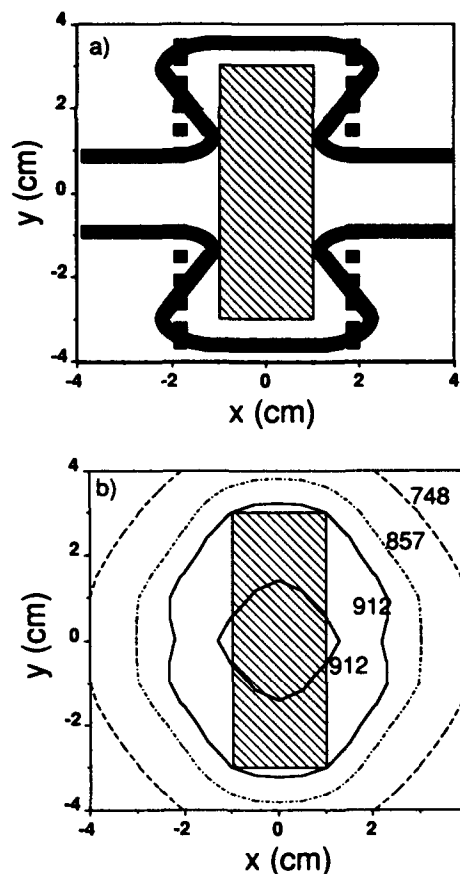


FIG. 9. Comparison of (a) 2 filament geometry (solid line) and area of measured temperature uniformity and (b) calculated temperature contours for straight filament approximation (dashed line). Other parameters:  $d_f=1.27$  mm,  $h_f=1$  cm.

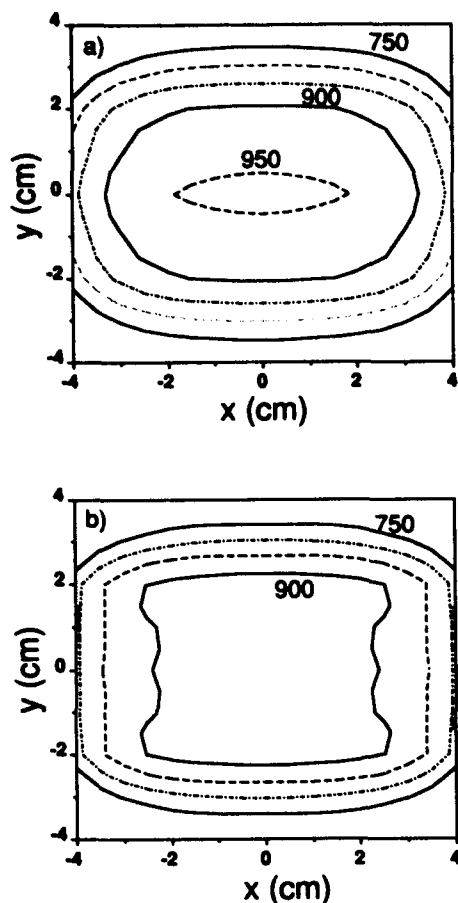


FIG. 10. Comparison of calculated temperature profiles for (a) 3 filaments at  $y=0, \pm 2$  cm:  $d_f=1.5$  mm,  $h_f=1$  cm,  $T_f=2600$  K; (b) 1 filament at  $y=0$  cm:  $d_f=1.2$  mm,  $h_f=1$  cm, 2 filaments at  $y=\pm 2$  cm:  $d_f=1.5$  mm,  $h_f=0.7$  cm. All filaments 10 cm long,  $T_f=2600$  K.

entire substrate comes in close proximity to the filaments at some point during rotation.

### E. Relationship to growth rates

Jansen and co-workers<sup>22</sup> have studied diamond deposition rates for various filament geometries. Film thicknesses were measured at different distances perpendicular to the middle of the filament(s) and found to be a strong function of position and filament geometry. Our normalized radiation flux profiles calculated from Eqs. (1)–(2) were compared with their reported normalized film thickness profiles (Fig. 12). Since the deposition time for these films was kept constant, it is clear that the growth rate profiles closely follow the variations in radiation flux. The maximum growth rate (on an absolute scale) for both case A and B was found to be the same, in agreement with the fact that the substrate was held at constant temperature. Thus, the consistently higher growth rates observed away from the center for the longer filament is due solely to geometry. Though the substrate was held at a nominal temperature of 900 °C by external heating, temperature variations across the substrate may remain due to radiation flux from the filament. In addition, the authors found that

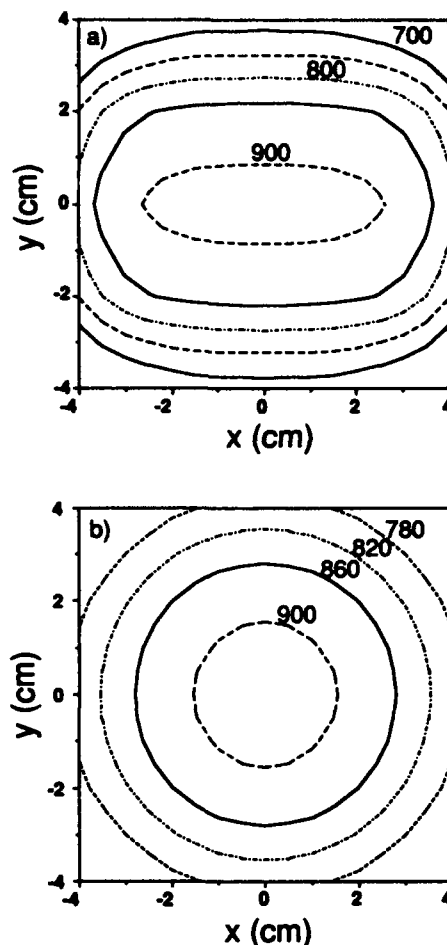


FIG. 11. Comparison of calculated temperature profiles for (a) stationary and (b) rotating substrates. Three 10 cm filaments separated by 2 cm. Other parameters are  $d_f=1.0$  mm,  $h_f=1.0$  cm,  $T_f=2600$  K.

the deposition rate was independent of filament diameter.<sup>22</sup> The normalized radiation flux is also independent of the filament diameter, depending solely on the filament position and length.

Another explanation is that the variations in growth rate may result from a spatial distribution in the flux of gaseous precursors and/or the H atom. As previously discussed, the H atom flux may have a similar dependence on filament geometry as radiation.

There is, however, a marked departure from this linear relationship for case D (two 4 in. filaments separated by 20 mm) where the growth rate at the center of the substrate deviates from the radiation flux profile. An explanation for this deviation may be depletion of gas-phase diamond precursors due to Soret diffusion.<sup>25</sup> In this case a hot zone between the two filaments is created where the relatively heavy carbon containing molecules are displaced by hydrogen molecules and atoms. In case C (two 4 in. filaments separated by 9 mm) this zone is much smaller and enough precursors can diffuse in from the sides so as not to limit the growth rate.

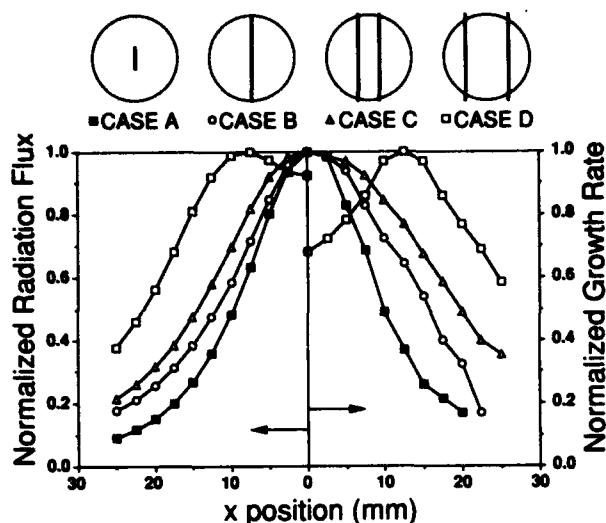


FIG. 12. A comparison between the normalized growth profiles as measured by Jansen and co-workers (Ref. 22) and normalized radiation flux profiles. Case A: one 0.5 in. filament, case B: one 4 in. filament, case C: two 4 in. filaments 9 mm apart, case D: two 4 in. filaments 20 mm apart. All cases  $d_f = 1.016$  mm,  $h_f = 1.2$  cm.

## V. CONCLUSIONS

An ability to grow uniform diamond films over a large area requires that the substrate temperature be held constant. Even in the presence of external heating, temperature gradients across the substrate may remain due to the proximity of the filament to the substrate. Heat transfer calculations were used to predict temperature profiles across the substrate as a function of filament shape and geometry. These calculations gave reasonable agreement with experimental measurements. It is evident that hydrogen recombination makes a significant contribution to the substrate temperature, but uniformity is determined by the geometric dependence of the radiation flux. We developed a two-filament geometry based on the calculations that yielded uniform substrate temperatures over a relatively large area. The effect of other deposition parameters was also discussed. We have demonstrated that for a number of filament geometries, a close match exists between the normalized radiation flux profiles and the growth rates. Cur-

rently, an effort is under way to use these results to develop filament geometries capable of depositing diamond films over large areas.

## ACKNOWLEDGMENTS

We gratefully acknowledge the support by the National Science Foundation under grant No. CTS 9006705 and the Office of Naval Research.

- <sup>1</sup>R. C. DeVries, *Ann. Rev. Mater. Sci.* **17**, 161 (1987).
- <sup>2</sup>J. C. Angus and C. C. Hayman, *Science* **241**, 913 (1988).
- <sup>3</sup>B. V. Spitsyn, L. L. Bouilov, and B. V. Deriyagin, *J. Cryst. Growth* **52**, 219 (1981).
- <sup>4</sup>K. Kobashi, K. Nishimura, Y. Kawate, and T. Horuchi, *Phys. Rev. B* **38**, 4067 (1988).
- <sup>5</sup>Y. Hirose and N. Kondo, Program and Book of Abstracts, 35th Japan Society of Applied Physics Spring Meeting, 1988, p. 434.
- <sup>6</sup>Y. Hirose and Y. Terasawa, *Jpn. J. Appl. Phys.* **25**, L619 (1981).
- <sup>7</sup>K. A. Snail, D. B. Oakes, J. E. Butler, and L. M. Hanssen, *Proceedings of the Second International Conference*, edited by R. Messier, J. T. Glass, J. E. Butler, and R. Roy (Materials Research Society, Pittsburgh, PA).
- <sup>8</sup>Y. Tzeng, C. C. Tiu, R. Phillips, T. Srivinyunon, and Y. Chen, *Appl. Phys. Lett.* **57**, 789 (1990).
- <sup>9</sup>F. Akatsuka and F. Shimura, *Applications of Diamond Films and Related Materials*, edited by Y. Tzeng, M. Yoshikawa, M. Murakawa, and A. Feldman, (Elsevier, Amsterdam, 1991), p. 379.
- <sup>10</sup>S. Matsumoto, Y. Sato, M. Kamo, and N. Setaka, *Jpn. J. Appl. Phys.* **21**, L183 (1982).
- <sup>11</sup>P. K. Bachmann, D. Leers, and H. Lydtin, *Diamond and Related Mater.* **1**, 1 (1991).
- <sup>12</sup>L. Schafer, M. Sattler, and C.-P. Klages, *Applications of Diamond Films and Related Materials*, edited by Y. Tzeng, M. Yoshikawa, M. Murakawa, and A. Feldman (Elsevier, Amsterdam, 1991), p. 453.
- <sup>13</sup>J. Nulman, *SPIE Proc. Rapid Isothermal Processing* **1189**, 72 (1989).
- <sup>14</sup>F. Kreith and M. S. Bohn, *Principles of Heat Transfer* (Harper and Row, New York, 1986).
- <sup>15</sup>M. Sommer and F. W. Smith, *J. Mater. Res.* **5**, 2433 (1990).
- <sup>16</sup>S. Benson, *Thermochemical Kinetics* (Wiley, New York, 1976).
- <sup>17</sup>W. L. Hsu, *Appl. Phys. Lett.* **59**, 1427 (1991).
- <sup>18</sup>M. Frenklach, *J. Appl. Phys.* **65**, 5142 (1989).
- <sup>19</sup>F. Jansen, I. Chen, and M. A. Machonkin, *J. Appl. Phys.* **66**, 5749 (1989).
- <sup>20</sup>U. Meier, K. Kohse-Hoinghaus, L. Schafer, and C. P. Klages, *Appl. Phys. Lett.* **58**, 571 (1991).
- <sup>21</sup>Purdue University, *Thermophysical Properties of High Temperature Solid Materials*, edited by Y. S. Touloukian (MacMillan, New York, 1970), Vol. 1, p. 1038.
- <sup>22</sup>F. Jansen, M. A. Machonkin, and D. E. Kuhman, *J. Vac. Sci. Technol.* **A 8**, 3785 (1990).
- <sup>23</sup>T. Debroy, K. Yankala, W. A. Yarbrough, and R. Messier, *J. Appl. Phys.* **68**, 2424 (1990).
- <sup>24</sup>D. G. Goodwin and G. G. Gavillet, *J. Appl. Phys.* **68**, 6393 (1990).
- <sup>25</sup>S. J. Harris and A. M. Weiner, *J. Appl. Phys.* **67**, 6520 (1990).



Reprinted from JOURNAL OF THE ELECTROCHEMICAL SOCIETY  
Vol. 140, No. 2, February 1993  
Printed in U.S.A.  
Copyright 1993

# Comparison of Tantalum and Rhenium Filaments in Diamond CVD Using Selective Carbon-13 Labeling

K. M. McNamara and K. K. Gleason

Department of Chemical Engineering, MIT, Cambridge, Massachusetts 02139

## ABSTRACT

Heterogeneous carbon scrambling at the hot-filament in thermally assisted diamond chemical vapor deposition has been investigated through isotopic labeling studies. Films were produced using acetone, preferentially labeled at either the methyl or carbonyl carbon, and  $^{13}\text{C}$  incorporation was determined from the shift of the first-order diamond one-phonon band in the Raman spectra. A comparison of the effects of carbide-forming materials, such as tantalum, and non-carbide formers, such as rhenium, is made. Results indicate that heterogeneous scrambling is limited in the rhenium case, which may prove useful in selective isotopic labeling studies. This study demonstrates the importance of heterogeneous reactions at the hot-filament and thus, has important implication for the modeling of these systems.

Hot-filament chemical vapor deposition (CVD) has been used extensively to produce diamond films at low-pressure.<sup>1-6</sup> One of the reasons cited for choosing this technique is the simplified gas-phase chemistry with respect to plasma systems. Species measurements have shown that the gas-phase concentrations of many carbon species in a typical hot-filament CVD environment, such as  $\text{C}_2\text{H}_2$ ,  $\text{CO}$ , and  $\text{CH}_4$ , approach those calculated at equilibrium for the filament temperature and reactor pressure.<sup>7-9</sup> In addition, there has been extensive kinetic modeling of the gas-phase chemistry within these systems.<sup>10-18</sup> While these homogeneous reactions have been explored in some detail, little information is available concerning the heterogeneous chemistry within the system. Of particular interest are heterogeneous reactions at the hottest surface in the reactor, the filament, which is often a carbide-forming refractory metal, such as tantalum or tungsten. Metals which do not form carbides, such as rhenium, have also been used successfully for filaments in diamond deposition. Comparison of these types of materials by selective isotopic labeling of the carbon source may shed light on the importance of heterogeneous reactions at the hot-filament.

Selective isotopic labeling has been used successfully to study the kinetics of combustion systems.<sup>19,20</sup> In many systems, however, the application of this technique is limited by rapid homogeneous

gas-phase or heterogeneous surface reactions which scramble or rearrange carbons from different sites in various species. Such scrambling is often rapid between hydrocarbon species.<sup>21</sup> However, this type of scrambling is not necessarily complete under all conditions. Chu *et al.* have shown that in cases where only partial scrambling occurs, selective isotopic labeling can be used to gain insight into the kinetics of diamond formation.<sup>21,22</sup>

The heterogeneous chemistry at carbide-forming filaments is a particularly interesting method by which carbon labels may scramble. If this type of reaction proceeds to a significant extent, the results of labeling studies may differ from those found in systems using method which do not form carbides. This has important implications for the modeling of hot-filament CVD where, to date, such reactions have not been considered.

Heterogeneous chemistry at the filament has been examined using hot-filament deposition under the operating conditions shown in Table I. Acetone was used as the carbon source, introducing the effects of oxygen on both the homogeneous and heterogeneous chemistry in the system. The acetone was selectively labeled at either the methyl or carbonyl carbon, as in previous work.<sup>9</sup> Acetone was chosen as the carbon source because it is expected to readily yield methyl radicals and  $\text{CO}$ . Although selectively labeled hydrocarbons in the gas-phase are expected to scramble completely in

Table I. Hot-filament CVD operating conditions

Filament temperature	2500-2600 K
Substrate temperature	1100 K
Filament/substrate distance	1 cm
Total pressure	200 Torr
H <sub>2</sub> flowrate	100 sccm
Acetone flowrate	2 sccm
Seed (natural diamond powder)	<0.25 $\mu$ m
Substrate material	silicon

gas phase reactions,<sup>21</sup> isotopic labeling studies have shown that homogeneous gas-phase scrambling of CO with hydrocarbons, under conditions similar to those in our system, is minimal.<sup>19,20</sup> Equilibrium calculations indicate that the final CO concentration at equilibrium is 99.999% of the initial carbonyl concentration.

The level of incorporation of <sup>13</sup>C into the growing diamond film was determined from the isotopic shift in the first-order Raman frequency. In this work, the <sup>13</sup>C concentration is determined from a second-order polynomial fit to the experimental data of Banholzer and Anthony, who used <sup>13</sup>C labeled high pressure synthetic diamond to measure the change in Raman frequency as a function of <sup>13</sup>C concentration.<sup>22</sup> These results have been confirmed by Chu *et al.* for <sup>13</sup>C-enriched diamond films as well.<sup>21,22</sup> The uncertainty in the Raman peak position is roughly  $\pm 2$  cm<sup>-1</sup> for macro-Raman;  $\pm 1.5$  cm<sup>-1</sup> for micro-Raman. This corresponds to an uncertainty of less than 4 and 3% in the <sup>13</sup>C enrichment for the macro- and micro-Raman, respectively. There is greater uncertainty in macro-Raman due to a decrease in the signal-to-noise ratio.

There are other factors, such as temperature<sup>24,25</sup> and stress in the film,<sup>26,27,28</sup> which can also cause the Raman band to shift. However, the temperature of the sample can be controlled by lowering the incident laser power, and stress shifts are typically small ( $\leq 5$  wavenumbers). To minimize the effects of stress shift, the same substrate material was used in all experiments, reducing the variation from sample to sample. In addition, the Raman frequency measured for natural abundance samples produced on silicon under similar conditions was 1332 cm<sup>-1</sup>, indicating that stress shifts observed on this material will be small.

In the first samples in Table II (TaM1 and TaC1), the acetone source (Cambridge Isotope, Inc.) was 99% <sup>13</sup>C-enriched at the selected carbon, giving overall gas-phase enrichments of 65 and 32.5% for the methyl and carbonyl-labeled cases, respectively. The filament was tantalum, pre-carburized in natural-abundance (1.1% <sup>13</sup>C) acetone for  $\sim 3$  h. Runs were carried out for 3-4 h at a growth rate of  $\sim 3$   $\mu$ m/h to yield 10 to 12  $\mu$ m thick continuous films. These films were pale gray in appearance and showed well-defined facets under optical microscopy. These films were further characterized by <sup>13</sup>C nuclear magnetic resonance spectroscopy (NMR), which showed only one peak, indicative of sp<sup>3</sup> bonded carbon.<sup>29</sup>

The macro-Raman spectra of the films are found in Fig. 1, showing the shifted one-phonon diamond band. The positions of the first order diamond Raman bands are tabulated in Table II, as are the calculated <sup>13</sup>C concentrations calculated using the experimental second-order polynomial. The concentrations determined were  $65 \pm 4\%$  and  $32 \pm 4\%$ , for the methyl and carbonyl-labeled cases, respectively, identical to the overall gas-phase enrichments within the experimental uncertainty. This most likely indicates complete scrambling of <sup>13</sup>C, which is surprising since CO carbons are not expected to undergo homogeneous scrambling in the gas-phase under these conditions.<sup>19,20</sup>

To verify this result, a similar experiment was carried out using selectively <sup>13</sup>C-enriched acetone with the same overall gas-phase

Table II. Results of <sup>13</sup>C enrichment studies.

Sample	Filament material	Label	% <sup>13</sup> C <sub>gas</sub>	% <sup>13</sup> C <sub>solid</sub>	Diamond one-phonon Raman shift $\nu$ (cm <sup>-1</sup> )
TaM1	Ta	methyl	65	$65 \pm 4$	1305
TaC1	Ta	carbonyl	32.5	$32 \pm 4$	1321
TaM2	Ta	methyl	22	$22 \pm 3$	1325
TaC2	Ta	carbonyl	22	$22 \pm 3$	1325
ReM	Re	methyl	22	$24 \pm 3$	1324
ReC	Re	carbonyl	22	$8 \pm 3$	1330

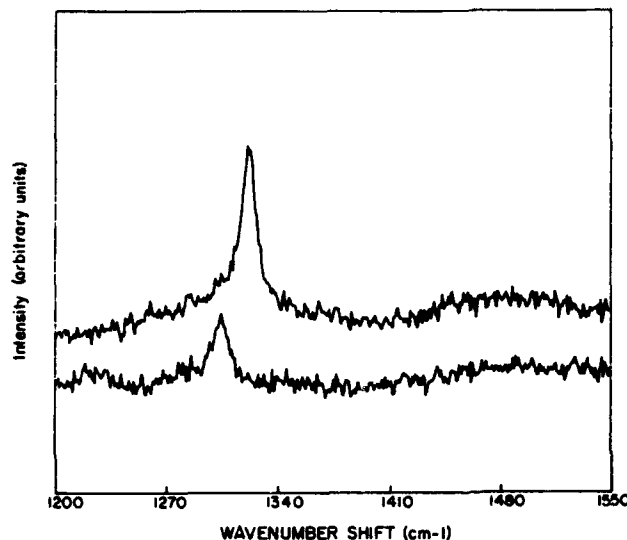


Fig. 1. Macro-Raman spectra of films with tantalum and 32.5 and 65% gas-phase enrichments for the carbonyl (top) and methyl (bottom) labels, respectively. The top (carbonyl) shows the first-order Raman frequency at 1321 cm<sup>-1</sup>, while the bottom (methyl) shift is 1305 cm<sup>-1</sup>.

enrichment of 22% (samples TaM2 and TaC2).<sup>9</sup> Again, the <sup>13</sup>C NMR spectra of these films shows only one peak at 36 ppm, indicative of sp<sup>3</sup> bonding. The overlap of the micro-Raman diamond one-phonon bands for these two films (Table II and Fig. 2) support the earlier findings that in both the methyl and carbonyl label case, the enrichment of the solid film closely matches that of the gas phase. Secondary ion mass spectroscopy (SIMS) was used to determine if the filament contributed to heterogeneous isotopic scrambling of the carbonyl label. The filament was first pre-carburized in natural abundance acetone before exposure to carbonyl-labeled acetone. Signals from the <sup>13</sup>C containing species were detected at a level several orders of magnitude higher than for the same experiment run under natural abundance acetone. The signal persisted throughout the 2000 Å SIMS depth profile of the tantalum filament exposed to the enriched acetone, indicating that significant heterogeneous exchange of the carbonyl carbon occurs even after the initial carburization period.<sup>9</sup>

To further test the assertion that heterogeneous exchange at the tantalum filament contributes to carbonyl carbon incorporation in the growing film, experiments were carried out under nominally

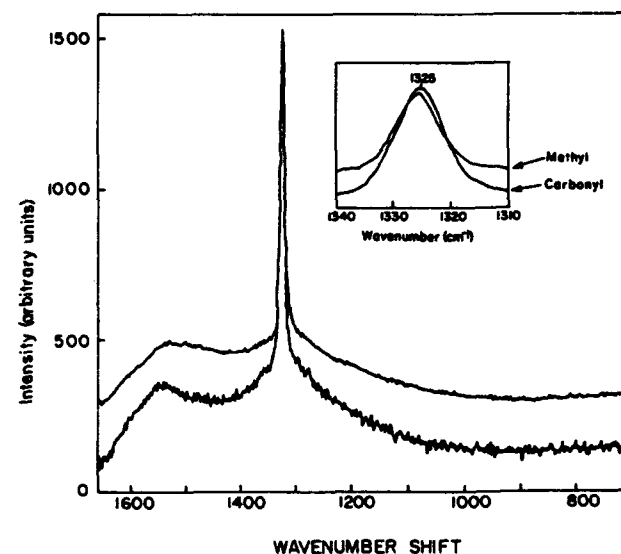


Fig. 2. Micro-Raman spectra of diamond films produced with a tantalum filament and a 22% gas-phase enrichment. Inset shows both the methyl (bottom) and the carbonyl (top) spectrum have a diamond peak shifted to 1325 cm<sup>-1</sup>.

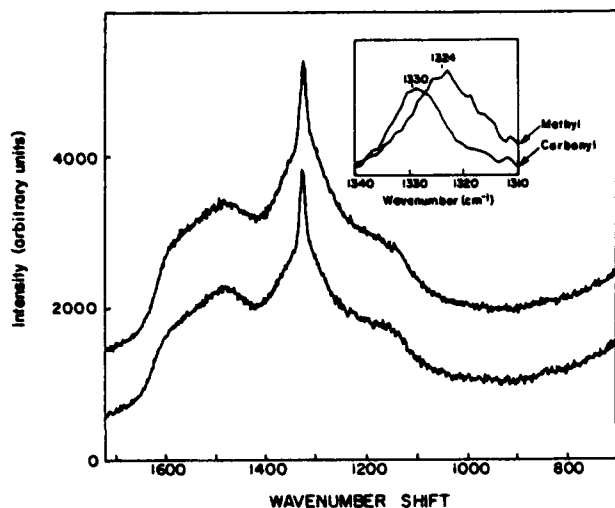


Fig. 3. Micro-Raman spectra of diamond films produced with a rhenium filament and a 22% gas-phase enrichment. The bottom spectrum (methyl) shows a shift in the diamond one-phonon band to  $1324\text{ cm}^{-1}$ , while the top spectrum (carbonyl) is only shifted to  $1330\text{ cm}^{-1}$ .

identical conditions with the exception of replacing the tantalum filament with a rhenium one and limiting the duration of the run ( $\sim 1\text{ }\mu\text{m}$  was deposited). Unlike tantalum, rhenium does not form a carbide and thus, reduces the likelihood of carbon exchange at the filament.<sup>30,31</sup> The overall gas-phase  $^{13}\text{C}$  enrichment in both the methyl and carbonyl-labeled cases (ReC and ReM), was 22%.

The micro-Raman spectra of the samples ReM and ReC are shown in Fig. 3. These spectra show a clear diamond band, shifted due to the isotopic enrichment, but also contain contributions associated with graphitic carbon. This apparent difference in film quality, relative to samples TaM1 and TaM2, may be, in part, a result of the superior sensitivity of the micro-Raman technique.<sup>32</sup> The shift of the first-order Raman band for these samples is recorded in Table II with the calculated  $^{13}\text{C}$  enrichment from the experimental second-order polynomial. The concentrations obtained were  $24 \pm 3\%$  and  $8 \pm 3\%$  for the methyl and carbonyl-labeled acetone, respectively. This dramatic decrease in the incorporation of carbonyl carbons when using a rhenium filament serves to highlight the importance of heterogeneous filament chemistry in hot-filament systems using carbide-forming filament materials.

Although the incorporation of carbonyl carbons is greatly reduced in the rhenium case, there is still some  $^{13}\text{C}$  in the film. This indicates that a small amount of CO may undergo conversion to hydrocarbon species by some other route. One possibility is that the enol form of acetone, whose concentration is expected to increase in a hydrogen environment,<sup>33</sup> may provide an alternative route for acetone decomposition, separating the oxygen from the carbonyl carbon. Also, the homogeneous gas-phase conversion of CO to hydrocarbon species may have a finite contribution. In addition, although carbon for heterogeneous exchange is not supplied by the rhenium filament, surface reactions at the filament are still possible and may contribute to the conversion of CO. Finally, CO may, in fact, act as a precursor for diamond growth at a significantly slower rate than hydrocarbon species.

In conclusion, we have demonstrated the importance of heterogeneous reactions at the hot-filament when a tantalum filament is employed. However, this effect is reduced when rhenium is the filament material. With this filament, selective labeling studies, which are limited by heterogeneous scrambling, may be more easily carried out. A significant portion of the CO carbon incorporated into diamond films when using a tantalum filament occurs through the mechanism of heterogeneous carbon exchange at the filament. It is expected that other carbide-forming materials, such as tung-

sten, will behave similarly to tantalum. This has important implications for the modeling of chemistry in these systems, which to date has not included such reactions.

The authors gratefully acknowledge the assistance of Mr. Leo Kenny of Tufts University, Dr. James E. Butler of the Naval Research Laboratory, and Mr. Dan Vesteyck for assistance in obtaining macro-Raman and micro-Raman spectra, respectively. We would like to acknowledge Dr. Mike Geis and Mr. Keith Krohn of Lincoln Laboratory for their assistance and the use of their reactor. We also gratefully acknowledge the financial support of the Office of Naval Research and NSF Grant No. CTS-9006705.

Manuscript submitted June 3, 1992; revised manuscript received Aug. 4, 1992.

MIT assisted in meeting the publication costs of this letter.

## REFERENCES

1. P. K. Bachmann, D. Leers, and H. Lydtin, *Diamond and Related Materials*, 1, 1 (1991).
2. R. C. DeVries, *Am. Rev. Mater. Sci.*, 17, 161 (1987).
3. J. C. Angus and C. C. Hayman, *Science*, 241, 913 (1988).
4. Y. Hirose and Y. Terasawa, *Jpn. J. Appl. Phys.*, 25, L519 (1986).
5. F. Akatsuka, Y. Hirose, and K. Komaki, *ibid.*, 27, 1600 (1987).
6. J. Suzuki, H. Kawarada, K. S. Mar, J. Wei, Y. Yokota, and A. Hiraki, *ibid.*, 28, 281 (1989).
7. F. G. Celli, P. E. Pehrsson, H.-t. Wang, and J. E. Butler, *J. Appl. Phys.*, 52, 2043 (1988).
8. J.-i. Suzuki, H. Kawarada, K.-s. Mar, J. Wei, Y. Yokota, and A. Hiraki, *Jpn. J. Appl. Phys.*, 28, 281 (1989).
9. K. M. McNamara and K. K. Gleason, *J. Appl. Phys.*, 71(6), 2884 (1992).
10. S. J. Harris, A. M. Weiner, and T. A. Perry, *Appl. Phys. Lett.*, 53, 1605 (1988).
11. S. J. Harris and A. M. Weiner, *J. Appl. Phys.*, 67, 6520 (1990).
12. S. J. Harris, A. M. Weiner, D. N. Belton, and S. J. Schmieg, *ibid.*, 66, 5353 (1989).
13. S. J. Harris, A. M. Weiner, and R. J. Blint, *Combust. Flame*, 72, 91 (1988).
14. M. Frenklich and H. Wang, *Physical Review B*, 43, 1520 (1991).
15. D. G. Goodwin and G. G. Gavillet, *J. Appl. Phys.*, 68, 6383 (1990).
16. M. A. Cappelli and P. H. Paul, *ibid.*, 67, 2596 (1990).
17. T. Debroy, K. Yankala, W. A. Yarbrough, and R. Messier, *ibid.*, 68, 2424 (1990).
18. W. L. Hsu, *ibid.*, 59, 1427 (1991).
19. R. E. Ferguson, *J. Chem. Phys.*, 23, 2065 (1955).
20. R. E. Ferguson, *Combustion and Flame*, 1, 431 (1957).
21. C. J. Chu, R. H. Hauge, M. P. D'Evelyn, and J. L. Margrave, *Mater. Res. Soc. Symp. Proc.*, 162, 85 (1989).
22. C. J. Chu, M. P. D'Evelyn, R. H. Hauge, and J. L. Margrave, *J. Appl. Phys.*, 70, 1695 (1991).
23. W. F. Banholzer and T. R. Anthony, *Thin Solid Films*, 212, 1 (1992).
24. H. Herchen and M. A. Cappelli, *Phys. Rev. B*, 43, 11740 (1991).
25. E. S. Zouboulis and M. Grimsditch, *ibid.*, 43, 12490 (1991).
26. A. Tardieu, F. Cansell, and J. P. Petit, *J. Appl. Phys.*, 68, 3243 (1990).
27. D. S. Knight and W. B. White, *J. Mater. Res.*, 4, 385 (1985).
28. T. P. Memagh and L. G. Liu, *J. Phys. Chem. Solids*, 52, 507 (1991).
29. K. M. McNamara, K. K. Gleason, and M. W. Geis, *Mat. Res. Soc. Symp. Proc.*, 162, 207 (1989).
30. R. Colton, *The Chemistry of Rhenium and Technetium*, p. 143, Interscience Publishers, New York (1965).
31. K. B. Lebedev, *The Chemistry of Rhenium*, p. 7, Butterworths, London (1962).
32. K. M. McNamara, K. K. Gleason, D. J. Vesteyck, and J. E. Butler, *Diamond and Related Materials*, 1, 1145 (1992).



# <sup>1</sup>H NMR studies on the effects of annealing on chemical-vapor-deposited (CVD) diamond

S. Mitra and K. K. Gleason\*

Department of Chemical Engineering, Massachusetts Institute of Technology, Cambridge, MA 02139 (U.S.A.)

## Abstract

A proton nuclear magnetic resonance (<sup>1</sup>H NMR) spectrum of diamond produced by chemical vapor deposition typically exhibits both a narrow lorentzian and a broad gaussian line. The spin-lattice relaxation time constants of the two components are different in one sample and vary from sample to sample. Typical values are in the range of approximately 50 ms to 1 s. There is little or no hydrogen evolution on annealing in a nitrogen atmosphere at temperatures less than 750 °C. However,  $T_1$  increases on annealing and the line shape changes as the contribution due to the narrow component decreases. The magnetization recovers as  $M = M_0[1 - \exp(-t/T_1)^n]$ , where  $0.5 \leq n \leq 1$ . The values of  $n$  and  $T_1$  increase with annealing indicating a change in the number of relaxation centers present in the sample.

## 1. Introduction

Widespread interest in synthetic diamond was renewed with the discovery that diamond films could be deposited at low temperatures and pressures using chemical vapor deposition [1]. In most of these processes, a carbon-containing gas (typically CH<sub>4</sub> or (CH<sub>3</sub>)<sub>2</sub>CO) and hydrogen are activated by a hot filament, microwave plasma or other means. Typical growth conditions employ excess hydrogen in the gas phase and, consequently, the deposited films often contain hydrogen.

The role of hydrogen in diamond films is still not completely understood. In other electronic materials the defect sites are passivated by hydrogen, thereby improving the quality of the material [2]. For example, defect states due to dangling bonds in amorphous silicon and grain boundaries in polycrystalline silicon can be passivated by hydrogen. This reduces the number of trapping sites and thus improves the opto-electronic properties of the film. In diamond, hydrogen incorporation has been found to correlate well with the integrated intensity of the CH stretch mode in the 8–10 μm IR region and is thus detrimental to its use as an IR window material [3–5]. In addition, the electrical resistivity of diamond has been shown to be closely connected to the amount of hydrogen incorporated in the film. Landstrass and Ravi [6] have shown that on moderate annealing the resistivity increases by a few orders of magnitude. However, this change is reversible since the original values of the electrical resistivity can be recovered when

the sample is hydrogenated in a hydrogen plasma for a few hours at elevated temperatures. Consequently, the nature of the electrically active sites and the role of hydrogen in passivating these sites remain interesting problems.

Earlier studies in this laboratory on large bulk (greater than ½ carat) single-crystal natural and synthetic diamond have failed to detect measurable quantities of hydrogen due to either an absence of bulk hydrogen or long relaxation times [5]. Contrary to expectations, the  $T_1$  values for hydrogen in chemical-vapor-deposited (CVD) diamond are short. It is well known, for example, that in the absence of paramagnetic centers, typical values of  $T_1$  are very long [7–10]. However, electron spin resonance (ESR) measurements on both hot filament films [8] and microwave plasma CVD films [11] have shown that the spin density is typically about  $10^{18} \text{ cm}^{-3}$  and due to dangling bonds from unsaturated carbon bonds. This is a rather high spin count and, consequently, the relaxation mechanism via the paramagnetic centers is expected to play an important role. Initial proton nuclear magnetic resonance (<sup>1</sup>H NMR) work on diamond films has shown that most of the hydrogen in CVD films is highly segregated and resides in regions of high density. These regions are thought to be surfaces of grain boundaries or crystallites. The NMR spectrum typically consists of a narrow lorentzian and a broad gaussian component. The lorentzian line is attributed to motional narrowing of rotating methyl groups which are in close spatial proximity to the hydrogen which gives rise to the broad gaussian component [3–5]. The <sup>1</sup>H spin-lattice relaxation rates are generally less than 1 s and appear in some cases to be temperature indepen-

\*Author to whom correspondence should be addressed.

dent, suggesting that paramagnetic species are the dominant spin-lattice relaxation centers.

## 2. Experimental details

The polycrystalline CVD diamond film HF-1 was deposited in a hot filament reactor. Sample AJ-1 was prepared by d.c. arc-jet. The thickness of both of these films was greater than 100  $\mu\text{m}$ . Electron microscopy revealed that while HF-1 was multifaceted, AJ-1 showed a ball-like surface morphology. The samples were of reasonable quality as their Raman spectra exhibited a strong peak at 1332  $\text{cm}^{-1}$  with little or no graphitic component.

The NMR experiments were performed on a home-built spectrometer operating at a  $^1\text{H}$  frequency of 270 MHz. The probe was designed such that very low levels of hydrogen (approximately  $5 \times 10^{16}$ ) could be detected. During the acquisition of the NMR spectra, the NMR probe was continuously purged with nitrogen to eliminate any signal due to ambient moisture. Both the NMR line shapes and spin-lattice relaxation ( $T_1$ ) were measured at room temperature for the as-deposited films and again after each annealing step.

Since the total area under the NMR absorption spectrum is proportional to the number of spins, the hydrogen content in the diamond films can be obtained by comparison with a reference standard. Care must be taken to allow for full spin-lattice relaxation of both components before such comparisons are made.

The spin-lattice relaxation time constant  $T_1$  was measured using the saturation recovery technique [12]. In this method, a  $(90^\circ - t - 90^\circ)_n$  pulse sequence is applied and the intensity of the NMR signal is measured for various values of the recycle delay time  $t$ . The magnetic relaxation was found to deviate from a pure exponential and was thus fitted to the empirical form given by

$$M = M_0[1 - \exp(-t/T_1)^n] \quad (1)$$

where  $M_0$  is the equilibrium magnetization and  $n$  is a constant constrained to values between 0.5 and 1.0. Since paramagnetic centers produce significant time varying magnetic fields at nearby  $^1\text{H}$ , they are efficient relaxation centers. Thus spin-lattice relaxation can occur by direct interaction with a paramagnetic center. The rate of this process decreases as the separation between the  $^1\text{H}$  and the center increases. In addition,  $^1\text{H}$  far from the center can also relax indirectly by communicating with  $^1\text{H}$  close to the center via spin diffusion. The value of  $n$  in eqn. (1) determines the relative rates of direct relaxation and of spin diffusion. In the case where spin diffusion is rapid,  $n=1$  indicating a standard exponential Bloch decay. When direct relaxation to the paramagnetic center dominates, the limiting value of  $n$  is 0.5 [7–9]. Thus the

value of  $n$  is indicative of the distribution of both paramagnetic centers and the  $^1\text{H}$  nuclei.

For each value of the recycle delay time  $t$ , the NMR spectrum was fitted to a narrow lorentzian and a broad gaussian line. If the spin-lattice relaxation time for each component is the same, then the line shape of the spectrum will be independent of  $t$ . However, if they are different the line shape will be a function of  $t$ .

## 3. Results and discussion

### 3.1. Unannealed samples

A common feature in the  $^1\text{H}$  NMR spectra for all unannealed and annealed samples is the presence of a narrow lorentzian and a broad gaussian line. The linewidths at half-width at half-maximum (HWHM) for both arc-jet and hot-filament deposited samples are typically  $4 \pm 1$  kHz and  $29 \pm 2$  kHz respectively. These values can be compared with those quoted by McNamara *et al.* [3]. They obtained linewidths ranging from 1.8 to 3.3 kHz for the narrow line and 25 to 33 kHz for the broad line. The NMR line shapes of AJ-1 and HF-1 are shown in Fig. 1.

The total hydrogen content [ $H_T$ ], the spin-lattice relaxation time constants of the broad gaussian component ( $T_{1G}$ ), the total signal ( $T_{1T}$ ) and the corresponding exponential parameter  $n$  (see eqn. (1)) for the as-deposited and annealed samples are summarized in Table 1. Both samples contain less than 0.5 at.% of hydrogen with relatively short  $T_1$ .

The percentage of total hydrogen which contributes to the narrow lorentzian line [ $X_L$ ] varies in the range 40%–50% in both samples. In HF-1 this ratio is a strong function of  $t$ , the recycle delay time in the saturation recovery experiment (Fig. 1(b)). In fact, [ $X_L$ ] varies from 16% at  $t=20$  ms to a maximum of approximately 47% at  $t=2$  s. Interestingly, the narrow component of AJ-1 does not exhibit a similar dependence on  $t$ .

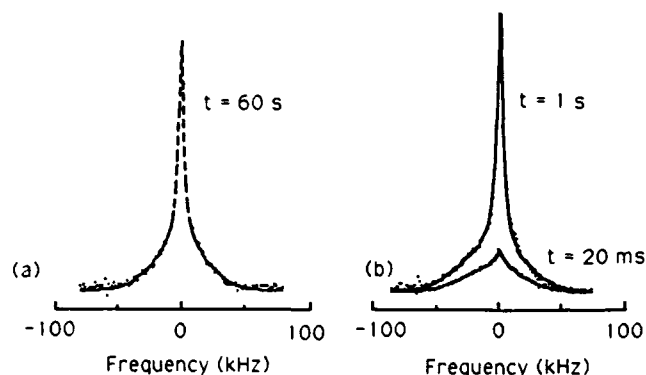


Fig. 1. Typical  $^1\text{H}$  NMR spectra of unannealed samples AJ-1 (a) and HF-1 (b). For HF-1, [ $X_L$ ] depends strongly on the recycle delay time  $t$ .

TABLE 1. Summary of NMR results on as-deposited and annealed samples. The uncertainties in  $n$  and  $T_1$  are estimated to be less than 5% and 15% respectively

Sample	Annealing temperature (°C)	[H <sub>T</sub> ] (at.%)	$n$ (gaussian)	$T_1$ (ms)	
				$T_{1G}$	$T_{1T}$
AJ-1	As-deposited	0.4	0.55	63	
	497	0.5	0.62	113	
	650	0.45	0.70	215	
	850	Trace	—	—	—
HF-1	As-deposited	0.2	0.50	50	210
	750	0.2	0.55	106	118

This systematic increase in the ratio of hydrogen giving rise to the lorentzian component reflects a longer relaxation time than its gaussian counterpart. Although not listed in Table 1, the spin-lattice relaxation time for the lorentzian component ( $T_{1L}$ ) was calculated to be approximately 0.9 s (with  $n=0.65$ ) in HF-1 and is thus much longer than the corresponding  $T_{1G}$ .

As mentioned earlier in this paper, although the total hydrogen content in the diamond films is low, it exists in regions of high density [2]. Consequently, magnetic relaxation by spin diffusion is also expected to play an important role. It is evident from the values of  $n$  (see Table 1) that the magnetization recovers as  $\exp(-t/T_1)^n$  where  $n < 1$ . This deviation from a pure exponential suggests that spin diffusion is not fast enough to equilibrate the magnetization in the entire system. Since the values of  $n$  lie between 0.5 and 0.75, it is an indication that relaxation via paramagnetic centers plays an important part. This is not surprising considering the typical spin densities expected in these samples [8, 11]. In addition to spin diffusion (which is due to homonuclear dipolar coupling) and nuclear coupling with paramagnetic centers, another source of relaxation centers is the rotating methyl groups. Since these constitute a substantial percentage of the total signal, they also play a major role. Since the rotation of the methyl groups can be slowed by lowering the temperature, a temperature-dependent  $T_1$  study should be able to differentiate between the two types of relaxation centers.

### 3.2. Effects of annealing

The total hydrogen content [H<sub>T</sub>], the spin-lattice relaxation time  $T_1$ , the parameter  $n$  and the NMR line shapes after each 2 h nitrogen anneal are summarized in Table 1. The largest change occurs in sample AJ-1 after an anneal at 850 °C. Subsequent NMR on this sample reveals that most of the hydrogen is evolved, since little or no signal can be observed even at a relatively long recycle delay time of 1 s. Visually, the sample also turns black indicating some graphitization. Interestingly, there is little or no evolution of hydrogen from any of the

samples on annealing at temperatures up to 750 °C. However, the NMR line shapes show marked changes from that of the as-deposited samples even at moderate anneal temperatures of 497 °C, indicating rearrangement of hydrogen within the system. Figure 2 shows the effect of annealing on the NMR line shapes.

Comparing the line shapes in Fig. 2 with that for the as-deposited samples (Fig. 1) shows that a clear effect of annealing is the reduction of the narrow line. This component, which comprises approximately 50% of the total signal in both AJ-1 and HF-1, decreases in strength to approximately 6%–10% after annealing at 650 °C and 750 °C respectively. Annealing also has a large effect on  $T_1$ . In order to understand the relaxation mechanism of hydrogen in diamond, only  $T_{1G}$  and its corresponding value of  $n$  are considered in the following analysis.

In both AJ-1 and HF-1,  $T_{1G}$  and  $n$  increase after each annealing step. The correlation between  $n$  and the spin-lattice relaxation time of the gaussian component is demonstrated in Fig. 3. An increase in  $n$  suggests that

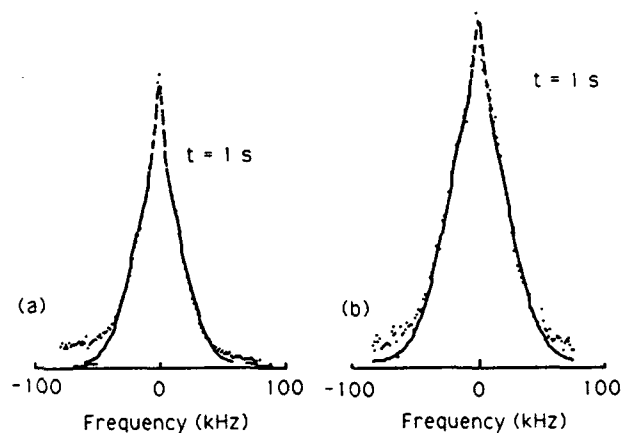


Fig. 2. Effect of a 2 h anneal on the NMR line shapes of samples AJ-1 (a) at 650 °C and HF-1 at 750 °C (b) (note the decrease in the intensity of the narrow component).

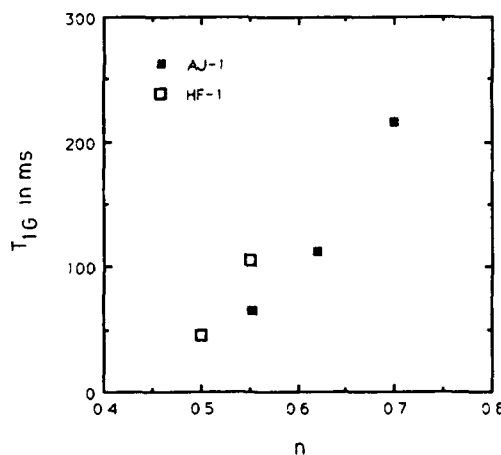


Fig. 3. The dependence of  $T_{1G}$  on  $n$ .

relaxation by spin diffusion becomes increasingly important. This speculation is further supported by the corresponding rise in  $T_{1G}$  which suggests that the number of relaxation centers (paramagnetic centers and/or rotating

$\text{CH}_3$  groups) decreases with annealing. Thus, on annealing, hydrogen from the methyl groups may become available to passivate unsaturated carbon bonds resulting in fewer paramagnetic centers and longer  $T_{1G}$ . The preferential breaking of  $-\text{CH}_3$  is not surprising. Thermal desorption experiments on hydrogenated amorphous silicon, for example, clearly indicate that  $\text{SiH}_3$  bonds are broken at a much lower temperature than  $\text{SiH}$  bonds [13]. In addition, the products formed during the loss of hydrogen from the rotating methyl groups will be static. Consequently, the hydrogen that originally gave rise to the narrow NMR line shape now contributes to the broad component. This redistribution of hydrogen preserves the total signal intensity. Thus while both  $T_{1G}$  and  $n$  increase,  $[\text{H}_T]$  remains unchanged.

Previous work has suggested that the hydrogen in these films is highly segregated and resides on two-dimensional surfaces such as grain boundaries [3–5]. Since grain boundaries are areas of high defect density, they contain a large number of carbon dangling bonds which are easily saturated by mobile H atoms (from broken methyl groups).

These observations are consistent with the trends observed in HF-1, which also shows a similar connection between  $n$  and  $T_{1G}$ . A comparison between the as-deposited and 750 °C annealed sample shows that while  $[\text{H}_T]$  remains constant, both  $T_{1G}$  and  $n$  increase on annealing. The value of  $[X_L]$  decreases from about 47% to about 8% and is independent of  $t$ .

#### 4. Conclusions

We have shown that moderate annealing below the deposition temperature leads to the rearrangement of hydrogen atoms which are present in synthetic CVD diamonds. The relaxation of magnetization varies from

the standard exponential Bloch decay. On annealing, the intensity of the narrow component decreases. This decrease is accompanied by a corresponding increase in both  $n$  and  $T_{1G}$ . Since grain boundaries are regions of high defect density, and most of the hydrogen is likely to reside in this region, it is thought that hydrogen from the broken methyl groups becomes available to passivate the carbon dangling bonds. This redistribution of hydrogen is observed even at moderate annealing temperatures.

#### Acknowledgments

This work was supported by a grant from the Office of Naval Research. We wish to thank Dr. Kevin Gray (Norton Co.) and Dr. Cliff Robinson (Raytheon Corporation) for supplying the samples and Ms. Elizabeth Oh for technical help in the laboratory.

#### References

- 1 P. K. Bachmann, D. Leers and H. Lydtin, *Diamond Relat. Mater.*, **1** (1991) 1.
- 2 T. Shimizu, *J. Non-Cryst. Solids*, **59, 60** (1983) 117.
- 3 K. M. McNamara, D. H. Levy, K. K. Gleason and C. J. Robinson, *Appl. Phys. Lett.*, **60** (1992) 580.
- 4 K. M. McNamara, K. K. Gleason and C. J. Robinson, *J. Vac. Sci. Technol. A*, **10** (1992) 3143.
- 5 D. H. Levy and K. K. Gleason, *J. Phys. Chem.*, **96** (1992) 8125.
- 6 M. I. Landstrass and K. V. Ravi, *Appl. Phys. Lett.*, **55** (1989) 1391.
- 7 M. J. R. Hoch and E. C. Reynhart, *Phys. Rev. B*, **37** (1988) 9222.
- 8 J. M. Redwing, T. W. Root and W. F. Banholzer, *J. Appl. Phys.*, submitted for publication.
- 9 P. M. Henrich, M. L. Colfield, R. H. Young and J. M. Hewitt, *J. Magn. Res.*, **58** (1984) 85.
- 10 M. J. Duijvestijn, C. Van Der Lugt, J. Smidt, R. A. Wind, K. W. Ziln and D. C. Staplin, *Chem. Phys. Lett.*, **102** (1983) 25.
- 11 I. Watanabe and K. Sugata, *Jpn. J. Appl. Phys.*, **27** (1988) 1808.
- 12 E. Fukushima and S. B. W. Roeder, *Experimental Pulse NMR: A Nuts and Bolts Approach*, Addison-Wesley, Reading, MA, 1981, p. 168.
- 13 J. A. McMillan and E. M. Peterson, *J. Appl. Phys.*, **50** (1979) 5238.

## Analysis of Fluorocarbon Plasma-Treated Diamond Powders by Solid-State Fluorine-19 Nuclear Magnetic Resonance

Bruce E. Scruggs and Karen K. Gleason\*

Department of Chemical Engineering, Massachusetts Institute of Technology, Cambridge, Massachusetts 02139

Received: March 1, 1993; In Final Form: June 17, 1993<sup>o</sup>

In this work, solid-state  $^{19}\text{F}$  NMR has been used to characterize fluorine on diamond powder surfaces after  $\text{CF}_4$  and 98%  $\text{CF}_4/2\%$   $\text{O}_2$  radio-frequency plasma treatment. The fluorine surface coverage of the pure  $\text{CF}_4$  treated powder was  $7.1 \times 10^{14}$  F/cm<sup>2</sup> while the other plasma yielded a much lower coverage,  $7.4 \times 10^{13}$  F/cm<sup>2</sup>. In both cases, only  $\text{CF}_x$  ( $x = 1-3$ ) functionalities were observed with the majority species being carbon monofluoride. Only 5–10% of the fluorine was bonded as  $\text{CF}_3$ . With high-speed magic-angle spinning, isotropic chemical shifts were resolved and assigned relative to  $\text{CFCl}_3$  as follows:  $\text{CF}$ ,  $148 \pm 1$  ppm;  $\text{CF}_2$ ,  $106 \pm 2$  and 123 ppm;  $\text{CF}_3$ ,  $78 \pm 1$  ppm. The peak at 123 ppm was only observed in the  $\text{CF}_4/\text{O}_2$  plasma-treated sample and is speculated to be the result of atomic fluorine etching of diamond. In this sample, the loss of spectral intensity at lower chemical shifts with storage time indicates the loss or rearrangement of  $\text{CF}_2$  and  $\text{CF}_3$ . NMR line shape broadening and variation in spin-lattice relaxation with decreasing temperature indicate the  $\text{CF}_x$  groups possess some degree of motion in addition to the rotation of  $\text{CF}_3$  groups about the  $\text{C}_3$  axis. This suggests amorphous fluorocarbon deposition, since  $\text{CF}$  and  $\text{CF}_2$  on crystalline diamond surfaces are expected to be essentially static. Multiple-quantum NMR indicates that fluorine coverage is not uniform. Some fluorine is relatively dispersed on the order of  $\sim 5$  Å while the remaining fluorine occurs in aggregates of greater than 40 nuclei. This is consistent with preferential deposition or reaction occurring at and around surface defects. Finally, these results may serve as a basis for reference in studying fluorine by NMR in fluorinated chemical vapor deposition diamond materials provided a sufficient amount of material is deposited.

### Introduction

Synthetic diamond films have typically been grown from an activated gas phase of dilute hydrocarbons, such as methane or acetylene, in hydrogen by a chemical vapor deposition (CVD) type process.<sup>1,2</sup> Diamond has also been formed from reactant mixtures which include carbon, hydrogen, and fluorine.<sup>3,4</sup> Recently, diamond films were grown on various non-diamond substrates at temperatures as low as 250 °C from a heated gas phase containing some fluorine.<sup>5</sup> This last work demonstrates the potential for fluorine-assisted diamond deposition on substrates of relatively low thermal stability, such as polymeric materials and electronic devices.

In addition, fluorine-treated diamond surfaces are of technological importance. Fluorination of diamond surfaces can enhance the chemical inertness and can potentially lower the coefficient of friction relative to unfluorinated diamond.<sup>6</sup> Recent studies have examined the oxidative resistance of fluorinated diamond materials.<sup>7,8</sup> Also, the electrical characteristics of a Schottky diode made from diamond have been altered by different plasma surface fluorination treatments.<sup>9</sup> The surface leakage current of the diode was decreased by a factor of 10 in going from diamond treated by a pure  $\text{CF}_4$  plasma to one treated by a 98%  $\text{CF}_4/2\%$   $\text{O}_2$  plasma. Thus, the state of fluorine on diamond surfaces influences the surface properties, impacting technological applications.

A variety of theoretical and experimental studies have been conducted to understand the chemical state of fluorine in diamond materials. Thermodynamic calculations focused on the growth of diamond from a fluorinated diamond(111) surface indicate the necessity of atomic hydrogen in the reactant mixture to sustain crystal growth.<sup>10</sup> In another theoretical study, the passivation of a diamond(100) surface by fluorine was done to examine ways in which surface carbon atoms could maintain  $\text{sp}^3$  hybridization.<sup>11</sup>

X-ray photoelectron spectroscopy (XPS) has been very useful for experimental characterization of fluorinated diamond surface states. The carbon 1s XPS peak displays large energy shifts on the order of 1–3 eV as a function of the number of fluorines bonded to the carbon.<sup>12</sup> XPS was used to identify a C–F terminated diamond surface grown from a  $\text{CF}_4/\text{H}_2$  plasma.<sup>3</sup> XPS has also been used in studies to evaluate a diamond surface after a variety of fluorination treatments designed to modify the surface properties of the diamond.<sup>13–15</sup> For example, atomic fluorine was found to react with the diamond(100) surface to yield a C–F terminated surface while molecular fluorine only reacts very slowly.<sup>13</sup>

In other research utilizing other analytical spectroscopies, secondary ion mass spectrometry (SIMS) has been used to quantify the average bulk concentration of fluorine in synthetic diamond. For example, SIMS indicates increasing fluorine content in diamond films made with higher  $\text{CF}_4$  concentrations in the gas-phase plasma.<sup>4</sup> Surface-sensitive infrared (IR) spectroscopy, specifically diffuse reflectance, was used to monitor the formation of fluorine functionalities on the surface of diamond powders as a function of plasma fluorination treatments.<sup>8</sup>

The objective of this work is to demonstrate the variety of information regarding fluorine in diamond materials which is available from solid-state  $^{19}\text{F}$  NMR experiments. Due to the relatively low sensitivity of NMR, a significant sample size is required. We have initially chosen to study fluorine coverage on diamond powder surfaces treated in pure  $\text{CF}_4$  and 98%  $\text{CF}_4/2\%$   $\text{O}_2$  radio-frequency plasmas, where the powder has a high surface area to volume ratio. The chemical state and environment of fluorine can be evaluated by NMR experiments analogous to studies of hydrogen in diamond materials by solid-state  $^1\text{H}$  NMR spectroscopy. In addition,  $^{19}\text{F}$  NMR is sensitive to fluorine in both the bulk and surface of a material. Thus, NMR could potentially be used to study fluorine at the crystalline grain boundaries of CVD diamond films. This information is most likely unobtainable by XPS and SIMS. The only stipulation, of

\* To whom correspondence should be addressed.

<sup>o</sup> Abstract published in *Advance ACS Abstracts*, August 15, 1993.

**TABLE I: Typical Chemical Shift Anisotropy for CF<sub>x</sub> Groups Bound to Carbon**

CF <sub>x</sub> group	$\Delta\sigma^a$ (ppm)	pattern shape
CF	100 <sup>b</sup>	axial
CF <sub>2</sub> (motionally averaged)	50–100 <sup>c,d</sup>	axial
CF <sub>2</sub> (static)	120–140 <sup>d,e</sup>	asymmetric
CF <sub>3</sub> (rotation about C <sub>3</sub> axis)	75 <sup>d</sup>	axial
CF <sub>3</sub> (static)	150 <sup>d</sup>	asymmetric

<sup>a</sup>  $\Delta\sigma = |\sigma_{11} - \sigma_{33}|$ , where  $\sigma_{11}$  and  $\sigma_{33}$  are the smallest and largest of the three principal components of the  $\sigma$  tensor. <sup>b</sup> Estimated from fluorinated graphite. <sup>c</sup> Dybowski, C. In *Solid State NMR of Polymers*; Mathias, L., Ed.; Plenum Press: New York, 1991; Chapter 1. <sup>d</sup> Vega, A. J.; English, A. D. *Macromolecules* 1980, 13, 1635. <sup>e</sup> Mehring, M.; Griffin, R. G.; Waugh, J. S. *J. Chem. Phys.* 1971, 55 (2), 746.

course, is that a significant amount of fluorine must exist in any particular environment for an NMR study to be useful.

Essentially, the same kinds of experiments which can be performed in solid-state proton NMR can be done in fluorine NMR.<sup>16,17</sup> Fluorine exists in nature as a 100% abundant, spin  $1/2$  nucleus, <sup>19</sup>F, having a magnetogyric ratio  $\gamma = 4.005$  kHz/G and, hence, high sensitivity, 83% relative to <sup>1</sup>H.<sup>17</sup> However, unlike <sup>1</sup>H, changes in the short-range bonding environment, order one bond, can induce large <sup>19</sup>F isotropic chemical shifts. Fluorine displays a total chemical shift range on the order of several hundred parts/million (ppm), while for <sup>1</sup>H this range is  $\sim 10$  ppm. We expect the main species in plasma fluorination of diamond powder to be CF<sub>x</sub> ( $x = 1$ –3) species where the carbon is bound to other carbon. As  $x$  increases, the fluorine electronic shielding is decreased, causing a decrease in the isotropic chemical shift. Typically, CF and CF<sub>3</sub> isotropic shifts differ by approximately 70 ppm.

Fluorine nuclei also typically display a large anisotropic component to the chemical shift. In the absence of isotropic reorientation, powders containing CF<sub>x</sub> will show a chemical shift anisotropy (CSA) powder pattern based on the orientation dependence of fluorine's electronic shielding tensor,  $\bar{\sigma}$ , with the imposed magnetic field,  $B_0$ . In Table I, the typical width and shape of the CSA powder patterns are characterized for CF<sub>x</sub> groups. Within a certain band of motional narrowing, CF<sub>2</sub> and CF<sub>3</sub> groups show axial patterns. As motions are reduced or frozen with the lowering of temperature, CF<sub>2</sub> and CF<sub>3</sub> patterns change shape and the CSA width increases. For a sample containing a single type of CF<sub>x</sub> group, the CSA pattern behavior may be enough to characterize that group. However, when a variety of CF<sub>x</sub> groups are present, the superposition of CSA powder patterns will obscure their identification, since the width of the powder patterns is greater than differences in isotropic chemical shift between CF<sub>x</sub> groups. We anticipate that fluorinated diamond surfaces may contain a combination of CF<sub>x</sub> species, where CF and CF<sub>2</sub> groups are essentially static at room temperature while CF<sub>3</sub> rotates about the C<sub>3</sub> axis displaying an axial CSA pattern. If fluorinated carbon deposits on the surface, we might expect additional modes of motion for the CF<sub>x</sub> species as observed in Teflon and other fluorinated polymers. As the temperature is lowered, these motions will freeze out, resulting in an increase in the CSA line broadening. Also, <sup>19</sup>F–<sup>19</sup>F dipole broadening will be increased since the dipole coupling will not be motionally averaged.

While the static fluorine spectra can be quite convoluted, the total fluorine content of the sample can easily be obtained from the total area of the line shape. Through high-speed magic-angle-spinning experiments,<sup>17</sup> the CSA powder pattern can be averaged and information on the number of CF<sub>x</sub> components and their identity may be achieved. In addition, magnetization relaxation experiments<sup>18</sup> can be performed to gain information on motional dynamics and fluorine environment.

The more advanced solid-state NMR technique, multiple-quantum NMR (MQ-NMR), has been used to ascertain magnetic

**TABLE II: Radio-Frequency Plasma (13.56 MHz) Treatment Conditions**

	diamond 1 (D1)	diamond 2 (D2)
plasma composition	100% CF <sub>4</sub>	98% CF <sub>4</sub> /2% O <sub>2</sub>
pressure (Torr)	1	1
treatment time (min)	10	10
rf power (W)	200	200

nuclei segregation. Solid-state MQ-NMR has been used to evaluate the state of a spin  $1/2$  dipole coupled network in materials on a maximum length scale of about 20 Å.<sup>19</sup> During this experiment, spin  $1/2$  nuclei are induced to participate in multiple spin correlations through strong dipole coupling interactions.<sup>20</sup> As the experimental excitation time is increased, weaker dipole couplings can be utilized to form larger spin correlations occurring over greater distances within the material. The distance of 20 Å simply represents the upper limit over which dipole couplings become negligible on experimental time scales currently obtainable.

If the number of spin  $1/2$  nuclei in strong dipolar communication is small (order 50 or less), then MQ-NMR can be used to quantify the number of nuclei in this finite dipole coupling network.<sup>21</sup> Finite dipole coupling networks have been identified in hydrogenated amorphous silicon<sup>22</sup> and in zeolites<sup>23</sup> and on catalyst particles<sup>24</sup> with isolated organic adsorbates.

Alternatively, if the number of spin  $1/2$  nuclei in strong dipolar communication is large (order 1000 or more), then multiple spin correlations will grow without bound as a function of excitation time.<sup>25</sup> The rate of multiple spin correlation is a function of the connectivity of the dipole coupling network.<sup>26,27</sup> Spin networks having larger numbers of nearest neighbors to a given nuclear site will form spin correlations at a greater rate than those with smaller numbers of nearest neighbors. Thus, on very small length scales, MQ-NMR can differentiate between a 3-dimensional network of spins, specifically nuclei distributed throughout the bulk of a material, and a 2-dimensional network, such as nuclei terminating the surface of a crystal.<sup>27</sup> Analogous results have been observed in "quasi-1-dimensional" distributions of protons in hydroxyapatite.<sup>28</sup>

Hence, through NMR experiments, we can determine the total fluorine content of the sample, identify the predominant fluorine groups, and monitor the motional dynamics of fluorine groups through variation of the sample temperature. In addition, through MQ-NMR experiments, the segregation of fluorine in diamond can be studied by probing the connectivity of the fluorine dipole-coupling network.

### Experimental Section

Natural diamond powder (99.9%) was obtained from Johnson Matthey/Aesar with a size classification of  $< 1$   $\mu$ m, indicating that the powder had been passed through a 1- $\mu$ m-mesh sieve. Significant area available for plasma treatment is required to provide sufficient signal to noise in NMR experiments. Two fluorocarbon plasma mixtures were used to treat the diamond powder. The powder was contained in a bottle roughly 1 cm in diameter, and the particle bed was approximately 1.5 cm deep. Plasma processing conditions are summarized in Table II. Prior to treatment, the available surface area was determined by the Brunauer–Emmett–Teller (BET) method<sup>29</sup> by Micromeritics Instrument Corp. of Norcross, GA. Other characterization was done using SEM to examine particle size and shape and XPS.

All static and MQ-NMR experiments were carried out on a home-built spectrometer operating at an <sup>19</sup>F Larmor frequency of 280.8 MHz. The sample probe was also home-built with a static coil roughly 7 mm in diameter by 25 mm in length and variable low-temperature capability. Controlled temperatures as low as 80 K have been obtained using cooled N<sub>2</sub> and a Lakeshore DRC-91C temperature controller. The  $\pi/2$  pulse time for all

experiments was set to approximately 1.6  $\mu$ s with a typical probe ringdown of 6  $\mu$ s, although the ringdown is somewhat temperature dependent. The total fluorine content of diamond samples was obtained by comparison of the total signal area to a calibration curve which was generated using poly(tetrafluoroethylene) (Aldrich) samples of known mass. Sample mass for NMR analysis was on the order of 1 g. The limit of detection, which is set by signal to noise considerations, is on the order of  $10^{17}$  F/sample on the home-built static probe and spectrometer. The longitudinal relaxation behavior ( $T_1$ ) was observed with the inversion recovery experiment.<sup>30</sup> Spin-echo experiments<sup>30</sup> to evaluate the homonuclear  $^{19}\text{F}$  dipole coupling strength were done with an echo delay of roughly 12  $\mu$ s and CYCLOPS detection<sup>31</sup> to attenuate zero noise. Unless otherwise indicated, all data were collected on samples at least 2 months after sample treatment.

The spectrometer is equipped with a digitally-controlled, variable-phase synthesizer to perform solid-state MQ-NMR experiments. The eight  $\pi/2$  pulse, even multiple-quantum (MQ) order selective sequence employed for this experiment has been described in previous studies.<sup>21,32</sup> The incremental spin preparation cycle time,  $\tau_c$ , was set at 31.2  $\mu$ s to compensate for off-resonance effects as much as possible. Phase cycling was typically done with 32 phase shifts, allowing detection of up to  $\pm 16$  MQ coherence orders. The effective number of spins correlated,  $N(\tau)$ , where  $\tau$  is the total preparation time, was obtained from a Gaussian fit to the nonzero MQ coherence intensities assuming a statistical analysis.<sup>21</sup> To allow for more extensive signal averaging, data at the longest excitation time,  $\tau = 218.4 \mu$ s, were collected using only the first 32 phase shifts of a 64 shift phase cycling experiment. The data were symmetrized and  $N(\tau)$  was evaluated. Similar analysis on data taken at shorter  $\tau$  indicates little influence on the value of the number of correlated spins. MQ-NMR experiments were performed at  $T = 150$  K to improve signal-to-noise considerations as well as to minimize the effects of molecular motion on the spectra.

High-speed magic-angle-spinning (MAS)<sup>17</sup> spectra were obtained on a Bruker AMX-400, with a fluorine field strength of 376.5 MHz, by Dr. Doug Burum of Bruker Instruments. The sample probe was operated with a  $\pi/2$  pulse time of 3.5  $\mu$ s at a rotor spinning speed of 15 kHz. It was also necessary to subtract a probe background signal to obtain reasonable sample spectra.

## Results and Discussion

**Surface Concentration of  $^{19}\text{F}$ .** Significant surface area available for plasma treatment is required to provide sufficient signal to noise for NMR experiments. Assuming a diamond powder of monodisperse 1- $\mu$ m cubes, this powder would have a surface area per mass of  $1.5 \times 10^4 \text{ cm}^2/\text{g}$ . The BET measurement of the surface area using krypton yields a value of  $9.8 \times 10^4 \text{ cm}^2/\text{g}$ . SEM analysis of the powder indicates irregularly-shaped particles on the order of a micron or smaller, which is consistent with a BET surface area measurement higher than the calculated value.

XPS analysis was done on diamond powders before and after plasma treatment. Since the particle surfaces are at random orientations to the X-ray beam, it is not possible to orient the sample such that the surface sensitivity is maximized. Consequently, while we could detect the presence of fluorine in plasma-treated powders from the appearance of the F 1s signal, identification of fluorine species through shifts in the C 1s peak was not possible.

The room temperature  $^{19}\text{F}$  free induction decay (FID) NMR spectra for samples D1 (100%  $\text{CF}_4$  plasma) and D2 (98%  $\text{CF}_4$ /2%  $\text{O}_2$  plasma) are shown in Figure 1. The range of shifts displayed is consistent with  $\text{CF}_x$  groups. Both samples show spectral features centered at 65 ppm and in the range 140–150 ppm. The complexity of the spectrum of sample D1 in the range 140–150 ppm clearly shows that these line shapes cannot be described by a single fluorine CSA powder pattern convoluted with dipolar broadening.

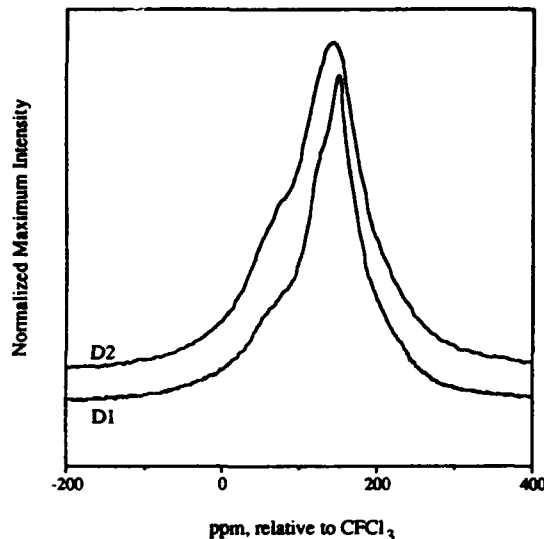


Figure 1. Room temperature free induction decay  $^{19}\text{F}$  NMR spectra of plasma-treated diamond powders, D1 and D2. The chemical shift axis in ppm is relative to the fluorine of  $\text{CFCF}_3$ . The peak intensity has been normalized to one.

TABLE III: High-Speed MAS  $^{19}\text{F}$  Spectra of Plasma-Treated Diamond Powders

sample	$\sigma_{\text{iso}}$ (ppm)	fwhh <sup>a</sup> (ppm)	% of total signal	sample	$\sigma_{\text{iso}}$ (ppm)	fwhh <sup>a</sup> (ppm)	% of total signal
D1	79	6	$5 \pm 5$	D2	78	5	$10 \pm 5$
	105	12	$25 \pm 5$		107	14	$15 \pm 5$
	148	$\leq 2$	$70 \pm 5$		123	14	$20 \pm 5$
					149	2	$55 \pm 5$

<sup>a</sup> Full width at half-height.

The fluorine content is obtained from the integrated NMR signal. The total fluorine content was  $7.0 \times 10^{19}$  F/g for sample D1 and  $7.3 \times 10^{18}$  F/g for sample D2. The fluorine content of D2 was determined from a spectrum taken within roughly a week of treatment. Thus, the fluorine content per unit surface area is equal to  $7.1 \times 10^{14}$  F/ $\text{cm}^2$  for D1 and  $7.4 \times 10^{13}$  F/ $\text{cm}^2$  for D2. The unreconstructed surface bond density of diamond is a function of the crystal face and is equal to  $3.1 \times 10^{15}$  bonds/ $\text{cm}^2$  for the (100) face,  $2.2 \times 10^{15}$  bonds/ $\text{cm}^2$  for the (110) face, and  $1.8 \times 10^{15}$  bonds/ $\text{cm}^2$  for the (111) face. Not all of these bonds may be available for fluorine chemisorption due to steric repulsive forces on the (100)<sup>25</sup> and the (110) faces. Since the C–F bond is most likely normal to the (111) face, little repulsion is anticipated on this crystal face for CF groups; however, more fluorinated carbon species like  $\text{CF}_3$  may encounter steric repulsion. The result is that the average bond density available for fluorine chemisorption will be somewhat less than the average bond density calculated from the unreconstructed crystal faces. With this stipulation aside, the coverage of sample D1 is roughly half of the average bond density of diamond, while the coverage of D2 is 10 times less than D1 as a result of 2%  $\text{O}_2$  addition to the plasma.

**Chemical Bonding Configurations.** If the primary broadening mechanisms of the NMR line shapes in Figure 1 are based on nuclear dipole coupling and CSA powder patterns, then high-speed magic-angle spinning should scale these interactions, allowing us to resolve individual isotropic chemical shifts. Figure 2, a and b, shows the high-speed MAS spectra of samples D1 and D2, respectively. The irregular base line in Figure 2b is probably the result of background subtraction. Table III summarizes the number of isotropic shifts, their full width at half-height (fwhh), and an estimate of the percent of the total signal each component comprises for the MAS spectra. There is good agreement between the isotropic chemical shifts,  $\sigma_{\text{iso}}$ , and line widths (fwhh) for the

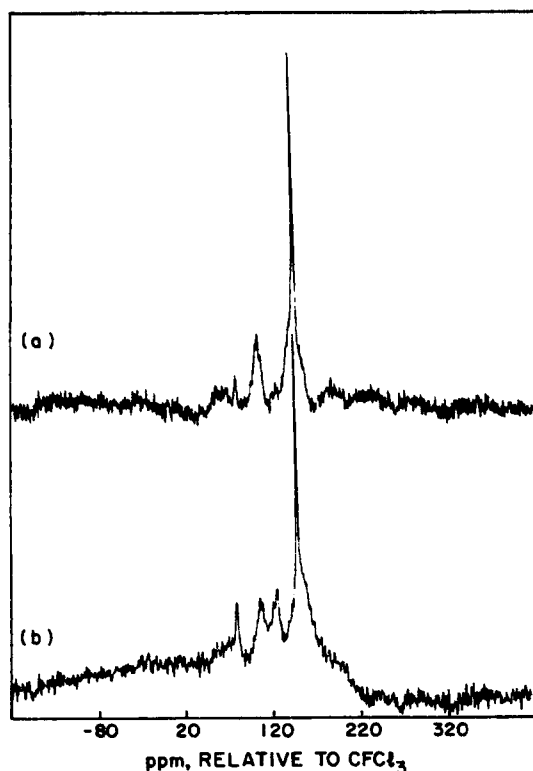


Figure 2. Room temperature high-speed (15 kHz) MAS  $^{19}\text{F}$  NMR spectra of plasma-treated diamond powder samples: (a) D1; (b) D2, after subtraction of probe background. The intensity of the spectra is in arbitrary units.

TABLE IV: Isotropic Chemical Shifts of Selected Fluorine Species in ppm

chemical species <sup>a</sup>	typical $\sigma_{\text{iso}}$ range <sup>b</sup>	chemical species <sup>a</sup>	typical $\sigma_{\text{iso}}$ range <sup>b</sup>
$\text{FOCR}_3$	-150 to -147	$\text{F}_2\text{CR}$	50 to 100
$\text{FC(O)R}$	-50 to -40	$\text{F}_2\text{CR}_2$	90 to 140
$\text{FC(O)OR}$	7 to 20	$\text{FCR}_3$	130 to 180

<sup>a</sup> R is carbon with  $\text{sp}^3$  hybridization. <sup>b</sup> Compiled from: Dungan, C. H.; Van Wazer, J. R. *Compilation of Reported  $^{19}\text{F}$  NMR Chemical Shifts*; Wiley-Interscience: New York, 1970. Wray, V. *Annu. Rep. NMR Spectrosc.*; Academic Press: London, 1980; Vol. 10B.

three species observed in D1 and the corresponding values for three of the four resonances observed in D2. To determine the type of fluorine signals observed, we compare the isotropic shifts of treated diamond to those listed in Table IV. The R group of these fluorine species represents a bond to carbon in the  $\text{sp}^3$ -hybridized state. Typical chemical shifts of oxygenated species such as fluoride esters, acyl fluorides, and hypofluorites fall far below the chemical shifts observed in D1 and D2. Based on the typical shift ranges of Table IV, the following assignments are made for the two diamond powders:  $\text{CF}_3$ ,  $78 \pm 1$  ppm;  $\text{CF}_2$ ,  $106 \pm 2$  ppm;  $\text{CF}$ ,  $148 \pm 1$  ppm. The 123 ppm peak is also likely to be assigned to a  $\text{CF}_2$  bonding configuration. Further support for shift assignments comes from the fwhh of the peaks. We expect that fluorine signals in similar environments, such as  $\text{CF}_2$ , should display similar line shape broadening under MAS conditions. Indeed, the  $\text{CF}$ ,  $\text{CF}_2$ , and  $\text{CF}_3$  peaks in both samples as assigned above have fwhh of  $2 \pm 1$ ,  $13 \pm 1$ , and  $6 \pm 1$  ppm, respectively. Thus, the similar line widths ( $13 \pm 1$  ppm) of the peaks at 107 and 123 ppm in D2 support the 123 ppm assignment as a  $\text{CF}_2$  group.

We also observed a loss of intensity of the feature at around 65 ppm in broad-line free induction decay (FID) NMR spectra of sample D2 comparing spectra taken within days after plasma treatment and 2 months later (Figure 3). These spectra have

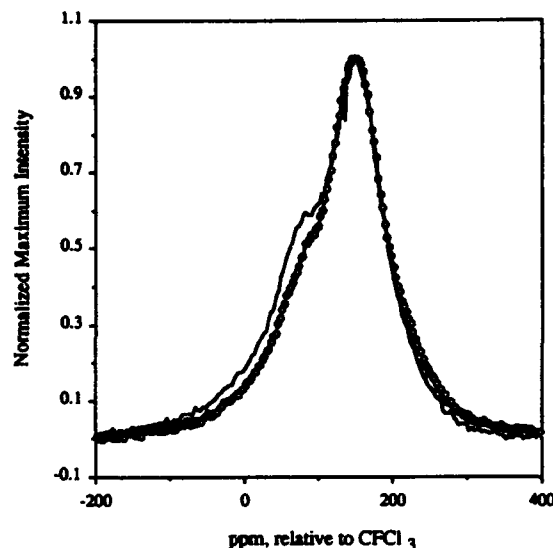


Figure 3. Room temperature FID  $^{19}\text{F}$  NMR spectra of sample D2 treated in a 98%  $\text{CF}_4$ /2%  $\text{O}_2$  plasma. The solid line spectrum was acquired a few days after treatment, while the spectrum outlined by open circles was acquired 2 months later. Both are normalized at their maximum intensity.

been plotted by normalizing the maximum intensity since the later spectrum was not taken under calibrated conditions. However, the sample was contained in an epoxy-sealed glass tube. This loss of intensity of the high-frequency shoulder feature would be consistent with rearrangement of sterically hindered  $\text{CF}_3$  (78 ppm) groups;<sup>10</sup> however, it may involve other  $\text{CF}_x$  species as well. Unfortunately, the first NMR data on sample D1 were acquired weeks after plasma treatment so that aging effects could not be examined in this sample.

So far, the total fluorine content and types of  $\text{CF}_x$  groups present have been investigated. The amount of fluorine in D1 is 10 times greater than on D2 and would cover roughly half of the available bonding sites if uniform coverage is assumed. The majority of fluorine in both samples exists as  $\text{CF}$  groups, approximately 70% in D1 and 55% in D2. In a previous study, carbon monofluorides were the primary result of  $\text{CF}_4$  and 5%  $\text{CF}_4/\text{Ar}$  plasma treatments of diamond powder as determined by IR spectroscopy.<sup>8</sup> The remaining fluorine is primarily in the  $\text{CF}_2$  state with 5–10% bonded as  $\text{CF}_3$ . One additional fluorine signal assigned to a  $\text{CF}_2$  group is found in D2 (98%  $\text{CF}_4$ /2%  $\text{O}_2$ ) which is not in D1 (100%  $\text{CF}_4$ ). Note that this peak at 123 ppm could not be attributed to oxygenated fluorocarbon species (Table IV). One plausible explanation might be that the carbon bonded to fluorine could occupy two different types of bonding sites on the diamond surface. Each type of bonding site could result in a different amount of bond strain to the carbon in the  $\text{CF}_2$  unit, causing the chemical shift difference observed between  $\text{CF}_2$  units.

**Molecular Motion.** Motion of fluorinated species on the diamond powder surfaces is evidenced in Figure 4, a and b, where the FID spectra of D1 and D2, respectively, are overlaid as a function of temperature. The broadening of these spectra with decreasing temperature suggests the loss of motional degrees of freedom of fluorine-bonded carbons. The increase in fwhh for both samples in going from 298 to 150 K is roughly 20 kHz. No further significant changes in spectra were observed for either sample upon cooling below 150 K.

One of the contributions to line broadening is an increase in  $^{19}\text{F}$ - $^{19}\text{F}$  dipole coupling as the motionally-averaged couplings become static. This contribution is shown with spin echo experiments which eliminate broadening interactions which are linearly proportional to the  $z$  component of spin angular momentum, such as the chemical shift anisotropy (CSA). The broadening of the remaining line shape depends on the homonuclear dipole coupling, which is bilinear in  $z$  angular momentum.



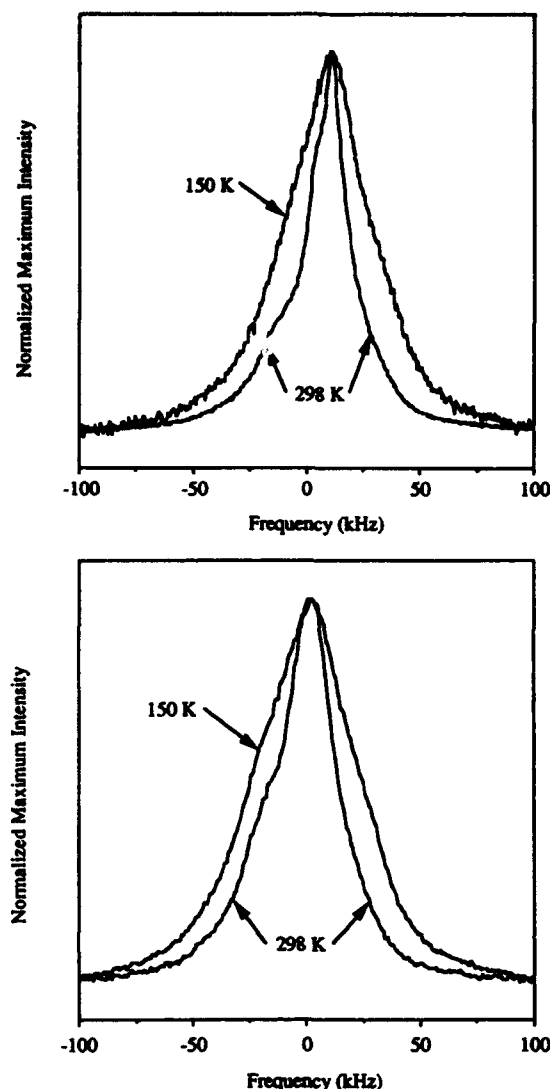


Figure 4. Variable-temperature free induction decay  $^{19}\text{F}$  NMR spectra of plasma-treated diamond powders. The abscissa is now in frequency units (kHz) to indicate the extent of broadening as a function of temperature. All peak intensities have been normalized to one. (a, top) D1; (b, bottom) D2.

Table V shows the temperature dependence of the  $^{19}\text{F}$ – $^{19}\text{F}$  dipolar field strength,  $M_2^{1/2}$ , the root of the dipole coupling second moment. At room temperature, the spin echo line shapes are best described by Lorentzians which are characteristic of a spin system undergoing motion.<sup>18</sup> For a Lorentzian,  $M_2^{1/2}$  can only be defined over some truncated range of frequency which we define as  $\pi$ -hwhh such that  $M_2^{1/2} = \text{hwhh}$ .<sup>16</sup> As samples are cooled, the spectra behave in a more Gaussian fashion having zero intensity in the high-frequency wings of the line shape, indicating that motion has been frozen. From Van Vleck's equation,<sup>18</sup> the values of  $M_2^{1/2}$  for D1 and D2 at 150 K are comparable to values calculated for static  $\text{CF}_2$  and  $\text{CF}_3$  groups which are 6.9 and 9.8 kHz, respectively. However, the increase in homonuclear fluorine dipole coupling cannot completely account for the amount of broadening observed at low temperatures in Figure 4.

Accompanying increases in the fluorine dipole coupling strength will also be increases in the width of the CSA powder pattern. At 273 K, the trifluoromethyl group of  $\text{CF}_3\text{COOAg}$  displays an axial CSA pattern with an absolute shift range of 21 kHz at a magnetic field strength of 281 MHz. At 83 K after the methyl rotation is frozen, the CSA pattern assumes an asymmetric shape with an absolute shift range of 38 kHz.<sup>33</sup> The static transition occurs at roughly 160 K. Similar CSA broadening has been

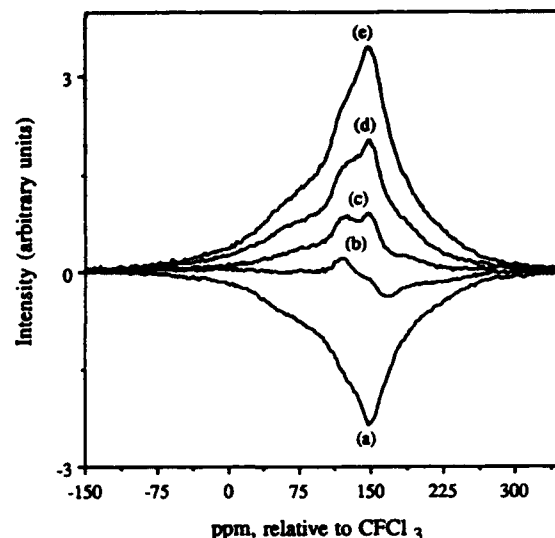


Figure 5.  $T_1$  inversion recovery of sample D1 at 298 K. The inversion recovery delay,  $\tau$ , is as follows: (a) 0.001, (b) 0.03, (c) 0.1, (d) 0.4, and (e) 10.0 s.

TABLE V: Dipolar Field Strength of Diamond Samples as a Function of Temperature

temp (K)	D1 $M_2^{1/2}$ (kHz)	D2 $M_2^{1/2}$ (kHz)	temp (K)	D1 $M_2^{1/2}$ (kHz)	D2 $M_2^{1/2}$ (kHz)
298	5.0 <sup>a</sup>	5.0 <sup>a</sup>	110	8.0	
150	6.6	7.1	100		8.0

<sup>a</sup> Lorentzian truncated at a bandwidth equal to  $\pi$ -hwhh (hwhh = half-width at half-height).

observed in the  $\text{CF}_2$  groups of Teflon which are free to move by chain motion.<sup>34</sup> Given the magnitude of broadening which can be achieved through changes in the CSA patterns of fluorine groups, it is possible that a significant portion of the broadening observed in Figure 4a,b can be attributed to CSA broadening upon freezing of motion. This would explain, in particular, the broadening which occurs between 0 and 50 kHz (roughly 150–330 ppm). At room temperature for  $\text{CF}_x$  groups terminating an ideal diamond surface, we would expect  $\text{CF}_3$  groups to rotate about its  $\text{C}_3$  axis while  $\text{CF}_2$  and  $\text{CF}$  were essentially static. Since  $\text{CF}_3$  groups represent only  $\leq 10\%$  of the total signal, it is unreasonable to think that the freezing of  $\text{CF}_3$  rotation alone could be responsible for this line shape broadening. This would imply that some motional narrowing of  $\text{CF}_2$  and/or  $\text{CF}$  components is occurring and, therefore, that fluorocarbon deposition is significant during plasma treatment.

The  $T_1$  inversion recovery behavior is displayed in Figures 5 and 6 for samples D1 and D2, respectively. The signal immediately after inversion is shown in trace (a) of both figures. Intermediate traces, Figures 5b–d and 6b–e, represent the spectra after various delays are allowed following signal inversion. At long delays, Figures 5e and 6f, the equilibrium spectra are observed. The relaxation in both cases is inhomogeneous, which is to say that different components of the line shape relax at different rates. For example, in Figure 5b, the spectral intensity at 120 ppm is positive while negative intensity, indicating a slower spin–lattice relaxation rate, is observed at 165 ppm. This would suggest that components with different relaxation rates are isolated or only weakly dipole coupled. This dipole structuring can occur through orientation differences of crystal faces and also through differences in fluorine segregation on a given crystal surface. Strong dipole couplings between spins would provide a pathway for magnetic spin diffusion and, hence, equilibration of magnetic relaxation rates between strongly dipole coupled spins. Sample D1 seems to display three distinct relaxation components at roughly 70, 120, and 150 ppm while D2 has two resolvable components at approximately 85 and 150 ppm.  $T_1$  inversion

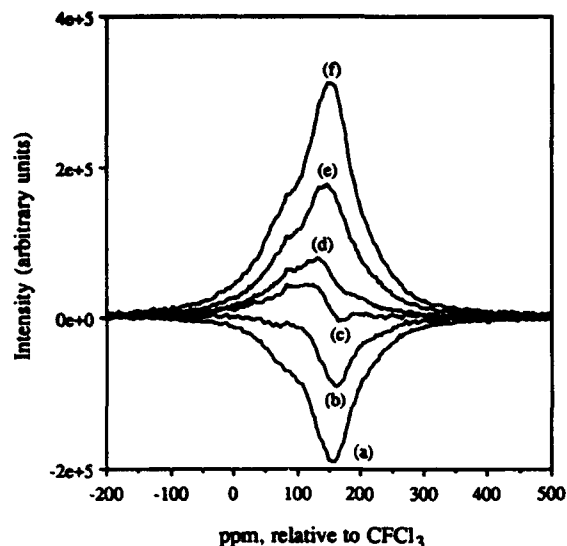


Figure 6.  $T_1$  inversion recovery of sample D2 at 298 K. The inversion recovery delay,  $\tau$ , is as follows: (a) 0.01, (b) 0.04, (c) 0.1, (d) 0.15, (e) 0.4, and (f) 4.0 s.

experiments at lower temperatures also show inhomogeneous relaxation behavior; however, the number of distinct components is completely obscured by line broadening.

Multiple-pulse homonuclear dipole decoupling<sup>35,36</sup> is typically used to resolve CSA powder patterns<sup>34</sup> and has proven useful in spin-lattice relaxation phenomena<sup>16</sup> by averaging homonuclear dipole broadening. A large external magnetic field increases the NMR signal-to-noise ratio as well as increasing the absolute isotropic chemical shift and CSA powder pattern width. Our field at 280 MHz for  $^{19}\text{F}$  is not enough to separate and resolve individual  $\text{CF}_x$  CSA patterns which have intensity from 50 to 100 kHz (180 to 360 ppm) in width (see Figure 5). The useful spectral window for multiple-pulse decoupling sequences on our spectrometer is roughly 40 kHz, which is limited by zero noise and other artifacts. Hence, we have encountered difficulties in implementing a homonuclear dipole decoupling sequence due to limited frequency bandwidths as well as low signal to noise.

In Figures 7, a and b, the quantity  $\ln\{(1 - M_z(\tau)/M_0)/2\}$  is plotted versus the inversion recovery delay,  $\tau$ , for D1 and D2, respectively.  $M_z(\tau)$  is the  $z$ -component magnetization at time  $\tau$ , and  $M_0$  is the equilibrium  $z$  magnetization. For purely exponential spin-lattice relaxation, the Bloch equations applied to the inversion recovery experiment predict such plots will yield straight lines. However, both samples yield nonlinear plots. Complications arise concerning this relaxation theory for two reasons. First, the samples are inhomogeneous in their relaxation behavior. Second,  $^{19}\text{F}$  magnetization in the solid state can relax by a variety of mechanism: dipole-dipole interactions, chemical shift anisotropy, and interactions with paramagnetic centers. As the fluorine motion is frozen, relaxation via CSA and Larmor frequency dipole fluctuations caused by motion become negligible. Upon cooling to 150 K, the relaxation rate of both samples decreases, indicating the loss of the two motion-induced mechanisms. However, relaxation is still relatively rapid, on a time scale of approximately 1 s. Cooling the sample, D2, further to 100 K does little to alter the relaxation rate. This behavior would indicate that the dominant relaxation mechanism in D2 occurs through paramagnetic centers at temperatures between 100 and 150 K. This mechanism can be relatively temperature insensitive at a given concentration of centers over a 50 K temperature range.<sup>37</sup> Paramagnetic relaxation is consistent with relaxation observed for hydrogen on diamond surfaces.<sup>26</sup>

Due to the inhomogeneous nature of the  $T_1$  relaxation, no attempt is made to evaluate relaxation data for a value of  $T_1$ . This would require assuming some type of relaxation mechanism

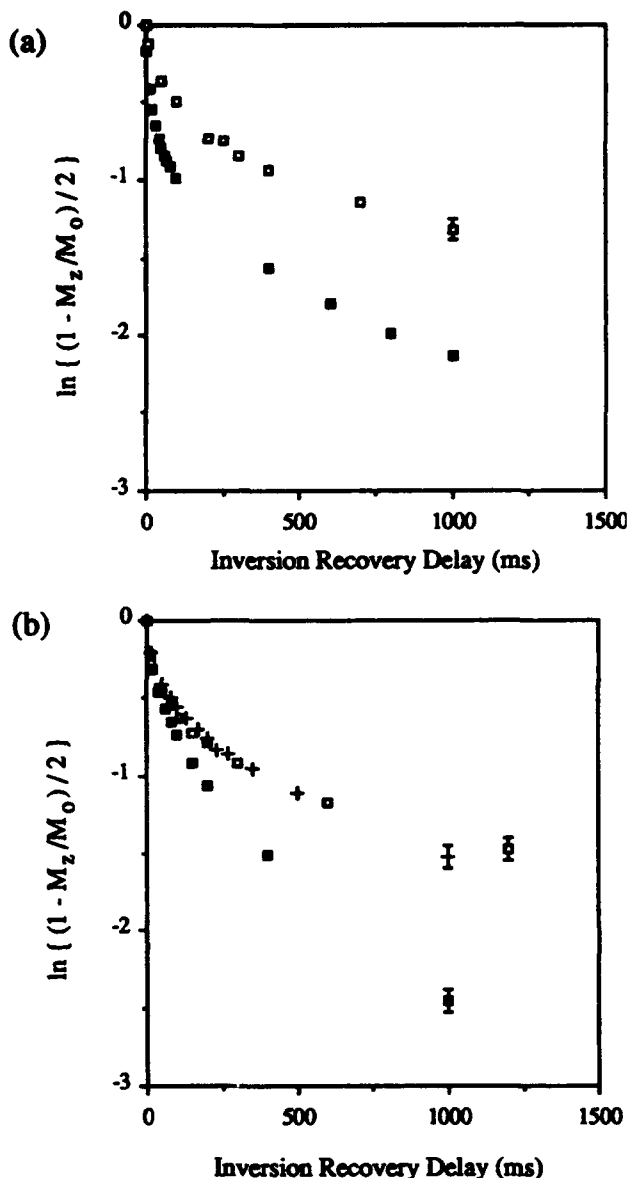


Figure 7. Relaxation function,  $\ln\{(1 - M_z/M_0)/2\}$ , versus the inversion recovery delay,  $\tau$ , at various temperatures: 298 K (solid squares); 150 K (open squares); 100 K (plus). For an exponential Bloch-type decay, this plot should be linear. (a) D1; (b) D2.

for magnetization such as interactions with paramagnetic centers or motional centers or a mechanism involving both dipole-dipole induced spin diffusion and one of these interactions.<sup>18</sup> For a mechanism involving paramagnetic centers in the absence of spin diffusion, we would expect the relaxation function  $\ln\{(1 - M_z(\tau)/M_0)/2\}$  to be linear on a time scale  $\tau^{1/2}$ , where  $\tau$  is the inversion recovery delay.<sup>38</sup> However, agreement to this sort of a function could also result due to multicomponent relaxation behavior. The direct comparison of the initial relaxation rate of the two diamond samples is plotted as a function of the inversion recovery delay in Figure 8 at 298 and 150 K. We observe that D1 relaxes somewhat faster than D2 at 298 K while the relaxation rates are more comparable at 150 K. This would indicate that motion contributes more to the relaxation of D1 than D2 at room temperature. At temperatures where motion is severely inhibited, paramagnetic relaxation is predominant and relaxation rates are comparable between the two samples. The order of magnitude estimate for the  $T_1$  time constant is 500 ms for both D1 and D2 at a temperature of 150 K.

**Surface Distribution of  $^{19}\text{F}$ .** In a final set of experiments, MQ-NMR is used to evaluate the distribution of fluorine on the surface

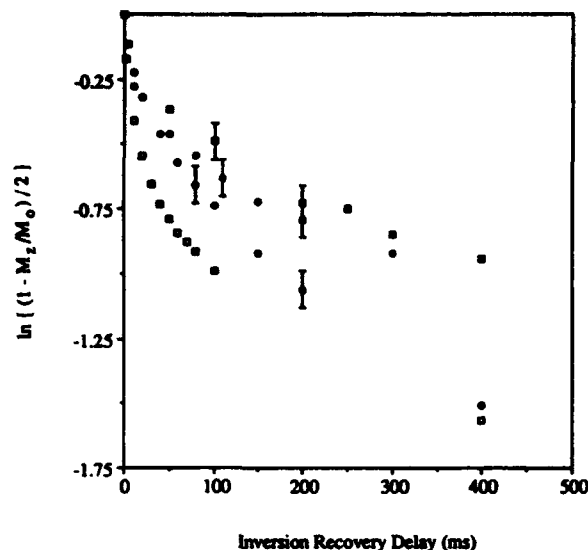


Figure 8. Initial relaxation function behavior versus the inversion recovery delay,  $\tau$ , in milliseconds for both samples at various temperatures: D1, 298 K (open squares) and 150 K (solid squares); D2, 298 K (open circles) and 150 K (solid circles).

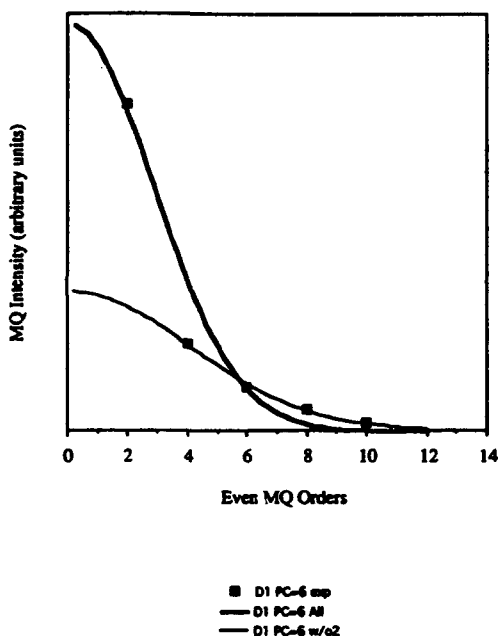


Figure 9. MQ spectrum of sample D1 at 150 K at an excitation time  $\tau_{\text{MQ}} = 187.2 \mu\text{s}$ . The bold line is a Gaussian fit to all intensities of experimental MQ orders (solid squares), while the narrow line is a Gaussian fit to the experimental higher MQ orders neglecting the 2-quantum order.

of the treated diamond powders. Only sample D1 was studied with MQ-NMR since sample D2 provided insufficient signal. Roughly  $5 \times 10^{19}$  fluorine/sample are required for MQ-NMR analysis in these types of materials. In Figure 9, the MQ order intensities are plotted as a function of the MQ order at an excitation time  $\tau_{\text{MQ}} = 187.2 \mu\text{s}$  for D1 at 150 K. As mentioned in the Experimental Section, the number of correlated spins is determined from a Gaussian fit to the nonzero orders. The bold line in Figure 9 represents a Gaussian fit to all even orders up to 10, while the narrow line is a Gaussian fit neglecting the two-quantum order. The poor fit of the bold line to all orders ( $R^2 = 0.916$ ) in conjunction with the excellent fit neglecting the two-quantum signal ( $R^2 = 0.994$ ) would indicate that the two-quantum intensity is not consistent with the higher MQ order intensities. This phenomenon is evident at  $\tau_{\text{MQ}} = 62.4 \mu\text{s}$  and increases in severity as time progresses. This type of behavior has also been observed

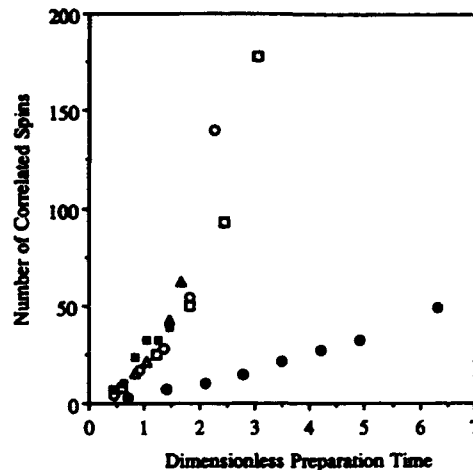


Figure 10. Plot of the number of correlated spins from MQ spectra as a function of the dimensionless preparation time. The dimensionless preparation time is defined as  $M_z^{1/2}/\tau_{\text{MQ}}$ . The symbols are defined as follows: D1 (solid squares);  $\text{CaF}_2$  (open squares); NaF (open circles); CsF (open triangles);  $\text{NaAsF}_6$  (X); hydrogenated diamond powder (solid circle). Fluoride salt data comes from ref 39, and the hydrogenated diamond powder is from ref 26. All data were taken at 298 K, except for D1 which was taken at 150 K.

in proton MQ studies of adsorbed molecules.<sup>23</sup> It is not likely to be the result of faster relaxation of higher MQ order coherences with respect to the two-quantum coherence since this phenomenon is not observed in the MQ-NMR analysis of hydrogen on diamond powder surfaces.<sup>26</sup> We propose that this type of signal is the result of the superposition of MQ signals from relatively dispersed fluorine in weak dipolar communication and aggregated nuclei in stronger dipolar communication. The increased intensity of the two-quantum signal could be attributed to correlation of disperse fluorine nuclei on the surface of the diamond powder. Since this MQ intensity distribution did not occur initially, but only developed after an extended period of excitation time, two-quantum intensity in excess of that predicted by a Gaussian fit to higher-order coherences could evolve from random  $\text{CF}_x$  groups within a proximity of several angstroms. A weak two-quantum signal, attributed to fluorine correlations between nuclei on two different isotropically rotating metal fluoride anions, was observed in mixtures of triphenylsulfonium hexafluoroantimonate solubilized in poly(methyl methacrylate) films.<sup>19</sup> This behavior was not seen in the hydrogenated diamond powder due to high surface coverage which would minimize the presence of isolated hydrogen sites. The higher MQ order intensities are indicative of extended fluorine dipolar networks involving many nuclei in strong dipolar communication analogous to the behavior of aggregates of  $\text{Ph}_3\text{SSbF}_6$  in poly(*n*-butyl methacrylate).<sup>19</sup>

In Figure 10, the number of correlated fluorine nuclei, derived from a Gaussian fit<sup>21</sup> to data analogous to that in Figure 10 as a function of  $\tau_{\text{MQ}}$  neglecting the two-quantum signal, is plotted as a function of the excitation time scaled by the dipolar field strength,  $M_z^{1/2}$ , in Table V for D1 at 150 K. The rate of spin correlation has been related to the dipolar field strength<sup>25,39</sup> and the dimensionality of the spin network.<sup>26,27</sup> Scaling the preparation time by the dipolar field strength allows us to evaluate the influence of the dimensionality of the spin network on a very small length scale, order 10 Å. For comparison, the plasma-treated powder, D1, is plotted along with 3-dimensional fluorine lattices,  $\text{CaF}_2$ , NaF, and CsF,<sup>39</sup> and a surface distribution of hydrogen on diamond powder.<sup>26</sup> The spin correlation rate of the extended fluorine network of D1 indicate a 3-dimensional distribution on a very small length scale (10–20 Å).

MQ-NMR experiments indicate that fluorine exists in two environments on the diamond powder surface of sample D1. In one environment, fluorine is in close proximity to other fluorines,

forming relatively strong dipole coupled spin networks, while in the other, fluorine is close to relatively few other fluorines. The dispersed fluorine phase is consistent with  $T_1$  inhomogeneous relaxation behavior, which indicates that not all of the fluorine in the sample is in strong dipolar communication on a given crystal surface. In both samples D1 and D2, fluorine on the diamond surface has some degree of motion as indicated by the broadening of the FID line shapes and the slowing of  $T_1$  relaxation as the temperature is lowered. Although no MQ-NMR data exist for sample D2, it seems likely that fluorine coverage on both samples is very similar except for the total amount, given the similarity of static FID, magic-angle-spinning FID, and  $T_1$  relaxation experimental results.

**Plasma Chemistry.** The plasma chemistry involved in these fluorination treatments is a complex function of many variables such as pressure, power discharge, geometry, and reactant flow rate, as well as the substrate to be treated. In keeping these parameters constant in both plasma treatments, the primary issue becomes the influence of oxygen addition to a  $CF_4$  plasma. Much work has been done to examine  $CF_4$  and  $CF_4/O_2$  plasma chemistry due to the technological applications in etching silicon and silicon oxide.<sup>40-46</sup> In a typical  $CF_4$  plasma, gas-phase neutrals include F,  $CF$ ,  $CF_2$ , and  $CF_3$ . Ions will not be considered here as plasma species are required which have a lifetime sufficient for diffusion into the diamond powder bed and reaction with diamond surfaces. In this physical situation,  $CF_2$  is potentially the only fluorocarbon species stable enough to undergo diffusion into the powder bed.<sup>44,45</sup>  $CF_3$  undergoes rapid reaction with F to re-form  $CF_4$  and with itself to form  $C_2F_6$ , which is also a minor product of a  $CF_4$  plasma.<sup>41,44</sup>  $CF$  is also only present in levels comparable to  $CF_3$  due to its reactivity.<sup>44</sup> Atomic fluorine is also present in relatively high concentrations such that it is also a potential reactant with diamond surfaces.<sup>41,42,44</sup> Hence, the products of interest which could potentially react with the powder are primarily F and  $CF_2$ .

Thus, surface reactions would most likely involve absorption of fluorocarbon species and atomic fluorine and etching reactions by atomic fluorine. However, in previous work, exposure of the diamond(100) face to atomic fluorine yields a carbon monofluoride surface layer which is resistant to desorption up to 700 K.<sup>13</sup> In addition, since atomic fluorine cannot penetrate the diamond lattice through the (111) or (100) face, atomic fluorine is not expected to be a strong diamond etchant at or near room temperature. Hence,  $CF_2$  and  $CF_3$  species on the diamond samples are probably the result of amorphous fluorocarbon deposition. This would be consistent with motion and aggregation of fluorine observed by NMR.

The addition of molecular oxygen serves to scavenge carbon from the plasma chemistry and increase the concentration of fluorine atoms. Fluorocarbon species are bound by the reaction of  $CF_3$  and  $CF_2$  groups with atomic oxygen to form primarily  $COF_2$ ,  $CO_2$ , and CO depending on the percent of  $O_2$  added.<sup>43</sup> The formation of  $C_2F_6$ , which is a recombination product of  $CF_3$ , is minimized by the addition of  $O_2$  to  $CF_4$  plasmas as a result of the reaction of  $CF_3$  with atomic oxygen.<sup>41</sup> One of the primary ways in which the F concentration is increased is that O consumes species which undergo reaction with F.<sup>40</sup> For instance, the consumption of  $CF_3$  reduces the probability of re-forming  $CF_4$  from  $CF_3$  and F. In addition, the reaction of O with  $CF_3$  and  $CF_2$  to form  $COF_2$ ,  $CO_2$ , and CO serves to liberate F from these fluorocarbon species.<sup>43</sup> In previous experimental work,<sup>42</sup> the addition of 5%  $O_2$  to a  $CF_4$  plasma increased the F concentration 5-fold while cutting the  $CF_2$  concentration in half.

The major difference in fluorine surface coverage between samples D1 and D2 is a reduction by approximately a factor of 10 in the amount of fluorine with the addition of 2%  $O_2$  to the  $CF_4$  plasma. This would seem to emphasize the significance of fluorocarbon deposition in these plasma treatments although atomic fluorine may etch the amorphous fluorocarbon deposit as

well. This could explain the additional signal peak at 123 ppm in sample, D2, which does not exist in sample, D1. NMR signals at 106 and 123 ppm were previously assigned to  $CF_2$  species. Atomic fluorine etching of the amorphous fluorocarbon deposit could introduce both saturated and unsaturated  $CF_2$  species, for example.

Oxygen may also interact directly with the diamond powder. Significant chemisorption, near complete surface coverage, was obtained with oxygen on diamond powder at 420 °C. Although, at 25 °C, the coverage of chemisorbed oxygen on diamond is one-fourth that at 420 °C.<sup>47</sup> Also, molecular oxygen has been used to oxidize diamond materials at about 100 Å/min at 650 °C. However, diamond at roughly 100 °C treated with plasma-activated oxygen is etched at only order 10 Å/min.<sup>48</sup> Adsorption of oxygen and etching of diamond by oxygen may compete with fluorine deposition or remove fluorinated material. The direct interaction of oxygen with diamond in the 98%  $CF_4$ /2%  $O_2$  plasma is, however, most likely insignificant. The amount of oxygen available for direct interaction is probably small owing to gas-phase consumption. Furthermore, the diamond powder is unheated, which has been observed to lessen the reactivity of oxygen on diamond.

Clearly, further work needs to be done to clarify the roles of  $CF_x$  deposition and atomic fluorine in the resultant fluorine surface coverage of diamond material. One possibility would be to treat diamond in plasmas which generate atomic fluorine without the production of fluorocarbon species. Thus, one could study the role of atomic fluorine in diamond materials independently from fluorine deposited on diamond surfaces through fluorocarbon absorption. Potential plasma reactants might be  $F_2$ ,  $NF_3$ , or  $SF_6$ . Molecular fluorine is particularly attractive since the only active neutral species should be atomic fluorine. We might expect the absorption on the material of interest of  $SF_2$  or  $NF_x$  species to occur to some extent, although little chemisorbed  $SF_x$  species were observed in an XPS study of a single-crystal diamond(111) treated in an  $SF_6$  plasma.<sup>50</sup> For studies with NMR,  $SF_6$  may be more useful than  $NF_3$ .  $NF_x$  species' chemical shifts overlap the region of  $CF_x$  shifts, while the overwhelming majority of  $SF_x$  chemical shifts occur in the negative range of chemical shifts relative to  $CFCl_3$ .<sup>51</sup>

## Conclusions

Results from  $^{19}F$  NMR experiments can provide information on the nature of fluorocarbon plasma-treated diamond surfaces. Fluorine is bonded as  $CF_x$  ( $x = 1, 2, \text{ or } 3$ ) groups with the major component being CF. The isotropic chemical shifts are assigned as follows: CF,  $148 \pm 1$  ppm;  $CF_2$ , 123 and  $106 \pm 1$  ppm;  $CF_3$ ,  $78 \pm 1$  ppm relative to  $CFCl_3$ . The  $CF_2$  peak at 123 ppm is present only in the sample treated with the  $CF_4/O_2$  plasma. A pure  $CF_4$  plasma covers the equivalent of approximately half of the available surface bond density with fluorine while the addition of 2%  $O_2$  to the plasma reduces the fluorine coverage by a factor of 10. Hence, the type of  $CF_x$  species deposited by both plasmas is similar, primarily CF, while the total amount differs drastically. MQ-NMR analysis of diamond grit treated in the pure  $CF_4$  plasma has shown that fluorine is not distributed uniformly but appears to be located in two different environments on the surface. In one environment, fluorine is located in close proximity to neighboring fluorine, creating a relatively strong, extensive dipolar network ( $>40$  dipole coupled  $^{19}F$ ) with an apparent 3-dimensional structure. In the second environment, fluorine is relatively isolated from other fluorine nuclei ( $\sim 5$  Å), indicating the chemisorption of fluorocarbon species on surfaces with a low density of chemisorbed fluorine. Variable-temperature  $T_1$  relaxation studies have indicated some fluorine on the diamond surfaces undergoes motion at room temperature, which is almost completely frozen out below 150 K. The presence of paramagnetic centers is indicated by the relatively fast relaxation of fluorine magnetization

even after this motion has been frozen out. The majority of fluorine observed in these samples is probably deposited by fluorocarbon deposition for two reasons. First, the amount of fluorine deposition decreases with decreasing fluorocarbon concentration in the plasma. Second, treatment of the diamond-(100) face with atomic fluorine yields a carbon monofluoride surface<sup>13</sup> which could not account for the CF<sub>2</sub> and CF<sub>3</sub> species observed in these samples. Fluorocarbon deposition would also be consistent with the motion and aggregation of fluorine observed by NMR. These results may explain differences in the surface leakage current of the diamond Schottky diodes receiving CF<sub>4</sub> and CF<sub>4</sub>/O<sub>2</sub> plasma treatments.<sup>9</sup> Further work is needed to evaluate the function of atomic fluorine and fluorocarbon species in producing the observed fluorine diamond coverages. This may illuminate the mechanism by which the CF<sub>4</sub> peak at 123 ppm is formed in the CF<sub>4</sub>/O<sub>2</sub> plasma but not in the pure CF<sub>4</sub> plasma. Finally, the information obtained in this work concerning fluorine chemical species, isotropic chemical shifts, motion, and segregation may also serve as a reference for <sup>19</sup>F NMR of fluorine-assisted CVD diamond since the same kind of information is desired in this case as well.

**Acknowledgment.** This work has been supported by the Office of Naval Research. We are grateful to Dr. Michael Geis and Mr. Keith Krohn of Lincoln Laboratories for plasma treatment of diamond grit and to Dr. Douglas Burum and Dr. Martine Ziliox of Bruker Instruments for high-speed MAS <sup>19</sup>F NMR spectra of samples. We thank Prof. Herbert Sawin of the Chemical Engineering Department at MIT for helpful technical discussions and Ms. Deborah Haney of Mobil Chemical for SEM micrographs of diamond samples.

#### References and Notes

- Geis, M. W.; Angus, J. C. *Sci. Am.* 1992, Oct 84.
- Bechmann, P. K.; Leers, D.; Lydtin, H. *Diamond Relat. Mater.* 1991, 1, 1 and references therein.
- Rudder, R. A.; Hudson, G. C.; Posthill, J. B.; Thomas, R. E.; Markunas, R. J. *Appl. Phys. Lett.* 1991, 59 (7), 791.
- Kadono, M.; Inoue, T.; Miyazaki, A.; Yamazaki, S. *Appl. Phys. Lett.* 1992, 61 (7), 772.
- Patterson, D. E.; Bai, B. J.; Chu, C. J.; Hauge, R. H.; Margrave, J. L. In *Proceedings of the Second International Conference on New Diamond Science and Technology*; Sept 1990; Materials Research Society: Pittsburgh, 1990; p 433.
- Hsu, D. S. Y.; Turner, N. H. In *4th SDIO/IST Diamond Technology Initiative Symposium*; Crystal City, VA, 1989; p WP-7.
- Grannen, K. J.; Tsai, D. V.; Meilunas, R. J.; Chang, R. P. H. *Appl. Phys. Lett.* 1991, 59 (6), 745.
- Patterson, D. E.; Hauge, R. H.; Margrave, J. L. *MRS Symp. Proc.* 1989, 140, 351.
- Geis, M. W. Personal communication.
- Harris, S. J.; Belton, D. N. *Appl. Phys. Lett.* 1991, 59, (16), 1949.
- Pickett, W. E.; Pederson, M. R. *MRS Symposium Proceedings*, April Meeting; MRS: Pittsburgh, 1992, in press.
- Clark, D. T. In *Handbook of X-Ray and Ultraviolet Photoelectron Spectroscopy*; Briggs, D., Ed.; Heyden: London, 1977; Chapter 6.
- Freedman, A.; Stinespring, C. D. *Appl. Phys. Lett.* 1990, 57 (12), 1194.
- Morar, J. F.; Himpsel, F. J.; Hollinger, G.; Jordan, J. L.; Hughes, G.; McFeely, F. R. *Phys. Rev. B* 1986, 33 (2), 1340.
- Kasai, H.; Kogoma, M.; Moriwaki, T.; Okazaki, S. *J. Phys. D: Appl. Phys.* 1986, 19, L225.
- Mehring, M. *Principles of High Resolution NMR in Solids*, 2nd ed.; Springer-Verlag: New York, 1983.
- Gerstein, B. C.; Dybowski, C. R. *Transient Techniques in NMR of Solids: An Introduction to Theory and Practice*; Academic Press: Orlando, FL, 1985.
- Abragam, A. *The Principles of Nuclear Magnetism*; Oxford University Press: Oxford, 1961.
- Scruggs, B. E.; Gleason, K. K. *Macromolecules* 1992, 25 (7), 1864.
- Yen, Y.-S.; Pines, A. *J. Chem. Phys.* 1983, 78 (6), 1983.
- Baum, J.; Pines, A. *J. Am. Chem. Soc.* 1986, 108 (24), 7447.
- Baum, J.; Gleason, K. K.; Pines, A.; Garrowsay, A. N.; Reimer, J. A. *Phys. Rev. Lett.* 1986, 56 (13), 1377.
- Chmelka, B. F.; Pearson, J. G.; Liu, S. B.; Ryo, R.; de Menorval, L. C.; Pines, A. *J. Phys. Chem.* 1991, 95 (1), 303.
- Hwang, S.-J.; King, T. S.; Gerstein, B. C. *Catal. Lett.* 1991, 8, 367.
- Baum, J.; Munowitz, M.; Garrowsay, A. N.; Pines, A. *J. Chem. Phys.* 1985, 83 (5), 2015.
- Levy, D. H.; Gleason, K. K. *J. Phys. Chem.* 1992, 96 (20), 8125.
- Scruggs, B. E.; Gleason, K. K. *Chem. Phys.* 1992, 166, 367.
- Cho, G.; Yezinowski, J. P. Submitted to *Chem. Phys. Lett.*
- Satterfield, C. N. *Heterogeneous Catalysis in Practice*; McGraw-Hill: New York, 1980; Chapter 5.
- Derome, A. E. *Modern NMR Techniques for Chemistry Research*; Pergamon Press: Oxford, 1987; Chapter 4.
- Hoult, D. I.; Richards, R. E. *Proc. R. Soc. London A* 1975, 344, 311.
- Gleason, K. K.; Petrich, M. A.; Reimer, J. A. *Phys. Rev. B* 1987, 36 (6), 3259.
- Mehring, M.; Griffin, R. G.; Waugh, J. S. *J. Chem. Phys.* 1971, 55 (2), 746.
- Vega, A. J.; English, A. D. *Macromolecules* 1988, 13 (6), 1635.
- Rhim, W.-K.; Elleman, D. D.; Vaughan, R. W. *J. Chem. Phys.* 1973, 59 (7), 3740.
- Barum, D. P.; Rhim, W. K. *J. Chem. Phys.* 1979, 71 (2), 944.
- Tse, D.; Lowe, I. J. *Phys. Rev.* 1968, 166 (2), 166.
- Tse, D.; Hartmann, S. R. *Phys. Rev. Lett.* 1968, 21 (8), 511.
- Scruggs, B. E.; Gleason, K. K. *J. Magn. Reson.* 1992, 99, 149.
- Mogab, C. J.; Adams, A. C.; Flamm, D. L. *J. Appl. Phys.* 1978, 49 (7), 3796.
- Smolinsky, G.; Flamm, D. L. *J. Appl. Phys.* 1979, 50 (7), 4982.
- Flamm, D. L.; Donnelly, V. M.; Ibbotson, D. E. *J. Vac. Sci. Technol. B* 1983, 1 (1), 23.
- Plumb, I. C.; Ryan, K. R. *Plasma Chem. Plasma Process.* 1986, 6 (3), 205.
- Ryan, K. R.; Plumb, I. C. *Plasma Chem. Plasma Process.* 1986, 6 (3), 231.
- Booth, J. P.; Hancock, G.; Perry, N. D.; Toogood, M. J. *J. Appl. Phys.* 1989, 66 (11), 5251.
- Buchman, L.-M.; Heinrich, F.; Hoffmann, P.; Janes, J. J. *Appl. Phys.* 1990, 67 (8), 3635.
- Sappok, R.; Boehm, H. P. *Carbon* 1968, 6, 283.
- Joshi, A.; Nimmagadda, R. *J. Mater. Res.* 1991, 6 (7), 1484.
- Yasuda, H. *Plasma Polymerization*; Academic Press: Orlando, FL, 1985; Chapter 7 and 8.
- Cadman, P.; Scott, J. D.; Thomas, J. M. *J. Chem. Soc., Chem. Commun.* 1975, 16, 654.
- Dungan, C. H.; Van Wazer, J. R. *Compilation of Reported <sup>19</sup>F NMR Chemical Shifts*; Wiley-Interscience: New York, 1970.

# **<sup>1</sup>H NMR OF COMBUSTION DEPOSITED AND HYDROGEN PLASMA TREATED DIAMOND**

S. Mitra and K. K. Gleason  
Department of Chemical Engineering  
Massachusetts Institute of Technology  
Cambridge, MA 02139

and

K. V. Ravi  
Lockheed Missile & Space Company  
Research and Development Division  
3251 Hanover Street  
Palo Alto, CA 94304-1191

Polycrystalline diamond films deposited from an oxyacetylene flame were studied by <sup>1</sup>H nuclear magnetic resonance (NMR). Unlike hot-filament films, no hydrogen was detected by NMR in the as-deposited combustion film. Thus, the diamond surfaces and grain boundaries produced under hot-filament and combustion chemical vapor deposition (CVD) differ. Exposure to a hydrogen plasma while holding the film at 800 °C, produces a significant hydrogen concentration which can be detected by NMR. This concentration is consistent with the passivation of grain boundary sites. In addition, the NMR spectrum of plasma treated film exhibits a narrow and a broad component, as typically seen for hot-filament CVD materials. Since bulk diffusivity is likely to be slow, the hydrogen plasma treatment most likely passivates grain boundary sites in the film. In addition, its fast, non-exponential <sup>1</sup>H NMR spin-lattice relaxation indicates direct communication between protons and relaxation centers, suggesting that paramagnetic surface states are also present at the grain boundaries. Since hydrogen atoms are very mobile in diamond films at 800°C, passivation of defects containing unpaired electrons is possible. The degree of such passivation is expected to strongly influence hopping conduction of electrons in diamond films.

## **INTRODUCTION**

Chemical vapor deposition (CVD) of diamond films has been achieved over a wide range of conditions,<sup>1</sup> often employing a large fraction of hydrogen in the gas reactant mixture. This hydrogen has been proposed to both stabilize the growing diamond surface and to etch graphitic carbon. Low levels of hydrogen incorporation affect the properties of

diamond thin film. In other materials, such as polycrystalline and amorphous silicon, passivation of defect sites by hydrogen can improve the opto-electronic properties.<sup>2</sup> In diamond, higher hydrogen contents correlate with increased absorption in the 8 - 10 μm wavelength region, degrading its performance as an infrared window.<sup>3,4</sup> Also, the electrical resistivity of diamond has been observed to depend on hydrogen incorporation.<sup>5</sup> Moderate annealing produces resistivity changes of a few orders of magnitude, attributed to the loss of hydrogen from the films. Resistivity can be restored by exposing the films to a hydrogen plasma at elevated temperatures. Thus, the dynamics of hydrogen incorporation, rearrangement and evolution in polycrystalline diamond film are of technological interest.

Nuclear magnetic resonance (NMR) is a useful technique for probing hydrogen distributions. In samples which are free of paramagnetic defects, NMR experiments are quantitative in that each <sup>1</sup>H nucleus gives rise to the same integrated signal intensity, regardless of its bonding environment. In samples containing paramagnetic impurities, a small fraction of nuclei in close proximity to such defects will remain undetected as a result of extreme line broadening due to interaction with the unpaired electron of the paramagnetic impurity.<sup>6</sup> The ability to quantitatively relate IR and NMR results also confirms that paramagnetic defects do not shield a large number of the protons from NMR detection in the films examined to date.<sup>4</sup>

Previous <sup>1</sup>H NMR work has shown that most of the hydrogen in hot-filament CVD films is segregated and exists in regions of high proton density. These regions are thought to be surfaces of grain boundaries and crystallites.<sup>3,4,6,7</sup> This hypothesis would predict that hydrogen in diamond is relatively mobile, since diffusion at grain boundaries is expected to be more rapid than in the bulk. The <sup>1</sup>H NMR spectrum typically consists of a narrow Lorentzian and a broad Gaussian component. The Lorentzian line is attributed to motional narrowing of the rotating methyl groups while the Gaussian component arises from static hydrogen.<sup>3</sup>

The spin-lattice relaxation for <sup>1</sup>H in CVD deposited diamond generally occurs in < 1 s and is often temperature independent.<sup>6,7</sup> This suggests that paramagnetic species are the dominant spin-lattice relaxation centers. Indeed, electron spin resonance (ESR) of microwave plasma CVD films show high paramagnetic densities, ranging from 10<sup>18</sup> to 10<sup>19</sup> cm<sup>-3</sup>.<sup>8</sup> These paramagnetic centers have been attributed to dangling bonds from unsaturated carbon atoms. In addition, the rotating methyl groups which contribute to the narrow component of the NMR spectra can also act as relaxation centers and could give rise to a temperature dependent spin-lattice relaxation in diamond films with a large Lorentzian component in their NMR spectra.

In this paper, the hydrogen distribution in combustion deposited films is examined for the first time by <sup>1</sup>H NMR. These measurements are compared to the previous results on hot-filament material. Also, a nominally identical as-deposited combustion film was exposed to an external source of hydrogen atoms (a hydrogen plasma) in order to determine whether diffusion of hydrogen into the heated film can be observed.

## EXPERIMENTAL

Two samples were deposited by an oxyacetylene torch under nominally identical conditions. During deposition, the substrate temperature was maintained at 800°C. One sample from this pair was subsequently heated to 800°C and exposed to hydrogen plasma for 4 hrs at 30 torr.

Room-temperature NMR lineshapes and spin-lattice relaxation measurements were obtained for both combustion CVD films using a homebuilt spectrometer operating at a  $^1\text{H}$  frequency of 270 MHz with a probe designed for low level hydrogen detection.<sup>9</sup> Hydrogen content in the films was obtained by comparing the integrated area of the NMR spectra allowing 5 s between signal averages.

The spin-lattice relaxation time constant,  $T_1$ , was measured using the standard saturation recovery technique.<sup>10</sup> In this method a  $(90^\circ-\tau-90^\circ)_n$  pulse sequence is applied and the intensity of the NMR signal was measured for various values of the recycle time delay  $\tau$ . The data was fitted to the empirical equation,

$$M(\tau) = M_0 [1 - \exp(-\tau/T_1)^n] \quad (1)$$

where  $M_0$  is the equilibrium magnetization and  $n$  is a constant constrained to values between 0.5 and 1.0. Spin-lattice relaxation of a given proton is expected either through a direct interaction with a relaxation center, such as a paramagnetic site, or indirectly via spin diffusion communication with another  $^1\text{H}$  closer to such a center. When indirect relaxation via spin diffusion dominates,  $n = 1$  indicating a standard exponential Bloch decay. On the other hand when direct relaxation to a paramagnetic center dominates, the limiting value of  $n$  is 0.5,<sup>6</sup> while an intermediate value is indicative of relaxations via both mechanisms.

## RESULTS AND DISCUSSION

In striking contrast to previous work on hot-filament films,<sup>3,4,7,8</sup> no hydrogen could be observed in the as-deposited combustion CVD diamond film (Fig. 1). This sample may have a very low hydrogen content. Our detection limit of  $\sim 5 \times 10^{16}$  per sample, corresponds to a detectable hydrogen content of  $< 10^{15} \text{ cm}^{-3}$ . This result would not be entirely surprising in that the concentration of hydrogen in gas-phase of the combustion reactor is lower than that in the hot-filament reactor. An alternative interpretation is that a high concentration of paramagnetic centers near the protons in this sample renders them undetectable by NMR. A final possibility is that the NMR spin-lattice relaxation rate in this sample is an order of magnitude slower than any other diamond film studied to date. Another method of measuring the hydrogen content of this sample is needed to decide between these possibilities. Nevertheless, the as-deposited combustion film is very different from the films examined by  $^1\text{H}$  NMR to date.

After plasma hydrogenation, the NMR measured hydrogen increases significantly to  $7.0 \times 10^{20} \text{ cm}^{-3}$  (0.40 at. %). The magnitude of this concentration is consistent with complete hydrogen passivation of all the grain boundary area in the film and comparable to concentrations detected in hot-filament CVD films. The hypothesis that hydrogen is located primarily at grain boundaries of the polycrystalline diamond films is also consistent with the expectation that the diffusion of atomic hydrogen from the plasma into the film is likely to be much faster along grain boundaries than through the bulk.

The  $^1\text{H}$  NMR spectra of the plasma treated combustion deposited film displays a two component NMR spectrum (Fig. 1) very similar in nature to that seen in hot-filament films. The narrow Lorentzian and a broad Gaussian component with half width at half maximums (HWHM) of  $34 \pm 1 \text{ kHz}$  and  $8 \pm 3 \text{ kHz}$ , respectively, are comparable to results from hot-filament CVD films. Only  $8 \pm 3\%$  of the hydrogen in the plasma treated sample contributes to the Lorentzian behavior. These methyl groups may be created by multiple hydrogenation of a "strained" site.

The broad Gaussian component and the narrow Lorentzian component have identical non-exponential spin-lattice relaxation behavior. Figure 2 shows that values of  $T_1 = 200 \text{ ms}$  and  $n = 0.5$  used in eq. 1 fit this data. Since  $n = 0.5$ , direct relaxation via paramagnetic centers is likely to be dominant mode of spin-lattice relaxation in these samples. Thus, the majority of hydrogen contributing to both the narrow and broad components of the NMR lineshape are within several hundred angstroms of a paramagnetic defect. If hydrogen is located at surfaces and grain boundaries as previously suggested,<sup>3,4,6</sup> this indicates that some of the paramagnetic defects are likely to be surface states which result from incomplete hydrogen passivation and/or surface reconstruction. Note that not all paramagnetic sites are required to be surface states. Given the relatively high concentration of unpaired electrons in polycrystalline diamond<sup>9</sup> it is likely that bulk ESR-active defects also exist as is the case in natural diamond.<sup>10</sup>

The number density of dangling bonds on the surfaces is expected to have a measurable effect on the transport of electrons in diamond through hopping conduction. Conductivity via this mechanism is expected to decrease as the distance between the trapping sites increases. The observed passivation of diamond surfaces and grain boundaries by a hydrogen plasma treatment would be expected to greatly influence the density of the electrically active surface states.

## CONCLUSIONS

Polycrystalline diamond films deposited by an oxyacetylene flame have little or no hydrogen which can be detected by NMR, unlike their hot-filament CVD counterparts. However, after combustion deposited material is heated to 800°C while exposed to a hydrogen plasma, a two component NMR absorption spectrum is obtained. This spectra is similar to those of the hot-filament films. Since diffusivity of the hydrogen into the bulk is

likely to be slow, the hydrogen plasma treatment most likely creates passivated hydrogen terminated surfaces at grain boundaries in the film similar in nature to those in the hot-filament material. This experiment confirms the previous hypothesis that the majority of hydrogen observed by NMR exists at surfaces and grain boundaries in polycrystalline diamond films.

Thus, the diamond surfaces and grain boundaries produced under hot-filament and combustion CVD are different. These surfaces are either created during deposition or result upon bringing the film to ambient conditions in the reactor. If the assumption is made that the observed surfaces represent the nature of the growing interface, differences in heterogeneous growth models for hot-filament versus combustion synthesis diamond films are required. The degree of hydrogen passivation of paramagnetic surface states is expected to strongly influence hopping conduction of electrons in diamond films.

#### ACKNOWLEDGEMENTS

We gratefully acknowledge the financial support of the Office of Naval Research.

#### REFERENCES

1. P. K. Bachman, D. Leers, and H. Lydtin, *Diamond and Related Materials* **1**, 1 (1991).
2. S. J. Pearton, J. W. Corbett, M. Stivala, *Hydrogen in Crystalline Semiconductors*, Springer-Verlag (1992).
3. K. M. McNamara, D. H. Levy, K. K. Gleason, and C. J. Robinson, *Appl. Phys. Lett.* **60**, 580 (1992).
4. K. M. McNamara, K. K. Gleason, and C. J. Robinson, *J. Vac. Sci. & Tech A* **10**, 3143 (1992).
5. M. I. Landstrass and K. V. Ravi, *Appl. Phys. Lett.* **55**, 1391 (1989).
6. R. M. Henrich, M. L. Colfield, R. H. Young, and J. M. Hewitt, *J. Mag. Res.* **58**, 85 (1984).
7. D. H. Levy and K. K. Gleason, *J. Phys. Chem.* **31**, 8125 (1992).
8. S. Mitra and K. K. Gleason, *Diamond and Related Materials* (in press).
9. I. Watanabe and K. Sugata, *Jpn. J. Appl. Phys.* **27**, 1808 (1988).

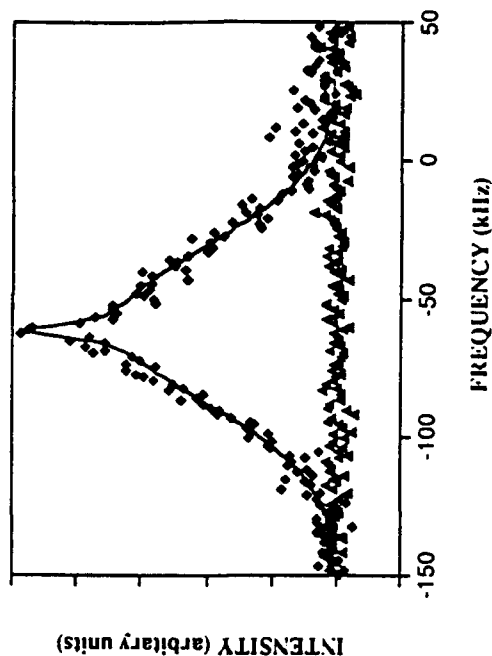


Figure 1  $^1\text{H}$  NMR spectra of as deposited combustion CVD film (triangles), showing no detectable signal. After annealing in a hydrogen plasma, hydrogen is detected (diamonds). The solid line shows the least squares fit of this data to the sum of a broad Gaussian and a narrow Lorentzian.

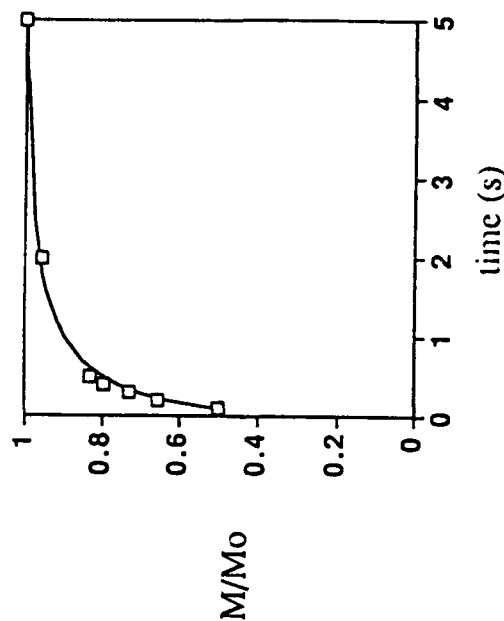


Figure 2. NMR spin-lattice relaxation data (squares) for combustion CVD film after annealing in a hydrogen plasma. The solid line represents the predicted recovery (eqn. 1) using values of  $T_1 = 200$  ms and  $n = 0.5$ .



## COMPARISON OF TANTALUM AND RHENIUM FILAMENTS IN CVD DIAMOND USING SELECTIVE C-13 LABELING

K.M. McNamara and K.K. Gleason  
Department of Chemical Engineering  
Massachusetts Institute of Technology  
Cambridge, MA 02139

Heterogeneous carbon scrambling at the hot-filament in thermally assisted diamond chemical vapor deposition has been investigated through isotopic labeling studies. Films were produced using acetone, preferentially labeled at either the methyl or carbonyl carbon, and  $^{13}\text{C}$  incorporation was determined by Raman and  $^{13}\text{C}$  NMR spectroscopy. A comparison of carbide-forming materials, such as tantalum, and non-carbide formers, such as rhenium, is made. Using a tantalum filament results in the carbonyl and methyl carbons of acetone being incorporated into the growing diamond film with equal efficiency. Secondary ion mass spectroscopy (SIMS) reveals that heterogeneous exchange reactions at the tantalum filament are responsible for this phenomenon. Heterogeneous scrambling is limited in the rhenium case, which may prove useful in selective isotopic labeling studies. This study demonstrates the importance of heterogeneous reactions at the hot-filament and thus, has important implications for the modeling of these systems.

### INTRODUCTION

Hot-filament chemical vapor deposition (CVD) has been widely used to produce diamond films at low-pressure (1,2). The gas-phase chemistry of these reactors is relatively well characterized and many of the kinetic parameters required to model these systems (3-7) are known from the combustion literature. However, heterogeneous reactions are rarely considered in the modelling of hot-filament CVD reactors.

Previously, selective  $^{13}\text{C}$  isotopic labeling has been used to evaluate combustion mechanisms by tracing the pathway followed by a particular carbon site (8-9). The main limitation of this approach is that rapid homogeneous gas-phase or heterogeneous surface reactions can completely rearrange carbons between chemically distinct sites in various species. This phenomena, known as isotopic scrambling, is often rapid between hydrocarbon species (10). Partial scrambling is also possible. Chu et al. have shown

that in cases where only partial scrambling occurs, selective isotopic labeling is still a useful tool for studying the kinetics of diamond formation (10,11).

The heterogeneous chemistry at filament surfaces is a particularly interesting method by which carbon labels may scramble. Since the filament is the highest temperature surface in the reactor, it is a more likely site for heterogeneous reaction than the water cooled aluminum reactor walls. Such heterogeneous exchange between the filament and gas-phase carbon atoms should alter the  $^{13}\text{C}$  enrichment of the filament and can be detected by secondary ion mass spectroscopy (SIMS). Filaments can be made of either carbide-forming refractory metal, such as tantalum or tungsten or of metals which do not form carbides, such as rhenium. Differences in the heterogeneous reactions occurring on these two types of filament materials will be studied here.

Acetone was chosen as the carbon source because it is expected to readily yield methyl radicals and CO and can be selectively labeled at either the methyl or carbonyl site. This selective labeling will allow us to examine differences between chemistry experienced by the carbon atoms in each bonding environment of the acetone molecule. In addition, previous isotopic labeling studies have shown that homogeneous gas-phase scrambling of CO with hydrocarbons, under conditions similar to those in our system, is minimal (8,9). Finally, acetone introduces the effects of oxygen on both the homogeneous and heterogeneous chemistry in the system.

### EXPERIMENTAL

Four  $^{13}\text{C}$  enriched polycrystalline diamond films were produced in a hot-filament reactor using an acetone flow rate of 2 sccm. The type of enrichment (methyl or carbonyl) and filament used (tantalum or rhenium) is shown in Table I. In all cases, 22% of all carbon atoms (methyl and carbonyl) in the gas-feed were  $^{13}\text{C}$ . The silicon substrates employed were seeded with 0.25  $\mu\text{m}$  natural diamond particles. The temperature of the silicon substrate was  $\sim 1150\text{K}$ , and the total pressure in the reactor was 200 torr. The hydrogen flowrate was held fixed at 100 sccm. The filament used to thermally activate the gas feed was either a tantalum or rhenium wire, resistively heated to  $\sim 2600\text{K}$ . The filaments were treated in natural-abundance (1.1%  $^{13}\text{C}$ ) acetone for  $\sim 3$  hrs to allow carburization, if any. All films were pale grey in appearance and showed well-defined facets under optical microscopy.

The incorporation of the selectively labeled feed into the deposited diamond films will be characterized by both Raman and  $^{13}\text{C}$  NMR spectroscopy(12). The isotopic shift in the first-order Raman frequency has been correlated to  $^{13}\text{C}$  enrichment in both CVD diamond (10,11) and in high pressure synthetic diamond (13). Using the latter data, the  $^{13}\text{C}$  concentration is determined with an estimated uncertainty of  $\pm 3$  at. % using a second-order polynomial fit (Fig. 1). Temperature and stress shifts of the Raman band

were assumed to be small, since low laser power and silicon substrates were employed throughout (14). The  $^{13}\text{C}$  enrichment was also calculated from the linewidth of the NMR diamond peak using the van Vleck equation (15). This linewidth is linearly proportional to the degree isotopic enrichment, when other line broadening mechanisms are assumed to be negligible.

## RESULTS AND DISCUSSION

The micro-Raman spectra of the two films produced using a tantalum filament, TaM and TaC, show strong absorbances at  $1325\text{ cm}^{-1}$ . The isotopic shift of the  $1332\text{ cm}^{-1}$  the one-phonon diamond band in both Raman spectrum is  $1324\text{ cm}^{-1}$ , corresponding to a 22% enrichment (Fig. 1). In addition the static, direct-polarization  $^{13}\text{C}$  NMR spectra of film TaM and TaC (Fig. 2) show a single peak centered at 36 ppm having a 3.0 kHz linewidth (FWHM), indicating the  $^{13}\text{C}$  enrichment of both films of 22% using the van Vleck equation, the enrichments of both films is calculated to be 22%. This confirms the Raman findings that the enrichment of the film matches that of the CVD reactants for these two films. Thus, both techniques indicated the enrichment of the two films is identical and equal to that of the overall gas-phase enrichment used during the deposition, in agreement with earlier findings (16). Thus, complete scrambling of  $^{13}\text{C}$  label is most likely occurring. This result is surprising since CO carbons are not expected to undergo homogeneous scrambling in the gas-phase under these conditions (8,9).

Table I. Summary of filament studies

Sample	Filament	Label	% $\text{C-}^{13}_{\text{gas}}$	% $\text{C-}^{13}_{\text{solid}}$	Raman shift ( $\text{cm}^{-1}$ )
TaM	Ta	methyl	22	$22 \pm 3$	1325
TaC	Ta	carbonyl	22	$22 \pm 3$	1325
ReM	Re	methyl	22	$25 \pm 3$	1324
ReC	Re	carbonyl	22	$7 \pm 3$	1330

SIMS was used to determine if the filament contributed to heterogeneous isotopic scrambling of the carbon labels (17). Two tantalum filaments were carburized for several hours in unenriched acetone/ $\text{H}_2$  mixture. The first filament received no additional treatment. Its SIMS spectrum (Fig. 3a) shows peaks at 193 and 195 amu, representing Ta $^{12}\text{C}$  and its hydride Ta $^{12}\text{CH}$ , respectively, while TaO and TaOH appear at 197 and 198 amu, respectively. The second filament underwent an additional treatment, exposure to 22%  $^{13}\text{C}$  enriched acetone, labeled at the carbonyl carbon for several hours at typical operating conditions. The SIMS spectrum of this filament shows peaks at 193, 195,

197, and 198 amu appear as before. However, two additional peaks appear at 194 and 196 amu, indicating the presence of Ta $^{13}\text{C}$  and Ta $^{13}\text{CH}$ , respectively. Depth profiling of the filament to  $> 2000\text{ \AA}$  gives similar  $^{13}\text{C}$  levels, indicating that exchange has occurred on the interior as well as the surface of the filament. This carbon exchange at the filament can account for the identical efficiency of enrichment of diamond films obtained from either methyl-labeled or carbonyl-labeled  $^{13}\text{C}$  acetone.

Heterogeneous exchange at the filament can further be considered by examining the results from the films ReM and ReC grown using a rhenium filament. The likelihood of carbon exchange at the filament is expected to be reduced since, unlike tantalum, rhenium does not form a carbide (18,19). The micro-Raman spectra of the samples ReM and ReC show a clear diamond band, shifted due to the isotopic enrichment (14). The concentrations obtained were  $24 \pm 3\%$  and  $8 \pm 3\%$  for the methyl and carbonyl-labeled acetone, respectively (Table I). This dramatic decrease in the incorporation of carbonyl carbons when using a rhenium filament serves to highlight the importance of heterogeneous filament chemistry in hot-filament systems using carbide-forming filament materials.

The incorporation of carbonyl carbons is greatly reduced but not eliminated when rhenium is used. A small amount of CO may undergo conversion to hydrocarbon species by some other route (17). One possibility is that the enol form of acetone, whose concentration is expected to increase in a hydrogen environment (20), may provide an alternative route for acetone decomposition, separating the oxygen from the carbonyl carbon. Also, the homogeneous gas-phase conversion of CO to hydrocarbon species may have a finite contribution. In addition, although carbon for heterogeneous exchange is not supplied by the rhenium filament, surface reactions at the filament are still possible and may contribute to the conversion of CO. Finally, CO may, in fact, act as a precursor for diamond growth at a significantly slower rate than hydrocarbon species.

## CONCLUSIONS

The importance of heterogeneous reactions at tantalum hot-filaments has been demonstrated. After the initial carburization period, heterogeneous carbon exchange continues at tantalum filament during film deposition. Similar behavior is expected with other carbide forming metals like tungsten. A significant portion of the CO carbon incorporated into diamond films when using a tantalum filament occurs through the mechanism of heterogeneous carbon exchange at the filament. Heterogeneous scrambling of carbon labels is reduced when rhenium, a non-carbide forming filament, is used. Thus, selective labeling studies which have heterogeneous scrambling limitations may benefit from using rhenium filaments. The kinetic modeling of hot-filament reactors has general not included these heterogeneous reactions. For species near chemical equilibrium at the condition adjacent to the filament itself, only small changes will result

in predicted species concentrations. However, for other species, the effect of heterogeneous reactions is likely to be significant.

#### ACKNOWLEDGEMENTS

The authors gratefully acknowledge the assistance of and Mr. Dan Vesteyck and Dr. James E. Butler of the Naval Research Laboratory for assistance in obtaining nitro-Raman spectra. Also, Dr. Mike Geis and Mr. Keith Krohn of Lincoln Laboratory are thanked for their assistance and the use of their reactor. We also gratefully acknowledge the financial support of the Office of Naval Research and NSF Grant No. CTS-9006705.

#### REFERENCES

1. P.K.Bachmann, D.Leers, and H.Lydim, Diamond and Related Materials, 1,1 (1991).
2. R. C. DeVries, Am. Rev. Mater. Sci. 17, 161 (1987).
3. S. J. Harris, A. M. Weiner and T. A. Perry, Appl. Phys. Lett., 53, 1605 (1988).
4. M. Frenklach and H. Wang, Physical Review B, 43, 1520 (1991).
5. D. G. Goodwin and G. G. Gavillet, J. Appl. Phys., 68, 6393 (1990).
6. M. A. Cappelli and P. H. Paul, J. Appl. Phys., 67, 2596 (1990).
7. T. Debroy, K. Yankala, W. A. Yarbrough and R. Messier, J. Appl. Phys., 68, 2424 (1990).
8. R.E. Ferguson, J. Chem. Phys. 23, 2085 (1955).
9. R.E. Ferguson, Combustion and Flame 1, 431 (1957).
10. C.J. Chu, R.H.Hague, M.P.D'Evelyn, and J.L. Margrave, Mater. Res. Soc. Symp. Proc. 162 (1989).
11. C.J.Chu, M.P.D'Evelyn, R.H.Hauge, & J.L.Margrave, J.Appl.Phys., 70 (1991).
12. K.M.McNamara, K.K. Gleason, D.J. Vesteyck, and J.E. Butler, Diamond and Related Materials, 1, 1145 (1992).
13. R.M. Chrenko, J. Appl. Phys., 63, 5873 (1988).
14. K.M. McNamara and K.K. Gleason, J. Electrochem. Soc., 140, L22 (1993).
15. J.H. van Vleck, Phys. Rev. 74, 1168 (1948).
16. K.M. McNamara, K.K. Gleason, and M.W. Geis, Mat. Res. Soc. Symp. Proc., 162, 207 (1989).
17. K.M. McNamara and K.K. Gleason, J. Appl. Phys., 71, 2884 (1992).
18. R. Colton, The Chemistry of Rhenium and Technetium, Interscience Publishers, New York (1965).
19. K.B. Lebedev, The Chemistry of Rhenium, Butterworths, London (1962).
20. A. Streitwieser Jr., and C.H. Heathcock, Introduction to Organic Chemistry, Macmillan Publishing Co., Inc., New York (1981).

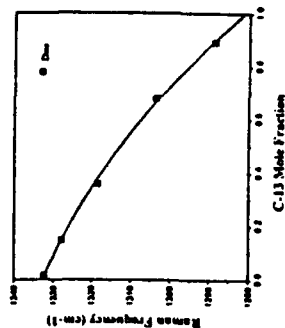


Fig.1 Isotopic shift of Raman one-phonon peak. The line is a best-fit second-order polynomial to the data from ref. 13 (squares).

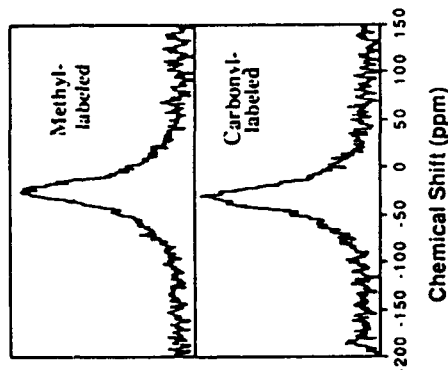


Fig.2 Direct-polarization  $^{13}\text{C}$  NMR of TaM (top) and TaC (bottom). Only  $\text{sp}^3$  bonded carbon is detected. Both linewidths correspond to enrichments of 22% (1 ppm = 50 Hz)

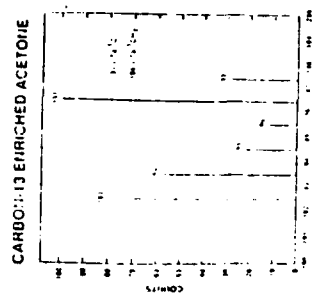
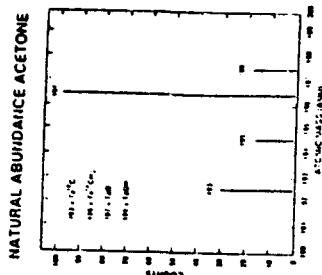


Fig.3 SIMS spectra of Ta filaments after carburization in natural abundance acetone and after (a) no further treatment and (b) subsequently exposed to acetone enriched at the carbonyl site. Additional peaks in (b) indicate heterogeneous exchange.

## Radial Distribution of Hydrogen in Chemical Vapor Deposited Diamond

Karen Mary McNamara<sup>†</sup> and Karen K. Gleason\*

Department of Chemical Engineering, Massachusetts Institute of Technology,  
Cambridge, Massachusetts 02139

Received July 7, 1993. Revised Manuscript Received October 15, 1993\*

At the center of a (100) oriented microwave plasma diamond film, a hydrogen concentration of 0.120 at. % was measured by solid-state nuclear magnetic resonance (NMR) spectroscopy. Somewhat lower contents were found for the central regions hot-filament and dc arc-jet materials, 0.031 and 0.023 at. %, respectively. However, the NMR line shapes are similar in all three cases, indicating similar bonding environments for the hydrogen. Radial variations in hydrogen content in the hot-filament and dc arc-jet samples were also observed by NMR. Regions with higher hydrogen contents also gave rise to increased absorption in the CH stretch region of the IR spectra and an increased background signal in the Raman spectra. Similarities in hydrogen content and distribution in these films indicates that a common mechanism for hydrogen incorporation at the growing diamond surface. Understanding such mechanisms is important for producing diamond films with uniform properties over large areas.

### Introduction

The unique properties of diamond, such as its high thermal conductivity, mechanical characteristics, optical transmission, and electronic properties, make it an attractive material for many applications.<sup>1-4</sup> Recent advances allowing the production of high-quality diamond films have generated substantial interest in research laboratories throughout the world. These high-quality materials are produced by a variety of methods including microwave plasma, hot-filament, and dc arc-jet chemical vapor deposition (CVD). Although large differences in growth rates exist between these methods, all seem capable of producing highly faceted polycrystalline films with little evidence of non-diamond carbon.

The primary difference between most of the CVD techniques used to deposit diamond is the method by which energy is introduced into the gas phase. The reactant mixture is typically quite similar consisting of dilute hydrocarbon species (0.5–2.0%) in hydrogen.<sup>2-4</sup> Energy is introduced in order to dissociate and excite these gases, allowing hydrocarbon fragments and hydrogen atoms to reach the growth surface which is maintained at 800–1000 °C. Hot-filament and dc discharges have maximum gas-phase temperatures of ~2500 K, yielding growth rates on the order of 1 μm/h. Dc arc-jet plasmas have gas-phase temperatures of 4500 K or more and can yield deposition rates of >100 μm/h.<sup>4</sup> The properties of the diamond, from run to run and also spatially within the sample, should be effected by the conditions and species which prevail at the surface of the growing film. Due to the relatively high pressure and light emission in diamond growing environments, it is difficult to examine the state of the growing

surface *in situ*. Differences observed by *ex situ* detection, however, may give some insight into the differences in growth mechanisms in various systems.

This paper examines the hydrogen content of hot-filament, dc arc-jet and microwave plasma CVD diamond films by solid-state nuclear magnetic resonance (NMR) spectroscopy. This extends our early work using <sup>1</sup>H NMR, which focused only on hot-filament materials.<sup>5,6</sup> In addition, variations of hydrogen content as a function of radial position in the sample will be measured for the dc arc-jet and hot-filament films. Hydrogen content was chosen as a useful indicator of diamond quality because it correlates well with IR transmission<sup>5,6</sup> and is also proposed to effect electrical properties, such as resistivity.<sup>7</sup> In addition, the quantitative NMR measurements will be related to the results of more commonly employed diamond characterization techniques.

### Experimental Section

Three free-standing diamond films were produced from CH<sub>4</sub> and H<sub>2</sub> by microwave plasma (MW), dc arc jet (DC), and hot-filament (HF) CVD, respectively. Further details of the MW and DC depositions are proprietary. The HF CVD sample was deposited at a rate of 1.87 μm/h from 1% CH<sub>4</sub> in H<sub>2</sub> onto a thick, rotating, 1-in.-diameter silicon wafer substrate at a pressure of 100 Torr. The tantalum filament was maintained at a temperature of 2375 K, at a distance of 4 mm from the substrate.

The microwave film was obtained from the center of a >500-μm-thick dark film. The dc arc-jet material was ~400-μm-thick and also appeared dark. Samples from this film were obtained at 0.5-in. intervals across the 4.0-in. disk. Finally, the hot-filament sample was only ~50 μm thick with a gray-white appearance, and samples were obtained at 0.25-in. intervals across the 1.0+ in. disk.

All of the films were analyzed using Raman spectroscopy, infrared (IR) spectroscopy, X-ray diffraction, scanning electron microscopy (SEM), and solid-state nuclear magnetic resonance

<sup>†</sup> Current address: General Electric Corporate Research and Development, Schenectady, NY 12301.

\* To whom correspondence should be addressed.

Abstract published in *Advance ACS Abstracts*, December 1, 1993.

(1) Geis, M. W.; Angus, J. C. *Sci. Am.* 1992, 267, 84.

(2) Angus, J. C.; Hayman, C. C. *Science* 1988, 241, 241.

(3) DeVries, R. C. *Annu. Rev. Mater. Sci.* 1987, 161, 161.

(4) Bachman, P. K.; D. Leers, D.; Lydtin, H. *Diamond Relat. Mater.* 1991, 1, 1.

(5) McNamara, K. M.; Levy, D. H.; Gleason, K. K.; Robinson, C. J. *Appl. Phys. Lett.* 1992, 60, 580.

(6) McNamara, K. M.; Gleason, K. K.; Robinson, C. J. *J. Vac. Sci. Technol. A* 1992, 10, 3143.

(7) Landstrass, M. I.; Ravi, K. V. *Appl. Phys. Lett.* 1989, 10, 975.

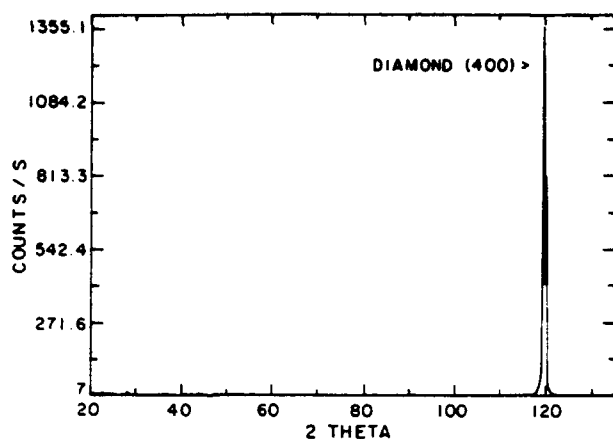


Figure 1. X-ray diffraction pattern for the microwave CVD film, showing predominant orientation in the  $\langle 100 \rangle$  direction.

(NMR) spectroscopy. The dc arc-jet and hot-filament films were examined for radial variations by these techniques. Since NMR measures average bulk concentration of the material residing in the sample probe, this radial resolution was achieved by sectioning these samples for individual measurements. Thick diamond samples were prepared for analysis by laser cutting, while thinner samples could be sectioned by hand. All samples were free standing and examined intact without crushing. No polishing of the interface exposed upon substrate removal was performed. We cannot distinguish if this region of initial growth has a different hydrogen content from subsequently grown material because NMR does not provide depth resolution. However, our previous work<sup>5,6</sup> does not show a strong relationship between film thickness and total hydrogen content, indicating that such an initial region does not contribute significantly to the overall hydrogen content measured by NMR.

Solid-state  $^1\text{H}$  NMR spectra were obtained at a static magnetic field of 6.7 T, giving a  $^1\text{H}$  Larmor frequency of 270 MHz, as described previously.<sup>5,6</sup> Approximately 1500 signal averages were performed at room temperature. A delay of 5 s between averages allows for complete spin-lattice relaxation of the protons. Comparison of the total integrated area under the spectrum obtained from a diamond film of a given weight with that of a poly(methyl methacrylate) (PMMA) standard yields quantitative hydrogen contents for the samples.<sup>9</sup>

### Results and Discussion

As anticipated based on previous reports,<sup>9,10</sup> SEM micrographs of the microwave film showed a relatively smooth surface with an average grain size of  $\sim 5 \mu\text{m}$ , predominantly oriented in the  $\langle 100 \rangle$  direction, as confirmed using X-ray diffraction (Figure 1). The SEM micrographs of the hot-filament and dc arc-jet prepared samples show significantly higher surface roughness with average grain sizes of  $10\text{--}15 \mu\text{m}$  and  $\sim 70 \mu\text{m}$ , respectively. The SEM and XRD analysis also show a smaller degree of orientation, primarily along the  $\langle 110 \rangle$  direction.

The solid-state  $^1\text{H}$  NMR spectra of the films deposited by each method are shown in Figure 2a–c. For the dc arc jet (Figure 2b) and hot-filament films (Figure 2c), spectra for both the central ( $R = 0.0$ ) and one of the outer regions ( $R > 0$ ) are shown. For the microwave sample (Figure 2a), only a single spectrum was obtained. To facilitate line-shape comparison, each of the three parts of Figure 2, has a different normalization factor. However, within Figure 2b, the ratio of intensities of the two spectra equals the

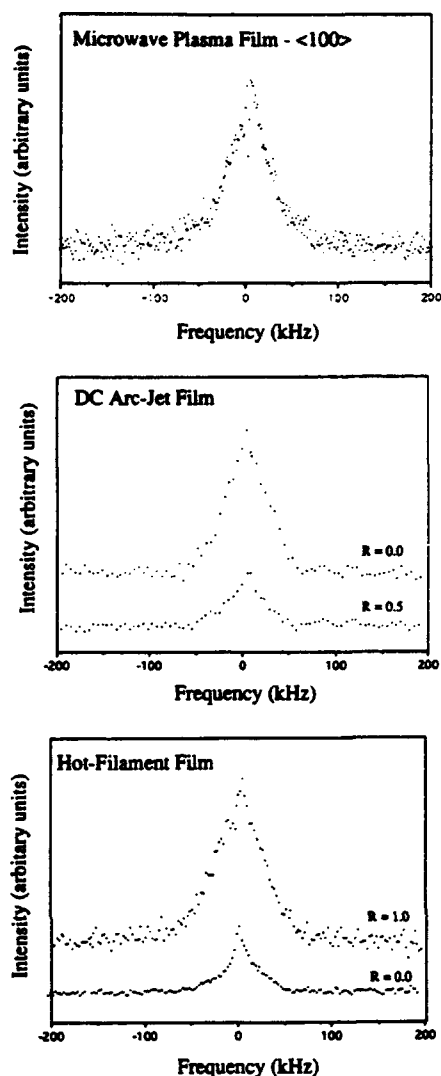


Figure 2. Solid-state  $^1\text{H}$  NMR spectra from (a) microwave, (b) dc arc-jet, and (c) hot-filament CVD diamond films. All spectra show similar line shapes. For the dc arc-jet film (b), the integrated intensity of the spectra from the center ( $R = 0.0$ ) versus that at a radius of 1 in. ( $R = 0.5$ ) of the dc arc-jet film, indicates a decrease in the hydrogen content by a factor of  $\sim 2.5$ . For the hot-filament film (c), the intensity difference between the integrated area for the center ( $R = 0.00$ ) and the outer edge ( $R = 1.00$ ) indicates an  $\sim 7$ -fold increase.

ratio of their hydrogen contents. The same is true for the spectra in Figure 2c.

Each line shape in Figure 2 contains two components, a narrow Lorentzian and a broad Gaussian, consistent with the observations of earlier NMR studies.<sup>5,6</sup> In that work, the narrow Lorentzian component of the line shape is associated with motionally averaged hydrogen. The Gaussian component, on the other hand, is attributed to static, densely packed hydrogen. Here, as in the earlier investigations, a majority of the hydrogen is associated with the broad component (i.e., static hydrogen) and only a small fraction is motionally narrowed. Previously, multiple-quantum NMR has shown the static, densely clustered hydrogen to be primarily distributed on two-dimensional surfaces rather than on three-dimensional lattices.<sup>11</sup> Hydrogen passivation of grain boundary and growth surfaces in the polycrystalline films could account for observed hydrogen incorporation levels. Indeed, films

(8) Levy, D. H.; Gleason, K. K. *J. Vac. Sci. Technol. A* 1993, 11, 195.

(9) Wild, C.; Koidl, P.; Müller-Seibert, W.; Walcher, H.; Kohl, R.; Herres, N.; Locher, R.; Samlenski, R. *Diamond Relat. Mater.* 1993, 2, 158.

(10) Dischler, B.; Wild, C.; Müller-Seibert, W.; Koidl, P. *Physica B* 1993, 185, 217.

(11) Levy, D. H.; Gleason, K. K. *J. Phys. Chem.* 1992, 96, 8125.

Table 1. Summary of Radial Variation for Dc Arc-Jet Diamond Film

normalized radial position	$R = 0.00$	$R = 0.25$	$R = 0.50$	$R = 0.75$
at. % H	0.023	0.020	0.009	0.026
fwhm <sub>NMR</sub> (kHz)	58.4	56.4	57.0	60.1
fwhm <sub>L</sub>	6.6	8.0	9.6	7.0
fwhm <sub>1332</sub> Raman (cm <sup>-1</sup> )	17.3	13.5	9.3	9.3

with larger grain boundary areas (i.e., smaller crystallite sizes) have higher hydrogen contents.<sup>6</sup> However, hydrogen decoration of surfaces associated with defects internal to the crystallites cannot be ruled out. In films with higher hydrogen contents (>1 at. %) than those previously examined by multiple-quantum NMR, additional types of hydrogen incorporation may also exist. It is interesting that the characteristics of the NMR line shape, and thus the local hydrogen bonding environment, do not change significantly with deposition technique. This may indicate a common surface process occurs under these different conditions.

Integration of the NMR line shapes show that the hydrogen content of the microwave sample is approximately an order of magnitude higher (0.120 at. %) than those observed in the center of the hot-filament (0.031 at. %) and dc arc-jet (0.023 at. %) samples. Although hot-filament films with such high hydrogen contents have been previously observed by NMR, they are not common.<sup>5,6</sup> For hydrogen contents of >0.1 at. %, the concentrations measured by NMR are somewhat lower than calculated from the CH stretch IR region, although good agreement between the two techniques was found at lower concentrations.<sup>6</sup> Between 0.4 and 0.9 at. % H has been measured by IR spectroscopy for (100) textured microwave films,<sup>10</sup> in rough agreement, although slightly higher, than the NMR measurement of the textured microwave sample used in this study. There are several possible explanations for this relatively high hydrogen concentration of this sample. First, the surface area available for hydrogen passivation could be larger. In support of this hypothesis, its 5- $\mu$ m crystallite size is relatively small compared to films previously studied by NMR. In addition, crystallite size evolves with film thickness.<sup>10</sup> This evolution may lead to more grain boundary area in a strongly (100) textured film as compared to the more commonly weakly (110) textured material. Another possibility is that the (100) texture exposes surfaces which allow a higher hydrogen packing density or that additional locations for hydrogen incorporation exist, such as a non-diamond phase. However, such changes are not apparent in the NMR line width which is determined by the distribution of proton spacings.

Radial variations in hydrogen content were observed for both the hot-filament and dc arc-jet diamond. Samples from the dc arc-jet material were laser cut 5-mm diameter disks cut at 0.5-in. intervals along the 2-in. radius of the film. Labeling from center to edge and normalizing, samples are taken at  $R = 0.00$ ,  $R = 0.25$ ,  $R = 0.50$ , and  $R = 0.75$ . Note that no sample was obtained from the outer edge of the film. The hydrogen concentrations obtained from the total integrated area under the NMR line shape are listed in Table I. Also listed are the full-width at half-maximum (fwhm) of both the Gaussian and Lorentzian components of the NMR line. A comparison of the <sup>1</sup>H NMR line shapes obtained at the center of the sample ( $R = 0.00$ ) and 1.0 in. from the center ( $R = 0.50$ ) are shown in Figure 2b. The integrated area under the line shapes

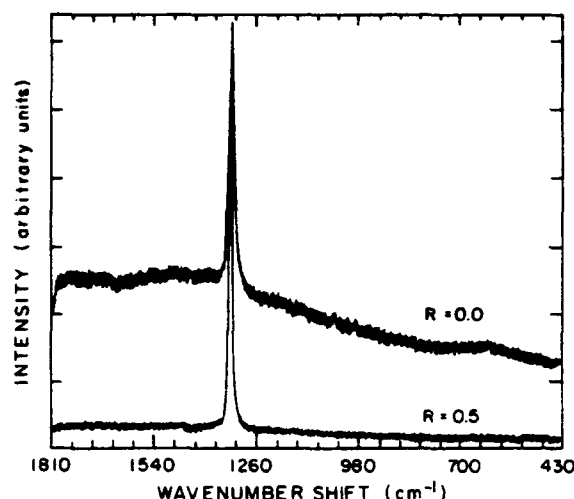


Figure 3. Raman spectra taken from the dc arc-jet sample at  $R = 0.00$  and  $R = 0.50$ . No artificial offset imposed on these spectra, indicating a larger background signal at  $R = 0.00$ . The linewidth of the 1332 cm<sup>-1</sup> peak (Table I) is also broader at this central position.

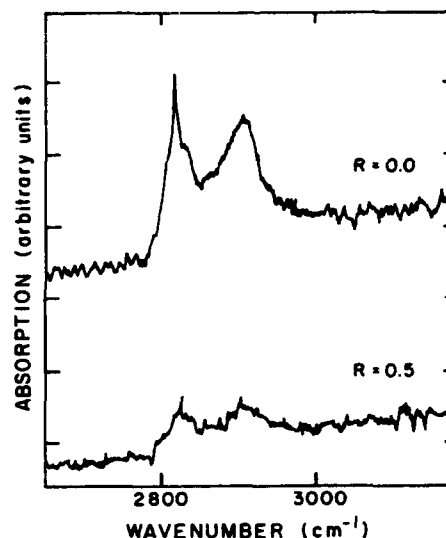


Figure 4. Infrared spectra of samples taken from the dc arc-jet sample at  $R = 0.00$  and  $R = 0.50$ . The absorption in the CH stretch region is larger at  $R = 0.00$ , consistent with the <sup>1</sup>H NMR results (Figure 2b). Also, a strong mode at ~2820 cm<sup>-1</sup> is apparent in the  $R = 0.0$  spectrum.

indicate that the center piece contains more than twice the amount of hydrogen (0.023 at. %) found in the sample obtained 1 in. from the center (0.009 at. %). The shape of the NMR line, however, does not change significantly.

Comparison of the two corresponding Raman spectra (Figure 3) shows a larger fwhm for the 1332-cm<sup>-1</sup> peak (Table I) and an increase in background signal intensity for the central ( $R = 0.0$ ) region. Note that the offset between the two Raman spectra in Figure 3 is real and not artificially produced.

In addition, the IR spectrum (Figure 4) of the dc arc film shows an increase in the CH-stretch absorption in the center of the film, in agreement with the higher hydrogen observed by NMR. These IR spectra also show a strong absorption at 2820 cm<sup>-1</sup>, from the central region of the film ( $R = 0$ ). This absorption occurs at lower wavenumbers than CH<sub>2</sub> bonding configurations in polycrystalline diamond and diamond-like carbon films and has previously been observed in CVD diamond films.<sup>6,10</sup> A tentative assignment of this mode as monohydride species at

**Table 2. Summary of Radial Variation for Hot-Filament Diamond Film**

normalized radial position	$R = 0.00$	$R = 0.50$	$R = 1.00$
at. % H	0.031	0.039	0.229
fwhm <sub>G</sub> NMR (kHz)	62.2	69.6	72.9
fwhm <sub>L</sub> NMR (kHz)	10.5	17.6	8.8
fwhm <sub>1332</sub> Raman (cm <sup>-1</sup> )	6.1	6.1	5.5

dislocations or similar defect sites has been suggested.<sup>10</sup> Another possibility is related to IR studies of organic molecules where stretching frequencies between 2810–2820 and 2805–2870 cm<sup>-1</sup> have been cited for  $\nu$ -OCH<sub>3</sub> and  $\nu$ -NCH<sub>3</sub> groups, respectively.<sup>12</sup> The prevalence of oxygen and nitrogen as impurities or as intentionally introduced components in the gas phase of diamond deposition environments suggests that  $\nu$ -OCH<sub>3</sub> or  $\nu$ -NCH<sub>3</sub> groups might account for the 2820-cm<sup>-1</sup> absorption in polycrystalline diamond. Further work is required before a definitive assignment of this mode is made and its relationship to the diamond growth process is established.

Results for the radial variation of the hot-filament CVD diamond were obtained from sections broken from the sample at 0.25 inch intervals along the 0.5+ inch radius of the film and are recorded in Table 2. Labeling from center to edge and normalizing, samples are taken at  $R = 0.00$ ,  $R = 0.50$ , and  $R = 1.00$ . The variations in the fwhm of both NMR components and the 1332-cm<sup>-1</sup> peak in the Raman spectra are also recorded in Table 2. A significant increase in hydrogen content from 0.031 at. % to 0.229 at. % is observed in the <sup>1</sup>H NMR spectra (Figure 2a) obtained from diamond located near the edge ( $R = 1.00$ ) as compared to the center ( $R = 0.00$ ) of this sample. Although there is an increase of almost an order of magnitude in hydrogen concentration, little variation is observed in either the fwhm or the NMR line shapes.

The central and edge samples from the hot-filament film have similar 1332 cm<sup>-1</sup> peak fwhm in the Raman spectra (see Table 2). Thus, higher hydrogen content does not relate to increased broadness of the Raman one-phonon mode, as was seen in the dc arc-jet film (Figure 3). However, the background in the  $R = 1.0$  Raman spectra of the hot-filament material is larger than for the  $R = 0.0$  spectra (note that no artificial offset was introduced in Figure 5). In both the dc arc-jet (Figure 3) and hot-filament (Figure 5) samples, a larger Raman background was noted for regions of higher hydrogen content. This observation may only be a coincidence and does not necessarily indicate a cause-and-effect relationship. However, higher hydrogen contents are expected as grain boundary area and the fraction of non-diamond-bonded phases increases. These two trends could also influence phenomena which might give rise to the Raman background signal such as luminescence, scattering or absorption of non-diamond phases. Indeed, a peak at  $\sim 1500$  cm<sup>-1</sup> is observed at  $R = 1.0$  (Figure 5) indicating the presence of non-diamond carbon in this region of relatively high hydrogen content.<sup>13</sup>

The larger CH stretch absorption observed at  $R = 1.0$  in Figure 6 indicates a significantly higher hydrogen content at the edge of the hot-filament film, in agreement with the NMR results (Figure 2c). As previously observed,<sup>6,10</sup> the characteristic symmetric and asymmetric stretching modes of CH<sub>2</sub> groups at  $\sim 2850$  and  $\sim 2920$  cm<sup>-1</sup> are clearly visible in the  $R = 1.0$  IR spectra. The

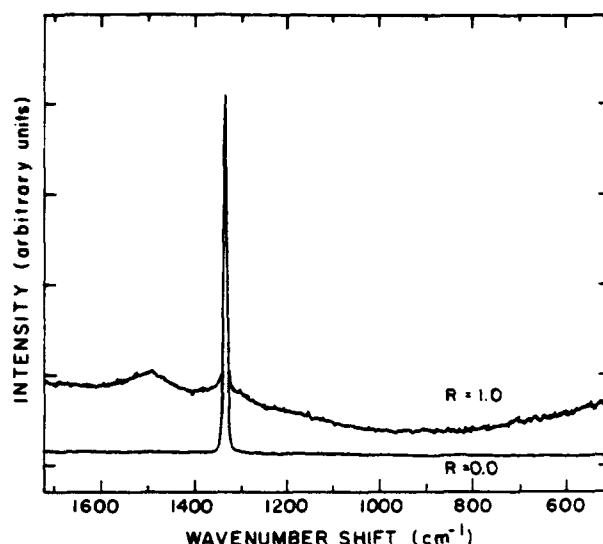


**Figure 5.** Raman spectra taken from the center ( $R = 0.0$ ) and outer edge ( $R = 1.0$ ) of the hot-filament film. Increased background is observed in the  $R = 1.0$  sample, which contains no artificial offset.

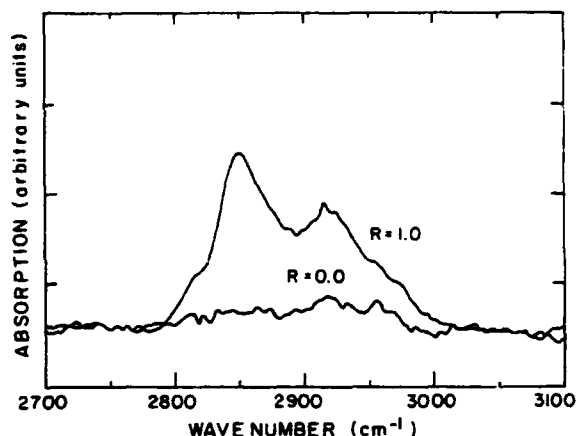


**Figure 6.** IR spectra taken from the hot-filament samples at  $R = 0.00$  and  $R = 1.00$ . The sharp increase in absorption in the CH stretch region at  $R = 1.00$  is consistent with the <sup>1</sup>H NMR results (Figure 2c). Strong stretching modes from CH<sub>2</sub> groups dominate the  $R = 1.0$  spectrum.

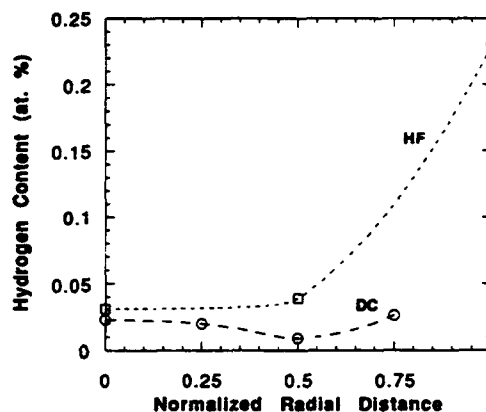


**Figure 7.** Hydrogen content of the dc arc-jet and hot-filament CVD diamond films as a function of normalized radial position.

mode at  $\sim 2820$  cm<sup>-1</sup> is also apparent in Figure 6, although less intense than for the dc arc-jet film (Figure 4).

Figure 7 shows a plot of the variation in hydrogen content as a function of normalized radial position for the hot-filament and dc arc-jet samples. The material located away from the edges of both samples have surprisingly

(12) Bellamy, L. J. *The Infrared Spectra of Complex Molecules*; Chapman and Hall Ltd.: London, 1960; Vol. 2.

(13) Knight, D. S.; White, W. B. *J. Mater. Res.* 1985, 4, 5873.

similar hydrogen contents,  $\sim 0.01$ – $0.04$  at. %, despite the difference expected for the growth rates in dc arc-jet and hot-filament environments.<sup>4</sup> Thus, the similarity in hydrogen content in the two films may indicate that hydrogen incorporation is controlled by surface processes which are similar in both systems. The results, however, are not identical. The hot filament diamond film shows a significant increase in hydrogen with radial position, while the trend in the arc-jet film is unclear. A slight increase is observed in the outermost region, but no samples were obtained less than  $1/2$  in. from the edge. There is also a minimum in the hydrogen content at the position halfway between the center and edge of the sample ( $R = 0.50$ ).

The fact that similar hydrogen contents are observed in the center of the growth region on both samples may indicate a similar mechanism for diamond formation in both processes. The variations in hydrogen content, on the other hand, may result from fluctuations in the gas-phase concentrations above the growth surface, nonuniformities in surface temperature, orientation of the crystallite growth surface, and surface area of these crystallites. The importance of these factors may differ between the two growth environments and even between different reactors of the same type, which serves to highlight the importance of understanding surface chemistry and controlling local reactor conditions in these systems in order to control film properties. This becomes particularly important for large area samples.

It is important to consider the effects of these variations in hydrogen content on the properties of diamond films. As an example, it has been demonstrated that hydrogen content can be quantitatively correlated with absorption in the CH stretch region in the IR spectrum (see Figures 6 and 9).<sup>5,6</sup> In addition, there is a qualitative correlation between hydrogen content and the film's absorption in the 8–10- $\mu\text{m}$  region.<sup>14</sup> This absorption is particularly important in the application of CVD diamond for infrared windows. Significant variations in this absorption would not permit the use of such large area diamond films in these applications. These nonuniformities also raise questions about the definition of specifications on diamond samples. One might expect to see specifications developed which include both the maximum absorbance or other characteristics of interest and the maximum tolerable variation in that parameter.

### Conclusions

Low hydrogen contents, as measured by  $^1\text{H}$  NMR, were observed at the centers of three polycrystalline diamond films deposited by distinctly different processes: microwave plasma (MW, 0.120 at. %), dc arc-jet (DC, 0.023 at. %) and hot-filament (HF, 0.031 at. %) CVD. This result is in agreement with a previous study of a series of hot-filament films, all of which contained  $<0.25$  at. % H. Thus, the three CVD methods studied here (MW, DC, and HF), may have a similar mechanism for hydrogen incorporation despite their expected differences in growth rate and gas-phase composition. Hydrogen incorporation at internal surfaces such as grain boundaries could account for this similarity. This would support the hypothesis of hydrogen termination of the growing surfaces in these three different CVD environments. In addition, the hydrogen contents of the diamond films are extremely low compared to those for typical hydrogenated amorphous carbon films prepared

by radiofrequency plasma CVD ( $\sim 10$  to  $>50$  at. %).<sup>15</sup> Thus, very little of such a heavily hydrogenated amorphous carbon can exist in polycrystalline diamond.

The distribution of surfaces available for hydrogen passivation should vary with the texture of a polycrystalline diamond film and thus produce changes in the  $^1\text{H}$  NMR line shape. However, the MW film, which displays (100) oriented crystals at the surface, has a similar proton NMR line shape to the DC and HF films which have a weaker (110) preferred orientation. If only surfaces from the large oriented crystallites were being observed, the expected hydrogen content of the MW would be quite low. However, the highly textured MW film has an order of magnitude higher hydrogen content than the central regions of the DC and HF materials. Thus, other surfaces, such as from smaller crystallites which are covered over during growth or from internal void surfaces within crystallites, most likely dominate the NMR spectra of the MW film.

The CH stretch region of the IR spectra allows observation of the distribution of covalent bonding environments for hydrogen in polycrystalline diamond. Clear differences are seen between films and spatially within a single film. In particular, the  $\text{CH}_2$  stretching modes can be well defined. In addition, some film regions contain a distinct mode at  $\sim 2820\text{ cm}^{-1}$ , which lacks a defined assignment. This mode is not observed in hydrogenated amorphous carbon films and represents a distinct configuration of hydrogen in polycrystalline diamond. A one-to-one correspondence exists between the remaining absorptions in the  $\text{CH}_x$  stretching region of diamond and those of hydrogenated amorphous carbon films.<sup>6,10</sup> If these environments represent the growing diamond surface, there is a large heterogeneity of surface sites during polycrystalline film growth.

Using  $^1\text{H}$  NMR, significant radial hydrogen concentrations variations were observed in the HF film, from 0.031 at. % at the center to 0.229 at. % at the edge. Regions with higher hydrogen contents also gave rise to increased background signals Raman spectra, although no cause-and-effect relationship may exist. Thus, despite the high diffusivities of gas-phase species HFCVD diamond reactors and steps taken to minimize thermal gradients at the growth surface (thick substrates and sample rotation), variations in hydrogen content can occur. Such differences in hydrogen content are known to affect the optical quality of diamond and will likely impact other properties, as well. Better understanding of the surface kinetics, gas-phase kinetics and mass transport is required to reduce spatial variations in film quality, particularly in large area films.

**Acknowledgment.** The authors are grateful Dr. Kevin Gray of Norton Company and to Dr. Cliff Robinson of Raytheon Co. for contributing samples and IR spectra for this work and to Dr. Peter Koidl of the Fraunhofer Institut für Angewandte Festkörperphysik for contributing the highly oriented diamond film. We would also like to thank Dr. James E. Butler and Daniel J. Vestyck of the Naval Research Laboratory for help with the Raman spectroscopy and Michael Kwan of MIT for assistance with the SEM work. Finally, we are grateful to the Office of Naval Research, the National Science Foundation (NSF Grant No. CTS-9006705), who provided funding for this work.



## USING ZEOLITES AS SUBSTRATES FOR DIAMOND THIN FILM DEPOSITION

MICHAEL C. KWAN AND KAREN K. GLEASON

Massachusetts Institute of Technology, Department of Chemical Engineering, 66-462,  
Cambridge, MA, 02139

### ABSTRACT

Zeolites have been used as a potential substrate for CVD diamond deposition. By saturating the pore channels of a silicalite crystal, which are spaced approximately 10 Å apart, with hydrocarbon seeds to induce and control nucleation, films have been grown in a hot filament chemical vapor deposition (HFCVD) system under standard deposition conditions, using acetone as the carbon source. The hydrocarbons used were adamantane, naphthalene, anthracene, 2,3-benzanthracene, and 1,2:5,6-dibenzanthracene. To enhance nucleation, a high pressure pre-deposition period was used initially.

Characterization of these films through electron diffraction and Auger electron spectroscopy indicates that polycrystalline  $\beta$ -SiC imbedded in an amorphous matrix is initially formed and large, well faceted diamond crystals are subsequently nucleated.

### INTRODUCTION

Diamond is a technologically interesting material because of its unusual combination of extreme mechanical, thermal, and electrical properties. It is the hardest material known ( $10^4$  kg/mm<sup>2</sup>) and has the highest thermal conductivity of any material (20 W/cm-K). In addition, it has a band-gap of 5.45 eV, a hole mobility of 1600 cm<sup>2</sup>/V-s, and an electron mobility of 1900 cm<sup>2</sup>/V-s, all of which makes diamond a superb candidate for high temperature, high speed electronic devices. One of the primary barriers which must be now overcome to realize this technology is the heteroepitaxy of either a single crystal or very high quality, oriented polycrystalline film.

One approach which has been taken is to control the sites for nucleation of diamond through the shape modification of the substrate surface. Geis, *et al.* demonstrated a mosaic film technique in which a smooth, high-quality film was grown from oriented diamond seeds placed in 100  $\mu$ m spaced inverted, square pyramids that had been etched into a silicon wafer<sup>1</sup>. Recently, Spitzl, *et al.* reported on the deposition of micron thick diamond films on porous silicon substrates of varying porosity<sup>2</sup>. Depending on the etching conditions used and the doping of the substrate, the randomly distributed features on porous silicon can have an interpore spacing of anywhere from 5 nm to 200 nm.

According to Wild *et al.*, (100) textured films can be produced from randomly oriented nuclei once the film is made sufficiently thick<sup>3</sup>. Modeling shows that the film thickness required to generate well-textured films depends on the initial spacing of the nuclei; closely spaced nuclei allow the formation of a textured film at smaller film thicknesses than do widely spaced nuclei<sup>4</sup>. When compared with the mosaic film technique, growth on porous silicon represents a three orders of magnitude decrease in the spacing of the nucleation centers. Therefore it is expected that films grown on porous silicon would require considerably less time to achieve a well-formed morphology. Here we have attempted to extend this concept to yet smaller spacings, employing zeolites as substrates for diamond deposition.

### Zeolites

Zeolites, also known as molecular sieves, are a general class of nanoporous, crystalline materials that are widely used in the chemical industry as catalysts and adsorbents. Most zeolites are aluminosilicates and have a general composition of  $H_mAl_mSi_{m-n}O_{2m}$ . Some also

incorporate low molecular weight, singly charged cations such as sodium and magnesium. At the other end of the spectrum, materials such as silicalite are composed solely of Si and O. Since zeolites become more thermally stable as their Si/Al ratio increases, silicalite, which is stable to 1200 °C was selected as a substrate for diamond deposition. Because of their crystallinity, zeolite surfaces display a distinct, regular structure composed of pore openings that range from 2-15 Å separated by interpore spacings which range from 5-31 Å. In particular, silicalite, which has a ZSM-5 crystal structure, has pores that are 5.5 Å in diameter and are spaced 12 Å to 20 Å apart, depending on the particular direction and crystal face. When compared with porous silicon substrates, the nucleation sites on a silicalite crystal are then potentially two orders of magnitude closer together.

In this study, the silicalite crystals used are uniformly 60 x 15 x 15 µm in size. Examples are shown in Figure 1.

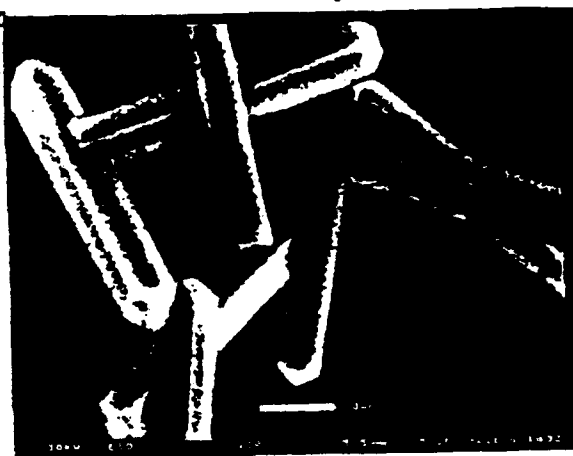


Figure 1: silicalite crystals

## EXPERIMENTAL SECTION

All of the experiments were performed with a hot filament chemical vapor deposition (HFCVD) system using hydrogen and acetone as the feed gases. The gases were activated with a planar, S-shaped tantalum filament. The substrate temperature was monitored by a K-type thermocouple contacting the back of the silicon wafer. Typical deposition conditions were gas feeds of 150 sccm of H<sub>2</sub>, 1.5 sccm of acetone, and a substrate temperature of 780 °C. The reactor pressure was 100 torr during the first ½ hour of deposition and was changed to 20 torr for the remaining 2 hours. When silicon wafers seeded with 0.5 µm diamond grit were used as substrates for this process, well faceted, ~7 µm thick polycrystalline diamond films resulted. Runs without the initial high pressure period resulted in etching of the silicalite crystals, probably due to the flux of H-atoms.

### sp<sup>3</sup> Bonded Hydrocarbon Seed

Matsumoto and Matsui have previously suggested that adamantane (C<sub>10</sub>H<sub>16</sub>; see Figure 2) and similar hydrocarbon cage compounds may act as "embryos" for diamond nucleation<sup>5</sup>. Working from the hypothesis that some form of sp<sup>3</sup>-bonded carbon acts as the nuclei for diamond formation, we used adamantane as our model compound. In addition, adamantane has an diameter of approximately 4 Å which should allow it to diffuse through the silicalite pores easily. Seeding was accomplished by placing the calcined zeolite powder into a solution of adamantane in methylene chloride for several days.

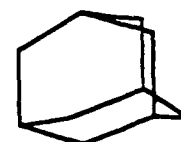


Figure 2

Scanning electron microscopy (SEM) and transmission electron microscopy (TEM) were used to analyze the post-deposition samples. SEM was performed via a ElectroScan Environment Scanning Electron Microscope and no special sample preparation was necessary. TEM films were prepared by subjecting the as-deposited samples to a hydrogen-only feed in the HFCVD reactor for half an hour; any remaining silicalite crystals or non-diamond carbon films were etched away. The residual material was then scraped onto a number of carbon film coated TEM grids for analysis.

### sp<sup>2</sup> Bonded Hydrocarbon Seed

It has also been proposed that diamond nucleation begins at the "edges" of sp<sup>2</sup>-bonded carbon compounds. In particular, Angus has reported the growth of diamond particles from the

edges of the basal planes of highly oriented pyrolytic graphite (HOPG) and from perylene tetracarboxylic acid dianhydride<sup>6</sup>. To investigate this possibility, a homologous series of linear polyaromatic hydrocarbons was also used as hydrocarbon seeds. They were naphthalene, anthracene, 2,3-benzanthracene, and 1,2:5,6-dibenzanthracene (see Figure 3). In addition, experiments were performed with acetone feeds of 0.0 and 1.0 sccm during the initial high pressure period to test the hypothesis that the local C-concentration at the zeolite surface may have been over high and leading to amorphous C deposition.

The analysis and characterization of samples were performed through SEM and Auger electron spectroscopy (AES). Samples for AES were prepared by manually moving and embedding the zeolite crystals into indium foil.

## RESULTS

### sp<sup>3</sup> Bonded Hydrocarbon Seed

The SEM result is displayed in Figure 4 and shows a shattered silicalite shaped shell. This translucent film is also accompanied by secondary nucleation of diamond on the film and on the silicon wafer.

The TEM image from an approximately 1  $\mu\text{m}^2$  film is shown in Figure 5. Note that it is composed of crystalline regions of roughly 10 Å diameter within an otherwise amorphous matrix. The electron diffraction pattern is shown in Figure 6a and graphically in Figure 6b; it identifies the crystalline component as  $\beta$ -SiC.

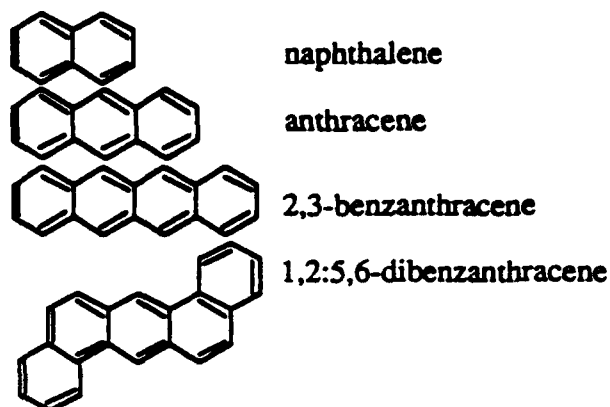


Figure 3



Figure 4: SEM of film on zeolite

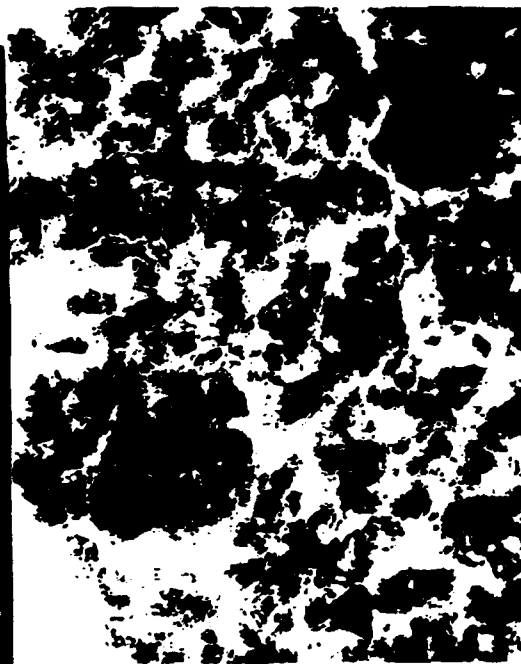


Figure 5: TEM of film on zeolite

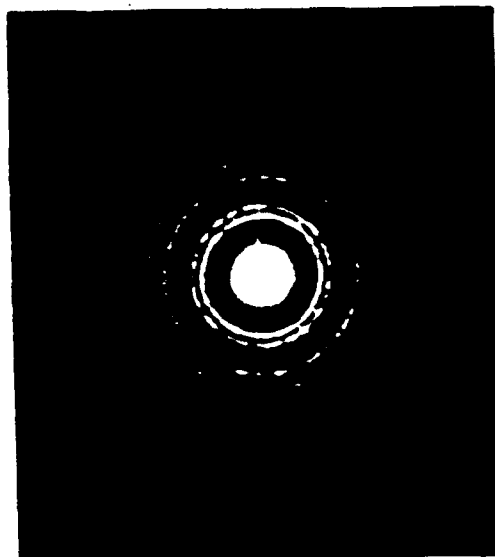


Figure 6a: electron diffraction pattern for adamantane seeded experiment

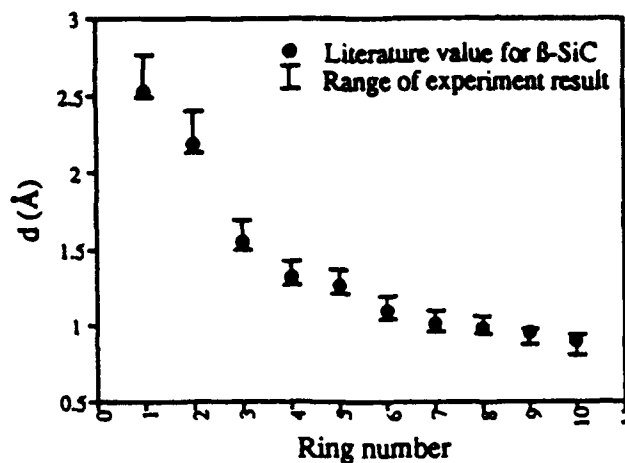


Figure 6b: electron diffraction result for adamantane seeded experiment

### sp<sup>2</sup> Bonded Hydrocarbon Seed

Figures 7a and b show the SEM results from the anthracene seeded experiments in which 1.0 sccm of acetone was used initially; Figure 7c shows the result from the 0.0 sccm experiment. The smooth coating on the zeolite in Figure 7a is most likely an amorphous carbon coating. Figure 7b is a higher magnification image of one of the point nucleated diamond particles shown in Figure 7a. Similar nucleation behavior has been observed by Li, *et al.* in the case of diamond nucleation on the edges of HOPG<sup>7</sup>. Because the SEM images from the experiments involving 2,3-benzanthracene and 1,2:5,6-dibenzanthracene showed that the majority of the zeolites were etched, it was concluded that the relatively large size of the seeds prevented them from diffusing into the zeolite pores and no further analysis was done upon those samples.



Figure 7a: SEM of zeolite from anthracene seeded experiment

Figure 7b: higher magnification picture of Figure 7a

In addition to analyzing the experimental samples via AES, standard spectra were taken of a free-standing HFCVD diamond film and of a crystalline graphite powder; they are displayed in Figures 8a and b, respectively. The distinguishing features to note are in the region immediately preceding the 272 eV C-KLL transition. Figure 8c is an AES spectra of  $\beta$ -SiC from Kaplan<sup>8</sup>. In Figure 9 shows another silicalite crystal from the sample shown in Figure 7c. An AES spectrum was taken from the outlined area after sputtering with a 1.5 keV  $\text{Ar}^+$  ion gun at a flux of  $9.8 \times 10^{18}$

$\text{cm}^{-2}$  and is shown in Figure 8d. Prior to sputtering, the sample exhibited an amorphous carbon spectra characteristic of adventitious carbon contamination. While the buckled film is clearly not diamond nor graphite, a careful comparison of Figures 8c and 8d indicate that the film is also not  $\beta$ -SiC.

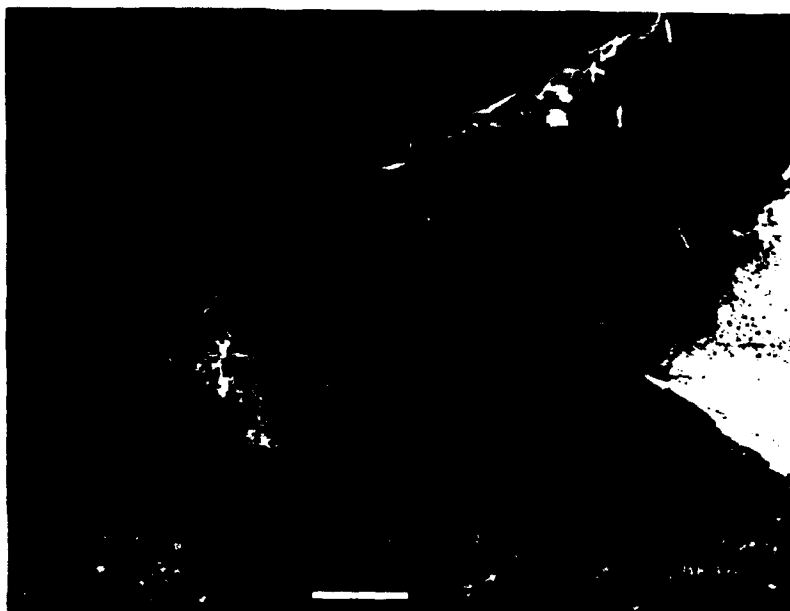


Figure 7c: SEM of zeolite from anthracene seeded experiment; 0.0 sccm initial feed

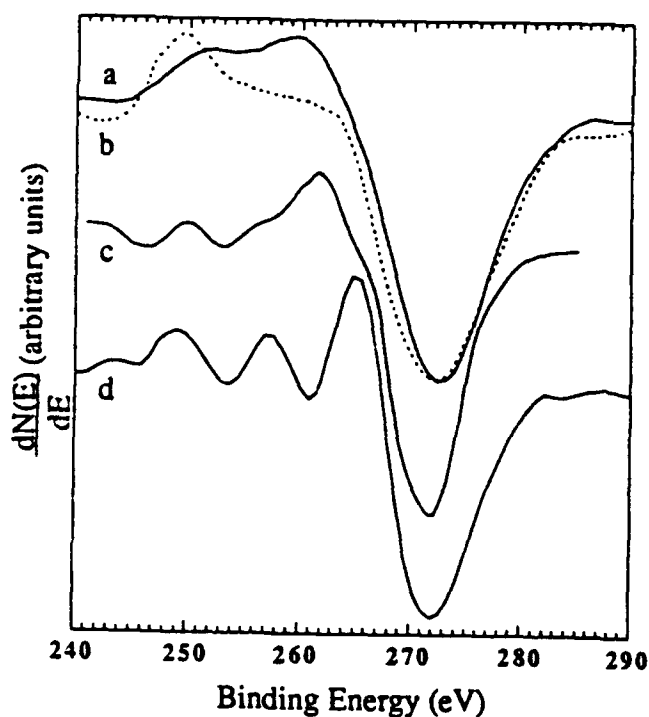


Figure 8: Auger spectroscopy results for: a) HFCVD film, b) crystalline graphite powder, c)  $\beta$ -SiC from Kaplan, d) film on zeolite from Fig. 9

## CONCLUSIONS

A novel method for controlling the nucleation of CVD diamond films at the molecular level has been proposed using zeolites as potential substrates. By saturating the pore channels of a silicalite crystal with hydrocarbon seeds to induce and control nucleation, films were grown in a HFCVD system. The hydrocarbons used were adamantane, naphthalene, anthracene, 2,3-benzanthracene, and 1,2:5,6-dibenzanthracene.

Characterization of the film from the adamantane seeded silicalites was through electron diffraction and indicated that it was

polycrystalline  $\beta$ -SiC imbedded in an amorphous matrix. Auger electron spectroscopy was performed on a film from an anthracene seeded silicalite. While a surface carbide layer was clearly indicated, it was not possible to identify the film as any single phase. Most likely, the film was again a mixture of crystalline and amorphous phases.

In conclusion, the concept of using a molecular scale patterned substrate to control the nucleation of a CVD generated diamond film is still potentially interesting process but would require either a crystalline, nanoporous, non-carbide former as the substrate or the use of a low temperature deposition process to avoid the carbide formation problem in the zeolites.

## ACKNOWLEDGMENTS

We gratefully acknowledge support from the Office of Naval Research.

## REFERENCES

1. M. W. Geis, H. I. Smith, A. Argoitia, J. Angus, G.-H. M. Ma, J. T. Glass, J. Butler, C. J. Robinson, and R. Pryor, *Appl. Phys. Lett.*, **58** (22), 2485 (1991).
2. R. Spitzl, V. Raiko, and J. Engemann, presented at the 4<sup>th</sup> European Conference on Diamond, Diamond-like and Related Materials, Albufeira and Algarve, Portugal, 1993 (unpublished).
3. C. Wild, P. Koidl, N. Herres, W. Müller-Sebert, and T. Eckermann, *Electrochem. Soc. Proc.*, **91-8**, 224 (1991).
4. C. Wild, P. Koidl, W. Müller-Sebert, H. Walcher, R. Kohl, N. Herres, and R. Locher, *Dia. Rel. Mat.*, **2**, 158 (1993).
5. S. Matsumoto, and Y. Matsui, *J. Mat. Sci.*, **18**, 1785 (1983).
6. J. C. Angus, Z. Li, M. Sundara, R. Gat, A. B. Anderson, S. P. Mehandru, and M. W. Geis in *2<sup>nd</sup> International Symposium on Diamond and Diamond Materials*, vol. **91-8**, 125, (1991).
7. Z. Li, L. Wang, T. Suzuki, A. Argoitia, P. Pirouz, and J. C. Angus, *J. Appl. Phys.*, **73** (2), 711 (1993).
8. R. Kaplan, *J. Appl. Phys.*, **56** (6), 1636 (1984).



Figure 9: zeolite used for Auger spectroscopy; spectra was taken by rastering over outlined area

## **Identification of Defects and Impurities in Chemical Vapor Deposited Diamond through Infrared Spectroscopy**

**K.M. McNamara\***, General Electric Company, Corporate Research and Development, Schenectady, NY 12301

**B.E. Williams**, General Electric Company, Superabrasives, Worthington, OH

**K.K. Gleason and B.E. Scruggs**, Department of Chemical Engineering, Massachusetts Institute of Technology, Cambridge, MA 02139

### **Abstract**

Hydrogen, oxygen, and nitrogen related defects in CVD diamond have been observed by infrared spectroscopy and found to effect optical absorptions in spectral regions of commercial interest. The origin of absorptions in the infrared spectrum at  $2820\text{ cm}^{-1}$  and  $2833\text{ cm}^{-1}$ , which have been observed previously without being understood, have been identified. The presence of these absorptions and the evidence of oxygen and nitrogen incorporation in CVD diamond have important implications for both the design of CVD diamond growth systems and the design of processes involving oxygen addition. In films which contain high hydrogen concentrations ( $> 0.2$  atomic %), some evidence has been found indicating the presence of a hydrogen environment, not present in films with lower hydrogen contents, which may be related to  $\text{sp}^2$  bonded carbon.

\*Author to whom correspondence should be addressed

## Introduction

Recent advancements in diamond deposition have made possible the formation of large area, free standing diamond sheets with optical properties approaching those of type IIa diamond. The ability to obtain diamond in dimensions which are not economically or otherwise feasible with natural diamond or high-pressure high-temperature (HPHT) synthetic stones, suggests a variety of new applications for this material. Polycrystalline diamond, however, contains grain boundaries and defects not present in single crystal stones. These impurities can lead to variations in the properties of the material, including optical absorption in regions of commercial interest, where none are observed in type IIa diamond. To control the optical properties of CVD (chemical vapor deposited) diamond, we need a better understanding of the defects which cause such absorptions and their origin.

A variety of techniques are used to deposit diamond films at an even wider variety of conditions.<sup>1-3</sup> A majority of CVD processes use a dilute mixture of some hydrocarbon (typically methane) in hydrogen. In addition, some processes use oxygen, added separately or as a constituent of the carbon source.<sup>4,5</sup> The effects of oxygen on growth rate and film quality, as defined by Raman spectroscopy, have been noted throughout the literature.<sup>6,7</sup> The effects of oxygen addition on film properties, however, has not been extensively explored.<sup>5</sup> This study addresses the fate of oxygen, as well as other impurities, introduced intentionally or otherwise, in CVD diamond growth.

Infrared (IR) spectroscopy has been used previously<sup>8-12</sup> to study hydrogen in CVD diamond. Here, it is used, in combination with other



techniques including nuclear magnetic resonance (NMR), x-ray photoelectron spectroscopy (XPS), and x-ray diffraction, to elucidate information not only about hydrogen and its bonding environment, but also about other impurities, such as nitrogen and oxygen. We will demonstrate that each of these impurities can have substantial effects on the optical absorption of diamond in areas of potential interest, including the 8-12  $\mu\text{m}$  wavelength region of the infrared spectrum.. In addition, we identify the origin of two peaks which have been observed previously in the CH-stretch region (2750-3300) of the IR spectra of CVD diamond,<sup>8-11</sup> but have not been understood until the present work.

## Experimental

The majority of the diamond films discussed in this work were made by a proprietary microwave CVD process under a variety of conditions. Conditions were chosen to produce material with a range of optical properties in order to observe the changes in defect content with increasing film quality. Other materials discussed here were produced by hot-filament CVD and DC arc-jet CVD. The conditions for the production of these materials have been discussed elsewhere.<sup>10</sup> In all cases, substrates were removed to yield free-standing diamond films ranging in thickness from 100  $\mu\text{m}$  to > 500  $\mu\text{m}$ . This substrate removal process, by dissolution in acid or other proprietary methods, does not alter or remove any portion of the diamond film. The films varied in visible transparency from opaque to water-clear. By comparing films of varying thickness which were produced under the same conditions, the variation in optical quality was determined to be primarily a function of process conditions rather than thickness. An example of the infrared transmission spectrum of a highly transparent CVD diamond film is shown in Figure 1. Note the

transmission in the 8-12  $\mu\text{m}$  region is  $\sim 70\%$ , approaching the that of the best natural diamond.

Infrared spectra were obtained on a Nicolet FTIR spectrometer. Films were examined as grown without polishing. Contributions due to surface and internal scattering processes were estimated using an appropriate polynomial baseline fit. The measured transmittance,  $T$ , is then converted to absorbance,  $A$ :

$$A = \ln(T_0/T) \quad (1)$$

where  $T_0$  refers to the polynomial fit. Spectra were obtained over a frequency range of 900 to 3500  $\text{cm}^{-1}$ . All diamond shows an intrinsic absorption in the two-phonon range between 1333 and 2666  $\text{cm}^{-1}$ . However, diamonds containing defects often show additional absorption in the symmetry forbidden one-phonon region below 1333  $\text{cm}^{-1}$  and in the region between 2750 and 3300  $\text{cm}^{-1}$ , known as the CH-stretch region. CH-stretch absorptions are particularly prevalent in CVD diamond.

In this study, nuclear magnetic resonance techniques have also been used to obtain quantitative information on hydrogen contents in CVD diamond films as well as some insight into the distribution and local environment of this hydrogen. Each hydrogen nucleus gives rise to the same signal intensity, regardless of its bonding environment, allowing the calculation of quantitative hydrogen contents by comparison to a known standard of known hydrogen content. Here, the standard is a polymethyl-methacrylate film deposited on a highly resistive silicon wafer. The hydrogen NMR lineshape from polymethyl-methacrylate is a Lorentzian with a full width at half-maximum (FWHM) equal to roughly 30 kHz. It is desirable to have a standard linewidth comparable to

that of the unknown so that the variations due to the influence of signal processing parameters is minimized.

Solid-state proton NMR spectra were obtained on a home-built 6.3 Tesla spectrometer. Spectra were obtained following a  $90^\circ$  pulse, where  $\pi/2 = 1.5 \mu\text{s}$ . Between  $5 \times 10^3$  and  $5 \times 10^4$  transients were acquired to achieve the desired signal-to-noise ratio. A recycle delay of 5 s was chosen to allow the system to return to equilibrium with the static magnetic field between acquisitions. A spin-lattice relaxation time of  $< 1$  s was determined previously for CVD diamond films of similar hydrogen content<sup>9</sup>, and is defined by the Bloch equation<sup>13</sup>:

$$\frac{M(t) - M_{eq}}{M_0 - M_{eq}} = \exp(-t/T_1) \quad (2)$$

where  $M(t)$  is the net magnetization parallel to the external magnetic field at time,  $t$ ;  $M_{eq}$  is the equilibrium magnetization; and  $M_0$  is the initial magnetization at time,  $t = 0$ . Spectra were acquired approximately 15 kHz off-resonance to avoid distortion of the Lorentzian component of the lineshape by zero frequency (DC) noise.

Diamond samples were obtained from intact free-standing films, laser-cut to dimensions suitable for the NMR probe coil which was 7 mm in diameter and 25 mm long. Samples were acid washed for one hour in a boiling solution of equal parts: deionized water, 96% sulfuric acid, and 70% nitric acid to eliminate any amorphous carbon generated in the laser cutting process. The detection limit for hydrogen in the spectrometer is  $10^{17}$  protons, which corresponds to  $\sim 4$  mg for a sample with a hydrogen content of 0.05 atomic %.

Other techniques used to examine the diamond samples discussed here include scanning electron microscopy (SEM), x-ray photoelectron spectroscopy, and x-ray diffraction. SEMs provide information about grain size and surface morphology, while x-ray diffraction reveals crystal orientation data. XPS was used to identify or confirm impurities incorporated in the films including nitrogen, oxygen, and a number of metallic impurities. This is primarily a surface technique with the capability of probing several hundred angstroms into the film when combined with argon sputtering.

## Results and Discussion

A total of 16 diamond films were made by microwave CVD for this study. The infrared spectra of a representative film is shown in Figure 2. It shows absorptions in the one, two, and three phonon regions, as do all of the films studied here. As mentioned earlier, the two phonon absorption between 1333 and 2666  $\text{cm}^{-1}$  is intrinsic to pure diamond. Thus, it can be used to normalize spectra from samples of varying thickness. It is the absorptions outside of this region which yield information about the impurities and defects in diamond. While varying in intensity with respect to the two phonon absorption, these one and three phonon absorptions appear at the same characteristic frequencies in all of the spectra discussed here.

The CH-stretch region (2750-3300  $\text{cm}^{-1}$ ) contains information about hydrogen bonded to carbon and other atoms, present as impurities, in diamond films. In this frequency range, we see the stretching vibrations of carbon-hydrogen bonds. The frequency of the bond vibration is shifted slightly for bonds in different local environments, allowing us to differentiate  $\text{CH}_x$  groups.<sup>15,16</sup> For example, the CH-stretch signatures of hydrogen bonded to  $\text{sp}^2$

bonded carbon appear above  $2950\text{ cm}^{-1}$ , while those associated with  $\text{sp}^3$  bonded carbon appear below  $3000\text{ cm}^{-1}$ .<sup>15,16</sup> Thus, IR spectroscopy yields information about the carbon bonding environment as well as that of hydrogen. Figure 3 shows the CH-stretch region of two typical diamond films.

Upon closer examination of the CH-stretch region in Figure 3, it is evident that some diamond films contain hydrogen bonded to  $\text{sp}^2$  carbon, while in other films, it is below the detection limit. Films containing  $\text{sp}^2$  bonded CH groups generally show higher overall hydrogen contents (see below) than those showing only absorptions below  $3000\text{ cm}^{-1}$ . The number of hydrogen atoms bonded to a single carbon will also cause variation in the frequency of the stretch vibration. Typical wavenumbers for  $\text{CH}_x$  stretch vibrations observed in diamonds are listed in Table I.<sup>9,11</sup> Using these approximate frequencies, we can perform a least squares fit to the experimentally measured CH-stretch absorption to determine the species present. However, there are still a large number of fitted parameters. It is possible to decrease the number of fitted parameters by setting the maximum peak widths as well. This is done by using an average of widths observed in this work and those observed in the literature.<sup>9,11,16</sup> The ratio of peak intensities for the symmetric and asymmetric line pairs were not set, however, since the diamond environment is ill-defined, and it is possible for this ratio to vary considerably. A common example of such behavior is observed in the infrared spectra of straight chain hydrocarbons such as tetradecane.<sup>21</sup>

The fits for two of the diamond films studied are also shown in Figure 3. The first film shows no  $\text{sp}^2$  bonded CH-stretch absorptions ( $>2950\text{ cm}^{-1}$ ), while the second shows an absorption at  $3025\text{ cm}^{-1}$ , indicative of an  $\text{sp}^2$  bonded CH

group. SEMs of the samples show a decline in the morphology of the second film, which is also consistent with an increase in  $sp^2$  bonded material. The dominant absorptions in both spectra appear near  $2850\text{ cm}^{-1}$  and  $2920\text{ cm}^{-1}$  and are indicative of the symmetric and asymmetric stretching of  $\text{CH}_2$  groups, respectively, where the carbon is  $sp^3$  bonded. Both of these spectra clearly demonstrate the inequality in absorption intensity for the symmetric and asymmetric absorptions of  $sp^3$  bonded  $\text{CH}_2$  groups in the diamond environment. This inequality, where the intensity of the asymmetric line is greater than that of the symmetric was observed in the majority of the films studied here, and is also observed in long-chain hydrocarbons.<sup>21</sup> About one-third of the films demonstrated equal intensities or slightly greater intensity in the symmetric line. The somewhat less intense absorptions present in the spectrum at  $2880\text{ cm}^{-1}$  and  $2960\text{ cm}^{-1}$  are similarly related to the symmetric and asymmetric stretching vibrations of  $sp^3$  bonded  $\text{CH}_3$  groups. These absorptions have been identified previously in CVD diamond as well,<sup>8-11</sup> and also demonstrate unequal absorption intensities. In addition, there is an absorption at  $\sim 3025\text{ cm}^{-1}$  in the second spectrum which is related to  $sp^2$  bonded  $\text{CH}$  groups and is not observed in CVD diamond which demonstrates high optical transmission and/or high thermal conductivity.

Two other absorptions have also been observed in CVD diamond, both here and in earlier studies, but their origin has remained unidentified.<sup>8-11</sup> These absorptions appear at frequencies below those normally observed for  $\text{CH}$  stretching vibrations in alkanes and amorphous carbon and are present to some extent in all of the samples studied here. They have been observed in films produced by microwave, hot-filament, and DC arc-jet deposition. One possibility which has been suggested, relates the peak at  $2820\text{ cm}^{-1}$  to the

hydrogen terminated <111> surface of diamond.<sup>11</sup> Here, we suggest that the absorptions at 2820 cm<sup>-1</sup> and 2833 cm<sup>-1</sup> can be attributed to nitrogen and oxygen related defects. They are the CH stretch vibrations of the carbon-hydrogen bond in an N-CH<sub>3</sub> and O-CH<sub>3</sub> group, respectively. Observation of these groups is well documented in the organic chemistry literature and is considered positive identification of such a group, as no other characteristic CH-stretch absorptions appear at such low frequencies.<sup>13-15</sup> Table II summarizes the CH stretch absorptions of all 16 films studied. Although areas for individual peaks are given, they are not intended to be quantitative. Even with the peak linewidths and central frequencies specified, the large number of remaining adjustable parameters and poor resolution of some spectral features leads to large uncertainties in the area of specific peaks. It is important to note, however, that some features of the spectra, specifically the relatively narrow peaks at 2820 cm<sup>-1</sup> and 2833 cm<sup>-1</sup>, are well resolved in all cases and show remarkable consistency in peak position.

The presence of oxygen and nitrogen is important in CVD diamond because these impurities are known to cause absorptions in the 8-12 μm wavelength region, where transparency is critical for many applications. Additional evidence of both oxygen and nitrogen incorporation in the films can be obtained on examination of this normally symmetry-disallowed one-phonon region. An expansion of the IR spectra shown in Figure 2, between 900 cm<sup>-1</sup> and 1800 cm<sup>-1</sup>, is shown in Figure 4. There are a number of absorptions present, many of which can be related to oxygen and nitrogen containing groups, including O-CH<sub>3</sub> and N-CH<sub>3</sub> specifically. These identifications are found in Table III.<sup>14-16</sup> In addition to the O-CH<sub>3</sub> and N-CH<sub>3</sub> groups, oxygen and nitrogen can be present in other forms, as well. For example, absorptions at 1130

and  $1350\text{ cm}^{-1}$  may be related to substitutional nitrogen defects<sup>12</sup>, and the peaks at  $1740$ ,  $2700$  and  $2730\text{ cm}^{-1}$  (see Figure 2) are suggestive of aldehyde groups.<sup>16</sup> The presence of substitutional nitrogen in the film discussed above was also confirmed by photoluminescence. Finally, XPS combined with sputtering was used to confirm the presence of both oxygen and nitrogen in several films, produced over the full range of process conditions, at depths of up to  $750\text{ \AA}$ . Evidence of carbon-oxygen bonding was observed in the O1s XPS spectra of all films, and evidence of  $\text{C}=\text{O}$  was observed in for several of those films demonstrating the three characteristic aldehyde peaks.

As mentioned above, evidence of  $\text{N-CH}_3$  and  $\text{O-CH}_3$  groups has been observed in the IR spectra of diamonds produced by a variety of techniques, including microwave, hot-filament, and DC-arc jet CVD, and in processes which intentionally added oxygen as well as those that did not.<sup>8-11</sup> This indicates that air leaks in diamond CVD reactors are sufficient to cause incorporation of both nitrogen and oxygen to levels which are detectable in the IR and cause optical absorptions in regions of commercial interest. This has important implications for the design of diamond growth systems, which are not generally of ultra-high vacuum quality at the present time. In addition, there are serious implications for the production of high optical quality CVD diamond in processes which require oxygen addition.

Additional information about the bonding environment of hydrogen in CVD diamond can be obtained from the IR data when combined with information obtained from solid-state NMR spectroscopy. This technique allows us to quantify the amount of hydrogen in all bonding configurations in the



sample. Figure 5 shows the  $^1\text{H}$  NMR spectrum of a typical diamond film. The spectra contains two components, a broad Gaussian and a narrow Lorentzian. The integrated area under the two peaks is directly proportional to the number of hydrogen nuclei in the sample. By comparison of the total signal intensity with that of a known standard, we can obtain quantitative hydrogen contents for the diamond films. These contents are listed in Table II.

The Lorentzian component makes up a relatively small fraction of the total NMR signal. This component has a narrow lineshape at 298 K which broadens significantly as the temperature is reduced to 100 K. Thus a small fraction of the hydrogen is mobile at room temperature. Hole burning studies indicate that the hydrogen related to the Lorentzian and Gaussian components are strongly dipole coupled, corresponding to a proton-proton separation of  $< 6\text{\AA}$ . The mobile hydrogen could arise from a small molecule trapped at a void or grain boundary or from a mobile group attached to the surface. While trapped  $\text{H}_2$  has been identified in amorphous silicon, its motion would not be expected to cease at or above 100 K, making its presence in polycrystalline diamond unlikely. However, mobile surface species such as methyl groups must also be considered. The IR spectroscopy results discussed above suggest that a number of types of surface methyl groups:  $\text{CH}_3$ ,  $\text{O-CH}_3$ , and  $\text{N-CH}_3$ . The  $\text{CH}_3$  group bonded directly to a diamond surface can rotate only about its  $\text{C}_3$  axis, which would allow insufficient motion to account for the narrowness typically observed in the Lorentzian component. However, methyl groups found at steps and growth ledges and those attached to heteroatom would have additional motional degrees of freedom and may account for the narrow Lorentzian lineshape. This is not unreasonable since such groups generally make up a very small fraction ( $\sim 1\%$ ), as does the Lorentzian component, of the hydrogen found in these samples.

The majority of the hydrogen in these samples contributes to the signal of the Gaussian component of the NMR lineshape. This component is related to static closely spaced hydrogen with an average interproton spacing of  $\sim 2 \text{ \AA}$ . This value is calculated from the van Vleck equation which relates the experimentally observed full-width at half-maximum (FWHM) of a Gaussian lineshape to the interproton spacing.<sup>18</sup> A simplified version of that equation is:

$$\text{FWHM}_G = 189.6(\sum r_{ij}^{-6})^{1/2} \text{ \AA}^3 \text{ kHz} \quad (3)$$

The calculated interproton spacing is significantly smaller than would be observed if static hydrogen atoms were uniformly distributed throughout the bulk, indicating instead regions of high local density. In addition, the presence of a dense, two-dimensional hydrogen phase in CVD diamond was been confirmed by multiple quantum NMR in an earlier study.<sup>19</sup> Both results are consistent with the interpretation of hydrogen terminated grain boundaries.

The correlation of the total hydrogen content with the normalized integrated intensity in the CH stretch region of the IR spectra indicates that most of the hydrogen found in these diamond films is covalently bonded to carbon. A plot of the normalized CH stretch area as a function of hydrogen content is shown in Figure 6. There is a linear relationship between the two for films with hydrogen contents below 0.2 atomic %. This is consistent with earlier results, which examined films with hydrogen contents of 0.1 atomic % or lower.<sup>8</sup> At hydrogen contents above 0.2 atomic %, this linear correlation no longer holds. Figure 6 suggests a different slope for these high hydrogen content films, however, there is insufficient data to draw conclusions about functionality. This type of behavior may be indicative of a different hydrogen containing phase,

present at higher hydrogen contents, which exhibits a different absorption coefficient from that found in films with lower hydrogen concentrations.

It is reasonable, then, to ask if the measured hydrogen contents are consistent with grain boundary coverage. Figure 7 shows SEM's of two of the films discussed in this work. It demonstrates the large disparity in grain size between and among individual films, as well as the difficulty in obtaining accurate grain size estimates for some of the materials. Variations in grain size as a function of film thickness interfere with the accurate estimate of grain boundary area, as well.<sup>20</sup> If we assume, for the sake of argument, that the grain sizes vary between 0.5 and 100  $\mu\text{m}$  with a surface coverage of  $3 \times 10^{15} \text{ H/cm}^2$  (which is within the range of values for various crystal planes of diamond), the highest hydrogen content which can be accounted for by grain boundary coverage (that is, a film with an average crystal size of 0.5  $\mu\text{m}$ ) is  $\sim 0.2$  atomic %. However, values as high as 0.5 atomic % have been observed in this work, indicating that some other form of hydrogen may exist.

It is interesting that the correlation between total hydrogen content and the absorption in the CH stretch region of the IR spectrum may indicate a change in absorption characteristics at 0.2 atomic % as well. This would support the model of hydrogen terminated grain boundaries in diamond films with low hydrogen content, while suggesting the presence a different hydrogen environment or combination of environments in films with hydrogen contents greater than 0.2 atomic %. Since each of these high hydrogen content films show evidence of  $\text{sp}^2$  bonded carbon in both the IR and Raman spectra, the presence of a different phase of hydrogen is not unreasonable.

## Conclusions

Infrared spectroscopy has been used to identify defects giving rise to optical absorptions in CVD diamond. These results have demonstrated the incorporation of hydrogen, nitrogen, and oxygen in CVD diamond films, each having some effect on the optical absorption in regions of commercial interest. This has important implications for processes which require oxygen addition to the growth environment as well as for the design of CVD diamond systems, since small air leaks are sufficient to cause observable oxygen and nitrogen incorporation. Absorptions due to nitrogen and oxygen groups which have not been previously understood in CVD diamond have been identified. In films which show some  $sp^2$  bonding and high hydrogen incorporation, evidence indicates that a different form of hydrogen, other than that found terminating the diamond surface at the grain boundaries, may be present.

## Acknowledgments

The authors would like to thank Dr. P.J. Codella, J.J. Chera, S.J. Duclos and Dr. J.A. Sutliff of General Electric Company, Corporate Research and Development for their assistance with portions of the analytical characterization for this work. MIT would also like to acknowledge the support of the Office of Naval Research.

## References

1. R. C. Devries, *Annu.Rev. Mater. Sci.*, **17**, 161 (1987).
2. F.G. Celii, and J.E. Butler, *Annu. Rev. Phys. Chem.*, **42**, 643 (1991).
3. P.K. Bachman, D. Leers, and H. Lydtin, *Diamond & Related Materials*, **1**, 1 (1991).
4. A. Inspektor, Y. Liou, T. McKenna, R. Messier, *Surface & Coatings Technology*, **39/40**, 211 (1989).
5. P.K. Bachman et. al., *Diamond Films '93*, in press (1993).
6. T. Kawato and K. Kondo, *Jpn. J. Apl. Phys.*, **26(9)**, 1429 (1987).
7. C.P. Chang, D.L. Flamm, D.E. Ibbotson, and J.A. Mucha, *J. Appl. Phys.*, **63(5)**, 1744 (1988).
8. K.M. McNamara, D.H. Levy, K.K. Gleason, and C.J. Robinson, *Appl. Phys. Lett.*, **60(5)**, 580 (1992).
9. K.M. McNamara, K.K. Gleason, and C.J. Robinson, *J. Vac. Sci. Technol. A*, **10(5)**, 3143 (1992).
10. K.M. McNamara and K.K. Gleason, *Chem. Mat.*, in press.
11. B. Dischler, C. Wild, W. Muller-Serbet, and P. Koidl, *Physica B*, **185**, 217 (1993).
12. C. Klein, T. Hartnett, R. Miller, and C.J. Robinson, *Proceedings of the 2nd International Conference on Diamond Materials* (ECS, Pennington, NJ 1991), 435.
13. A. Abragam, *The Principles of Nuclear Magnetism* (Oxford University, New York, 1983).
14. I.A. Degan, *Appl. Spec*, **22(3)**, 164, 1968.
15. L.J. Bellamy, *The Infrared Spectra of Complex Molecules*, Vol. 2, Chapman and Hall, NY, 1980.
16. G. Socrates, *Infrared Characteristic Group Frequencies*, John Wiley & Sons, NY, 1980.
17. H. Lock, R.A. Wind, G.E. Maciel, and C.E. Johnson, *J. Chem. Phys.* **99(5)**, 3363 (1993).
18. J.H. van Vleck, *Phys. Rev.* **74**, 1168 (1948).

19. D.H. Levy, and K.K. Gleason, J. Vac. Sci. & Technol. A, **11**, 195 (1993).
20. J.E. Graebner, S. Jin, G.W. Kammlot, J.A. Herb, and C.F. Gardner, Appl. Phys. Lett., **60**, 1576 (1992).
21. *Aldrich Library of FT-IR Spectra*, Edition 1, Vol. 1 & 2, Charles J. Pouchert, Editor, Milwaukee, WI., 1985.

## Figure Captions

**Figure 1.** Infrared transmission spectrum of a CVD diamond film demonstrating high optical transparency. Spectrum of natural diamond shown for comparison.

**Figure 2.** IR absorbtion spectrum of a CVD diamond film demonstrating significant absorbtions in the one, two, and three phonon regions. The y-axis is absorbance in arbitrary units.

**Figure 3.** Least-squares fit of characteristic peaks in the CH-stretch region of the IR spectra for two CVD diamond films. a) No  $sp^2$  related absorbtions. b) Absorbtions related to  $sp^2$  carbon. The y-axis is absorbance in arbitrary units.

**Figure 4.** Absorbtion in the one-phonon region of the IR spectrum of a typical CVD diamond sample. The y-axis is absorbance in arbitrary units.

**Figure 5.** Solid-state hydrogen NMR spectrum of a typical CVD diamond film, demonstrating characteristic Lorentzian and Gaussian lineshapes.

**Figure 6.** Correlation of the normalized absorbtion in the CH-stretch region of the RI spectra with the total hydrogen content, as measured by NMR, for 16 CVD diamond samples.

**Figure 7.** Scanning electron micro graphs (SEM) of two CVD diamond films demonstrating the variations in grain size between films and within individual samples.

Table I. Characteristic CH Stretching Vibration Frequencies

<u>Frequency (cm<sup>-1</sup>)</u>	<u>Characteristic Group</u>
2850	sym. sp <sup>3</sup> -CH <sub>2</sub>
2880	sym. sp <sup>3</sup> -CH <sub>3</sub>
2920	asym. sp <sup>3</sup> -CH <sub>2</sub>
2960	asym. sp <sup>3</sup> -CH <sub>3</sub>
2980	sym. sp <sup>2</sup> -CH <sub>2</sub>
3025	sp <sup>2</sup> -CH
3080	asym. sp <sup>2</sup> -CH <sub>2</sub>



**Table II. Areas of IR Absorptions Observed in the CH Stretch Region and Hydrogen Contents**

Frequency: (cm <sup>-1</sup> )	2820	2833	2850	2880	2920	2960	3025	H-content
	Relative Percentage of CH Stretch Area (%)							
Sample:								
1	8.1	3.2	21.9	24.5	26.9	15.4	---	0.045
2	9.3	6.5	16.7	21.1	28.9	12.8	4.7	0.320
3*	5.5	1.8	42.1	---	38.4	12.2	---	0.490
4	7.0	0.7	33.6	9.1	31.6	18.0	---	0.085
5	13.2	0.5	24.2	16.2	29.7	16.2	---	N/D
6*	17.7	0.8	27.4	18.4	17.9	17.8	---	0.027
7*	10.3	2.7	33.0	2.9	37.5	13.6	---	0.180
8	14.3	1.9	18.8	16.7	26.4	18.3	3.6	0.043
9	16.5	0.5	20.1	14.6	26.1	19.0	3.2	0.020
10	16.2	1.0	17.0	19.0	24.3	19.4	---	0.045
11*	10.4	0.8	23.0	21.5	23.8	17.2	3.1	0.092
12	9.9	1.8	20.0	20.3	27.1	17.3	3.3	0.150
13	18.0	1.0	12.1	21.6	26.4	20.9	---	0.039
14*	16.3	0.3	25.4	14.7	22.3	17.6	3.4	0.085
15*	14.4	1.9	9.6	26.3	21.1	26.7	---	0.027
16*	14.7	0.3	20.5	22.2	18.7	20.6	3.0	0.016

\*Indicates that these samples also show peaks at ~ 2700 cm<sup>-1</sup> and/or 2730 cm<sup>-1</sup>.  
N/D indicates no data available.

Table III. IR Absorptions Observed Below 1800 cm<sup>-1</sup>

<u>Frequency</u>	<u>Functional Group</u>
1740	C=O, stretch
1610	C=C, stretch, isolated
1500's	C=C, aromatic stretch
1450	O-CH <sub>3</sub> , N-CH <sub>3</sub> , deformation
	sp <sup>3</sup> -CH <sub>2</sub> , scissor
1375	N-CH <sub>3</sub> , scissor
	sp <sup>3</sup> -CH <sub>3</sub> , deformation
1350	substitutional N
1332	disallowed one-phonon mode
1250	C-N
	nitrogen-vacancy pair
1220	C-N, stretch
1130-1150	O-CH <sub>3</sub> , N-CH <sub>3</sub> , rock
	substitutional N
1030	O-CH <sub>3</sub> , deformation

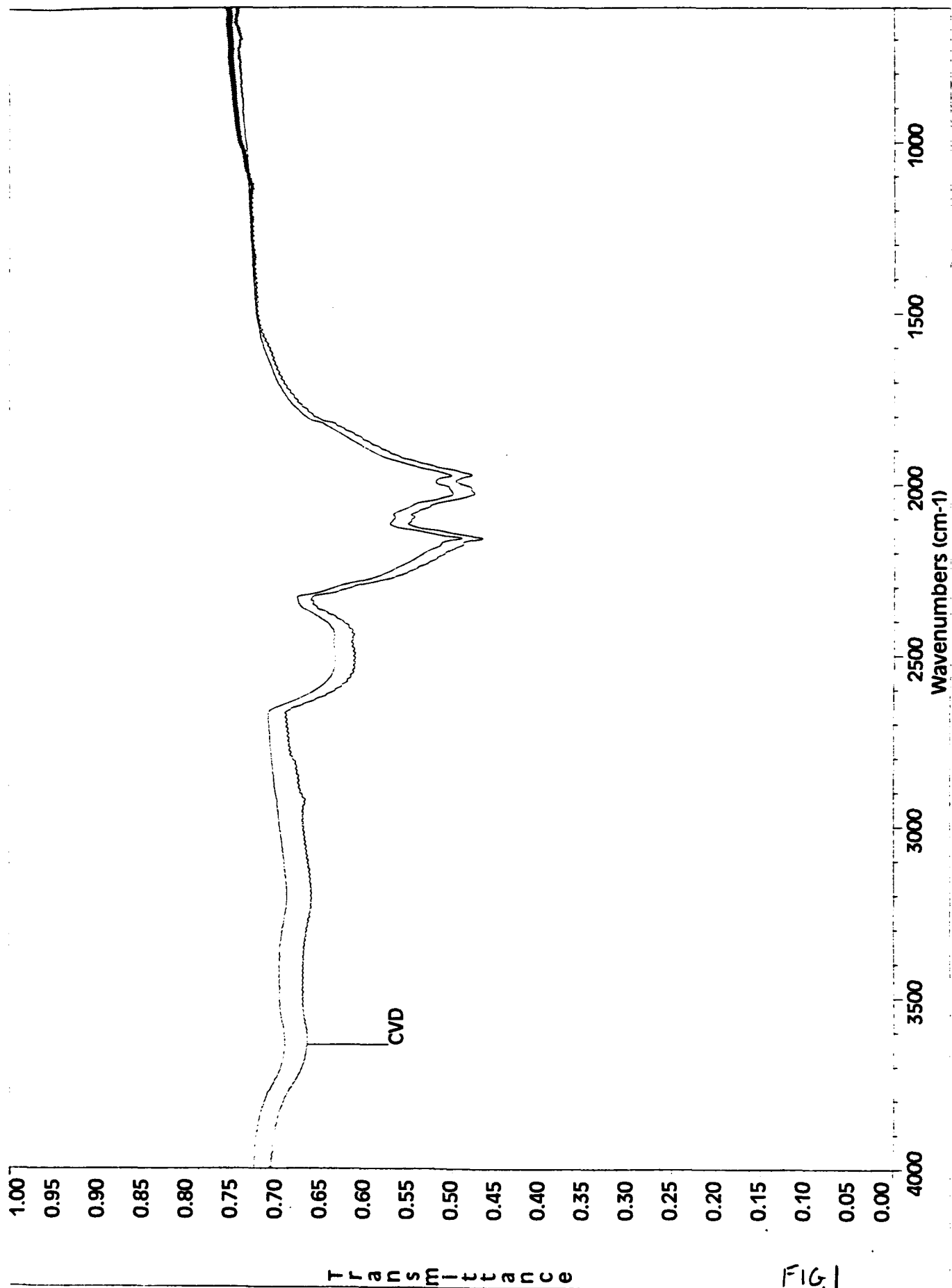


FIG. 1

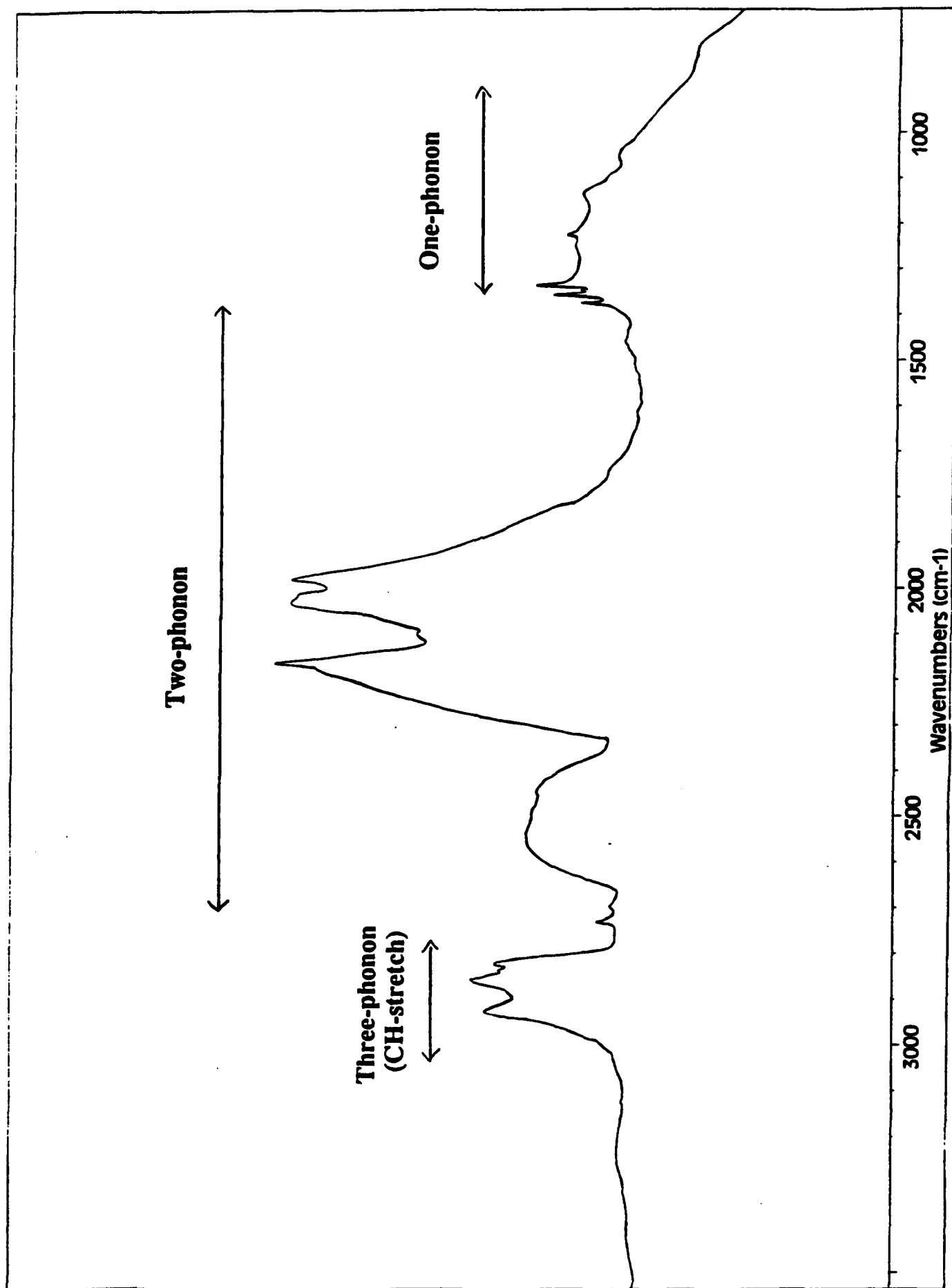


FIG 2

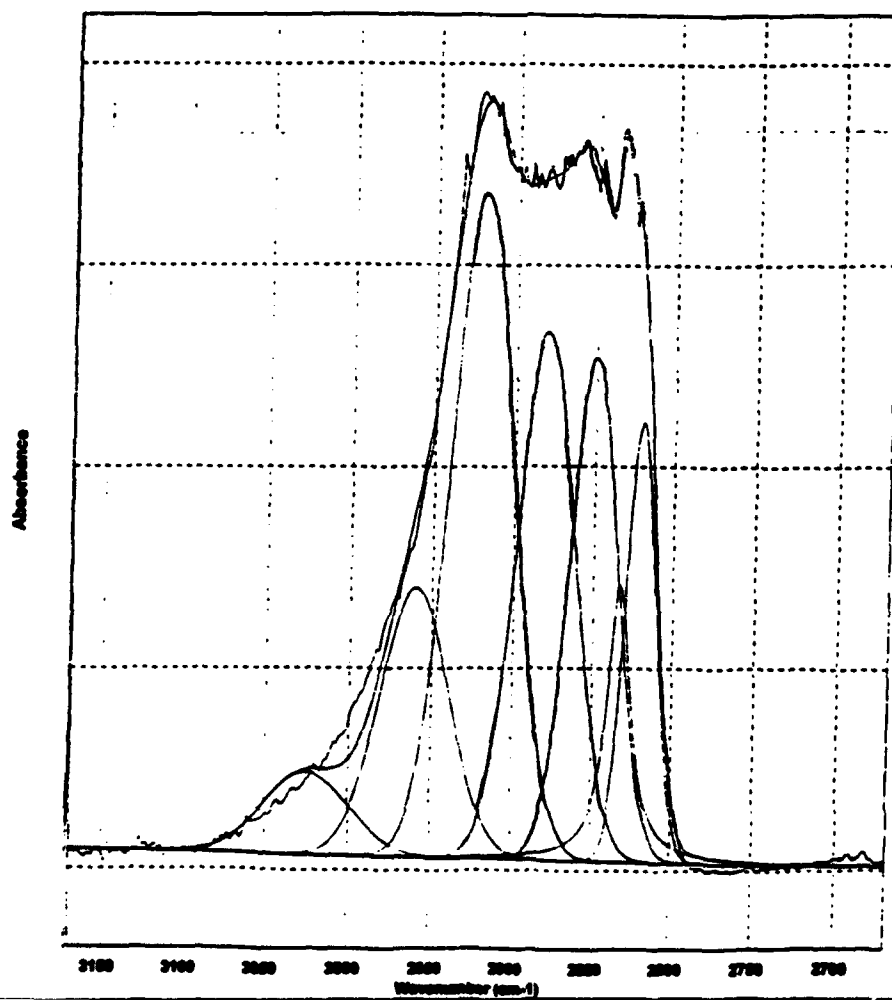
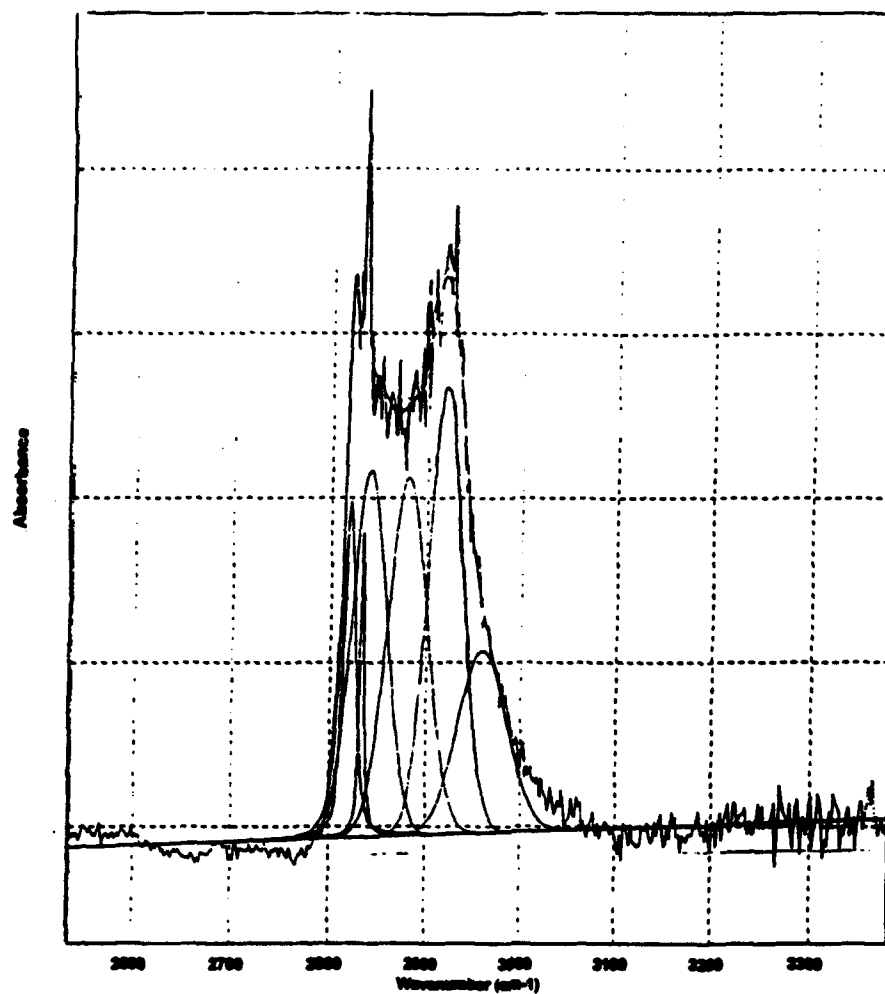


FIG 3

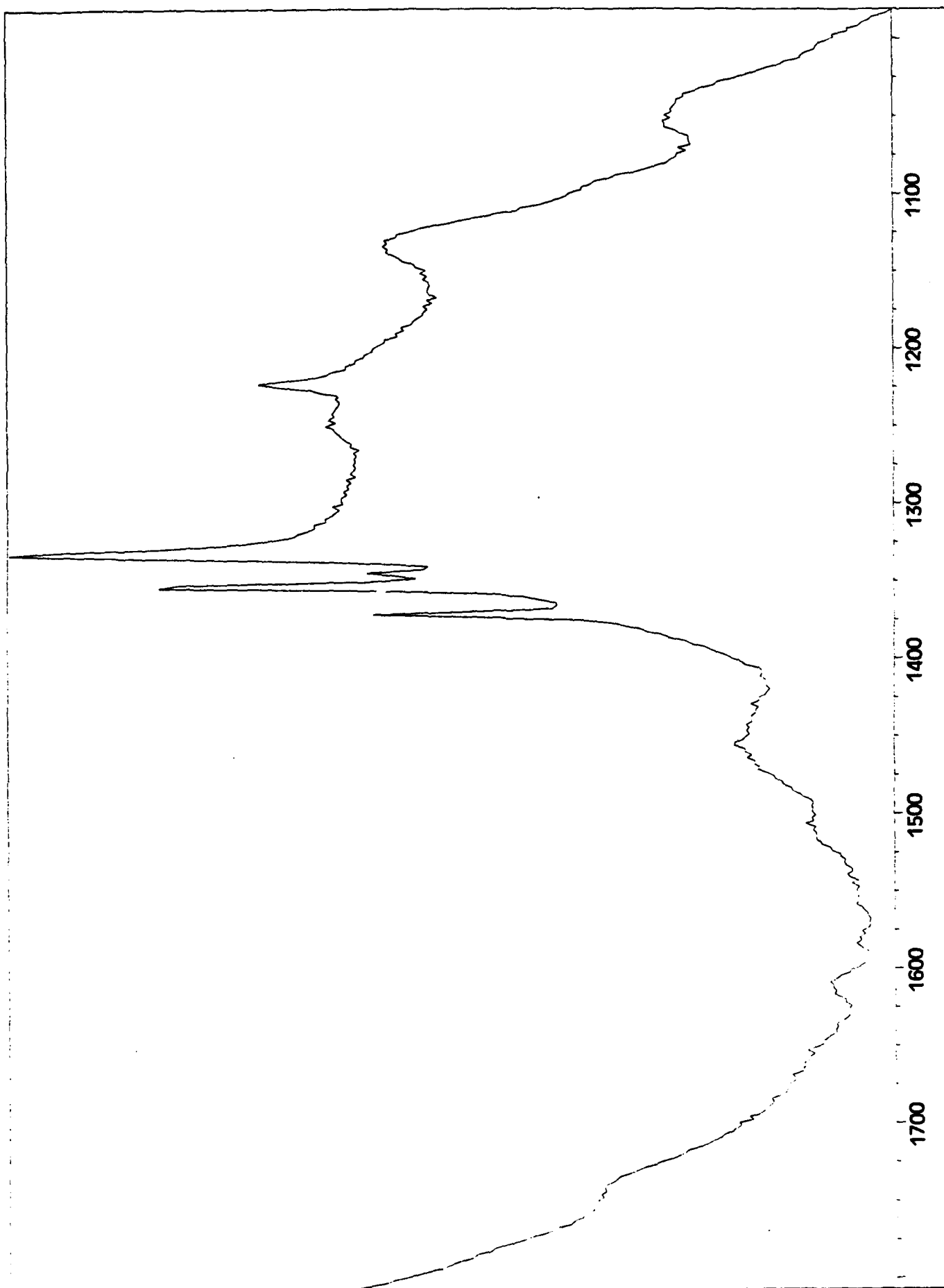


Figure 4

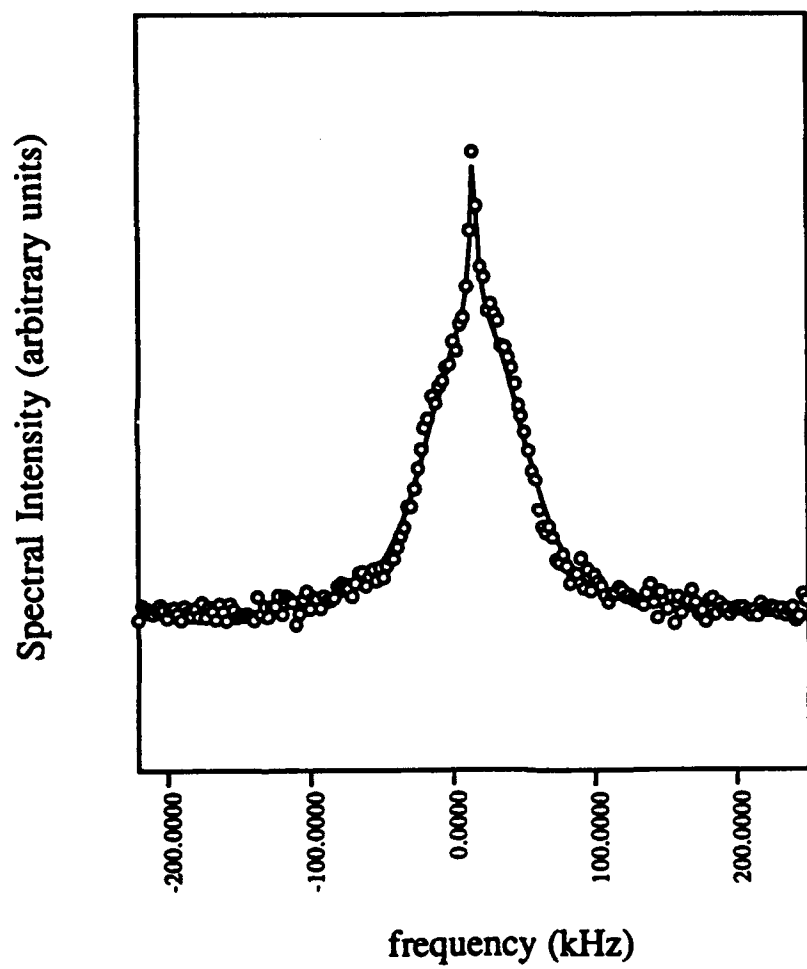


Figure 5

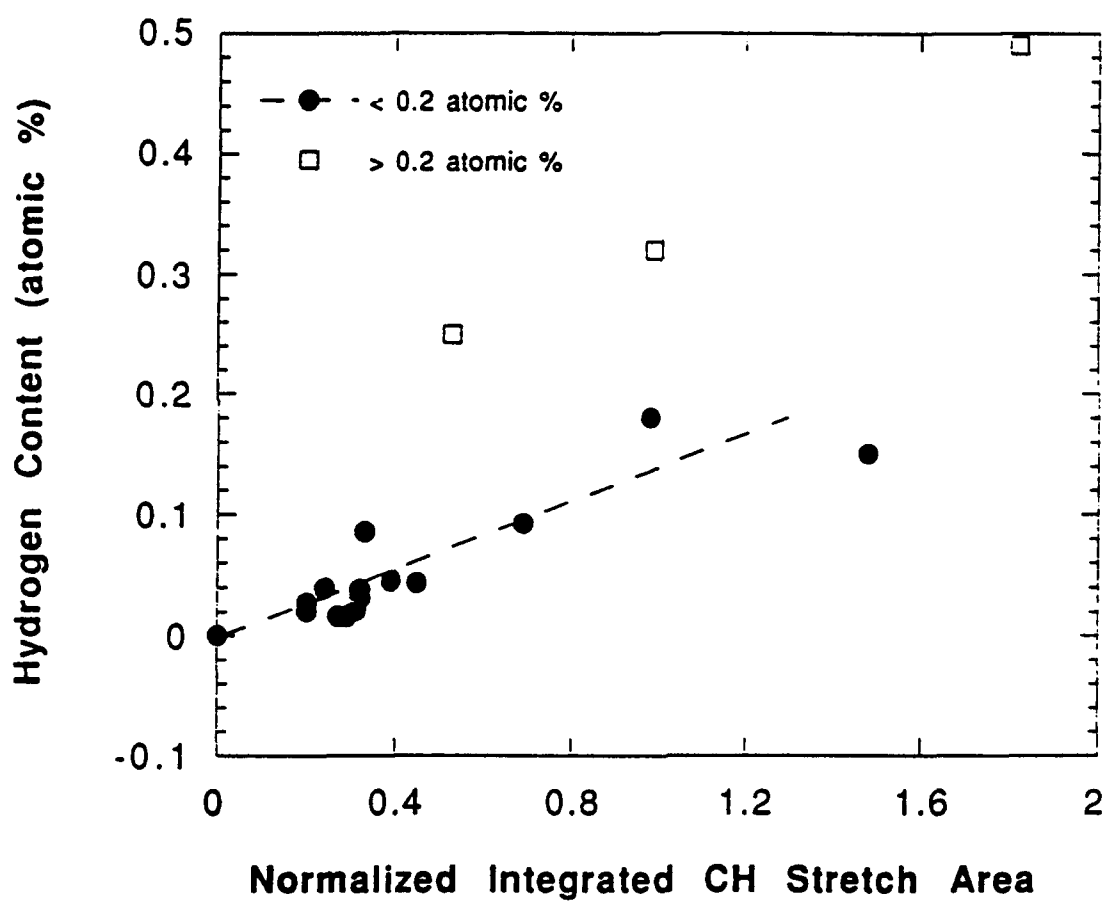


FIG 6



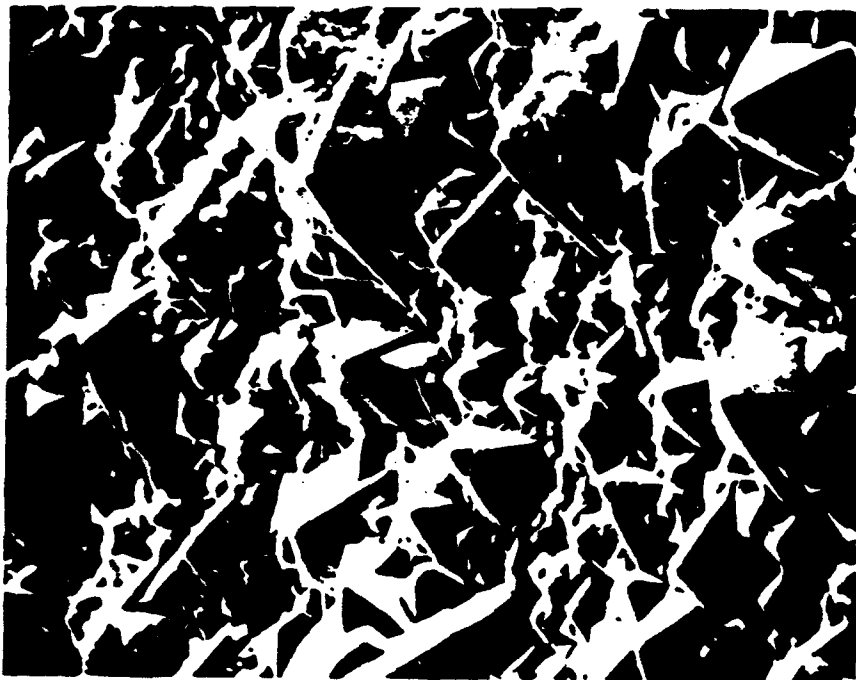
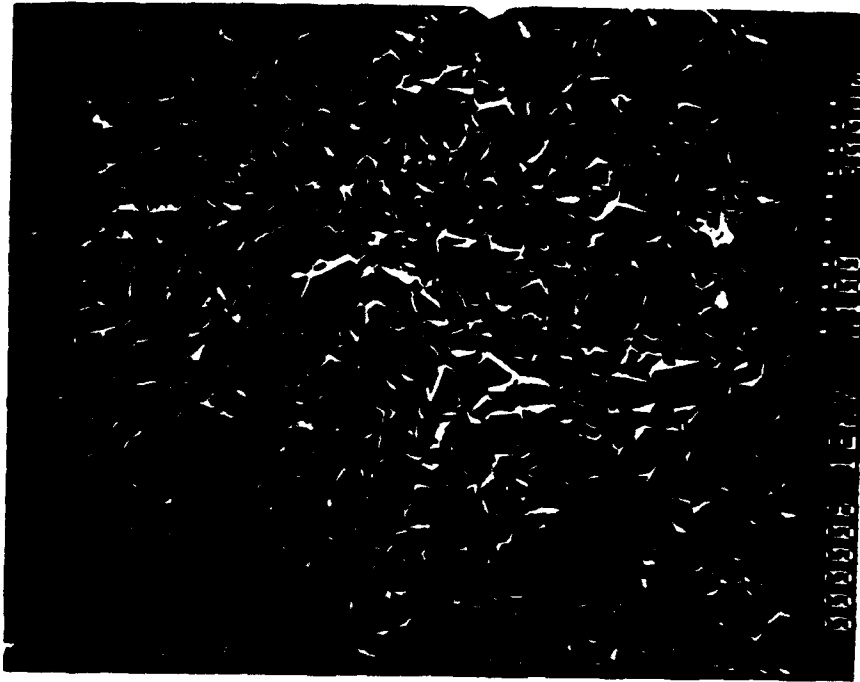


FIG. 7